

INTEGRATED MODELING APPROACH FOR SOLID OXIDE FUEL CELL-BASED POWER
GENERATING SYSTEM

by

JEONGPILL KI

Presented to the Faculty of the Graduate School of
The University of Texas at Arlington in Partial Fulfillment
of the Requirements
for the Degree of

DOCTOR OF PHILOSOPHY

THE UNIVERSITY OF TEXAS AT ARLINGTON

May 2013

Copyright © by JEONGPILL KI 2013

All Rights Reserved

Dedication

To God in Heaven

To my precious mother ImSun Park for her endless belief and love to me

To my wife SangSu Park for her eternal love, her outstanding support, and confidence to me

To my lovely daughter Ashley Ki; her presence itself is a present and blessing for me from God

Acknowledgements

I would like to express the deepest appreciation to my advisor, Dr. DaeJong Kim, who has the attitude and the substance of a genius/superman. Several times, I called him a superman in front of him during my research. He takes care of many things such as managing/earning projects, advising graduate students, taking care of his family, teaching undergraduate/graduate courses, etc at the same time. In my position, he seemed like a superman and I also would like to be like him in the future. He continuously and convincingly conveyed a spirit of adventure in regard to research and scholarship, and an excitement with respect to teaching. Without his guidance and persistent help, this dissertation would not have been possible. I also would like to thank my committee members, Dr. SeungMun You, Dr. Cheng Luo, Dr. Brain Dennis, and Dr. Fuqiang Liu for their encouraging words, thoughtful criticism, and time and attention during busy semesters.

I would like to thank all the faculty members of the Department of Mechanical Engineering at the University of Texas at Arlington for their generous sharing of their knowledge and resources throughout my graduate studies. I would like to thank the ME staff, Mrs. Denalia Gordon, who has always greeted and talked to me with a great smile and a warm heart and has helped me in many ways, and Mrs. Debi Barton, who assisted me with the administrative tasks necessary for completing my doctoral program. I am also grateful to Mrs. Janet Gober, Mrs. Sally Thompson, and Mrs. Louella Carpenter for their kind assistance when I need any help from them. I thank for the Catacel Company and Sierra Instruments for their sharing of resources and expertise with regard to Heat Exchanger, Reformer, mass flow controller, etc.

I would like to thank with my heart to my former and current colleagues, Mr. Prajwal Krishna Shetty, Mr. Ramesh Sadashiva, Dr. DongHyun Lee, Mr. Mohamed Hossain, Mr. Mahesh Varrey, Mr. Suman Shresta, Mr. Chris Wang, Mr. Srikanth Prasad (Cheeku), Mr. Srikant Yadav, Mr. Sandesh Gudamene, Mr. Lohit Yadav, Mr. Zain Kachwala, Mr. Songwei Wang, Mr. Tejas Patil, Mr. Behzad Zamanian Yazdi, Mr. Maulin Gajjar, and Mr. Mauricio Jaguan.

I am also greatly appreciating my spiritual mentors, Mr. KiYeon Yun, Pastor KyungHwan Park, Mr. EulGon Park, Pastor WooChul Lee, and Mrs. Cheryl's family for their spiritual prayer and love for our family. They showed me how to continuously live a life as a born-again Christian.

I would sincerely like to thank my younger brother, ChungGon Ki, His lovely wife HaeJung Park, my nephew MinChan Ki, and my future nephew anonymity. He helped my parents economically and spiritually on behalf of me. "Brother, without your help, I couldn't finish my degree here. I love you"

I thank my parents-in-law, MiJa Hwang and JongHyun Park for giving me such a wonderful wife to me. My mother-in-law continuously prayed for my family at dawn for several years. I really appreciate for your prayer. Actually, it was an invaluable help for me.

Last, I want to thank my parents, ImSun Park, and YoungHan Ki without whom I would never have been able to achieve so much. I especially wish to express my sincere love for my wife, SangSu Park with all my heart. She endures and endures for our common goal with me. "Thank you, my lovely wife. I am so lucky to meet you for my eternal partner. I love you" And, God gave us lovely daughter, Ashley. Without her, I couldn't stand this tough life in the United States. I bless and love you, Ashley.

March 25, 2013

Abstract

INTEGRATED MODELING APPROACH FOR SOLID OXIDE FUEL CELL-BASED POWER GENERATING SYSTEM

JEONGPILL KI, PhD

The University of Texas at Arlington, 2013

Supervising Professor: Dr. Daejong Kim

Solid oxide fuel cell (SOFC) systems have been recognized as the most advanced power generation system with the highest thermal efficiency with a compatibility with a wide variety of hydrocarbon fuels, synthetic gas from coal, hydrogen, etc. As a result of research focused on numerical studies for a tubular type- or a planar type-SOFC, fuel flexibility, design aspects of SOFC, materials, start-up process, and so on, SOFC technologies are remarkably being developed.

Currently, most research activities are limited to a component level characterization of single fuel cell stack or material research for catalyst, electrolyte, sealing process, etc. In other words, approaches for developing an integrated SOFC system with combined heat and power (CHP)/power generation system for transient analysis have been limited. During normal operating modes of a SOFC system, optimal control of fuel and air supply and anode gas recirculation relies on accurate dynamic analysis of the entire SOFC system. With this research, integrated modeling approaches of SOFC stack with heat exchanger (HEX), compact heat exchange reformer (CHER), steam supply system, compressor or blower, ducts, etc. were introduced and developed for a power generation system. And, simulational results were validated with experimental results.

The specific dynamic design tools for an integrated SOFC-based power generation system are as follows: 1) computational model for thermal dynamics of planar SOFC stack during stack heating process w/o production of electricity, 2) validation of simulational result of transient characteristics of the HEX with experimental result during the initial phase of start-up of small SOFC systems, 3) validation of simulational result of transient characteristics of the CHER with experimental result during the initial phase of start-up of small SOFC systems, and 4) development of model for dynamic communication between the developed stages out of fully integrated micro (~10kW) SOFC-based power generation systems.

As a result of the researches, the computational software was developed to investigate the start-up process of SOFC without producing electricity. And, novel transient codes were developed that explain the dynamics of HEX and CHER. Test rigs for the experiment of HEX and CHER were developed. Performances of the HEX and CHER were well demonstrated experimentally and were validated with simulational results. Each developed sub-module was integrated to build up the integrated SOFC system step by step. In the final session, the integrated module was completed by including an electricity production module. The developed integrated SOFC system module provides guidance for establishing the fundamental design characteristics and a direction for choosing suitable HEX, reformer, compressor, etc.

Table of Contents

Acknowledgements.....	iv
Abstract.....	vi
List of Illustrations	xii
List of Tables.....	xviii
List of Acronyms	xix
Chapter 1 Introduction to Solid Oxide Fuel Cell	1
1.1 SOFC components	1
1.1.1 Electrolyte.....	2
1.1.2 Cathode	3
1.1.3 Anode	3
1.1.4 Interconnector.....	4
1.1.5 Sealing material.....	5
1.2 Practical Cell and stack design	5
1.2.1 Tubular design.....	5
1.2.2 Planar design.....	8
1.3 Typical SOFC performance	8
1.3.1 Effect of pressure	8
1.3.2 Effect of Temperature.....	9
Chapter 2 Literature review and Scope of Research	10
2.1 Typical SOFC start-up process.....	10
2.2 Literature review on SOFC stack/system modeling	14
2.3 Scope of Research	15
2.4 Stack Heating	16

2.5 Heat Exchanger	17
2.6 Compact Heat Exchange Reformer (CHER)	18
2.7 SOFC Electric Power Generation Mode	21
2.8 Integration of each sub-module	22
Chapter 3 SOFC stack start up process	23
3.1 SOFC design and simulation work.....	23
3.2 Stack Discretization	25
3.3 Modeling	27
3.3.1 Momentum equation	27
3.3.2 Energy equation to gas flow	28
3.3.3 Energy equation to solid structures	29
3.3.4 Discretization	31
3.4 Results.....	32
Chapter 4 Heat Exchanger	53
4.1 Heat exchanger configuration	53
4.2 Flow channel modeling	55
4.3 Results.....	56
Chapter 5 Compact Heat Exchange Reformer	63
5.1 Scope of this research	63
5.2 CHER configuration and flow channel modeling.....	63
5.3 System Layout for the simulation.....	66
5.4 System Layout for the experiment	70

5.5 Modeling	73
5.5.1 Air channels.....	73
5.5.2 FSM channels.....	75
5.6 Results.....	79
5.6.1 Simulation.....	79
5.6.2 Equilibrium calculation of the molar fraction of each species due to the SR and WGS reactions	93
5.6.3 Experiment	95
Chapter 6 SOFC Electric Power Generation Mode.....	102
6.1 Modeling	102
6.1.1 Resistivity	102
6.1.2 Contact and Ionic Resistances	102
6.1.3 Reversible voltage	104
6.1.4 Activation loss and Ohmic loss.....	105
6.2 Electric circuit modeling	106
6.3 Thermal Dynamics of SOFC.....	110
6.4 Case studies	113
6.5 Results.....	114
Chapter 7 Integration of each sub-module.....	119
7.1 Introduction	121
7.2 Design process	122
7.3 Results.....	125
Chapter 8 Summary.....	133
8.1 SOFC start-up process	133

8.2 Both Simulation and Experiment of HEX	134
8.3 Simulation of CHER.....	134
8.4 Experiment of CHER	135
8.5 SOFC Electric Power Generation Mode	136
8.6 Integrated SOFC system	137
Appendix A A manual for 1-kW SOFC stack design	139
Appendix B ANSYS Fluent SOFC module manual	142
Appendix C Classification of all variables in each modul	149
Appendix D The HEX Experimental Set-up	173
Appendix E The CHER Experimental Set-up.....	179
Appendix F Etc.....	185
References.....	188
Biographical Information	194

List of Illustrations

Figure 1-1 Cross-section of a tubular SOFC [2]	7
Figure 1-2 Configuration of a tubular SOFC [3]	7
Figure 1-3 Cross-section of a four-chamber flat-tubular type SOFC [2]	7
Figure 2-1 Start up process of the integrated SOFC system, CI: cathode inlet plenum, CE: cathode exit plenum, AI: Anode inlet plenum, AE: Anode exit plenum, COMB: combustor, M/C: mixing chamber, and C: compressor; (a) Stage 1: SOFC stack start-up with combustor, (b) Stage 2: Initiation of anode fuel line with reformer (CHER), and (c) Stage 3: Recirculation of unused fuel to the reformer inlet	13
Figure 3-1 Configuration of a planar SOFC	23
Figure 3-2 Simplified interconnector model without assembly holes and inlet and exit holes replaced by straight inlet and exit regions	24
Figure 3-3 Schematic of a discretized interconnector	25
Figure 3-4 Fractionized control volume	26
Figure 3-5 (i, j) th unit element (i=1~N _x , j=1~N _y)	26
Figure 3-6 Dimensions of an element of planar SOFC	27
Figure 3-7 Schematic diagrams of heat transfers in the SOFC stack; (a) Heat transfer along x-direction and Heat transfer along flow direction (y-direction)	31
Figure 3-8 Typical blower map under constant mass flow mode	35
Figure 3-9 Typical blower map under constant speed mode	36
Figure 3-10 Temperature distributions of gases and structures of SOFC stack including outer solid structure (1min.); (a) anode, (b) cathode, (c) interconnector, and (d) MEA	37
Figure 3-11 Temperature distributions of gases and structures of SOFC stack including outer solid structure (30min.); (a) anode, (b) cathode, (c) interconnector, and (d) MEA	38
Figure 3-12 Temperature distributions of gases and structures of SOFC stack including outer solid structure (1hr.); (a) anode, (b) cathode, (c) interconnector, and (d) MEA	39

Figure 3-13 Temperature distributions of gases and structures of SOFC stack including outer solid structure (2hrs.); (a) anode, (b) cathode, (c) interconnector, and (d) MEA.....	40
Figure 3-14 Temperature on central area of 2 nd solid structure in Figure 3-4	41
Figure 3-15 Required pressure drop over time to maintain the required mass flow rate	42
Figure 3-16 Heating Energy vs. time (Hot air feeding method)	43
Figure 3-17 Schematic diagrams of heat transfer from Furnace to the SOFC stack; (a) Electric heating outline and (b) Heat transfer from the electric furnace	44
Figure 3-18 Block diagram of simple proportional control for furnace heating	45
Figure 3-19 Temperature distributions of gases and structures of SOFC stack including outer solid structure (1min.); (a) anode, (b) cathode, (c) interconnector, and (d) MEA.....	47
Figure 3-20 Temperature distributions of gases and structures of SOFC stack including outer solid structure (30min.); (a) anode, (b) cathode, (c) interconnector, and (d) MEA.....	48
Figure 3-21 Temperature distributions of gases and structures of SOFC stack including outer solid structure (1hr.); (a) anode, (b) cathode, (c) interconnector, and (d) MEA.....	49
Figure 3-22 Temperature distributions of gases and structures of SOFC stack including outer solid structure (2hr.); (a) anode, (b) cathode, (c) interconnector, and (d) MEA.....	50
Figure 3-23 Net heating energy with different furnace heat inputs.....	51
Figure 3-24 Net heating energy vs. time (furnace heating).....	51
Figure 3-25 Net heating energy comparison between furnace and hot air heating method.....	52
Figure 4-1 (a) Configuration of HEX, (b) Components of the HEX and (c) flow direction of air..	54
Figure 4-2 Schematic diagrams of heat transfers in HEX; (a) Heat transfer along x-direction (channels cross section view) and (b) Heat transfer along flow direction (y-direction)	56
Figure 4-3 (a) Air pre-heater and (b) electric cabinet	57
Figure 4-4 The HEX test rig, (a) schematic diagram of the experimental apparatus and (b) overview of the test rig	58

Figure 4-5 HEX inlet pressure, measured and interpolated; (a) Pressure of hot air at inlet and (b) Pressure of cold air at inlet	59
Figure 4-6 HEX inlet temperature, measured and interpolated; (a) Temperature of hot air at inlet and (b) Temperature of cold air at inlet	60
Figure 4-7 HEX outlet temperature, measured and simulated; (a) Temperature of hot air at outlet and (b) Temperature of cold air at outlet	61
Figure 4-8 Temperature distribution of HEX with time at specific C.V.	62
Figure 5-1 Configuration of the CHER and flow directions of gases; (a) Compact Heat Exchange Reformer (CHER) and (b) Flow directions of gases	64
Figure 5-2 (a) Corrugated fins and plates, (b) Simplified flow channel model of the CHER with unidirectional heat transfer, and (c) Model of thermal circuit.....	66
Figure 5-3 System layout for simulation of co-flow CHER	67
Figure 5-4 Coordinate system for model discretization (y is along the flow direction), $N_x=10$, $N_y=30$	68
Figure 5-5 Schematic diagrams of heat transfers in the CHER stack; (a) Heat transfer through convection and molecular (channels cross section view) and (b) Heat transfer through conduction along flow direction (y -coordinate).....	69
Figure 5-6 (a) Electric cabinet and (b) an inner view of controller units	70
Figure 5-7 The CHER test rig, (a) schematic diagram of the experimental apparatus and (b & c) overview of the test rig	72
Figure 5-8 Temperature distributions in each channel and plate (90 sec.) $T_{air}=600^{\circ}\text{C}$, $T_{FSM}=500^{\circ}\text{C}$, $T_{initial}=500^{\circ}\text{C}$, $SCR=2.5$, $\Delta P=1,000\text{Pa}$, $L=762\text{mm}$; (a) Air channel, (b) FSM channel, and (c) Plate.....	80
Figure 5-9 Temperature distributions in each channel and plate (90 sec.) $T_{air}=700^{\circ}\text{C}$, $T_{FSM}=600^{\circ}\text{C}$, $T_{initial}=600^{\circ}\text{C}$, $SCR=2.5$, $\Delta P=1,000\text{Pa}$, $L=762\text{mm}$; ; (a) Air channel, (b) FSM channel, and (c) Plate	81

Figure 5-10 Molar fractions of each species with different temperature sets at steady state in the central channel, SCR=2.5, $\Delta P=1,000\text{Pa}$, $L=762\text{mm}$; (a) CH_4 , (b) H_2O , (c) H_2 , (d) CO , and (e) CO_2	83
Figure 5-11 Mass flow rate of FSM and H_2 in central channel at different temperature; (a) FSM and (b) H_2	84
Figure 5-12 Temperature of FSM at various SCRs in the central channel.....	85
Figure 5-13 Molar fraction of each species inside FSM channel (SCR: 2.0, 90 sec.); (a) CH_4 , (b) H_2O , (c) H_2 , (d) CO , and (e) CO_2	86
Figure 5-14 Molar fraction of each species inside FSM channel (SCR: 2.5, 90 sec.); (a) CH_4 , (b) H_2O , (c) H_2 , (d) CO , and (e) CO_2	86
Figure 5-15 Molar fraction of each species inside FSM channel (SCR: 3.0, 90 sec.); (a) CH_4 , (b) H_2O , (c) H_2 , (d) CO , and (e) CO_2	87
Figure 5-16 Molar fractions of each species at various SCRs in the central channel; (a) CH_4 , (b) H_2O , (c) H_2 , (d) CO , and (e) CO_2	89
Figure 5-17 Mass flow rate of FSM, H_2 and CO in central channel with different ΔP ; (a) FSM, (b) H_2 , and (c) CO	90
Figure 5-18 Temperature distributions in the central channel at different ΔP ; (a) Air and (b) FSM	90
Figure 5-19 Mass flow rate of H_2 in central channel & temperatures of FSM and catalytic fin at outlet with different channel lengths.....	91
Figure 5-20 Temperatures and chemical compositions with different flow directions; (a) FSM, (b) Fin, (c) CH_4 & H_2O , and (d) H_2 & CO	92
Figure 5-21 Theoretic molar fraction of each species from the SR and WGS reaction; (a) with steam and (b) without steam.....	95
Figure 5-22 Comparison of molar fraction for each species among the experiment, equilibrium calculation, and simulation with the temperature variation.....	96

Figure 5-23 Reaction coordinates for the SR and WGS reaction with various temperatures and SCRs.....	97
Figure 5-24 Comparison of molar fraction for each species among the experiment, case study, and simulation with the SCR variation	99
Figure 5-25 Comparison of measured temperature with the simulation, where arrows show the flow direction of both the hot air and FSM.....	100
Figure 6-1 The names of each component and the nodal point in a planar SOFC stack.....	107
Figure 6-2 Cross section view of equivalent electrical circuit; i is flow direction, j is in-plane direction, and $k=1\sim N_{FC}-1$	108
Figure 6-3 Conductive heat transfer schematic between the rib and plate	112
Figure 6-4 Cell voltage as a function of current density at 1073K.....	114
Figure 6-5 I-V characteristic curves comparison.....	115
Figure 6-6 Cell voltage distribution in a planar SOFC at $0.5A/cm^2$	116
Figure 6-7 Molar fraction in the channels of H_2 and CO; (a) Molar fraction of H_2 and (b) Molar fraction of CO	117
Figure 7-1 Schematic of the integrated SOFC system module	119
Figure 7-2 Schematic of pressures and flow resistances at stage 1	123
Figure 7-3 Schematic of pressures and flow resistances at stage 2	124
Figure 7-4 Mass flow rates of air flowing through the HEX and cathode channels	126
Figure 7-5 Temperature profile of SOFC stack in the integrated system	127
Figure 7-6 Temperature profile of MEA in the SOFC stack.....	127
Figure 7-7 Temperature profiles of hot air, cold air, and plate in the HEX; (a) Interconnector, (b) Hot air, and (c) Cold air	128
Figure 7-8 Temperature profile of the CHER at the Stage 1	129
Figure 7-9 Temperature profiles of reformat gases and air in the CHER; (a) Reformat gases and (b) Air	130

Figure 7-10 Molar fraction of each species at reformer exit since fuel supply begins.....	131
Figure 7-11 Molar fraction of each species inside the FSM channels of the CHER; (a) H ₂ , (b) CO, and (c) CO ₂	132

List of Tables

Table 3-1 Design of 1 kW SOFC stack	33
Table 3-2 Geometric dimensions of SOFC stack	33
Table 3-3 Properties of MEA [56-59].....	34
Table 3-4 Number of elements in each sub-domain in Figure 3-4	34
Table 4-1 Geometric dimensions of HEX	54
Table 4-2 Properties of materials	55
Table 5-1 Geometric dimensions of a Control Volume	69
Table 5-2 Stoichiometric coefficients of each species due to the SR and WGS reactions.....	93
Table 5-3 Experimental results with various SCRs	98
Table 6-1 Contact Resistances of each component in SOFC.....	103
Table 6-2 KCL Equations for nodal points	109
Table 6-3 Equations for thermal dynamics of stack	113

List of Acronyms

AE	Anode Exit
AFB	Air Foil Bearing
AFC	Alkaline Fuel Cell
AI	Anode Inlet
APU	Auxiliary Power Unit
ATR	Auto Thermal Reforming
BOP	Balance Of Plants
CE	Cathode Exit
CFD	Computation Fluid Dynamics
CGO	Gd-doped Ceria
CHER	Compact Heat Exchange Reformer
CHP	Combined Heat and Power
CI	Cathode Inlet
COMB	COMBustion chamber
DAQ	Data Acquisition
DMFC	Direct Methanol Fuel Cell
DOE	Department Of Energy
FSM	Fuel-Steam-Mixture
GC	Gas Chromatography
GDL	Gas Diffusion Layer
GT	Gas Turbine
HEX	Heat EXchanger
IC	Internal Combustion
ID	Inner Diameter
KCL	Kirchhoff's Current Law
LSM	Mg-doped Lanthanum

MC	Mixing Chamber
MCFC	Molten Carbonate Fuel Cell
MEA	Membrane Electrode Assembly
MFC	Mass Flow Controller
NETL	National Energy Technology Laboratory
OCV	Open Circuit Voltage
PAFC	Phosphoric Acid Fuel Cell
PDE	Partial Differential Equation
PEMFC	Proton Exchange Membrane Fuel Cell
PM	Permanent Magnet
POX	Partial Oxidation
PT	Pressure Transducer
RK	Runge-Kutta
SCCM	Standard Cubic Centimeter per Minute
SCR	Steam-to-Carbon Ratio
SECA	Solid State Energy Conversion Alliance
SOFC	Solid Oxide Fuel Cell
SR	Steam Reforming
TUI	Text User Interface
WGS	Water Gas Shift
YSZ	Yttria-Stabilized-Zirconia

Chapter 1

Introduction to Solid Oxide Fuel Cell

In recent years, numerous studies have attempted to develop and improve many fuel cell types such as phosphoric acid fuel cell (PAFC), proton exchange membrane (PEM) fuel cell, molten carbonate fuel cell (MCFC), alkaline fuel cell (AFC), direct methanol fuel cell (DMFC), and solid oxide fuel cell (SOFC) as affordable clean power sources. Regardless of the type of cell, desired voltage output and power can be achieved by stacking a single fuel cell unit serially. However, each fuel cell type has different operating conditions (temperature and pressure ranges), fuel types, materials for each component, structures, etc.

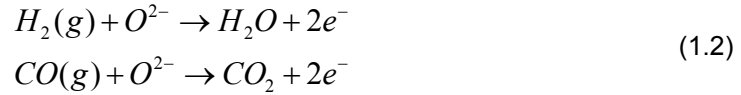
Great attention has been shown to the research of the SOFC due to a high operating temperature (600~1000°C) where ionic conduction by oxygen ions takes place and a flexibility of fuel-usage. In other words, the SOFC can be combined with other types of power generators such as a gas turbine (GT), heat exchanger (HEX), reformer, an after-burner, etc. to achieve high overall electrical power generation efficiency. Another attractive feature of a SOFC is the flexibility of fuel. Hydrocarbon fuels such as methane, propane, etc. can be directly utilized for SOFC, whereas other types of fuel cells have to rely on a clean supply of pure hydrogen for their operation due to an electrode poisoning from CO, a sensitive catalyst for sulfur and so on. These capabilities have made the SOFC an attractive promising technology for stationary power generation from kW to MW capacity range.

1.1 SOFC components

The SOFCs are composed of a porous anode, solid electrolyte (non-porous metal oxide) and porous cathode. On the cathode side, oxygen reduction reaction occurs,



On the anode side, the oxidation reaction of hydrogen or reformed hydrocarbon fuel occurs,



Fuel cell stacks contain an electrical interconnector, which links individual cells together in series or parallel to achieve a desired power output. Generally, two different interconnector materials for a SOFC can be considered. Firstly, conductive ceramic materials to be operated at high temperature (800~1000°C), and secondly, metallic alloys for lower temperature operation. Even if the design of SOFC interconnectors depends on the cell and stack design, the materials option is completely determined by physical and chemical steadiness under given operating conditions. And, the challenges of sealing the oxidant from fuel in planar SOFC stacks are significant. Like the SOFC interconnector, seal materials must be physically and chemically stable at operating conditions. And, sealing materials must be reasonable in cost and agreeable to low-cost stack manufacturing methods.

1.1.1 Electrolyte

The required properties for electrolyte are high ion conductivity, low electron conductivity, stability in the mood of oxidation/reduction, and stability for long-time operation. Ytria-Stabilized-Zirconia (YSZ), Mg-doped lanthanum gallate (LSGM), and Gd or Sm-doped ceria (CGO or CSO) are widely used for the electrolyte of SOFC.

The minimal operating temperature of a fuel cell depends on the produceable thickness of electrolyte. For example, the minimal operating temperatures for various electrolyte materials are ~700°C (YSZ), ~550°C (LSGM), ~550°C (CGO) with around 10μm thickness and 1×10^{-2} S/cm conductivity.

Zirconia-based electrolytes such as YSZ are suitable for SOFCs in the aspect of steady electrical/mechanical characteristics at high temperature operation but, can develop resistance layer such as $La_2Zr_2O_7$ by reacting with perovskite oxide electrode including lanthanum (La). LSGM has a higher ion conductivity than YSZ, and it can be used with perovskite cathode made of La transition metal oxide. This material is a superior oxide-ion electrolyte that provides

performance at 800°C comparable to YSZ at 1000°C. But, it generates a problem due to reactivity with NiO in LSGM-NiO composite anode. Ceria doped with rare-earth metals such as Gd and Sm attracts attention due to a high conductivity at relatively low temperature and is more stable than bismuth (Bi) oxide. But, it reduces the efficiency of the SOFC in the atmosphere of reduction ($pO_2=1\times 10^{-19}$ atm) due to the increase of electron conductivity from the reduction of Ce^{+4} to Ce^{+3} .

1.1.2 Cathode

Strontium-doped lanthanum manganite (LSM), a p-type semiconductor, is the most commonly used for the cathode material [1]. LSM is a perovskite structures that exhibit mixed ionic and electronic conductivity. LSM is especially popular for higher-temperature operation since a polarization of the cathode increases significantly as the SOFC temperature is lowered. Advantages of using the mixed (ionic and electronic) conducting oxides become apparent in cells operating at around 650°C.

There are two models that explain a cathode response. The first model is the cathode response inside the LSM with low oxygen ion conductivity. It is composed of an oxygen gas diffusion/dissociation toward pores, a diffusion in the direction of triple phase boundary (electrode/electrolyte/gas phase), and an ion transfer to electrolyte. The second model is a mixed conducting cathode response. The diffused oxygen molecules to porous structure are reduced to oxygen ions on the surface of mixed conducting cathode, triple phase boundary (cathode/electrolyte/gas). The reduced oxygen ions are diffused to the electrolyte through the surface of cathode and transferred to a site near the triple phase boundaries on the anode side.

1.1.3 Anode

The anode is mostly the thickest and strongest layer in each individual cell that provides the mechanical support because it has the smallest polarization losses. The oxidation reaction between the oxygen ions and the hydrogen produces heat as well as water and electricity. If the

fuel is a light hydrocarbon, methane, for example, another function of the anode is to act as a catalyst for steam reforming the fuel into hydrogen. This provides another operational benefit to the fuel cell stack because the reforming reaction is endothermic, which cools the stack internally.

The recent research for the anode focuses on YSZ and Ni/YSZ cermet, and the cermet has a thermal expansion coefficient comparable to that of the YSZ electrolyte. Because NiO cannot form a solid solution with YSZ at a low temperature, the cermet is produced by reducing process after NiO and YSZ are sintered together.

The anode has a high porosity (20~40%) so that mass transport of reactant and product gases is not inhibited. Like the cathode, it must have both electronic and ionic conductivity. There is some ohmic polarization loss at the interface between anode and the electrolyte and several developers are investigating bi-layer anodes in an attempt to reduce the Ohmic loss [1]. To suppress a formation of carbon as a result of internal reforming process, Ni can be replaced by copper. Cu is not involved in the formation of carbon as a catalyst, but it is effective as a current collector. To produce an excellent power density, cerium oxide must be added into anode material as a catalyst for oxidation.

1.1.4 Interconnector

The interconnector (also called a bipolar plate in planar fuel cells) can be either a metallic or ceramic layer that is sandwiched between neighboring fuel cells. Its purpose is to connect each cell in series. Because the interconnector is exposed to both the oxidizing and reducing side of the cell at high temperatures, it must be extremely stable. For this reason, ceramics have been more successful in the long term than metals as interconnector materials. However, these ceramic interconnector materials are very expensive as compared to metals. Nickel- and steel-based alloys are becoming more promising for lower temperature (600~800 °C) SOFCs. The material of choice for the interconnector in contact with YSZ is a metallic 95Cr-5Fe alloy. Ceramic-metal composites called 'cermet' are also under consideration,

as they have demonstrated thermal stability at high temperatures and excellent electrical conductivity.

1.1.5 Sealing material

The SOFC requires complete seals to prevent a fuel from mixing with an oxidant, and a sealing provides electrical insulation to stacks, particularly with the planar SOFCs. Seals required for a planar SOFC can be classified as metal–metal, ceramic–ceramic, and metal–ceramic seals depending on the applied materials. Glasses are most widely used to make metal–ceramic seals because these can be modified to have a very close match of thermal expansion with other fuel cell components, and glass seals show good air tightness along with good thermal and environmental stability. A particular problem for using the glass seals is the transition of silica from glasses, mainly on the anode side, causing degradation in cell performance.

1.2 Practical Cell and stack design

There are several different rudimentary design classifications for the SOFC stack such as the planar, tubular, monolithic, and segmented cell-in-series designs. Since planar and tubular cells are the most promising for continued development, two types of cell designs are explained in this chapter. The interest in tubular cells is unique to the SOFC, while all other types of fuel cells focus exclusively on planar designs.

1.2.1 Tubular design

The tubular SOFC was pioneered by the US Westinghouse Electric Corporation (currently Siemens Westinghouse Power Corporation or SWPC) in the late 1970s [1, 2]. It is composed of the same components as the planar SOFC, namely, the cathode, the anode, the electrolyte, and the interconnector, but in a different structure, as shown in Figure 1-1.

Air is injected through a thin alumina air supply tube located centrally inside each tubular fuel cell. Fuel flows along the outside of the tube, towards the open end. Heat generated

within the cell brings the air up to the operating temperature. One great advantage of the tubular design of the SOFC is that the gas-tight sealants can be eliminated due to the geometry. The tubular design is the seal-less tubular concept, which improves thermal stability and removes the need for the highly thermal-resistant sealants that are essential for the planar configuration.

In tubular SOFC technology (e.g. Acumentrics [3]), current is conducted axially along the tube. Interconnections are made at the end of the tube using various proprietary interconnection systems that connect cells within the stack. To minimize the in-plane resistance on the cathode side, a metallic current collector (typically silver) is applied. Acumentrics has shown the technology to be capable of repeated thermal cycling. Typical configuration is shown in Figure 1-2. The cells have been integrated into 2 kW stacks.

One drawback of the tubular type design is the more complex and limited range of cell manufacture methods [4]. Another disadvantage is high internal ohmic losses relative to the planar type design, due to the relatively long in-plane path that electrons must pass through the electrodes to and from the cell interconnector. Therefore, Siemens developed a flat-tubular type SOFC design with internal ribs for current flow, called the high power density (HPD) SOFC design to reduce additional ionic transport losses [5]. A cross-section view of a four-chamber flat tubular type SOFC is shown in Figure 1-3. Purely tubular cells have a power density at 1000°C of about $0.25\sim0.30\text{W}/\text{cm}^2$, in comparison to power densities of planar SOFCs, which can reach about $2\text{W}/\text{cm}^2$ [6]. The flattened tubular cells reduce this gap between tubular and planar designs considerably.

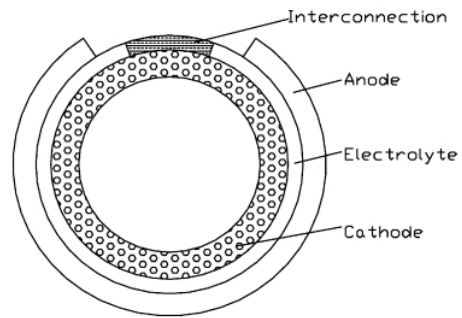


Figure 1-1 Cross-section of a tubular SOFC [2]

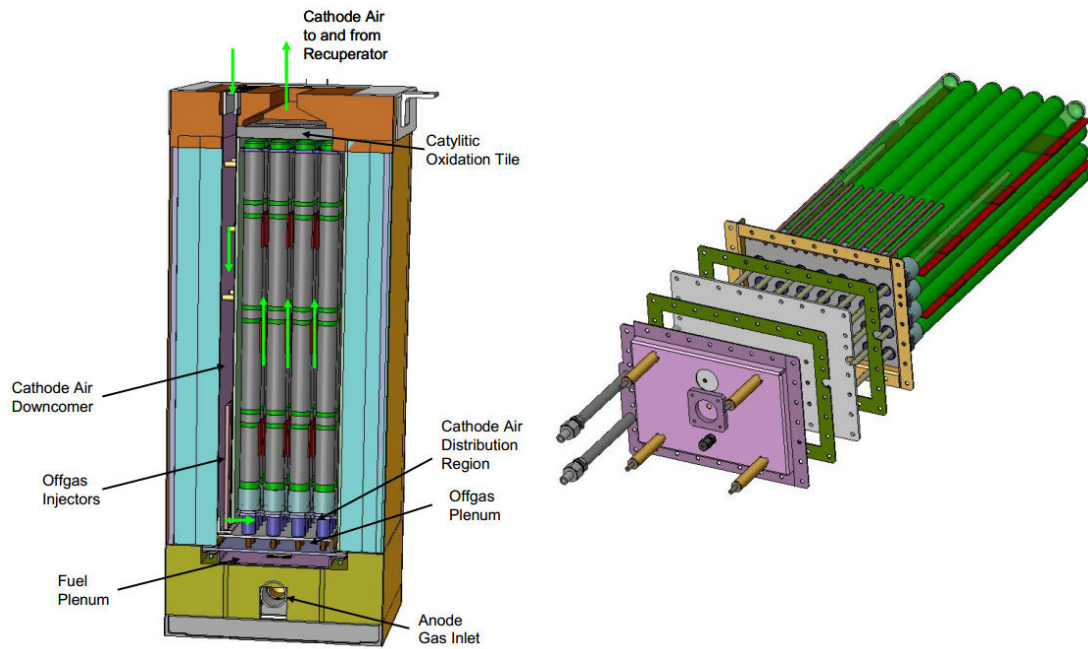


Figure 1-2 Configuration of a tubular SOFC [3]

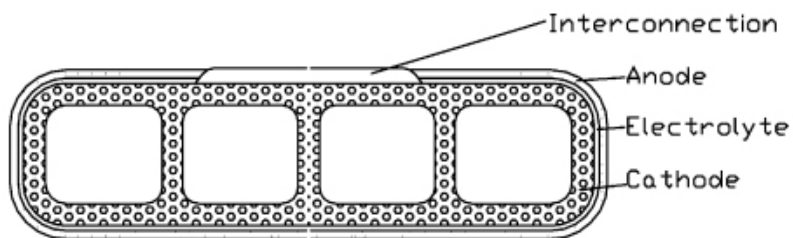


Figure 1-3 Cross-section of a four-chamber flat-tubular type SOFC [2]

1.2.2 Planar design

Since the planar SOFC is the topic of this research, the precise configuration of the planar SOFC is well explained in chapter 3.1.

1.3 Typical SOFC performance

The open circuit voltage (OCV) of SOFCs is lower than that of MCFCs and PAFCs. Numerous simulational results can be achieved by a mathematical analysis of the SOFCs. For example, the YSZ-electrolyte solid oxide fuel cell in this work shows higher power density than the CGO-electrolyte solid oxide fuel cell at the higher temperatures than 750°C [7]. Another SOFC stack test was performed by Bae et. al [8]. They developed a 1kW SOFC system for residential power generation application. Anode-supported single cells with YSZ or ScSZ (scandia-stabilized zirconia) were fabricated and were stacked to generate the desired 1kW power. The LSCF/ScSZ/Ni-YSZ (cathode/anode/electrolyte) single cell showed performance of 543mW/cm² at 650°C and 1680mW/cm² at 750°C. The voltage of 15-cell stack based on 5 cm×5 cm single cell (LSM/YSZ/Ni-YSZ, 150 mW per cell) was 12.5 V in hydrogen as fuel (120 SCCM per cell) at 750°C and decreased to about 10.9 V after 500 hours of operation. A 5-cell stack based on the LSCF/YSZ/FL/Ni-YSZ showed the maximum power density of 30 W, 25 W and 20 W at 750°C, 700°C and 650°C, respectively.

1.3.1 Effect of pressure

The influence of a pressure for the cell voltage starts from a differential equation of Gibb's free energy.

$$dG = -SdT + Vdp \quad (1.3)$$

Rewriting equation (1.3) as follows;

$$\left(\frac{dG}{dp} \right)_T = V \quad (1.4)$$

Considering a molar equivalent, the equation (1.4) becomes as follows;

$$\left(\frac{d(\Delta\hat{g})}{dp} \right)_T = \Delta\hat{v} \quad (1.5)$$

The relationship between Gibbs' energy and reversible cell voltage shows the equation(1.6).

$$\Delta\hat{g} = -nFE \quad (1.6)$$

Inserting (1.6) into(1.5), the cell voltage can be represented by a function of pressure.

$$\left(\frac{dE}{dp} \right)_T = -\frac{\Delta\hat{v}}{nF} \quad (1.7)$$

According to the equation(1.7), the change of reversible cell voltage with a varying pressure is relevant to a change of volume. If the change of volume of any response is negative, the cell voltage increases with an increasing pressure. This is a well-known Henry-Louis Le Chatelier's principle.

Generally, only gases bring on the noticeable change of volume. Applying an ideal gas law for equation(1.7), equation(1.7) is as follows.

$$\left(\frac{dE}{dp} \right)_T = -\frac{\Delta n_g RT}{nFp} \quad (1.8)$$

Here, Δn_g shows the total change of mole of a gas. If n_p is a number of moles of a product and n_r is a number of moles of a reactant, $\Delta n_g = n_p - n_r$.

1.3.2 Effect of Temperature

Likewise, when calculating the influence of temperature, the performance of most cell types decreases with increasing temperatures thermodynamically. Therefore, should the operating temperature of the fuel cell be as low as possible? The answer is "no." The higher temperature decreases the resistivity of the materials, and this reduces the ohmic losses within the cell. The ohmic losses are the most important type of loss in the SOFC. The reduction of the ohmic loss sufficiently compensates the thermodynamic loss with an increasing temperature. Normally, most actual cell performance enhances with increasing temperatures.

Chapter 2

Literature review and Scope of Research

Solid oxide fuel cell (SOFC) systems have been recognized as the most advanced power generation system with the highest thermal efficiency with a compatibility with a wide variety of hydrocarbon fuels, synthetic gas from coal, hydrogen, etc. The Department of Energy (DOE) Solid State Energy Conversion Alliance (SECA) program was initiated in 1999 [9] to develop utility scale SOFC-GT hybrid systems. Many companies [10-15] have been developing 1~10kW SOFC systems under the SECA program as an intermediate step toward utility scale SOFC-GT hybrid. These small SOFC systems have their own novel markets such as distributed stationary power, residential homes, auxiliary power unit (APU) for heavy-duty trucks, military applications, etc.

2.1 Typical SOFC start-up process

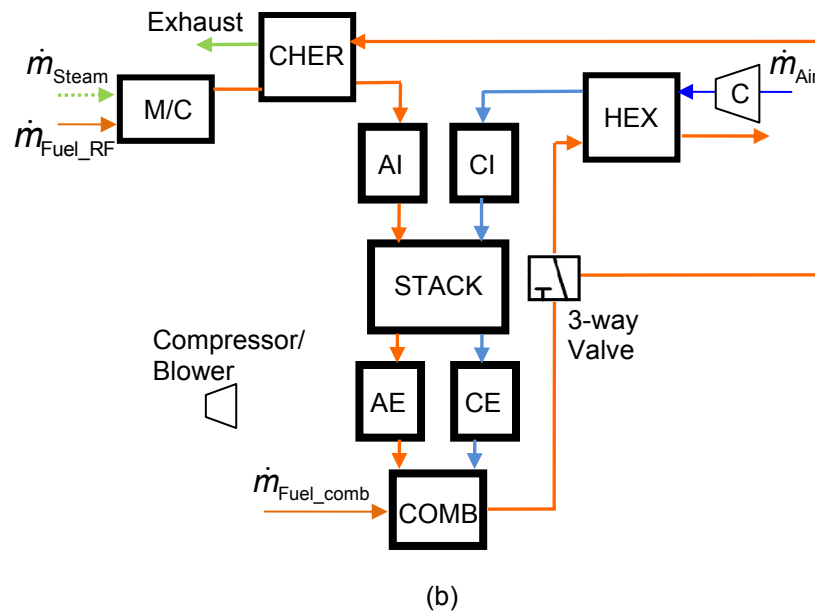
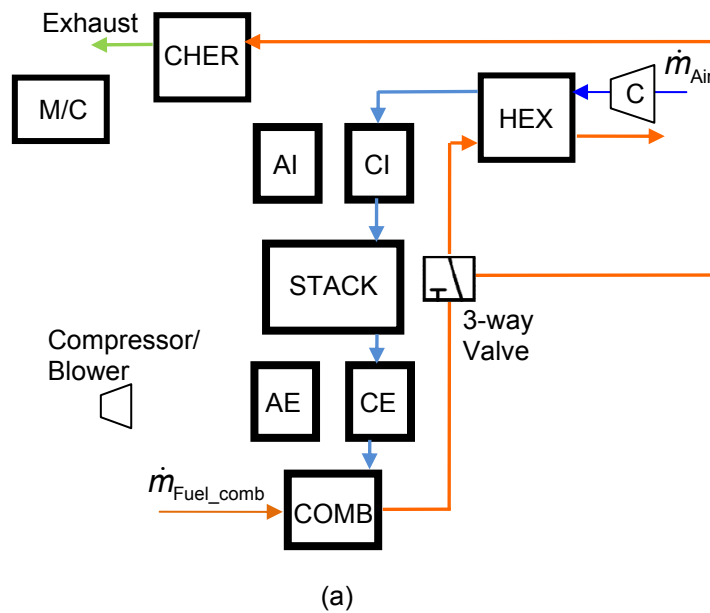
Even though a number of researches about various types of fuel cells have been performed for several decades in various sectors, there has been a common misconception that fuel cell-based power generation systems do not have any moving parts because the principle is based on direct energy conversion from electrochemical reactions. Fuel cell does not have any moving components. However, there should be many sub-systems/components (called balance of plant, BOP) such as the compressor, HEX, reformer, blower, etc. in order to draw air and fuel to the fuel cell stack and to discharge byproducts and exhaust heats to outside. Similarly, combustion chamber alone in the internal combustion engine cannot do anything without intake/exhaust valve systems, mechanical drive (crankshaft and valve system), and cooling systems.

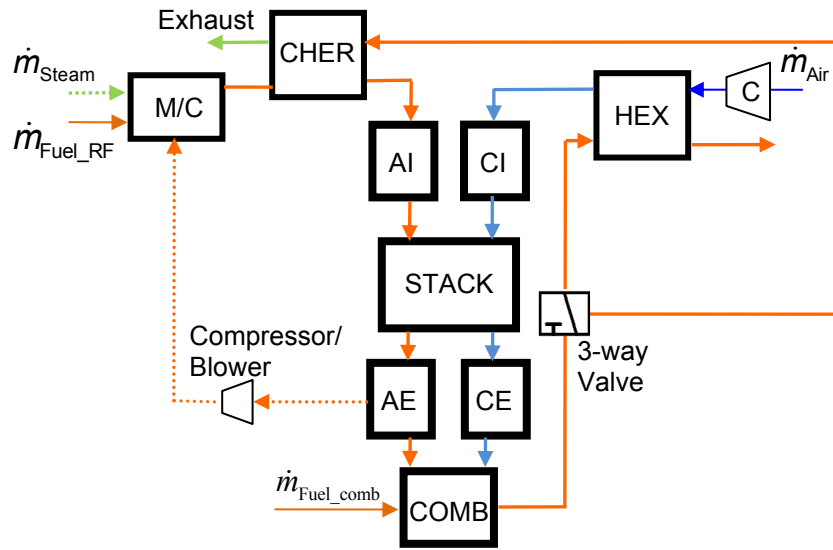
Currently, most research activities are limited to component level characterization of single fuel cell stack in laboratory conditions or material research for catalyst and electrolyte, and thus design tools for "SOFC system" are quite lacking. Unlike other types of fuel cells, the operating temperature of SOFC is between 500 and 1000°C, therefore the stack should be pre-

heated to the operating temperature by electrical heating or by providing hot air through cathode channels. In laboratory level tests for material development or cell performance evaluations, the stack may be heated inside a furnace without constraint of energy usage for the heating. However, for a SOFC-based power generation system to be stand-alone operating without too much involvement of an operator, all the balance of plants (BOP) should be optimized for minimum energy consumption during start up.

Figure 2-1 shows a typical block diagram representation of the start-up procedure of small SOFC systems (other configurations might be possible) that consisted of fuel supply system, stack, air HEX, combustor, and recirculation system of anode exhaust gas. Compact Heat Exchange Reformer (CHER) is the central part of the fuel supply system. A feasible start-up procedure of the systems (no standard procedure has been established) would be as following. At Stage 1, fuel is supplied to the combustor directly and air is supplied to the combustor through the cathode air line (main HEX → stack → combustor). The exhaust gas from the combustor supplies necessary thermal energy to the main HEX and CHER until they have reached certain prescribed temperatures. At Stage 2, once the CHER reaches the prescribed temperature, fuel-steam mixture (FSM) is supplied to CHER through the mixing chamber (M/C). Steam could be supplied through an external steam generator or steam separation unit from the exhaust gas. The FSM enters the CHER, which generates hydrogen-rich reformat gas to the stack through anode inlet plenum (AI). Once the stack begins to generate electric power, a blower begins to recirculate the steam-rich anode exhaust to the M/C allowing cutting off the external steam supply. At Stage 3, steam-neutral normal operation begins. The continuous operation of the combustor is essential to burn non-reacted residual fuel (20~30% of total supplied fuel to the stack). Additional fuel supply to the combustor would be optional depending on the required operating conditions of downstream components such as the main HEX and CHER gas side inlet temperatures, etc. Even if the HEX and CHER are connected in series in the diagram, they may be arranged in parallel.

As one can imagine, the start up process of stand-alone SOFC system requires careful control of all the BOPs to minimize total energy consumption and minimize thermal stress in the stack. In transient operation following load demand or during the start-up process, the HEX and stack may have the slowest thermal dynamics [16].





(c)

Figure 2-1 Start up process of the integrated SOFC system, CI: cathode inlet plenum, CE: cathode exit plenum, AI: Anode inlet plenum, AE: Anode exit plenum, COMB: combustor, M/C: mixing chamber, and C: compressor; (a) Stage 1: SOFC stack start-up with combustor, (b) Stage 2: Initiation of anode fuel line with reformer (CHER), and (c) Stage 3: Recirculation of unused fuel to the reformer inlet

The design of “stand-alone” SOFC systems is quite challenging in terms of an optimization of all BOPs and control strategy to minimize net energy consumption during the start-up. Even during normal operating modes, optimal control of fuel and air supply and anode gas recirculation relies on an accurate dynamic model of the whole SOFC system.

Here is one example that shows the complexity of the SOFC system operation. The SOFC system needs some type of oxidant for residual fuel from the anode to be burned. No fuel cell is operated in a stoichiometric condition to minimize irreversible loss related to the low fuel concentration toward the anode exit. Typical fuel utilization factor (consumed fuel divided by supplied fuel) is around 0.7~0.8, which means the residual fuel must exit the stack. Usually, a non-reacted fuel should be oxidized by using an afterburner, and the heat energy from the

afterburner should be used by heat exchangers to increase the temperature of incoming air and fuels. Operation with a high fuel utilization factor can lower emission levels but result in a poor efficiency and large temperature gradient within the fuel cell stack (limiting reliability and lifetime) due to large variations of local current density.

2.2 Literature review on SOFC stack/system modeling

In the stack level simulation, there are several researches [17-19] for the Stage 1 w/o considering dynamics of stack temperature. Achenbach [17] considered dynamics of stack temperature but continuity equations, other energy equations for gas species, and electrochemical reactions assume quasi steady state. Costamagna et al [18] developed a tubular SOFC simulation model and compared with the experimental data. Li et al [19] simulated the dynamic behavior of single planar SOFC stack by adopting time-dependent energy equations applied to both stack and gas flows. However, molar mass continuity equations were at steady state and momentum equation and pressure drop along the flow directions were not considered.

Simulations in the steady state performance simulation of SOFC-GT hybrid system have been popular due to simplicity of lumped model of SOFC and GT [20-23]. In those works, SOFC is modeled as one control volume with single temperature and pressure with certain constraints of thermodynamic properties and inlet conditions.

Shelton et al [24] present a transient model for the NETL Hybrid Performance Test facility using Simulink[®]. The model focuses on a 1-D model of duct flows and plenum dynamics. However, a HEX model is rather over-simplified without solving detailed energy, momentum, and mass continuity equations. Furthermore, a SOFC module is missing because the model simulates GT power plant with dummy air plenum (to mimic SOFC) and ducts. Recently, Mueller et al [25] presents a transient dynamic model of SOFC-GT hybrid including molar dynamic balance of species assuming the system is at adiabatic. However, both anode and cathode channels are modeled as single control volumes. Slippey [26] explains the dynamic

modeling and analysis of multiple SOFC system configurations. However, modeling methods and heat transfer networks are a 1-D model. And, no experiment was performed, i.e., no validation of simulation result with experiment happened.

2.3 Scope of Research

Due to the nature of complexity of a complete SOFC system, the system level design of SOFC has been quite challenging. Therefore, all sub-components including the SOFC stack are designed step by step for the small-scale SOFC system application. Firstly, the 1kW SOFC stack is modeled and the start-up module for the SOFC stack at the Stage 1 is developed. Secondly, the simulation module for the HEX is designed and validated by the experiment. Thirdly, the CHER module is created for the small SOFC system and verified by the experiment. Fourthly, the electric power generation module is designed and also validated by the experimental reference data found in published journal papers. Finally, an integrated SOFC system model is developed to ensure whether the designed sub-systems are appropriate for the designed SOFC system module.

Therefore, scope of the research is as follows.

- Development of computational model ("Start-up module") for transient simulation of stack heating process (Section 2.4)
- Development of computational model ("Heat exchanger module") for transient simulation of heat exchangers and experimental verification (Section 2.5)
- Development of computational model ("Reformer module") for transient simulation of external reformer (CHER) and experimental verification (Section 2.6)
- Development of computational model ("Stack module") for SOFC stack power generation (Section 2.7)
- Integration of four modules (Start-up, Heat exchanger, Reformer, Stack) (Section 2.8)

This research for modeling the integrated SOFC system supplies researchers with obvious guideline for selecting proper components to build up an entire SOFC system. It takes a lot of efforts to choose proper sub-systems with suitable conditions such as the length of the CHER/HEX, the mass flow rate of air and fuel, the capacity of combustor, etc. for the SOFC system. I am so confident that a fuel cell researcher can save a lot of time and effort to build up a complete SOFC system with the help of this research.

Literature review related to each subject is included in each section.

2.4 Stack Heating

The purpose of this analysis is to develop a thermal dynamic (transient) model of planar SOFC stack during the start-up process using hot air through the cathode channels or electric furnace before fuel cell electrochemical reaction occurs. The start-up process is Stage 1 described earlier in Figure 2-1(a). The ultimate goal of proper stack heating would be to minimize thermally induced stress within the stack and total energy consumption during the heating process. For the heating method using hot cathode air, mass flow rate and required pressure drop across the stack are closely coupled to each other through channel geometry and temperature of the air inside the channel.

Several approaches about start-up strategy in research, such as those in [27-30], have been performed in planar and tubular SOFC. Apfel et al [27] consider the thermal start-up process of 5 kW planar SOFC stack for cathode and anode co-flow conditions. However, the thermal analyses on only discretized cathode and anode gas volumes were considered and detailed geometrical parameters of the stack are not provided. Rancruel et al [28] simulate the start-up behavior of a SOFC-based auxiliary power unit including steam generator, reformer, and heat exchangers. Because all the subsystems and BOPs are considered in the simulation, accuracy of each subsystem is questionable. For example, heat exchangers that are similar to the stack in terms of structure are modeled as lumped matrix and without considering thermal mass of gases. Ferrari et al [29] present early stage start-up behavior (before fuel cell

electrochemical reaction begins) of a test rig mimicking SOFC-GT hybrid system consisted of emulators of turbomachinery, combustor, and stacks, and cathode recirculation ejector. The experimental verification of their Simulink®-based model was made for several start-up configurations. Barzi et al [30] present transient model of tubular SOFC. The model includes detailed electrical circuit network through tubular SOFC anode and cathode layers, and transient continuity, momentum, and energy equations for gas channels and solid structures. Their transient model simulations use a simple time integration method with internal iterations to match local current densities and cell operating conditions.

These studies mentioned above emphasize importance of technical challenges involved in the start-up behavior and transient operation of the SOFC-based power generation systems. However, unfortunately none of these studies provide detailed geometry or configuration of SOFC stacks that can be bench marked with any computational tool.

Details of the modeling is presented in Chapter 3.

2.5 Heat Exchanger

A heat exchanger (HEX) is a device for efficient heat transfer from one medium to another. The media may be separated by a solid wall, so that they never mix, or they may be in direct contact [31]. They are widely used in space heating, subsystem of fuel cell system, refrigeration, air conditioning, power plants, chemical plants, petrochemical plants, petroleum refineries, natural gas processing, and sewage treatment. One common example of a HEX is the radiator in a car [32].

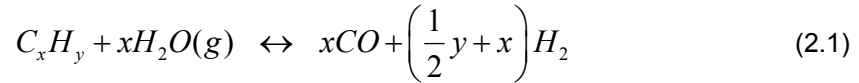
As shown in Figure 2-1(a), COMB burns fuel and heats air provided from the cathode exit and supplies HEX with hot air. And, the air at room temperature is provided to HEX in a counter-flow direction. The heat exchange process inside HEX occurs to provide sufficient thermal energy for start-up process to SOFC stack. The purpose of research is to develop the simulational thermal dynamic model of HEX and to verify the simulation results with experiment.

Details of the modeling is presented in Chapter 4.

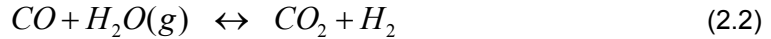
2.6 Compact Heat Exchange Reformer (CHER)

As shown in Figure 2-1, various mechanical or chemical devices should be considered with SOFC to comprise a complete system. The SOFC system is composed of several subsystems such as fuel/air processing system, power electronics, and thermal management systems. The fuel processing system is also composed of a series of catalytic chemical reactors, heat management devices, and reactants/products delivery systems. The main purpose of the fuel processing subsystem is to convert the hydrocarbon fuels into H₂-rich gases.

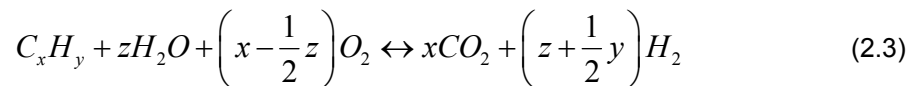
There are three established reforming methods for the production of hydrogen such as Steam Reforming (SR), Catalytic Partial Oxidation (CPO or POX), and Auto Thermal Reforming (ATR) [33]. SR is an endothermic reaction favored at high temperature with superheated steam over catalyst surfaces;



Because no oxygen in the air is involved in the reaction, the outlet stream is not diluted by nitrogen, and H₂ yield is the highest among the three reforming methods. To further increase the H₂ yield, the CO is shifted to H₂ via water gas shift (WGS) reaction;



Typically SR has been popular in large reactors [34] where slow transient response due to indirect heating [35] is not a main concern. POX reforming process [36-38] uses a small amount (less than stoichiometric amount) of oxygen to partially oxidize the fuel into a mixture of CO and H₂. ATR is a combination of SR and POX, and typically ATR reactors accomplish SR, POX, and WGS reactions in a single reactor. ATR considers these reactions as simultaneous processes that use the thermal energy from one reaction for the other endothermic reactions. An ideal stoichiometric ATR reaction with only CO₂ and H₂ as products would be



However, actual steam-to-carbon ratio (SCR) and oxygen-to-carbon ratio should be chosen such that the reaction is energy neutral as much as possible and coke formation is prohibited.

The current trend of research on SOFC systems is focused on less than 10kW scale, such as APUs for military vehicles and large heavy duty trucks, residential homes, small buildings, hospitals, schools, etc. While industrial-scale H_2 production systems based on SR reaction use hundreds of large and long reactor tubes containing a pelletized Ni-based catalyst without space limitation of heat and steam management subsystems, sub 10kW scale SOFC systems require compact fuel processing systems. Since the SR reaction is a highly endothermic process, the SR reactor must be provided with enough thermal energy. The thermal energy for SR reaction should come from either heat transfer through the reformer walls or preheating the fuel-steam-mixture (FSM). Any of these methods require large thermal management systems, and they are not suitable for small SOFC systems where space is mostly limited.

Internal reforming inside the SOFC stack is another common practice in small SOFC systems. Several experimental and modeling works were reported on internal reforming kinetic [39-46]. Achenbach and Riensche [39] carried out experiments to determine the kinetics of CH_4 steam reforming process considering both reforming and electrochemical reactions simultaneously. Peters et al. [40] consider the internal reforming of CH_4 in SOFC systems including anode gas recycling and effect of CO_2 . The endothermic SR reaction, which lowers the temperature of SOFC, reduces the amount of air passing through the cathode side for the cooling purpose [47]. Agnew et al. [41] present the influence of temperature and benefits of operating at elevated pressure on the reforming reaction kinetics. Parametric studies on the volume/surface area ratio, choice of catalyst, and catalyst metal loading have been performed through a combination of computer modeling and experimental measurements. However, the concrete modeling methods were not considered in detail. Nikooyeh et al. [42] present an effective 3-D modeling technique for both temperature and gas composition through the gas

channels and solid structure depending on various conditions. Janardhanan et al. [43] presents the performance analysis of a planar SOFC under direct internal reforming conditions with various operating parameters. Klein et al. [45] introduce SOFC systems with natural gas as a fuel. The methane from natural gas is converted into hydrogen by direct or gradual internal reforming within the tubular SOFC anode. Aguiar et al. [46] consider the application of SOFC with indirect internal reforming of methane, where the endothermic steam reforming reaction is thermally coupled to the exothermic oxidation reactions. Simulations for both counter-flow and co-flow configurations have been performed and compared.

The internal reforming inside the SOFC can simplify the system architecture. However, it causes significant and complicated temperature gradients inside the cell due to endothermic reforming reactions (in overall) and exothermic electrochemical reactions. In addition, the brittle ceramic electrolyte and interconnector metals have very different thermal expansion coefficients, and excessive thermal stress in the electrolyte is detrimental to the cell reliability.

As an alternative solution to the internal reforming inside the stack, an external reformer which integrates the heat management system and reforming system as one compact unit can save space and cost without causing too much thermal stress and degradation to the stack. A compact heat exchange reformer (CHER) which has a typical plate-fin co-flow or counter-flow configuration is such a system by allowing the reforming and heat exchanging processes to happen in a single compact unit.

However, there are only a few sources introducing modeling and/or experimental characterization of HEX-based reactors. Patel et al. [44] present a HEX-based reformer for PEMFC-based residential power generation system. The paper focuses on the dynamic response of heat exchange reformer for step variations in various input variables such as inlet gas flow rate and pressure and steam to carbon ratio. They consider how the step changes of various operating conditions such as gas flow rate, gas pressure, steam to methane ratio, and gas inlet temperature affect the dynamic performance of an heat exchange reformer. Anxionnaz

et al. [48] review various HEX/reactors such as spinning disk, micro-channel reactors, static mixers, oscillatory flow reactor, etc. They present various micro-structured HEX/reactors made of metallic foams, plate-fins, offset strip fins, corrugated fins, etc. Pan et al. [49] present the simulated characteristics of a compact plate-fin reformer which integrates endothermic and exothermic reactions into one unit. Their numerical model predicts the methanol conversion and the reformat composition in reforming chamber. Stefanidis et al. [50] present the steam reforming of methane on a rhodium/alumina-based multifunctional micro-reactor model. The micro-reactor is comprised of parallel catalytic plates and catalytic combustion and reforming takes place on opposite sides of the plates. They suggest that changing the catalyst surface area, internal and external mass transfer, and heat transfer through the reactor can lead to better performance. Zhang et al. [51] present a simple 1-D flow and heat transfer model of CHER at steady state. The distribution characteristics along the flow direction were presented, and some key factors such as SCR, catalyst reduced activity, and passage pressures were studied.

Details of the modeling is presented in Chapter 5.

2.7 SOFC Electric Power Generation Mode

After the Stage 2 as shown in Figure 2-1(b), SOFC stack is at high temperature. This high temperature also makes the incoming reformat gas to be further reformed within the anode channels of SOFC stack internally. This internal reforming process is included into the electricity generation sub-module. Internal reforming [52] of reformat gas from CHER is considered in this simulation. In other words, in the anode chamber, steam reforming (SR) and WGS happens at the corresponding local anode temperature. Computational model for electric power generation is developed for planar SOFC with total N_{FC} stacks.

The internal reforming inside the SOFC causes significant and complicated temperature gradients inside the cell due to endothermic reforming reactions (in overall) and exothermic electrochemical reactions. In addition, the brittle ceramic electrolyte and interconnected metals

have very different thermal expansion coefficients, and excessive thermal stress in the electrolyte is detrimental to the cell reliability.

The purpose of this analysis is to develop dynamic model of planar SOFC stack during the electrical power generation process using hot air from HEX and reformat from CHER when fuel cell electrochemical reaction occurs. The model was compared with several experimental data available in the open literature.

Details of the modeling is presented in Chapter 6.

2.8 Integration of each sub-module

The objectives of this research are to develop a non-linear computational model of the integrated SOFC system described in Figure 2-1 and to provide useful fundamental design characteristics such as suitable choices of HEX, reformer, compressor, etc. This model is on the basis of the satisfaction of conservation laws such as mass, force, energy and concentration of chemical species with specific source terms through the whole system. In other words, all boundary conditions for temperature, pressure, etc. should be satisfied with all conservation laws. For example, the cathode air inlet condition of the SOFC is directly affected by operating conditions of cold air from the outlet of HEX (located in front of SOFC) at the same time as the mass conservation law is acceptable.

Significant fuel cell parameters that can be varied are the pressure, temperature, and fuel/oxidant composition and utilization. In order to manipulate design parameters of the SOFC system with various design practices of each component, a wide range of operating design parameters are examined. In addition, the integrated SOFC system model is designed not only to simulate each of the operating conditions, but also to simulate different configurations, etc. And, this study presents rather general performance results using various operating conditions.

Details of the modeling is presented in Chapter 7

Chapter 3

SOFC stack start up process

3.1 SOFC design and simulation work

Figure 3-1 illustrates a planar SOFC stack consisting of the cathode, anode, electrolyte, and interconnector. In addition, Figure 3-1 shows the fuel gas and air feed holes through the stack. Although an air outlet and one more H_2 inlet were hidden in Figure 3-1, those holes exist symmetrically. Planar design is attractive since it is easy to manufacture and it uses less materials, hence potentially lower cost and high power density.

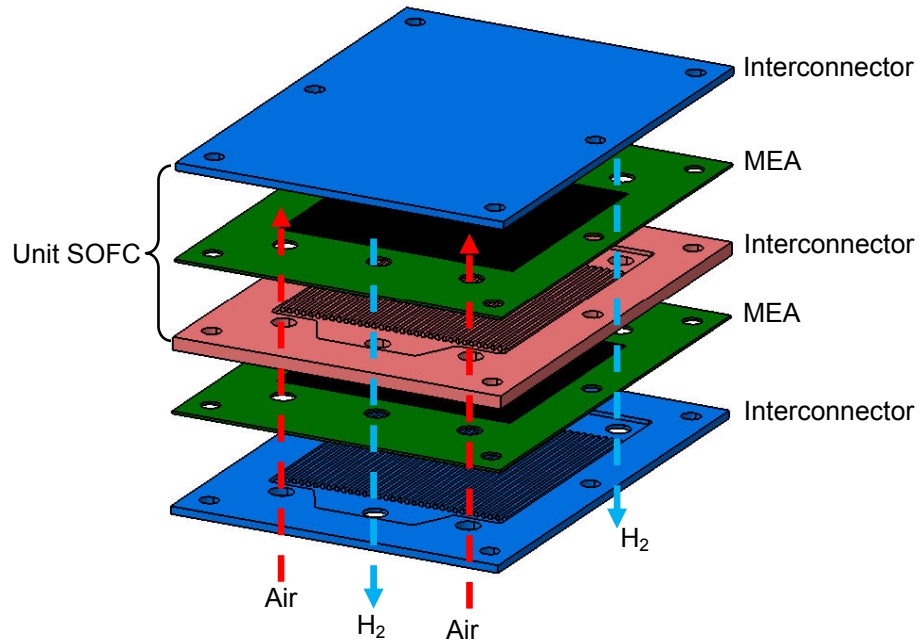


Figure 3-1 Configuration of a planar SOFC

In a real planar SOFC design, there are several connecting holes to join the structures. The locations and sizes of these holes are design-specific and there is no general rule for their sizes and locations. Therefore, for the modeling purpose, actual stack with these holes can be easily replaced by a simpler stack model without these holes but with the same thermal mass

as original one. There are also both fuel gas and air feed holes through the stack as shown in Figure 3-1.

Inlet supply holes for fuel gas and air can be modeled as single thermodynamic condition as combination of inlet temperature and pressure. Therefore, the inlet and exit holes for fuel gas and air can be modeled as boundary conditions with certain pressures. In addition, the inlet holes are thermal boundary conditions as well as pressure boundary conditions. Considering these aspects, an actual SOFC interconnector plate can be modeled as simple rectangular interconnector without these holes as shown in Figure 3-2, where inlet and exit thermodynamic boundary conditions are applied to the boundaries represented as red and blue lines in the figure. The flow from the inlet to the entrance of actual flow channels divided by current collecting ribs is mostly a two-dimensional flow with certain (very small) pressure drop.

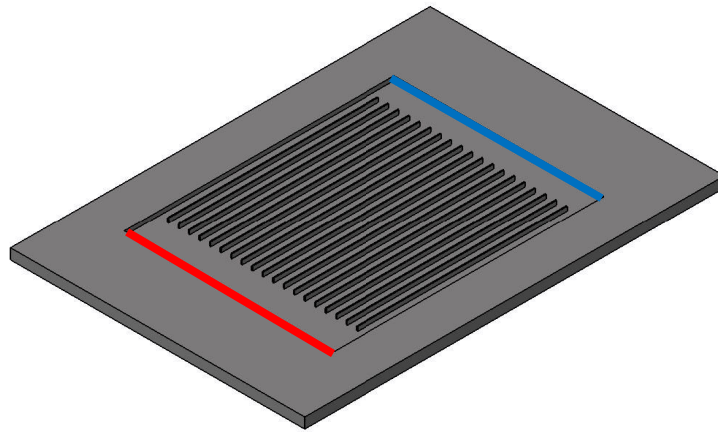


Figure 3-2 Simplified interconnector model without assembly holes and inlet and exit holes replaced by straight inlet and exit regions

Because the channel design between the inlet holes to the entrance of the channel is also design-specific, CFD simulation is the only method to analyze the detailed flow field. However, from thermal dynamics point of view of the stack, the detailed flow modeling through

computation-extensive CFD is not necessary. To capture realistic pressure drop and thermal interaction of the flow field with solid structures without sacrificing accuracy of the model, the flow field between the inlet represented as a red line in Figure 3-2 and the entrance of the channels is modeled as one-dimensional flows through virtual channels (not shown in Figure 3-2) divided by infinitely thin ribs, which do not contribute to flow resistances.

3.2 Stack Discretization

Stack flow passages are divided into N_y control volumes along the flow direction (y), and number of passages is $2N_x$ for both anode and cathode channels as shown in Figure 3-3.

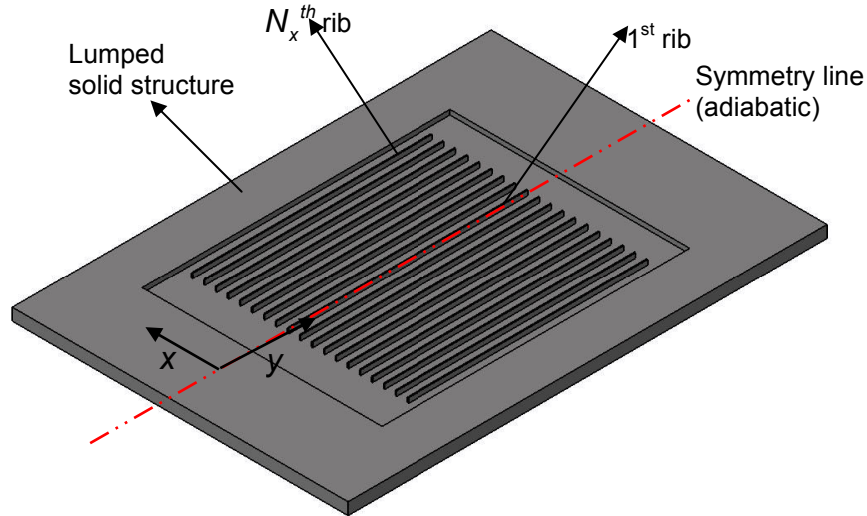


Figure 3-3 Schematic of a discretized interconnector

Because of geometrical symmetry, simulations are performed for a half of the flow channels and stack centerline is treated as adiabatic. One side of the interconnector plate may comprise a total of 10 sub-domains as shown in Figure 3-4. Domain 1 contains flow channels of air and fuel divided by ribs, domain 3 and 7 are flow entrance and exit regions without ribs and electrochemical reactions, other domains are outer solid structures.

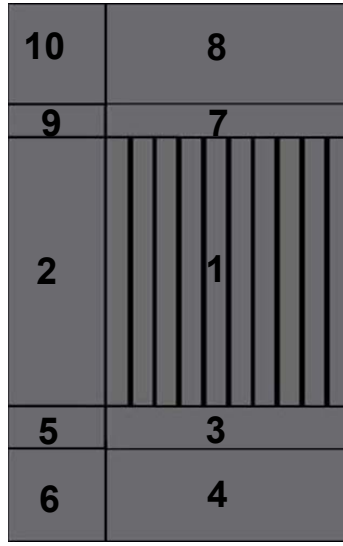


Figure 3-4 Fractionized control volume

The other side of interconnector plate is also divided by 10 sub-domains in a similar way. All the domains with solid structures are also divided into multiple finite elements. The energy equation, including storage terms, is applied to each element to simulate the temperature of each element in time domain.

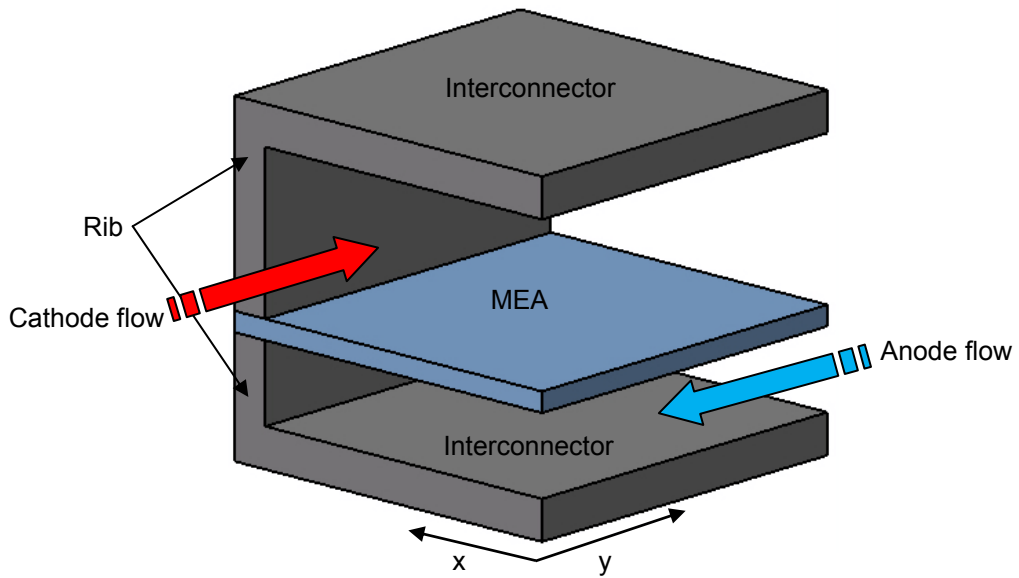


Figure 3-5 $(i, j)^{\text{th}}$ unit element ($i=1\sim N_x, j=1\sim N_y$)

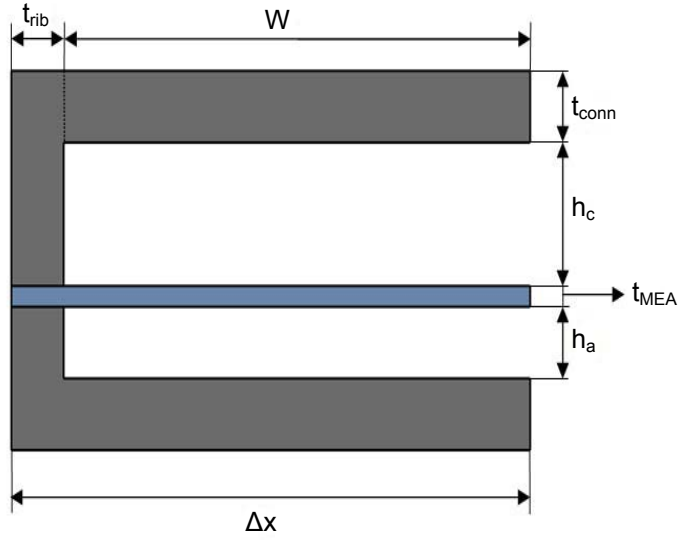


Figure 3-6 Dimensions of an element of planar SOFC

Figure 3-5 depicts $(i, j)^{\text{th}}$ unit element chosen from domain 1, with control volumes inside the element. Figure 3-6 shows notations for dimensions used in the simulations. The analysis method presented in this paper can be simulated for both counter and parallel flow configurations. In this work, it is assumed the anode (fuel) and cathode (air) flows are in a counter flow configurations like Figure 3-5. The inlet temperature and inlet pressures of the air and fuel gas (no fuel flow in this simulation) are specified as initial conditions.

3.3 Modeling

3.3.1 Momentum equation

If spatial fluctuation of mass flow rate inside the channel is not considered, i.e., $\partial \dot{m} / \partial x = 0$, mass flow rate is a function of only time. Using ideal gas law relating density,

pressure and temperature, $\rho = \frac{P}{R_{\text{gas}} T}$, momentum equation for air flow along one-dimensional

channel with hydraulic diameter of d_h is given by

$$\frac{\partial \dot{m}}{\partial t} = -A \frac{\partial p}{\partial x} - f_L \frac{\dot{m}^2}{2d_h} \frac{R_{gas} T_{avg}}{p_{avg} A} \quad (3.1)$$

, where f_L is average Darcy friction factor [53] along the flow channel length, which are evaluated as

$$\begin{aligned} f_L &= \frac{1}{L} \int_0^L \frac{64}{\text{Re}_x} dx : \text{Laminar} \\ f_L &= \frac{1}{L} \int_0^L \frac{0.316}{\text{Re}_x^{1/4}} dx : \text{Turbulent} \end{aligned} \quad (3.2)$$

Because mass flux rate is a function of only time, $\frac{\partial p}{\partial x}$ should be constant throughout the channel;

$$p = \Delta p \left(1 - \frac{x}{L} \right) + p_{exit} \quad (3.3)$$

Here, Δp is a pressure drop across the channel.

3.3.2 Energy equation to gas flow

If conduction within the gas and viscous heat dissipation are neglected, energy equation applied to both anode and cathode channels is written as

$$\frac{\partial T}{\partial t} = -\gamma \frac{RT}{p} \frac{\dot{m}}{A} \frac{\partial T}{\partial x} + \frac{RT}{p} \frac{\dot{q}_{to_gas}}{c_v} \quad (3.4)$$

where $\gamma = c_p / c_v$. \dot{q}_{to_gas} is total heat flux input to the control volume of interest per unit volume, and it is given by

$$\dot{q}_{to_gas} = \dot{q}_{Conn_gas} + \dot{q}_{MEA_gas} + \dot{q}_{ribs_gas} \quad (3.5)$$

where \dot{q}_{Conn_gas} is convective heat transfer from interconnector to gas channel, \dot{q}_{MEA_gas} is convective heat transfer from MEA to gas channel, and \dot{q}_{ribs_gas} is convective heat transfer from ribs to gas channel. Heat convection coefficients are evaluated at corresponding

reference film temperature which is an average temperature of gas in channel and surrounding solid structures. For example, the reference film temperature for convection coefficient for cathode channel is an average temperature of cathode air channel, MEA, interconnector, and cathode ribs. The following Nusselt numbers [54] were used.

For laminar flow ($Re < 2300$),

$$Nu_{D_h} = 3.66 + \frac{0.0668 \left(\frac{D_h}{L} \right) \cdot Re_{D_h} \cdot Pr}{1 + 0.04 \left[\left(\frac{D_h}{L} \right) \cdot Re_{D_h} \cdot Pr \right]^{\frac{2}{3}}} \quad (3.6)$$

For turbulent flow ($Re \geq 2300$),

$$Nu_{D_h} = \frac{\frac{f}{8} \cdot (Re_{D_h} - 1000) \cdot Pr}{1 + 12.7 \left(\frac{f}{8} \right)^{1/2} \cdot (Pr^{2/3} - 1)} \quad \text{where } f = \frac{0.316}{Re_{D_h}^{0.25}} \quad (3.7)$$

In most simulation conditions, flow was laminar. All the thermal properties such as Prandtl number and heat conduction coefficients were updated using temperatures found from previous time step in a frame of time integration scheme.

3.3.3 Energy equation to solid structures

Energy equation for MEA, interconnector, and ribs can be written as

$$\frac{\partial T_{MEA}}{\partial t} = \alpha_{MEA} \left(\frac{\partial^2 T_{MEA}}{\partial x^2} + \frac{\partial^2 T_{MEA}}{\partial y^2} \right) + \frac{\dot{q}_{to_MEA}}{\rho_{MEA} c_{v_MEA}} \quad (3.8)$$

$$\frac{\partial T_{Conn}}{\partial t} = \alpha_{Conn} \left(\frac{\partial^2 T_{Conn}}{\partial x^2} + \frac{\partial^2 T_{Conn}}{\partial y^2} \right) + \frac{\dot{q}_{to_Conn}}{\rho_{Conn} c_{v_Conn}} \quad (3.9)$$

$$\frac{\partial T_{Rib_A/C}}{\partial t} = \alpha_{Rib_A/C} \frac{\partial^2 T_{Rib_A/C}}{\partial x^2} + \frac{\dot{q}_{to_Rib_A/C}}{\rho_{Rib_A/C} c_{v_Rib_A/C}} \quad (3.10)$$

, where α_x (X=MEA, Conn, Rib) are thermal diffusivities, and \dot{q}_{to_X} (X=MEA, Conn, Rib) are heat convection to corresponding structure from surrounding gas channels. The subscripts, A/C, denote anode and cathode respectively. Figure 3-7 shows all the heat transport mechanisms (excluding radiation) within the stack including convections (superscript “conv”) and conductions (superscript “cond”) with their appropriate directions. Referring to Figure 3-7(a), heat flux terms in above equations are

$$\dot{q}_{to_MEA} = \dot{q}_{Cathode_MEA}^{conv} - \dot{q}_{MEA_Anode}^{conv} \quad (3.11)$$

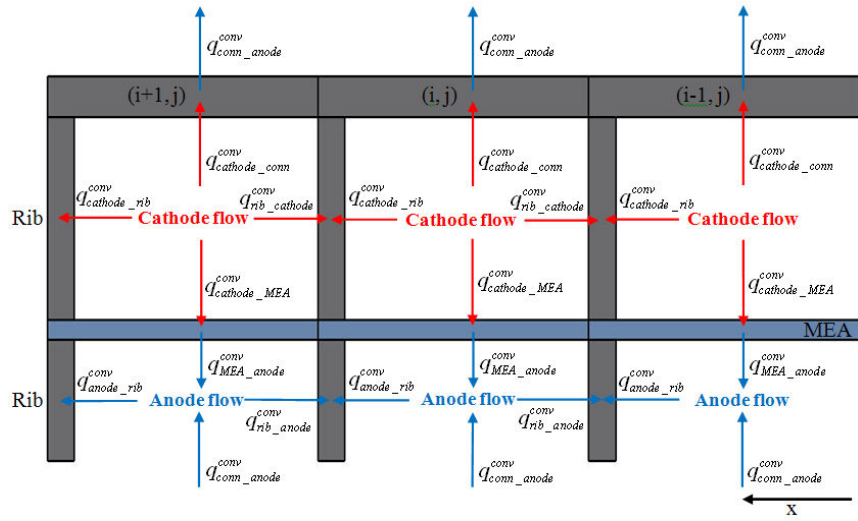
$$\dot{q}_{to_Conn} = \dot{q}_{Cathode_Conn}^{conv} - \dot{q}_{Conn_Anode}^{conv} \quad (3.12)$$

$$\dot{q}_{to_Rib_A} = \dot{q}_{Rib_Anode}^{conv} \quad (3.13)$$

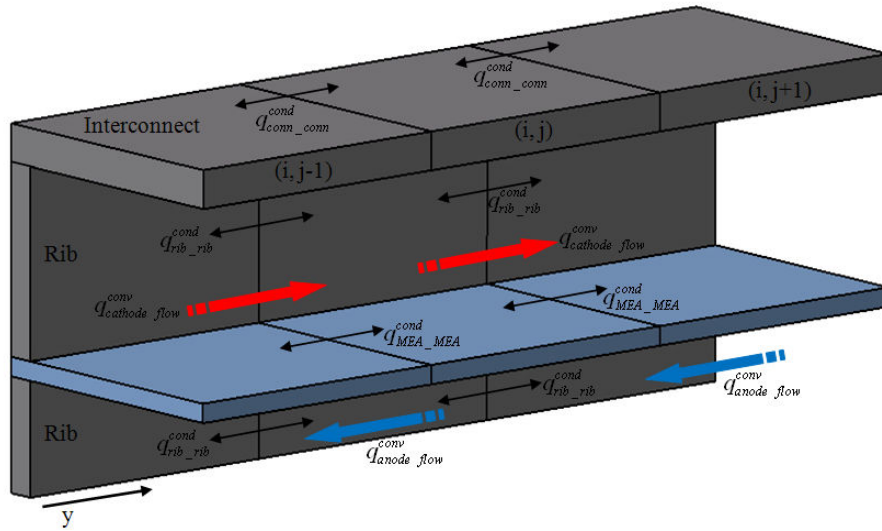
$$\dot{q}_{to_Rib_C} = \dot{q}_{Rib_Cathode}^{conv} \quad (3.14)$$

Equations(3.1), (3.4), and (3.8)~(3.10) comprise a complete set of non-linear differential equations for local gas temperature, local mass flow rate, and local temperature of MEA and interconnector. Boundary conditions are inlet gauge pressure, $p_{gauge_inlet}(t)$, with respect to exit pressure (i.e., pressure drop), and initial conditions for temperatures are all ambient temperature and initial conditions for mass flow rates in all the channels are zero.

In the simulation, hot air at constant temperature of 850°C is provided to the cathode channels at the inlet (the boundary between regions 3 and 4). In regions 3 and 7 in Figure 3-4, it is assumed that the flow is one dimensional through virtual flow channels divided by infinitely thin ribs, which do not contribute to flow resistances. Flow momentum and energy equations are applied to these virtual flow channels in regions 3 and 7. Energy equations are applied to solid structures in these regions. Pressure drop is specified between the inlet and exit of the stack and local pressures at the entrance and exit of the flow channel areas (boundary between regions 3 and 1 and boundary between regions 1 and 7) are internally calculated through mass conservation at these boundaries.



(a)



(b)

Figure 3-7 Schematic diagrams of heat transfers in the SOFC stack; (a) Heat transfer along x-direction and Heat transfer along flow direction (y-direction)

3.3.4 Discretization

All the first and second derivative terms in governing equations are discretized with the central difference method [55];

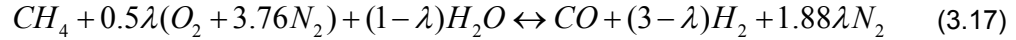
$$\left(\frac{\partial T}{\partial x}\right)_{i,j} = \frac{T_{i+1,j} - T_{i-1,j}}{2\Delta x}, \left(\frac{\partial T}{\partial y}\right)_{i,j} = \frac{T_{i,j+1} - T_{i,j-1}}{2\Delta y} \quad (3.15)$$

$$\left(\frac{\partial^2 T}{\partial x^2}\right)_{i,j} = \frac{T_{i+1,j} - 2T_{i,j} + T_{i-1,j}}{\Delta x^2}, \left(\frac{\partial^2 T}{\partial y^2}\right)_{i,j} = \frac{T_{i,j+1} - 2T_{i,j} + T_{i,j-1}}{\Delta y^2} \quad (3.16)$$

3.4 Results

Typical heating methods of a SOFC stack would be either electrical heating inside a furnace or using hot air through the cathode flow channels while the stack is insulated. The developed models in this paper were applied to stack-heating using both methods.

The 1 kW SOFC system was designed and simple thermodynamic analyses were performed to estimate a typical cathode air flow rate needed for the 1kW SOFC. Preliminary 1 kW SOFC stack flow channel dimensions were chosen based on steady state operating conditions assuming the fuel-gas stream is generated from methane (CH₄) ATR with the following balanced equations;



, where an air-to-fuel ratio $\lambda \approx 0.2\sim 0.3$ is typically used. Equilibrium composition of ATR exit was calculated using principle of minimization of Gibb's energy of formation assuming ATR exit temperature is at 950°C at $\lambda = 0.3$. Table 3-1 summarizes the design of the 1 kW SOFC stack for an oxygen utilization factor of 0.17 and a fuel utilization factor of 0.8. The Steam-to-Carbon ratio is about 1.88. The cathode air flow rate, 3.02 g/sec, calculated in Table 3-1 was used as the cathode flow rate for heating stack.

Table 3-1 Design of 1 kW SOFC stack

Item	Unit	Value
Voltage	V	0.7
Current density	A/cm ²	0.51
Active cell area	cm ²	400
Number of stack	ea.	7
Anode flow	g/s	0.25457
Cathode flow	g/s	3.02253
Anode inlet composition(950°C)		
H ₂	%	50.66
H ₂ O	%	31.28
CO	%	16.67
CO ₂	%	1.39

In addition, the electrolyte-supported SOFC was chosen to be simulated because this type has better chemical tolerance at high temperature. Table 3-2 provides the physical dimensions of the designed SOFC stack, and Table 3-3 shows the thermo-mechanical properties of MEA. In this simulation, thermo-mechanical properties of MEA are assumed to follow those of YSZ because the thickness of anode and cathode is relatively smaller than YSZ.

Table 3-2 Geometric dimensions of SOFC stack

Element	Description	Size(mm)
W	Channel width	8
t _{rib}	Rib thickness	2
t _{conn}	Interconnector thickness	1
h _c	Cathode channel height	2
t _{mea}	MEA thickness	0.28 [18]
h _a	Anode channel height	1

In this simulation, the cathode air at 850°C was supplied at cathode inlet, while there is no feeding of anode gases at anode inlets. All the faces of solid structures exposed to the

surrounding are assumed to be adiabatic (insulated). The number of segmental elements in each domain shown in Figure 3-4 is summarized in Table 3-4.

Table 3-3 Properties of MEA [56-59]

Element	Property	Value
Membrane(YSZ)	Density(kg/m ³)	5710
	Specific heat(J/kg·K)	606
	Thermal conductivity(W/m·K)	2.7
Anode(Ni-YSZ)	Density(kg/m ³)	4460
	Specific heat(J/kg·K)	595
	Thermal conductivity(W/m·K)	6
Cathode(LSM)	Density(kg/m ³)	4930
	Specific heat(J/kg·K)	573
	Thermal conductivity(W/m·K)	3

Table 3-4 Number of elements in each sub-domain in Figure 3-4

Region	x-direction	y-direction
1	10 (ribs number)	20
2	4	20
3	10	4
4	10	6
5	4	4
6	4	6
7	10	4
8	10	6
9	4	4
10	4	6

In the case of stack-heating using hot cathode air, two blower operating modes can be considered; one is constant mass flow mode and the other is constant speed mode. As stack is being heated up, flow resistance increases with temperature along the flow channel, and mass flow rate decreases gradually over time if the total pressure-drop across the stack is maintained constant. Therefore, if constant mass flow rate across the stack is desired during the heat up,

the blower operating points should follow the vertical dotted line shown in Figure 3-8, i.e., the blower speed should be increased to follow the required inlet pressure.

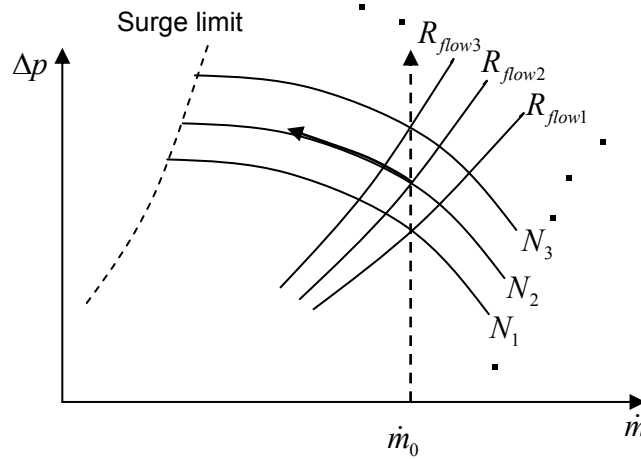


Figure 3-8 Typical blower map under constant mass flow mode

Another operating mode is at constant blower speed. When the blower is operated at constant speed, both pressure and mass flow rate change while stack is heated up. Because the blower is operated at constant speed, the operating point follows the constant speed curve in the blower performance map as shown in Figure 3-9. Depending on the initial blower setting speed, the blower can suffer surge before the stack reaches desired temperature if the flow resistance inside the stack increases beyond the blower surge limit.

Because a blower performance map is not available, simulations were performed for only constant mass flow rate mode, and required pressure drop to maintain the specified air mass flow rate was calculated at each time step. Once a blower map of appropriate blower is available, the constant speed mode could be simulated.

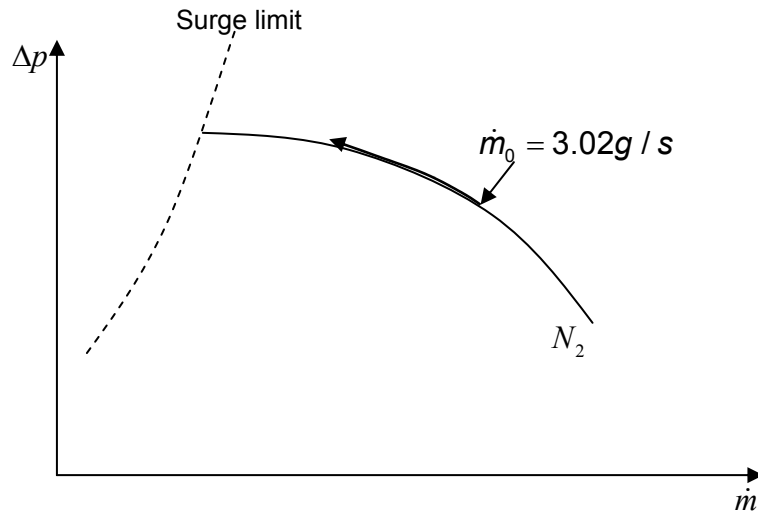


Figure 3-9 Typical blower map under constant speed mode

Figure 3-10~

(c)

(d)

Figure 3-13 show the temperature distributions over solid structure, rib, MEA, interconnector, and each channel after 1 minute, 30 minutes, 1 hour, and 2 hours, respectively. Figures (a) represent the temperature distributions of the anode gases and outer solid structures. Figures (b) show the temperature distributions of the cathode gases and solid structures. Figures (c) show the temperature distributions of interconnector and solid structures. Finally, the temperature distributions of MEA and outer solid structures are portrayed in Figures (d). In the early stage, the heat transfer occurs uniformly along x and y-direction. As time goes by, the high temperature distribution concentrates in the middle area because bulk solid structures are large heat sinks from outside of electrochemically active area. Also, the figures indicate that the maximum temperature zone is distributed widely throughout the cathode air inlet during the start-up. The downstream solid structures from the cathode inlet area have lower temperature all the time.

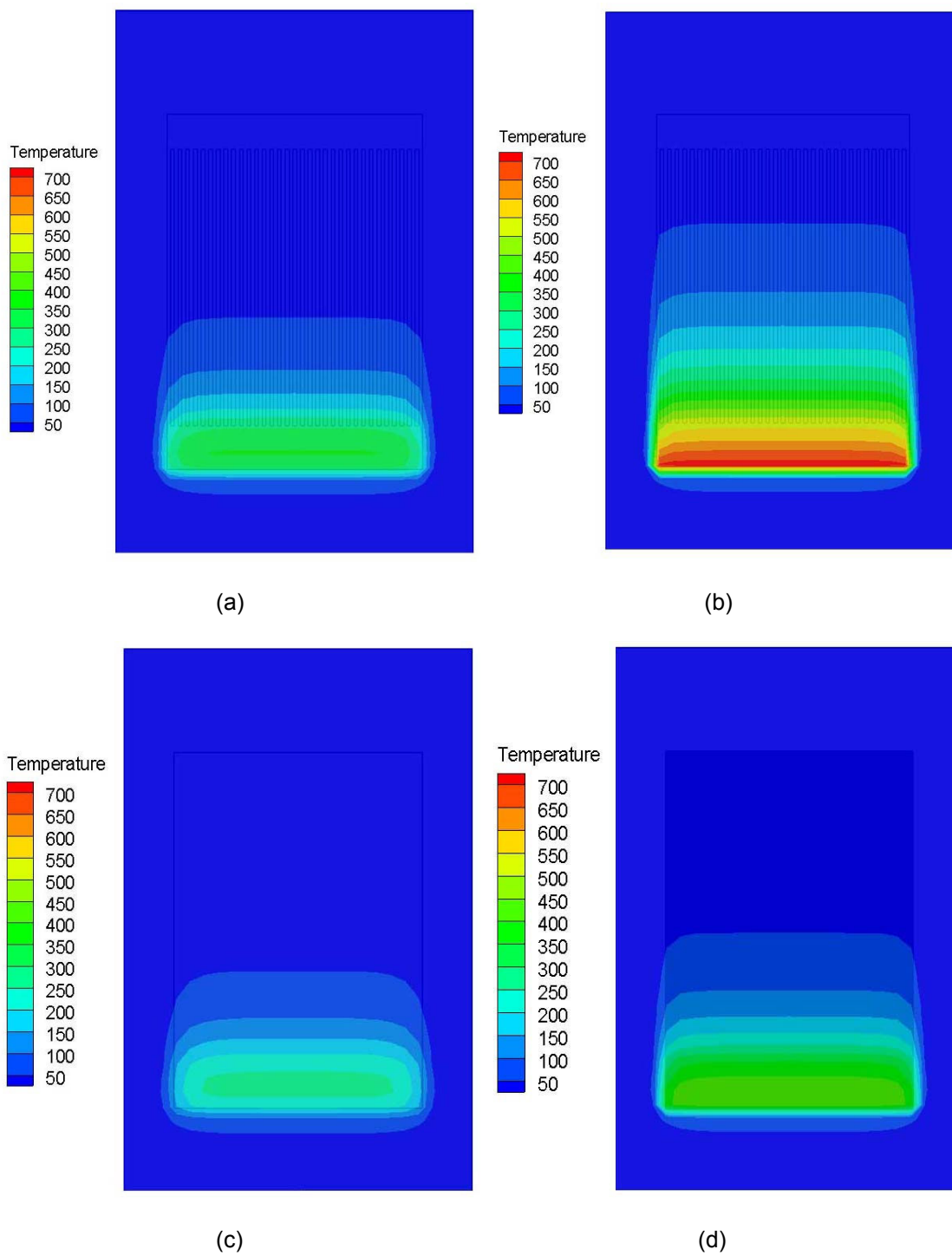


Figure 3-10 Temperature distributions of gases and structures of SOFC stack including outer solid structure (1min.); (a) anode, (b) cathode, (c) interconnector, and (d) MEA

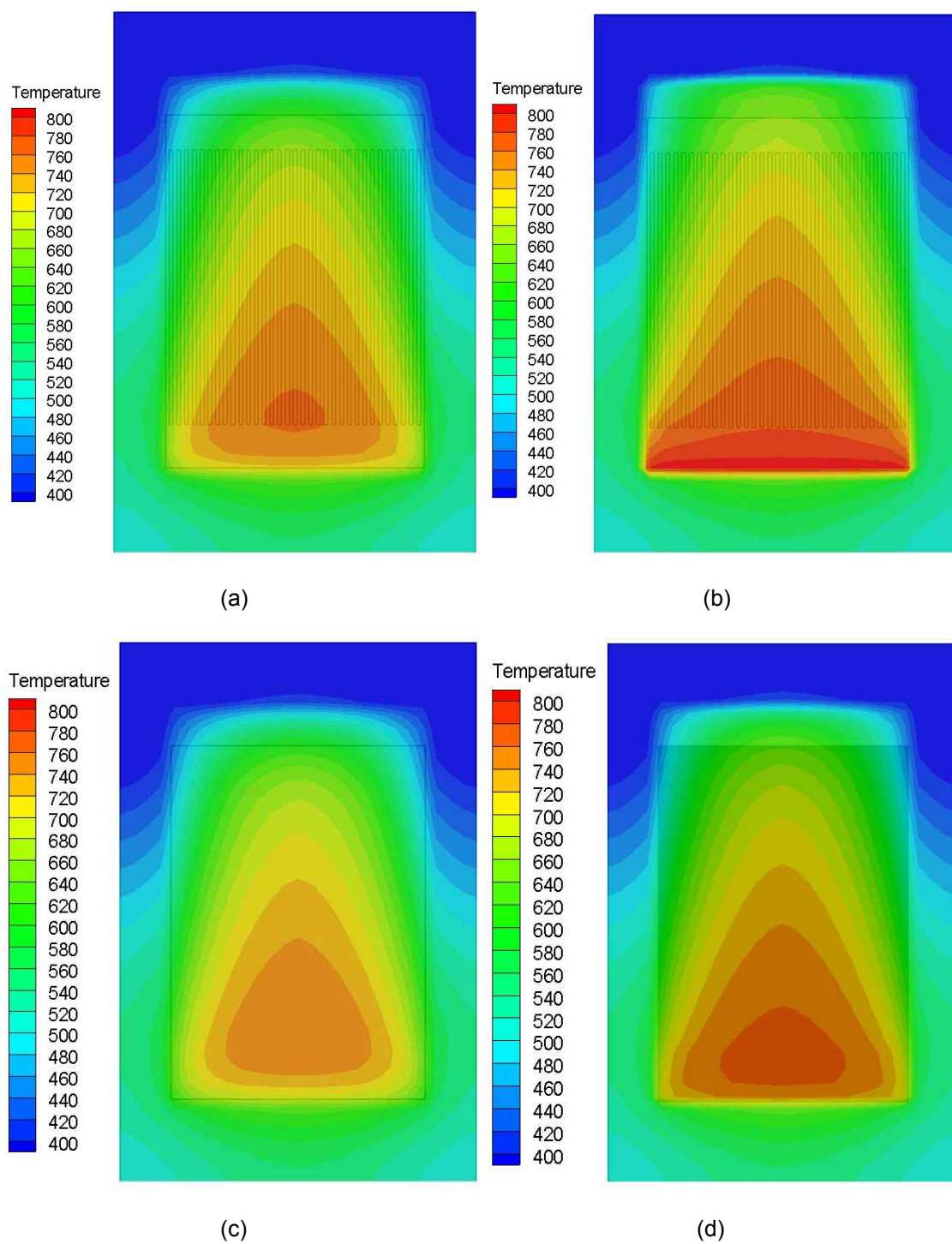


Figure 3-11 Temperature distributions of gases and structures of SOFC stack including outer solid structure (30min.); (a) anode, (b) cathode, (c) interconnector, and (d) MEA

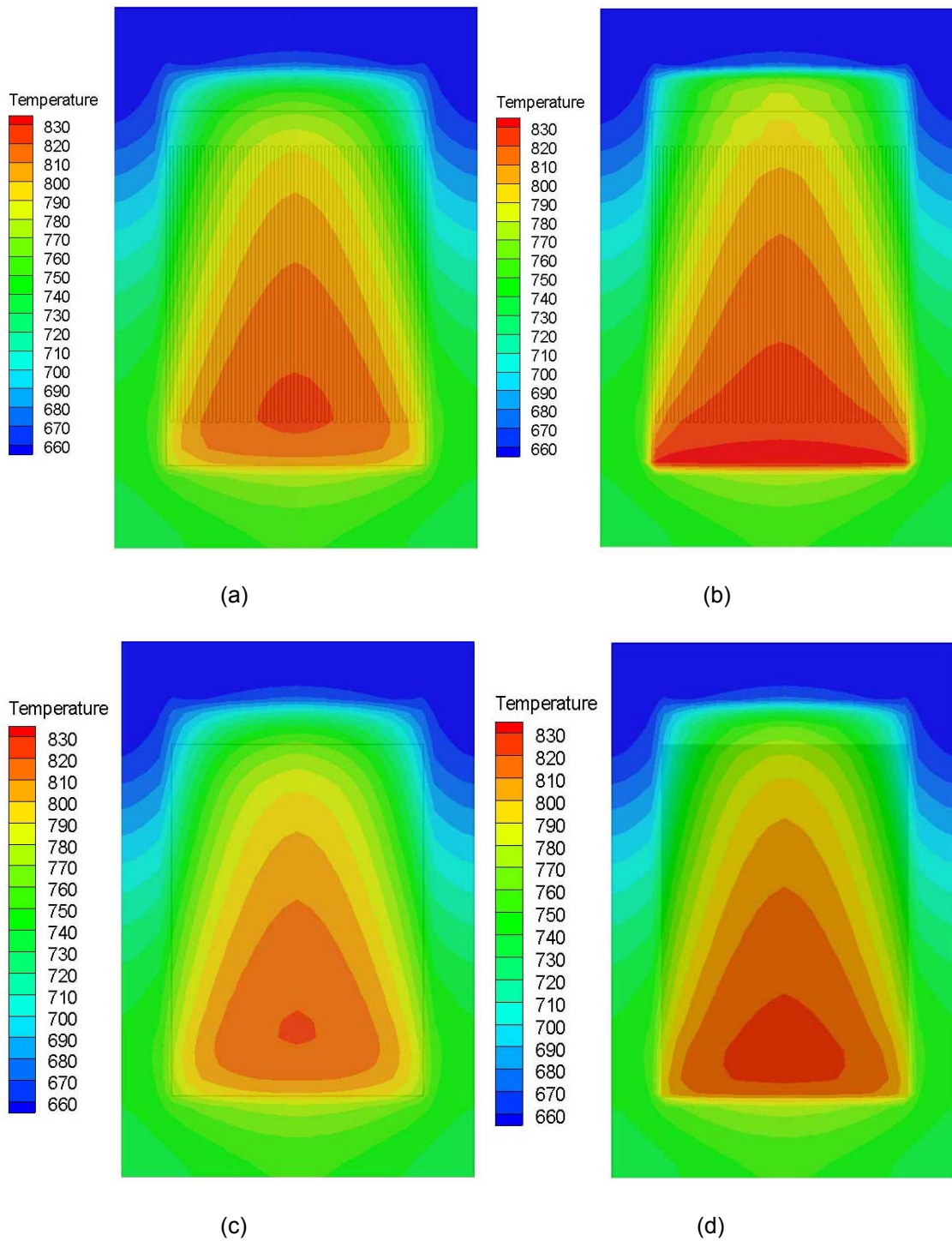


Figure 3-12 Temperature distributions of gases and structures of SOFC stack including outer solid structure (1hr.); (a) anode, (b) cathode, (c) interconnector, and (d) MEA

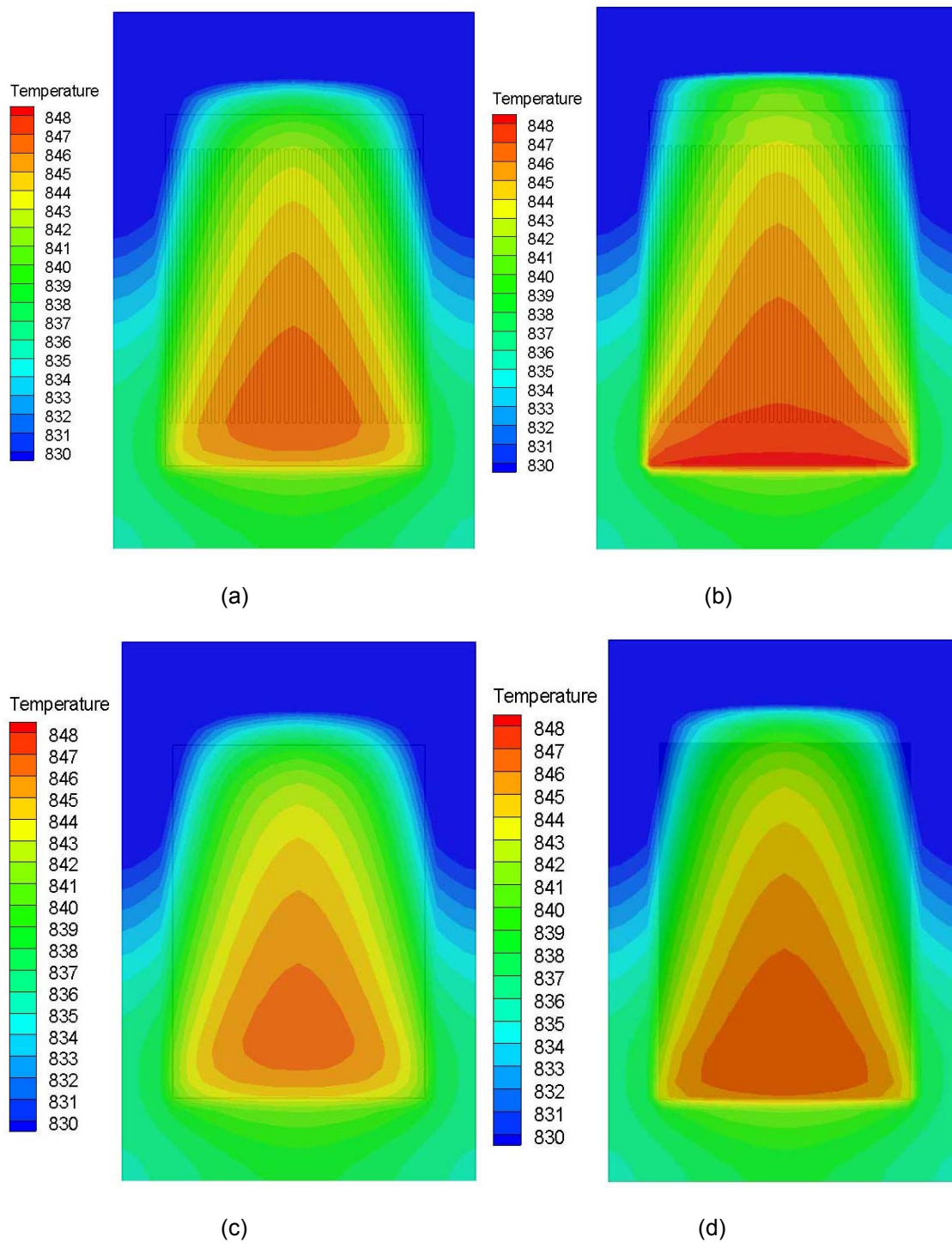


Figure 3-13 Temperature distributions of gases and structures of SOFC stack including outer solid structure (2hrs.); (a) anode, (b) cathode, (c) interconnector, and (d) MEA

The difference of temperature between air inside the cathode and anode channels was caused by the different channel height ($h_c=2\text{mm}$, $h_a=1\text{mm}$ in Table 3-2) and the larger thermal conductivity of interconnector compared to MEA. Therefore, it is reasonable that interconnector has relatively high temperature distribution compared to MEA. Figure 3-14 represents the evolution of temperature at the center of the outer solid structure. As Figure 3-14 shows, the temperature of solid structure increases rapidly from 20°C to about 650°C and then increases gradually to a final steady state temperature. In addition, the small difference of rib thickness does not affect the temperature of solid structures because the volume of total rib is much smaller than the total volume of solid structures.

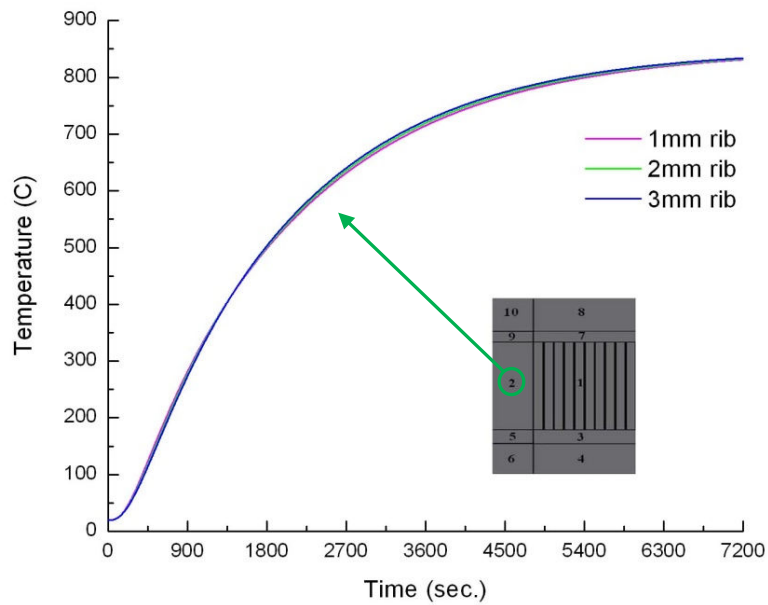


Figure 3-14 Temperature on central area of 2nd solid structure in Figure 3-4

As was mentioned before, simulation was performed with a constant air mass flow rate of 3.02g/s (cathode air flow rate during normal operation from Table 3-1). A simple numerical control algorithm was implemented to adjust pressure drop internally at every time step to maintain the specified mass flow rate. Figure 3-15 plots pressure drop across the stack to

maintain the constant flow rate of 3.02 g/s with different rib sizes. Notably, for 2mm rib, the required pressure drop increases from around 40 Pa to almost 2877 Pa after 2hrs of heating. The bigger rib size shows the larger pressure drop. In addition, it takes about 6450 seconds ($\cong 1.79$ hours) to reach the minimum temperature of 800°C within the stack. During that time, net heating energy of 1.2926kWh is required as shown in Figure 3-16.

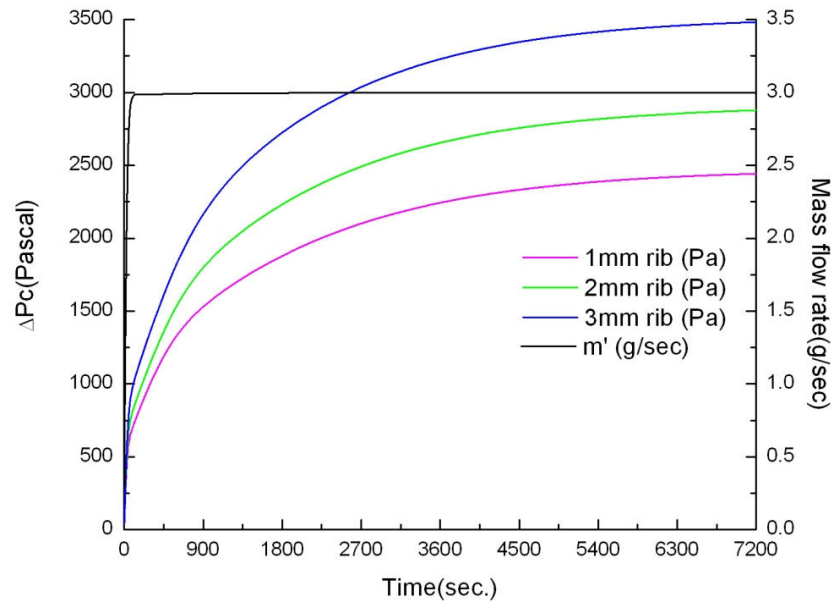


Figure 3-15 Required pressure drop over time to maintain the required mass flow rate

However, the heating method using the hot air feeding results in poor thermal efficiency. The heating efficiency was calculated by the equation below and is at most around 17%.

$$\eta_e = \frac{\text{Net Heating Energy}}{\text{Input Heating Energy}} = \frac{1.30651}{7.73926} = 0.1688 \quad (3.19)$$

A large amount of heating energy is lost through the exit flow out of the stack without contributing to heating of the SOFC stack, especially toward the end of heating once the stack has reached a certain high temperature. However, in an actual SOFC system with heat exchangers and a combustor, this stack exit flow would be directed to combustor with reduced

fuel flow rate to the combustor if constant combustor exit temperature is required for the gas HEX at the downstream which is used to generate hot cathode air for stack heating. In addition residual heat energy would be used for steam generation or fuel heating, etc. Therefore, actual efficiency in terms of total energy consumption during the heating would be much higher than that from(3.19).

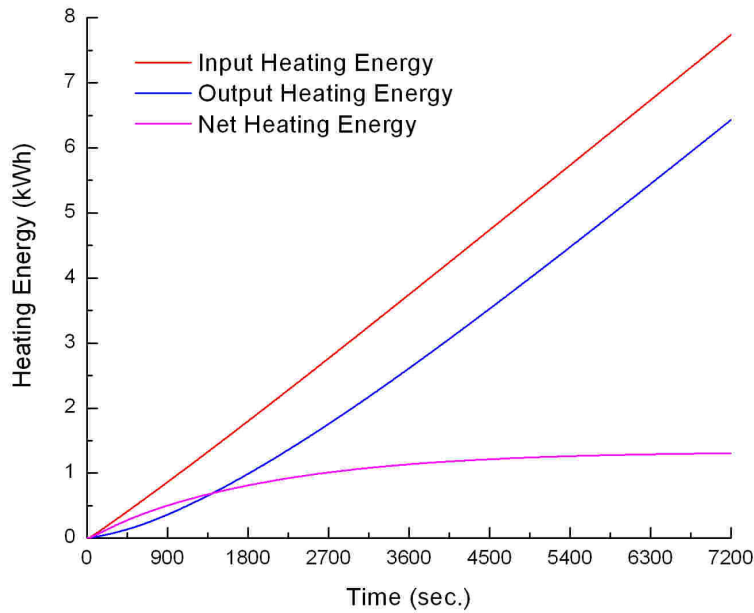
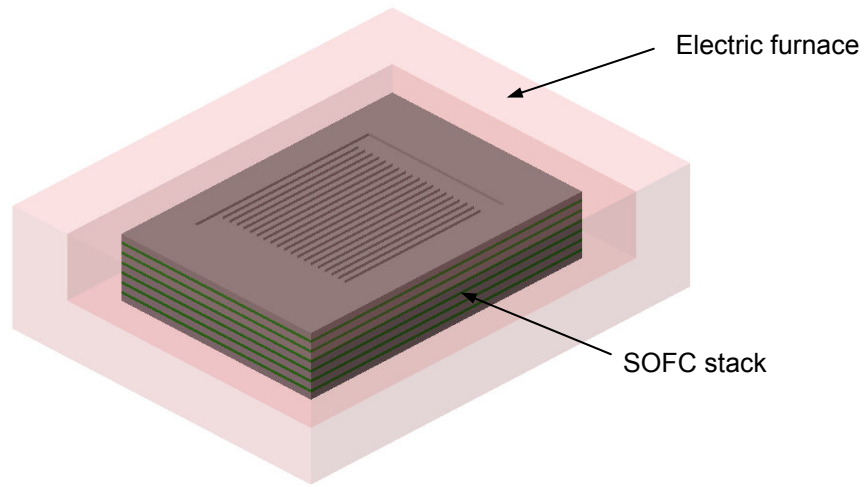
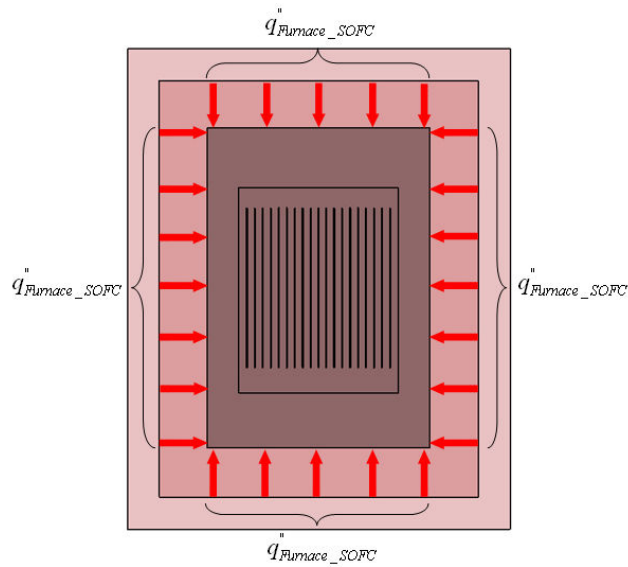


Figure 3-16 Heating Energy vs. time (Hot air feeding method)

Another stack heating method using an electric furnace was simulated with all of the cathode and anode channel flows at zero. In this heating method, a SOFC stack is inside an electric furnace as shown in Figure 3-17(a). In this analysis, there is a two-dimensional heat input shown as Figure 3-17(b) through the outer solid structure domains (2, 4, 5, 6, 8, 9 and 10 of Figure 3-4) from furnace to SOFC stack. In addition, the upper and lower sides are assumed to be insulated; this assumption is reasonable because the bottom surface of the stack should sit on a certain structure and the structure cannot be a heating element.



(a)



(b)

Figure 3-17 Schematic diagrams of heat transfer from Furnace to the SOFC stack; (a) Electric heating outline and (b) Heat transfer from the electric furnace

A preliminary simulation with a fixed heat flux of 1000W results in rapid and continuous increase of stack surface temperature above 1000°C, while the inside temperature remains

below 200°C because of the large thermal mass of the stack and large heat transfer resistance through thin MEA and interconnector. To avoid high thermal gradient that causes thermal stress during the heating process, the heat flux should be controlled to keep the surface temperature within certain limit. The easiest and most practically used method in actual electrical heating is to use a simple control algorithm to adjust heating rate. Any change of heating rate at certain time would be

$$\Delta\dot{q}(t) = K(T_{ref} - T_{max_ss}) \quad (3.20)$$

where K is proportional gain, T_{max_ss} is maximum surface temperature of solid structure and T_{ref} is a reference temperature of 850 °C. A block diagram of the numerical control algorithm is shown in Figure 3-18.

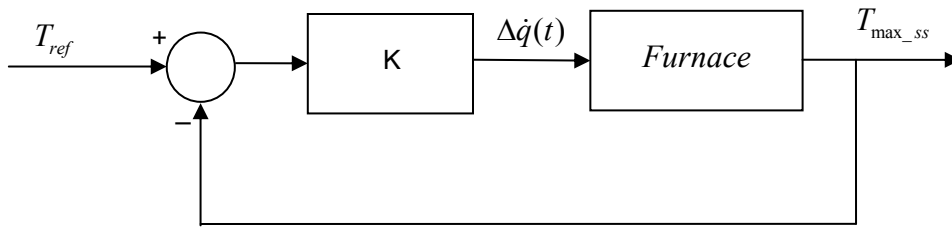


Figure 3-18 Block diagram of simple proportional control for furnace heating

One specific numerical value of input heating energy can be set as an initial condition. Initial heating power was chosen as 1000W with gain $K=100$. With $K=100$, overall SOFC stack temperature distribution can be found in (c)

(d)

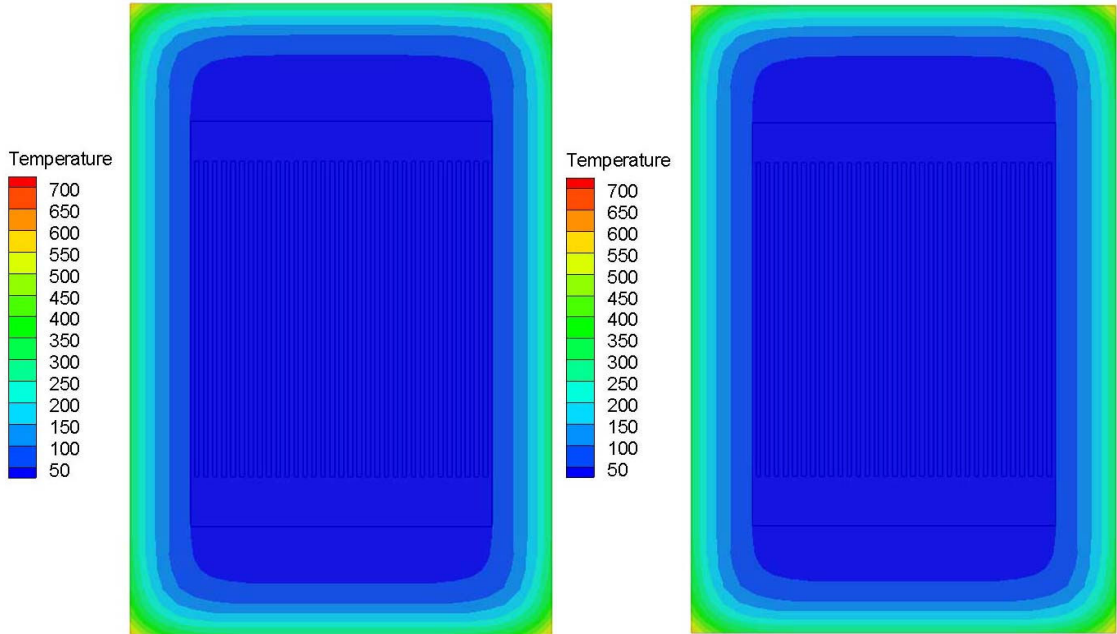
Figure 3-19~

(c)

(d)

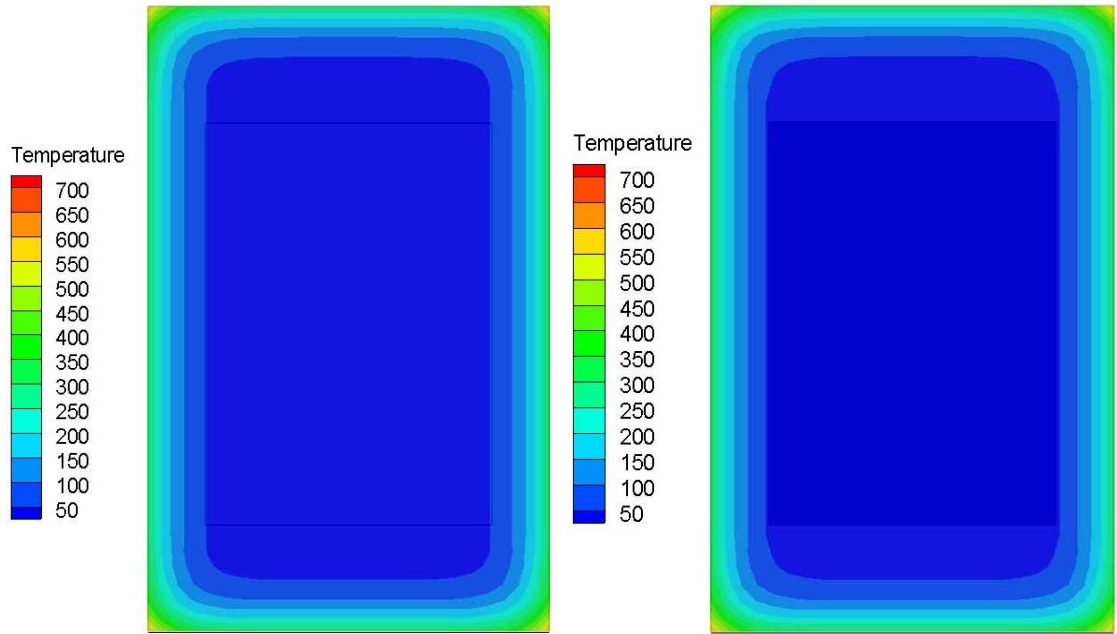
Figure 3-22. These figures depict the temperature distribution over solid structure, rib, MEA, interconnector, and each channel after 1 minute, 30 minutes, 1 hour and 2 hours, respectively.

As shown in the figures, all temperature distributions are symmetrical because each chosen stack is geometrically symmetric and uniform heat flux is applied at all surfaces.



(a)

(b)



(c)

(d)

Figure 3-19 Temperature distributions of gases and structures of SOFC stack including outer solid structure (1min.); (a) anode, (b) cathode, (c) interconnector, and (d) MEA

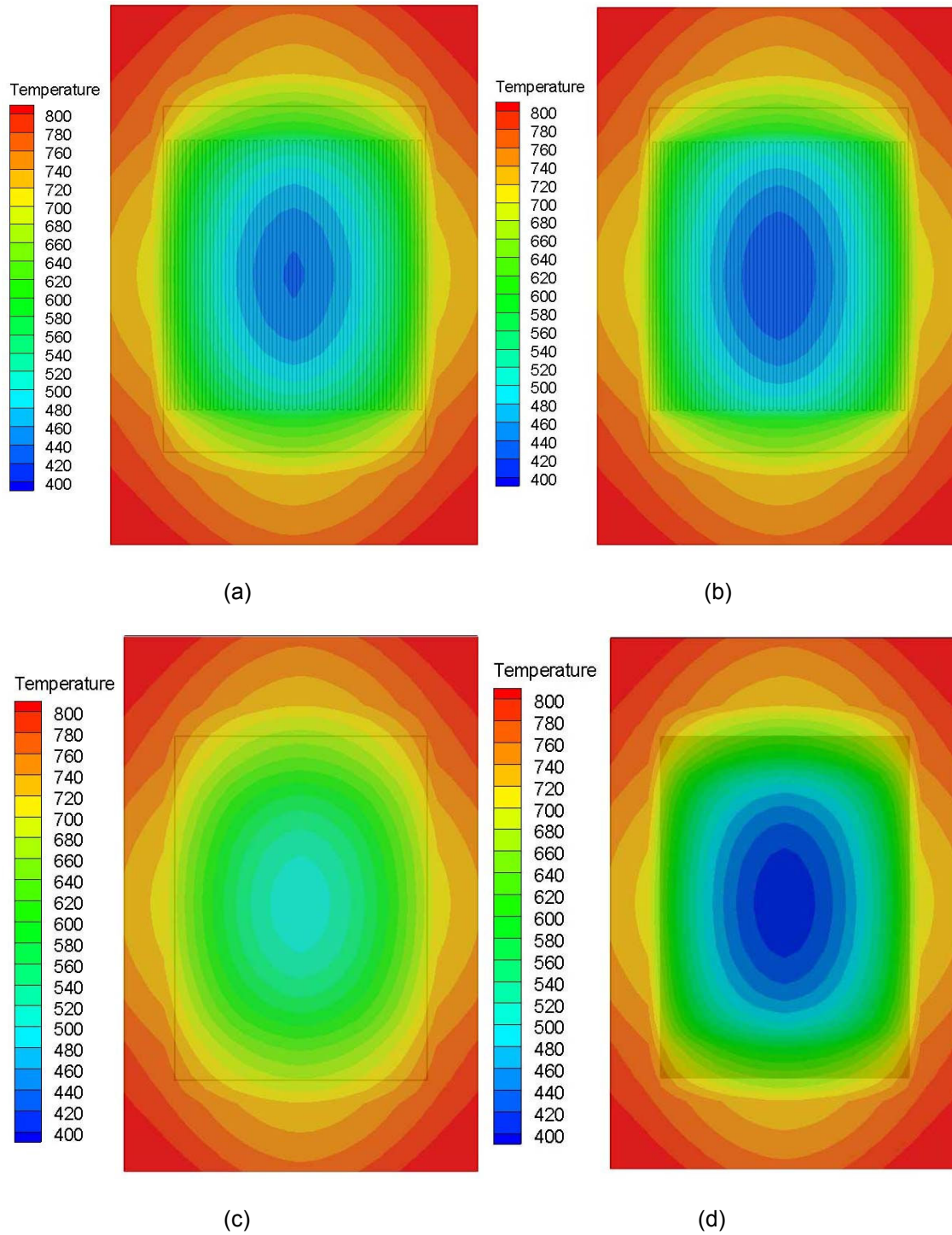


Figure 3-20 Temperature distributions of gases and structures of SOFC stack including outer solid structure (30min.); (a) anode, (b) cathode, (c) interconnector, and (d) MEA

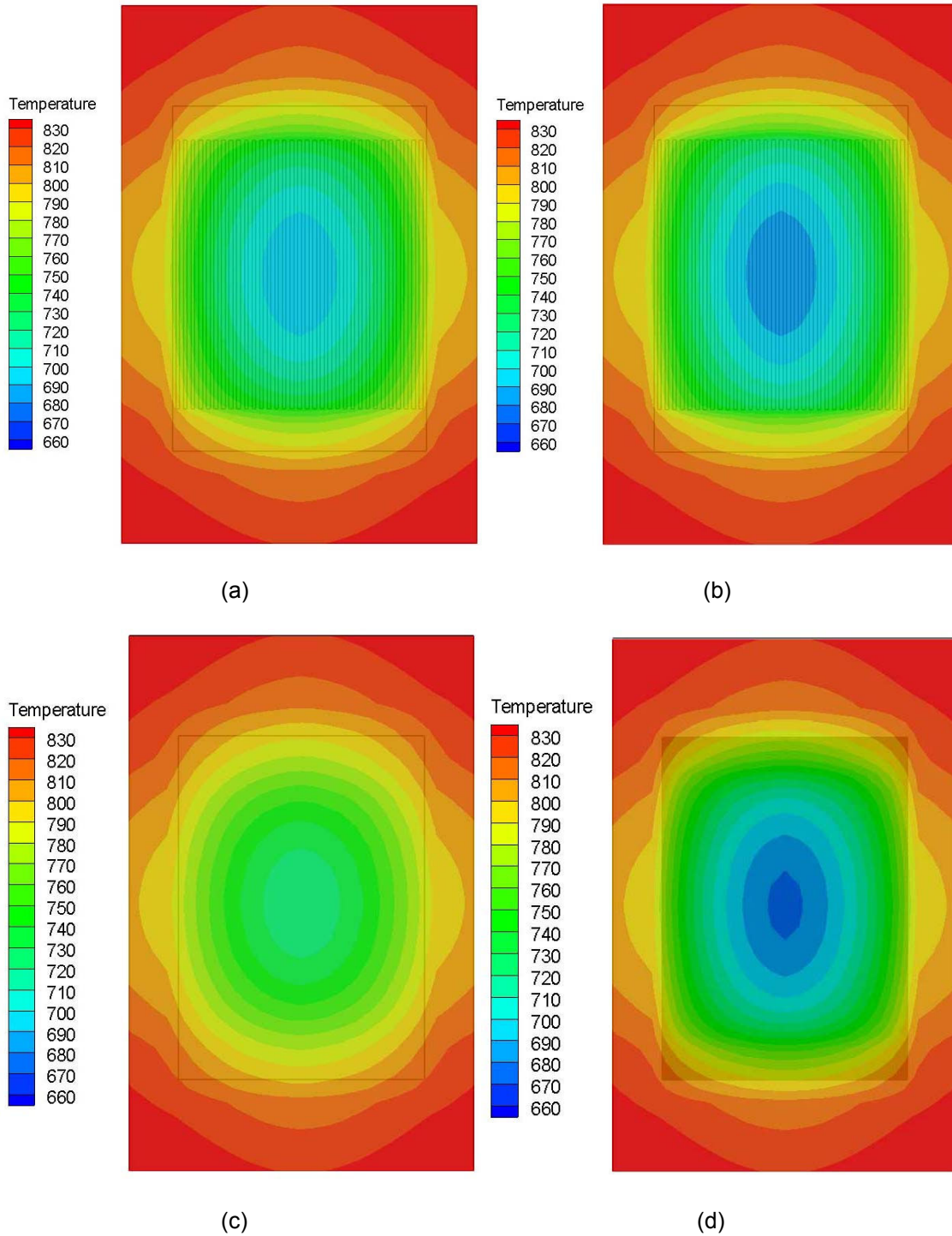
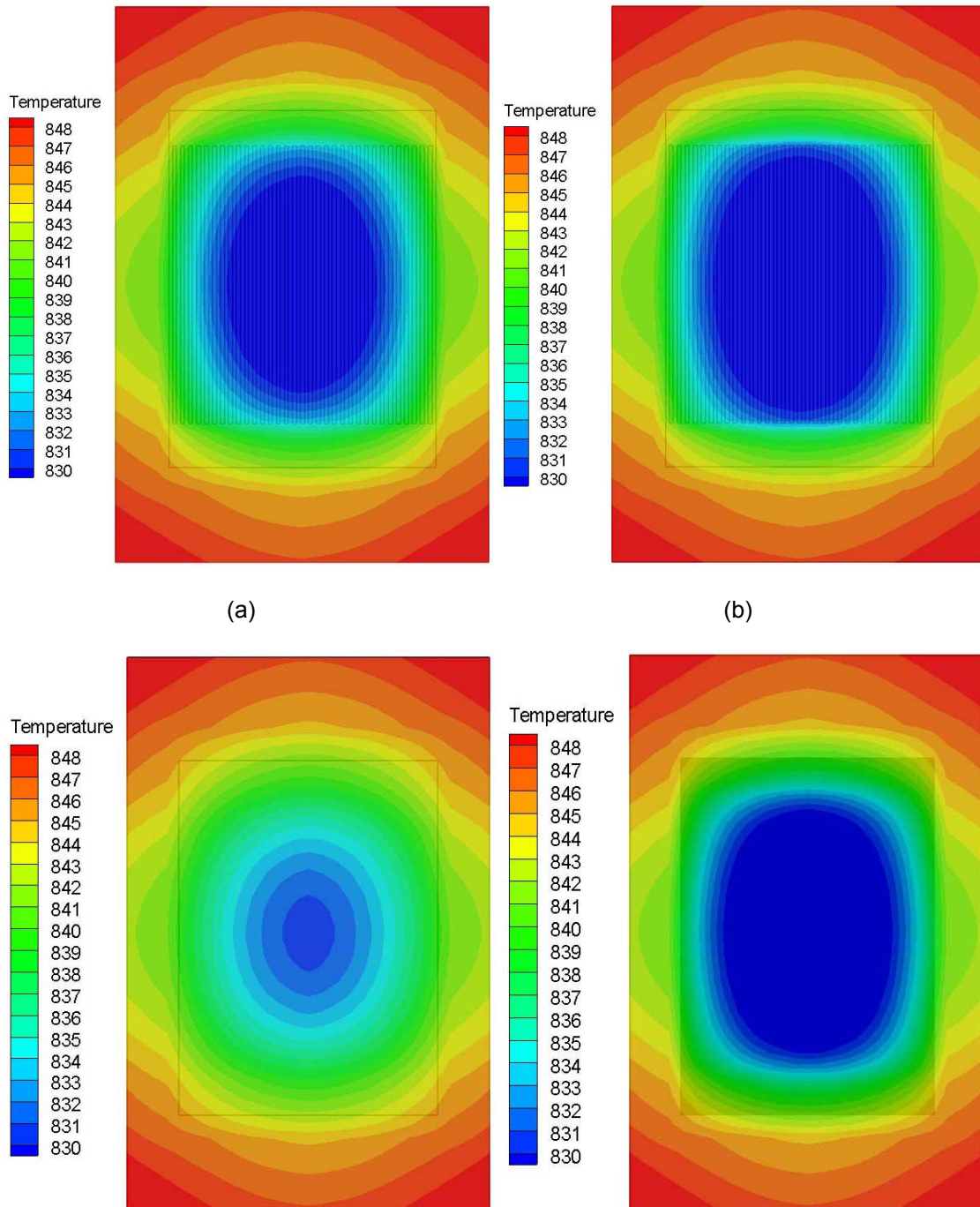


Figure 3-21 Temperature distributions of gases and structures of SOFC stack including outer solid structure (1hr.); (a) anode, (b) cathode, (c) interconnector, and (d) MEA



(c)

(d)

Figure 3-22 Temperature distributions of gases and structures of SOFC stack including outer solid structure (2hr.); (a) anode, (b) cathode, (c) interconnector, and (d) MEA

Unlike the heating method using cathode air, there is no distinctive difference of temperature distributions between structures and channels at the beginning. In addition, temperature gradient is always from the outer surface to the inside. The increase of temperature of anode channel is faster than cathode due to the shorter height of channel. In addition, the increase of temperature of interconnector is faster than MEA due to its larger thermal conductivity than MEA.

Because heating rate is adjusted following Eq.(3.20), once stack surface temperature reaches prescribed maximum allowable temperature, net heating energy can be found using the following equation;

$$E_{Furnace} = \int_0^{t_{end}} \dot{q}(t) dt \quad (3.21)$$

When an initial heating rate of 1000W was chosen, the total heating energy was found as 1.8768 kWh using (3.21) for a total heating time of 5980 seconds (\cong 1.66 hours) until the lowest temperature over entire stack reaches 800°C. Depending on initial heating rate, transient behavior of stack surface temperature can be different. Figure 3-23 shows the net heating energy for 2 hours for two different initial heating rates of 100W and 1000W. As Figure 3-23 implies, initial heating rate of 1000W causes rapid increase of stack surface temperature while initial heating rate of 100W gradually increases the stack surface temperature allowing less thermal gradient in the stack.

Figure 3-24 shows the net heating energy that was supplied to the SOFC stack with the electric furnace for 2 hours for different rib sizes. As shown in Figure 3-24, the net heating energy was not affected much (only 2~3% difference of net heating energy) by changing the rib sizes from 1mm to 3mm because total rib volume is negligible compared to the total stack volume.

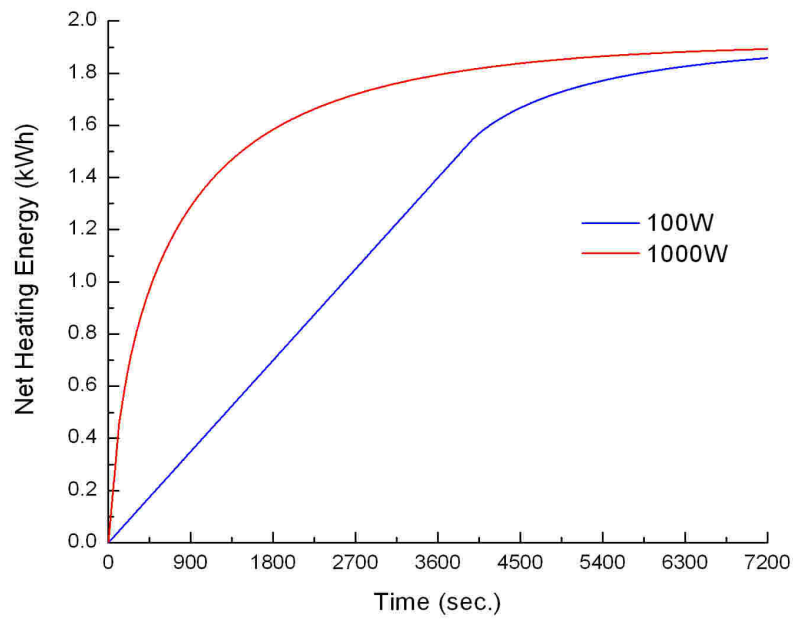


Figure 3-23 Net heating energy with different furnace heat inputs

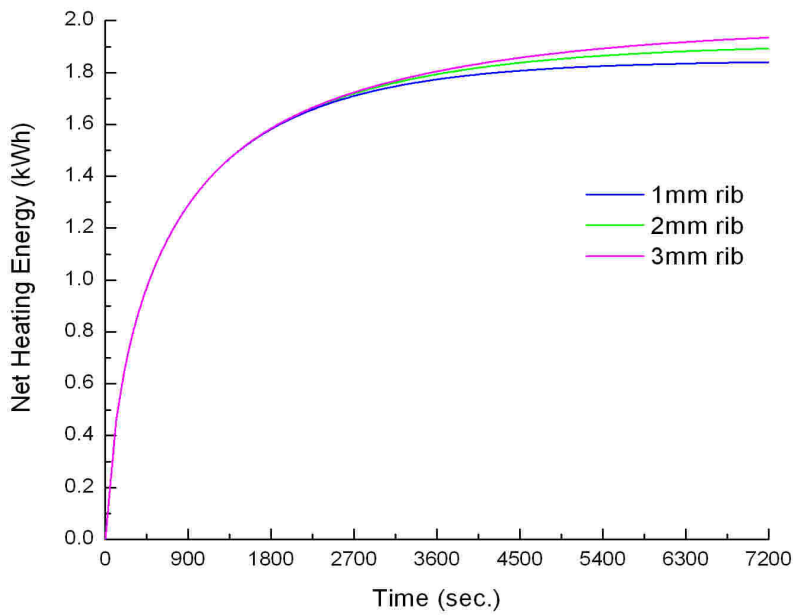


Figure 3-24 Net heating energy vs. time (furnace heating)

Figure 3-25 compares the net heating energy for both heating methods. When only net heating energy is considered, the hot air heating method requires less net heating energy than

the electric furnace heating method. The temperature range of the whole SOFC stack with hot air heating for 1 hour is around 202~220°C, while around 128~172 °C with furnace heating for 1 hour. In addition, after 2 hours of heating, the temperature ranges are 29~31 °C for hot air heating and 19~27 °C for furnace heating. However, different initial heating rates for furnace heating result in a different thermal gradient inside the stack. Likewise, different hot air flow rates result in a different thermal gradient inside the stack. Therefore, heating rates or hot air flow rates should be controlled accordingly depending on allowable maximum thermal stress or thermal gradient for specific stack design.

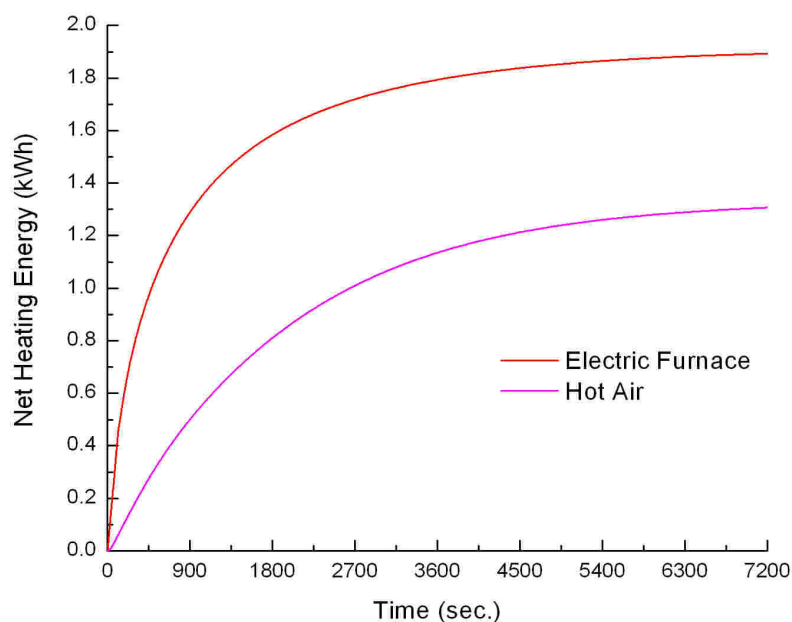


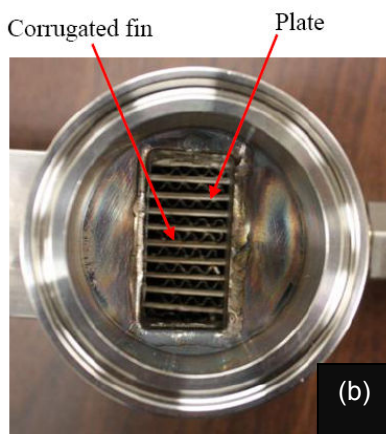
Figure 3-25 Net heating energy comparison between furnace and hot air heating method

Chapter 4

Heat Exchanger

4.1 Heat exchanger configuration

Figure 4-1(a) illustrates a commercial heat exchanger (HEX) acquired for the research. It is composed of corrugated fins, plates and outer parts such as Swagelok® for tube fitting and flanges for connecting with small pipes. And, Figure 4-1(b) shows the flow direction of both hot air and cold air through the HEX. The HEX can be easily bundled for larger HEX configuration and is also available as a reactor/reformer by depositing catalysts. Although a variety of corrugation geometries can be inserted into the HEX module to tailor an appropriate heat transfer and pressure drop, round-type of corrugated fins were inserted between plates as shown in Figure 4-1(b).



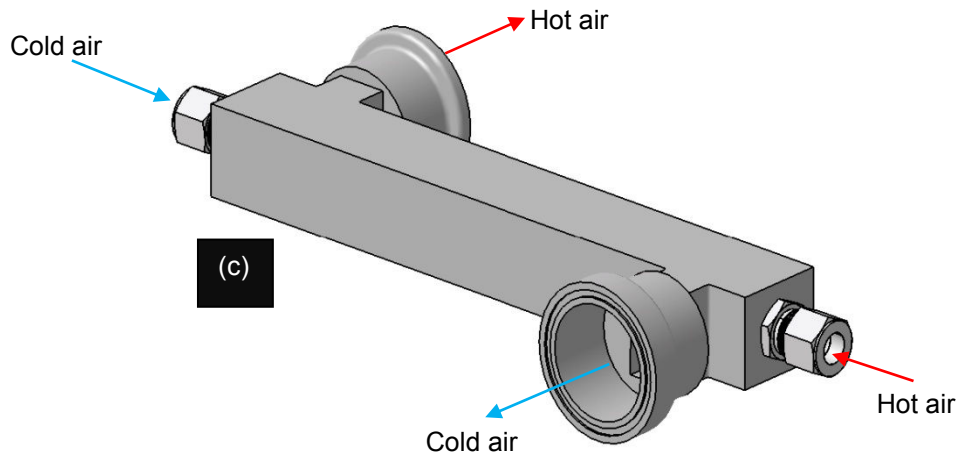


Figure 4-1 (a) Configuration of HEX, (b) Components of the HEX and (c) flow direction of air

Table 4-1 provides physical dimensions of the HEX, and Table 4-2 shows thermo-mechanical properties of materials of which are used for making plates and inserted fins. In this simulation, the material of the plates is Inconel 600 and the material of fins which are inserted between the channels is Fe-Cr alloy (Fe / Cr / Al / Y).

Table 4-1 Geometric dimensions of HEX

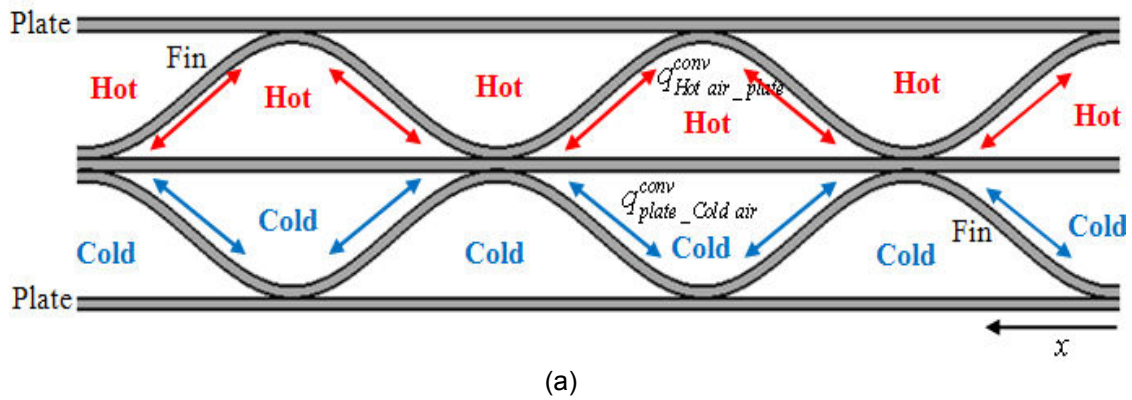
Element	Description	Size(mm)
L	Length of HEX	225
W	Width of HEX	38.1
t_{fin}	Fin thickness	0.1016
t_{plate}	Plate thickness	1.905
h_h	Hot air channel height	1.8
h_c	Cold air channel height	1.8

Table 4-2 Properties of materials

Element	Property	Value
Inconel 600	Density(kg/m ³)	8470
	Specific heat(J/kg·K)	444
	Thermal conductivity(W/m·K)	26.1
Fe-Cr Alloy	Density(kg/m ³)	7169.09
	Specific heat(J/kg·K)	460
	Thermal conductivity(W/m·K)	16

4.2 Flow channel modeling

The theoretical background such as heat transfer mechanisms, momentum and energy equations, discretization, etc. to model the HEX is the same as the method for the CHER in section 4.4. The only difference between the HEX and CHER, the FSM through lower channels was replaced by the cold air as shown in Figure 4-2. In other words, there is no chemical reaction inside both channels.



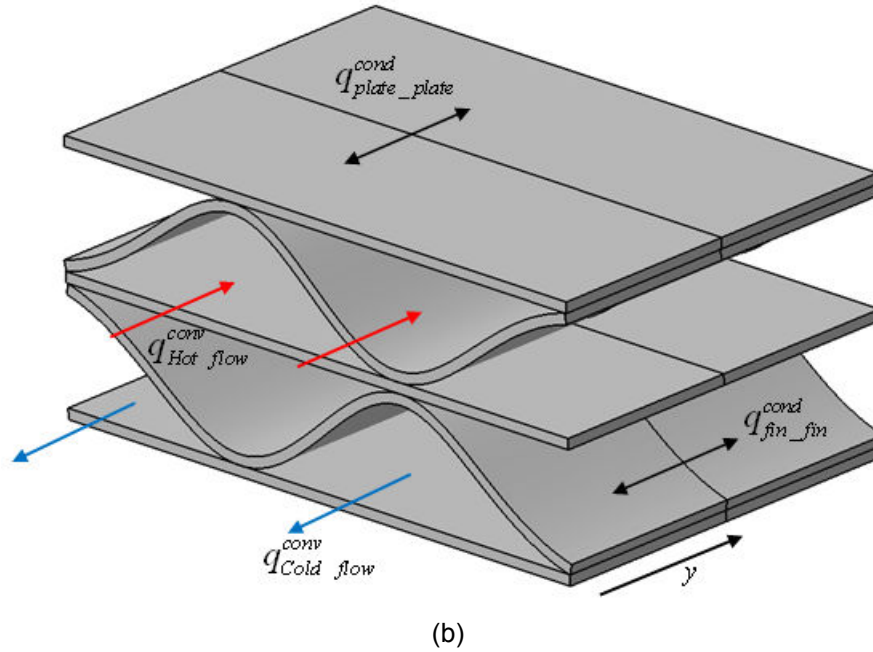


Figure 4-2 Schematic diagrams of heat transfers in HEX; (a) Heat transfer along x-direction (channels cross section view) and (b) Heat transfer along flow direction (y-direction)

4.3 Results

Firstly, transient simulation results focusing on temperature profiles inside both hot air and cold air channels of the HEX are discussed. In addition, the temperature profiles of all solid structures such as plates, fins, and outer walls are presented in this research. Concomitantly, any kind of desired thermal analytical result can be examined in this simulation and can be compared by experimental results.

An air pre-heater as shown in Figure 4-3(a) was used to supply the hot air for the HEX. Also, an electric cabinet as shown in Figure 4-3(b) was used for various purposes such as 1) power supply for the air pre-heater, 2) communication between air pre-heater and computer, 3) temperature measurement, 4) mass flow control, 5) external safety device.



Figure 4-3 (a) Air pre-heater and (b) electric cabinet

Figure 4-4 shows the simplified layout of the HEX test rig that is used for the experiment.

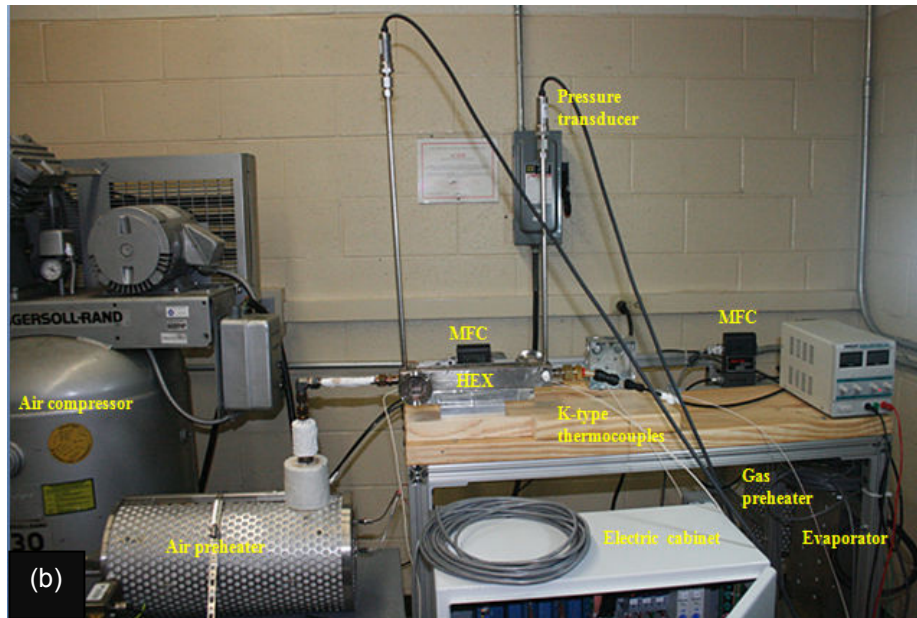
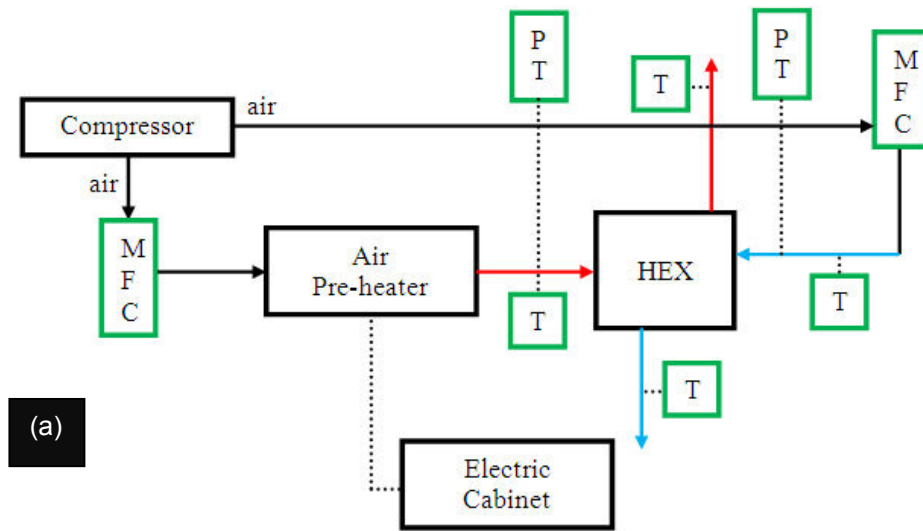


Figure 4-4 The HEX test rig, (a) schematic diagram of the experimental apparatus and (b) overview of the test rig

Here, PT represents a pressure transducer and T is a thermocouple. Both the hot air and cold air were supplied for the HEX at a constant mass flow rate. With digital mass flow controllers (MFC), mass flow rates are managed to follow the set-point mass flow rate which is

set at 1 gram per second on both sides in this experiment. The temperatures on both inlets were measured by the duplex insulated K type thermocouples and the pressures on both inlets were measured by the pressure transducers in real time. A computer controlled data acquisition (DAQ) hardware collects all the signal from thermocouples and transducers.

For the validation of simulation with the experiment, interpolating data from the experimental measurement were applied to this simulation for the initial input conditions of simulation such as pressures and temperatures on both inlets of the HEX. Figure 4-5 and Figure 4-6 show measured and interpolated pressures and temperatures on both inlets of the HEX. Both experiment and simulation were performed for total duration of 1,800 seconds. Simulation results were compared with experimental measurements.

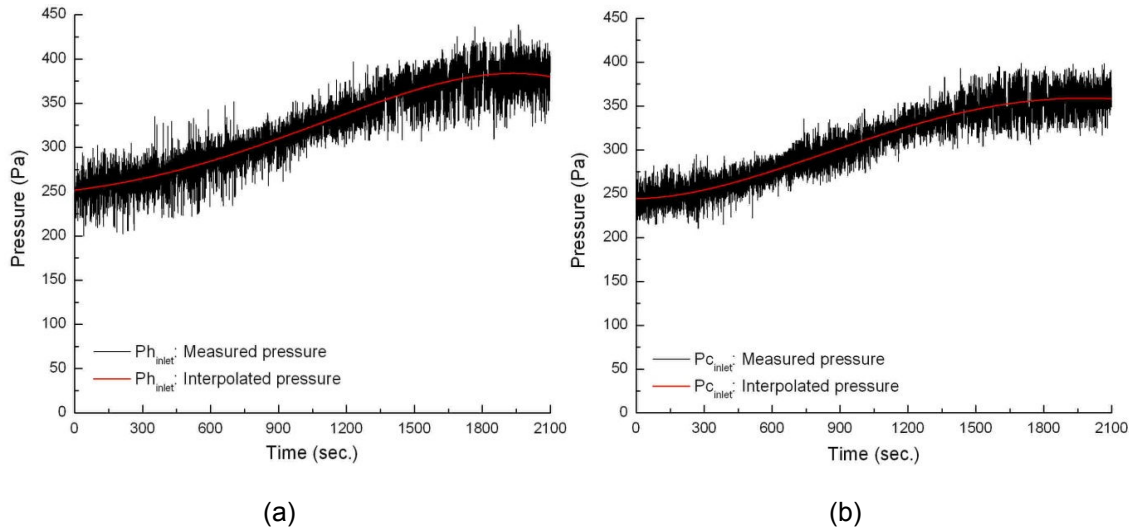


Figure 4-5 HEX inlet pressure, measured and interpolated; (a) Pressure of hot air at inlet and (b) Pressure of cold air at inlet

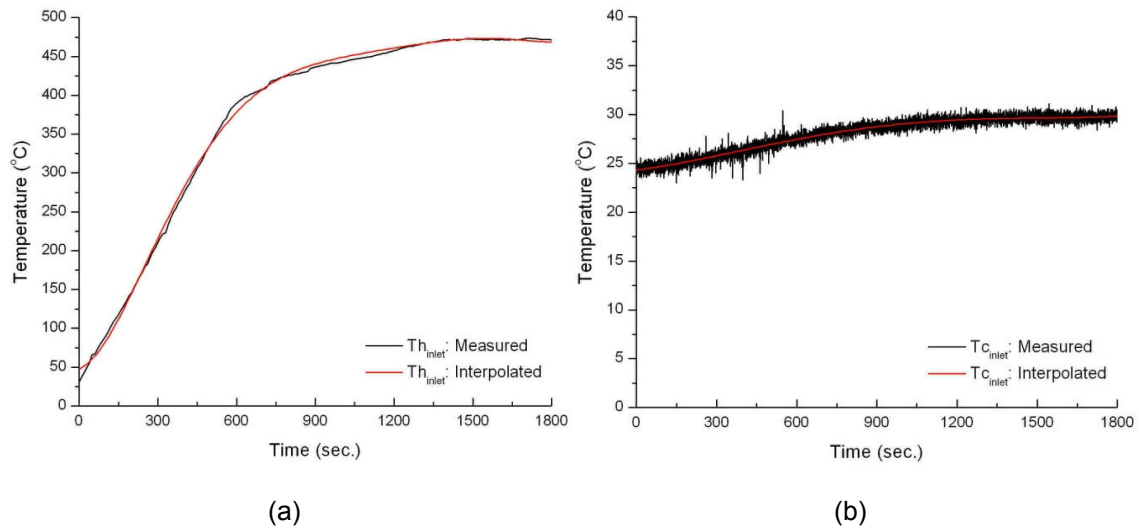


Figure 4-6 HEX inlet temperature, measured and interpolated; (a) Temperature of hot air at inlet and (b) Temperature of cold air at inlet

Measured and simulated temperatures of both the hot air and cold air at the outlet of the HEX were shown in (a) (b)

Figure 4-7, and the comparative results show a similar tendency between the measured data and predicted data. Although there are some discrepancies during the heat exchanging process, they can be estimated within about 20°C temperature difference. This difference can be acceptable for a real time model. However, it needs to be clarified that the causes of this discrepancy are due to uncertainty in mechanical properties and physical dimensions (hydraulic diameter, surface area, etc)..

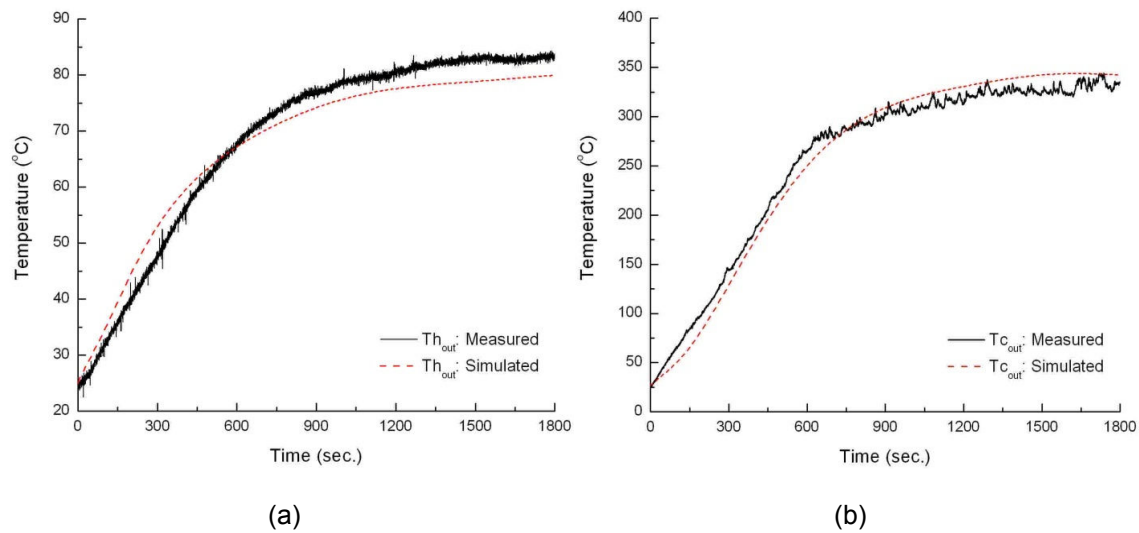


Figure 4-7 HEX outlet temperature, measured and simulated; (a) Temperature of hot air at outlet and (b) Temperature of cold air at outlet

With a geometric limitation, it is impossible to measure the temperatures of plate, fins, and both airs in the center of the HEX. However, if there are no noticeable temperature differences of both the simulation and experiment at the outlet of the HEX, other temperature distributions from the simulation are consistent with temperatures from the experiment. Temperature distributions at any considered control volume of each component can be achieved in this simulation. For example, the temperatures in the middle of the HEX can be shown in Figure 4-8. The HEX reaches steady state after operating 30 minutes.

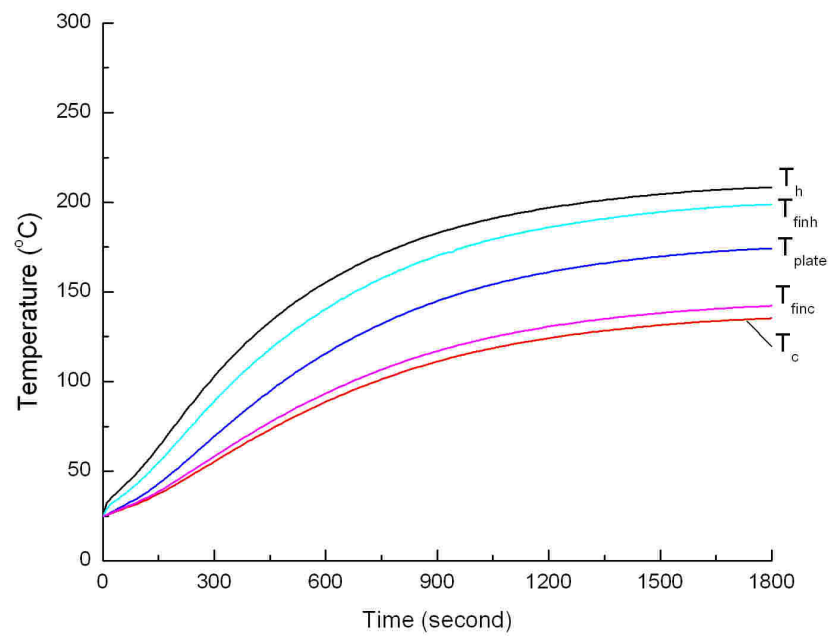


Figure 4-8 Temperature distribution of HEX with time at specific C.V.

Chapter 5

Compact Heat Exchange Reformer

5.1 Scope of this research

This chapter focuses on the simulation of transient characteristics of the compact heat exchange reformer (CHER) during the initial phase of Stage 2 described in Figure 2-1(b), where the stack and CHER have been already heated up to a specified design temperature, and the FSM is ready to be fed into the CHER. In addition, SR reaction with WGS reaction was chosen as the most appropriate reforming model for the CHER characterization. Even if a combustion gas would be used as a thermal energy source to the CHER, the current model in the research will approximate the exhaust gas as air. The CHER is modeled as two-dimensional array of finite control volumes (see modeling section for details). All the finite control volumes in the air channels and solid structures are modeled with transient energy equations. All the control volumes in FSM channels will be also modeled with transient energy equations and dynamic molar balance equations. Both reaction enthalpy and convection heat transfer due to convective flow of reactants and products between the catalyst-coated fins and FSM channels are considered. Several parametric simulations were performed as methane as a primary fuel mixed with steam to evaluate the performance of the CHER as a function of different operating temperature, steam-to-carbon ratio at the inlet, pressure gradient across the CHER, channel length, and flow configuration (co-flow and counter-flow).

5.2 CHER configuration and flow channel modeling

Figure 5-1 shows the CHER purchased from a commercial supplier, which is composed of corrugated inserts (fins) separate by plates. The figure also shows the flow directions of FSM, reformat gas (H_2 , CO , CO_2), and air.

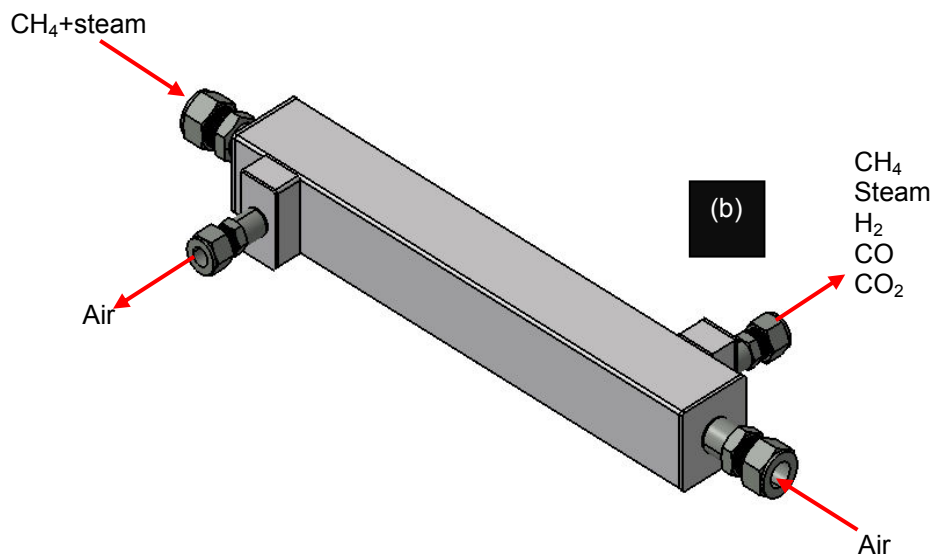
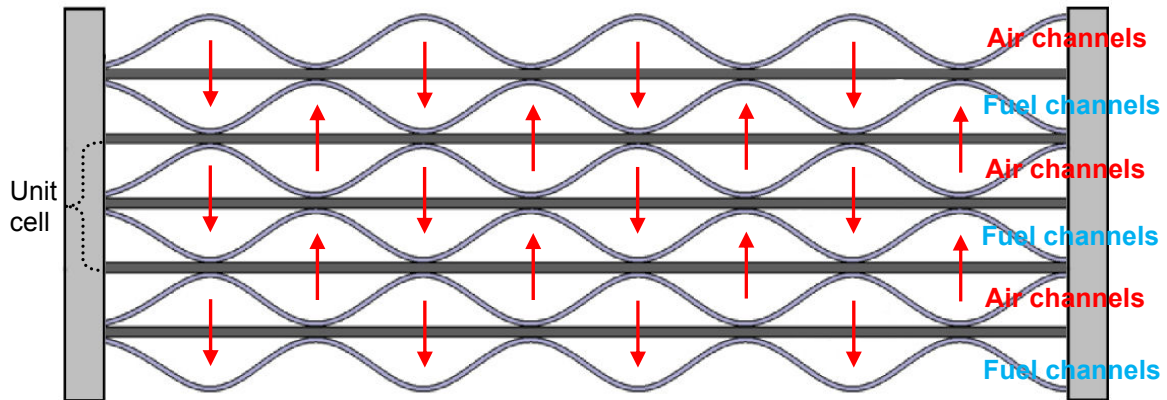


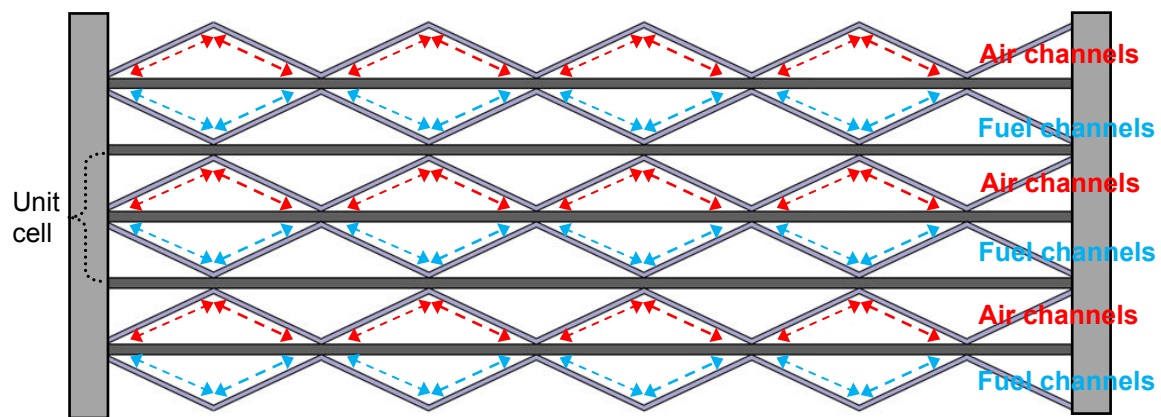
Figure 5-1 Configuration of the CHER and flow directions of gases; (a) Compact Heat Exchange Reformer (CHER) and (b) Flow directions of gases

The corrugated fins inserted between the plates divide the air and FSM streams as shown in Figure 5-2(a). One layer is with hot air channels separated by fins and the other layer is for FSM channels separated by catalyst-coated fins. These layers are repeated as co-flow or counter-flow plate-fin gas HEX configuration. Figure 5-2(b) is the slightly simplified fin geometry with heat conduction paths within the fins, which is acceptable for the purpose of the current

research that focuses on the transient thermal dynamics of the CHER with simplified 1-D flow through the each channel.



(a)



(b)

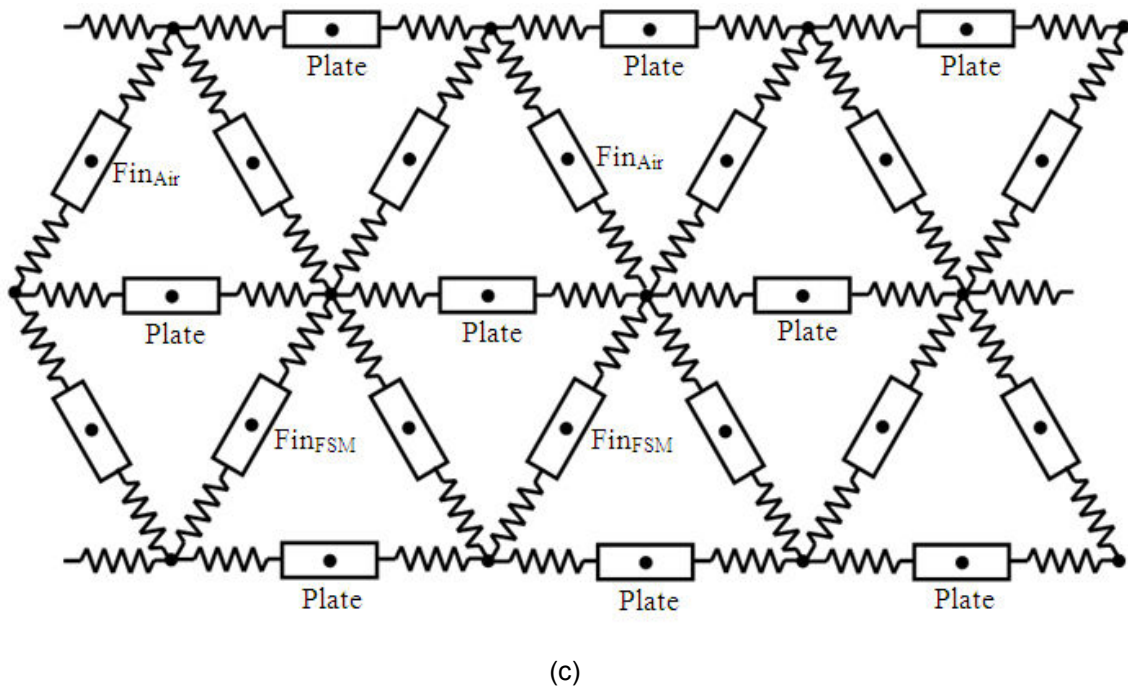


Figure 5-2 (a) Corrugated fins and plates, (b) Simplified flow channel model of the CHER with unidirectional heat transfer, and (c) Model of thermal circuit

In addition, the current model assumes identical behaviors among all the unit cell layers along the vertical direction. The assumption was based on the fact that the CHER design in the research can be stacked along the vertical direction to scale up the total capacity of the CHER. However, stacking along the in-plane direction (horizontal direction) is prohibited due to the inlet and exit flanges (see Figure 5-1). Therefore, variation along the horizontal direction should be considered, and thus total control volume array is two-dimensional, i.e., along the flow and in-plane directions. Figure 5-2(c) presents the model of thermal circuit for unit cell particularly from Figure 5-2(b). All conductive heat transfer between plate and fins for both sides were considered with this thermal circuit model.

5.3 System Layout for the simulation

Figure 5-3 describes the layout of the system to be used to analyze the performance of the CHER. For flow and thermal modeling, proper thermal and pressure boundary conditions

should be applied. Particularly, the inlet region in front of each gas channel should be modeled carefully because the flow resistances of the connecting tube (i.e. Swagelok® adapters) are not negligible. The plenums should also be in front of both inlets of the FSM and air side to mimic the fuel-steam mixing chamber.

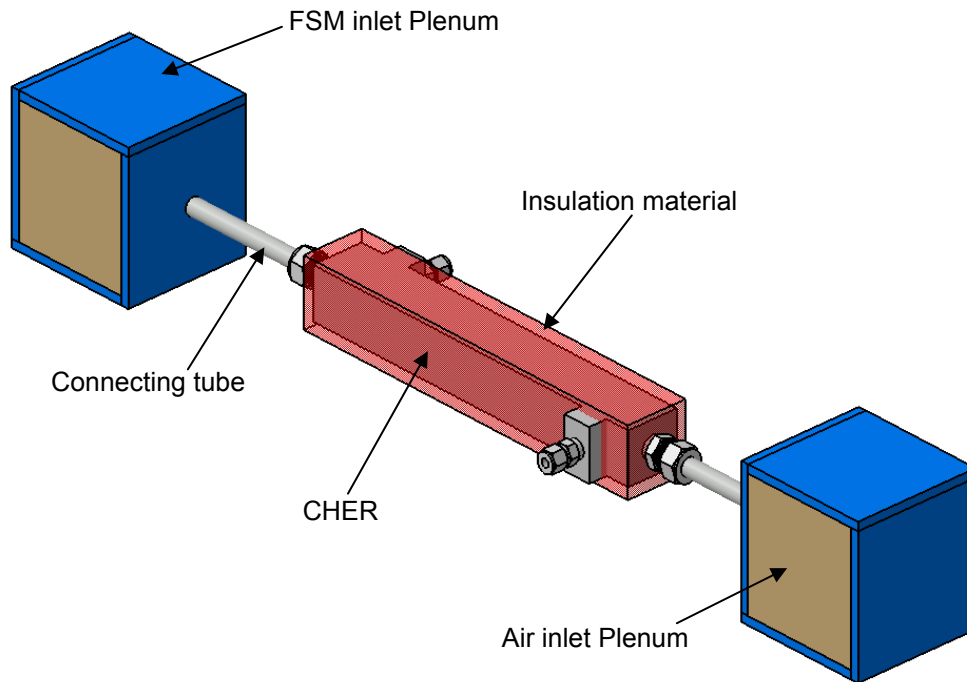


Figure 5-3 System layout for simulation of co-flow CHER

Figure 5-4 shows a coordinate system for the model discretization. Flow direction represents the y-coordinate. And the x-coordinate shows perpendicular coordinate to the y-coordinate. The number of channels divided by fins is N_x and each flow channel is divided by N_y control volumes along the flow direction for both air and FSM channels as shown in Figure 5-4.

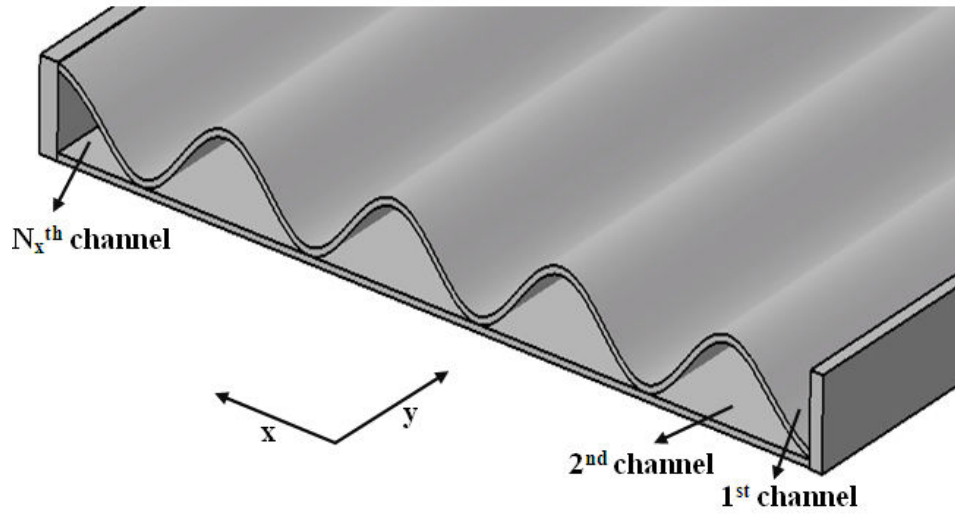
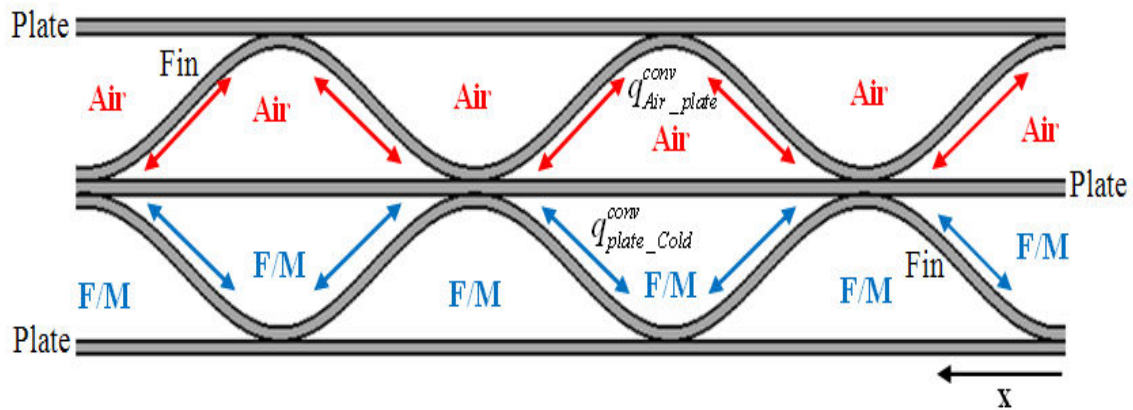
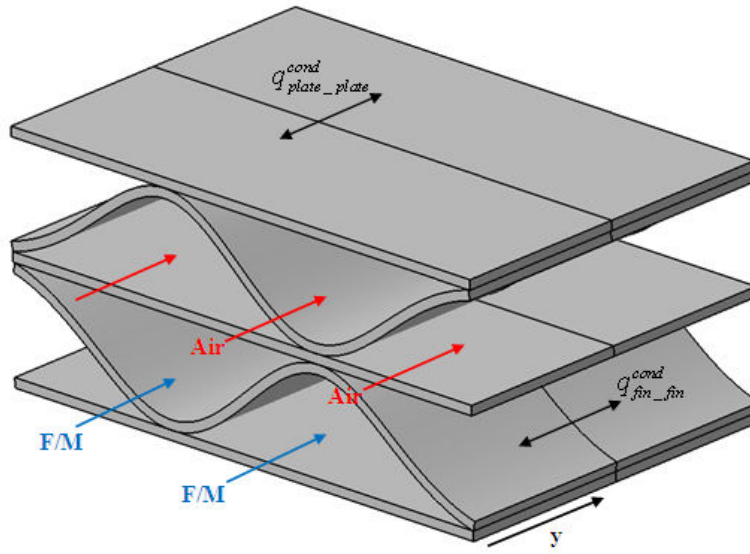


Figure 5-4 Coordinate system for model discretization (y is along the flow direction), $N_x=10$, $N_y=30$

Figure 5-5 describes more details of each control volume with heat transfer mechanisms. Hot air at certain temperature (at air inlet plenum) flows to positive y -direction in the upper channels and FSM at certain prescribed temperature (at FSM inlet plenum) flows in the lower channels to the same direction, i.e., as a co-flow configuration.



(a)



(b)

Figure 5-5 Schematic diagrams of heat transfers in the CHER stack; (a) Heat transfer through convection and molecular (channels cross section view) and (b) Heat transfer through conduction along flow direction (y-coordinate)

Although Figure 5-5 shows only one layer among all stacks, the repetitive heat transfer scheme was considered for the entire heat transfer analyses. The representation of conductive heat transfers among all solid structures was skipped due to the lack of space in Figure 5-5(a).

Table 5-1 summarizes the dimensions of the CHER which are channel pitch, heights of both air and FSM channels, and thicknesses of plate and each fin used in the simulation.

Table 5-1 Geometric dimensions of a Control Volume

Description	Size (mm)
Fin thickness	0.1016
Plate thickness	1.905
Channel pitch	8.467
Air channel height	1.8
FSM channel height	1.8

5.4 System Layout for the experiment

In simulation-based research, the combustion gas was used as a thermal energy source to the CHER as shown in Figure 2-1(b). However, the CHER is heated up to a specified design temperature by flowing the hot air through air channels. The air preheater is used to heat the air and the gas preheater is used to heat the FSM and the evaporator generates the steam to be supplied for the SR process. The experiment was performed by various hot air inlet temperatures and SCRs. The specific inlet temperatures of both the air and FSM are controlled by an electric cabinet as shown in Figure 5-6 that includes several PID controllers and thermocouple panels and the SCR is controlled by the mass flow controller for CH₄ and water metering pump for water. Water at a constant flow rate is evaporated by the evaporator/steam generator.

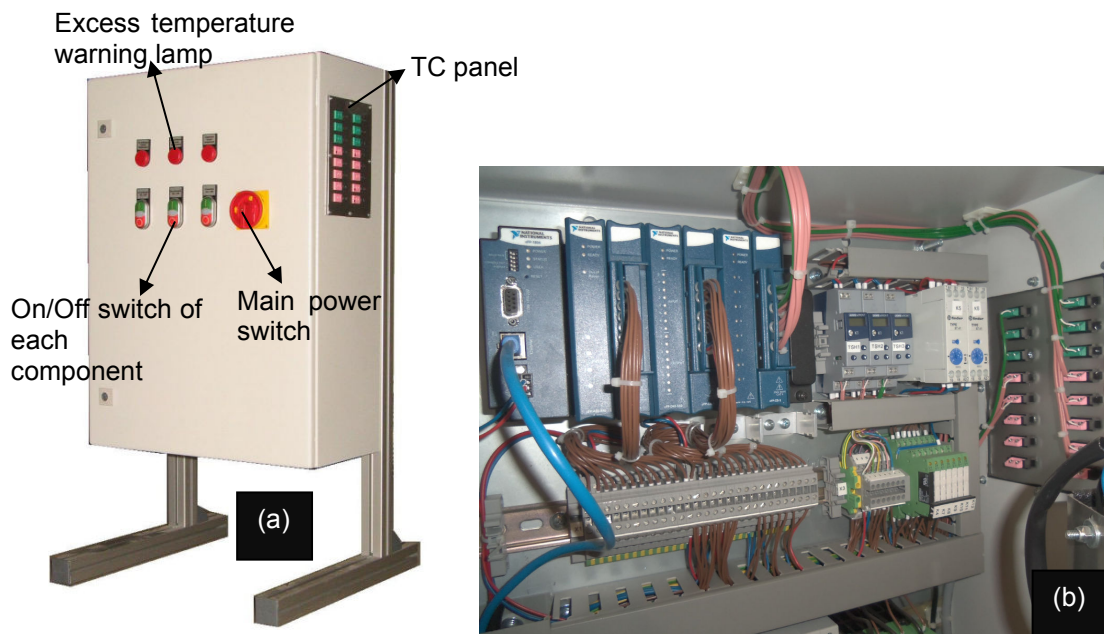


Figure 5-6 (a) Electric cabinet and (b) an inner view of controller units

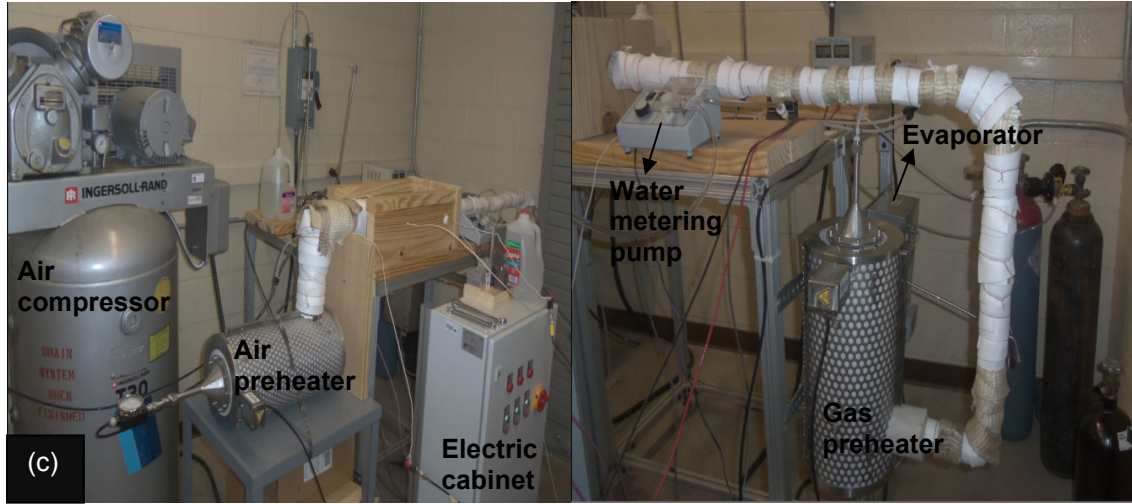


Figure 5-7 The CHER test rig, (a) schematic diagram of the experimental apparatus and (b & c) overview of the test rig

Figure 5-7 describes the schematic diagram and experimental apparatus of the CHER test rig that is used for the experiment. Although Figure 5-7 does not show a precise thermal insulation process for the CHER and all tubes, the outer solid walls of the CHER and all connecting tubes were completely insulated with surrounding by the ceramic tape, fiber product for an ultra-high temperature ($\sim 2600^{\circ}\text{F}$), and wood. Here, GC represents a gas chromatography and T stands for thermocouple. As mentioned earlier, the air, N_2 , CH_4 , and steam are supplied with the CHER at a constant mass flow rate by using the digital MFCs.

Nitrogen is used as an inert carrier gas to heat the channels on the reforming side. The mass flow rate of the air is set at 1.0 gram per second (g/s) on the air side and the mass flow rates of CH_4 and H_2O are set at 0.04 g/s and 0.09 g/s each on the reforming side to maintain the SCR over 2.0. The mass flow rate of CH_4 can be calculated by equation(4.1).

$$\dot{m}_{\text{CH}_4} = \frac{1}{\text{SCR}_{\text{set}}} \cdot \dot{m}_{\text{H}_2\text{O}} \cdot \frac{M_{\text{CH}_4}}{M_{\text{H}_2\text{O}}} \quad (4.1)$$

, where \dot{m} is the mass flow rate and M is the molecular weight and SCR_{set} represents the set steam to carbon ratio.

The temperatures on the inlet and outlet of both the air and reforming side are measured by the duplex insulated K-type thermocouples in real time. An appropriate data acquisition (DAQ) hardware was chosen for acquiring the electric signals from the thermocouples. The reaction products are sampled by a flex-foil gas bag for quantitative analysis with Gas Chromatography (GC).

5.5 Modeling

5.5.1 Air channels

Besides the plenums, the inlet of air channels is a small dead volume distributing the air to all the channel layers. The temperature and pressure of the dead volume serve as true boundary conditions to the air flows through the channels. The properties of the dead volume should be found from mass and energy conservation applied to the inlet dead volume. Because the flow resistance between the plenum and inlet volume is insulated, inlet temperature is the same as that of the plenum. The inlet pressure, P_{Air_inlet} , at the air side is determined by the following equation.

$$\rho_{Plenum_Air} \frac{P_{Plenum_Air} - P_{Inlet_Air}}{R_{ct_Air}} = \sum \dot{m}_{ch_Air} \quad (4.2)$$

ρ_{Plenum_Air} , P_{Plenum_Air} represent the density and pressure of air at the plenum, $\sum \dot{m}_{ch_Air}$ is total mass flow rate into all the air channels, and R_{ct_Air} is the flow resistance of connecting tube between the plenum and inlet volume given as

$$R_{ct} = \frac{1}{A_{ct_Air}} \sqrt{f_{ct_Air} (P_{Plenum_Air} - P_{Inlet_Air}) \frac{\rho_{Plenum_Air} L_{ct_Air}}{2d_h}} \quad (4.3)$$

where f_{ct_Air} is total friction factor, which is a combination of Darcy's friction factor [53] for laminar flow through the connecting tube and all the other parasitic parameters related to the entrance and Swagelok. \dot{m}_{ch_Air} is found from the flow momentum equation applied to each air

flow channel. Neglecting the spatial fluctuation of mass flow rate inside the channel (i.e., $\partial \dot{m}_{ch_Air} / \partial y = 0$), the mass flow rate is a function of only time (through the changes in air properties). Using the ideal gas law relating density, pressure, and temperature, the momentum equation for the air flow along the one-dimensional channel with a hydraulic diameter of D_h is given by

$$\dot{m}_{ch_Air} = \frac{\rho_{avg_air} D_h^2 A_{ch_Air} \Delta p_{ch_Air}}{32 \mu_{air} L_y} \quad (4.4)$$

If the conduction within the air and viscous heat dissipation are neglected, the *transient* energy equation applied to the air channels is written as

$$\frac{\partial T_{ch_Air}}{\partial t} = -\frac{c_p}{c_v} \frac{R_{Air} T_{ch_Air}}{p_{Air}} \frac{\dot{m}_{ch_Air}}{A_{ch_Air}} \frac{\partial T_{ch_Air}}{\partial y} + \frac{RT_{ch_Air}}{p_{Air}} \frac{\dot{q}_{to_air}}{c_v} \quad (4.5)$$

where \dot{q}_{to_air} is the total heat flux input per unit volume of the control volume, and it is given by

$$\dot{q}_{to_air} = \dot{q}_{plate_air} + \dot{q}_{fin_air} \quad (4.6)$$

Here, \dot{q}_{plate_air} is convection heat transfer from the plate to air, and \dot{q}_{fin_air} is convection heat transfer from fins to the air channel. To find the heat convection coefficients, h_{air} , the average temperature of the air in channel, plate, and fins was used as the reference temperature for the air properties (Prandtl number Pr , heat conduction coefficient k_{air} , and viscosity) used in the following equations for Nusselt number [54] of laminar flow,

$$\frac{h_{air} D_h}{k_{air}} = Nu_{D_h} = 3.66 + \frac{0.0668 \left(\frac{D_h}{L} \right) \cdot Re_{D_h} \cdot Pr}{1 + 0.04 \left[\left(\frac{D_h}{L} \right) \cdot Re_{D_h} \cdot Pr \right]^{\frac{2}{3}}} \quad (4.7)$$

Energy equations for plate and fins in the air side can be written as

$$\rho_{plate} C_{v_plate} \frac{\partial T_{plate}}{\partial t} = k_{plate} \left(\frac{\partial^2 T_{plate}}{\partial x^2} + \frac{\partial^2 T_{plate}}{\partial y^2} \right) + \dot{q}_{to_plate} \quad (4.8)$$

$$\rho_{fin} C_{v_fin} \frac{\partial T_{fin_air}}{\partial t} = k_{fin} \left(\frac{\partial^2 T_{fin_air}}{\partial \tilde{x}^2} + \frac{\partial^2 T_{fin_air}}{\partial y^2} \right) + \dot{q}_{to_fin} \quad (4.9)$$

, where k_X (X =plate and fin) represents the thermal conductivities. \dot{q}_{to_plate} is a summation of 1) the convection from the air and FSM to the plate, and 2) the conduction between the plate and fins of the air and FSM sides. And, \dot{q}_{to_fin} is the summation of 1) the convection from the air to the fin and 2) the conduction between the fin and plate. The expressions for \dot{q}_{to_plate} and \dot{q}_{to_fin} are given by;

$$\dot{q}_{to_plate} = \dot{q}_{air_plate}^{conv} - \dot{q}_{plate_FSM}^{conv} + \dot{q}_{fin_plate}^{cond} - \dot{q}_{plate_fin}^{cond} \quad (4.10)$$

$$\dot{q}_{to_fin} = \dot{q}_{air_fin}^{conv} + \dot{q}_{plate_fin}^{cond} \quad (4.11)$$

where superscripts ‘conv’ and ‘cond’ denote convection and conduction, respectively.

5.5.2 FSM channels

Heat energy from the air channels are used for SR reactions in the FSM side. Figure 5-5 shows all the heat transport mechanisms including convections and conductions with their appropriate directions excluding radiations (The thickness of plates was exaggerated).

A dynamic model of the CHER FSM channels is developed for CH_4 as a primary fuel but the model can be applied to other fuels such as JP-A and diesel. General balanced equations for SR and WGS reaction are represented by



The conversion rate of CH₄ into H₂ by SR at $(i, j)^{th}$ control volume (index are omitted in the following equations for brevity) inside the FSM channels is described by forward reaction rate, $k_{CH_4_SR}(T_{fin_FSM})$, and equilibrium constant for SR reaction, $K_{P_SR}(T_{fin_FSM})$;

$$\dot{n}_{CH_4}|_{SR} = k_{CH_4_SR}(T_{fin_FSM}) \left(Q_{CH_4} Q_{H_2O} - \frac{Q_{H_2}^3 Q_{CO}}{K_{P_SR}(T_{fin_FSM})} \right) \quad (4.14)$$

, where $Q_i (i = species)$ is the activity of the species defined as its partial pressure in bar. The conversion rate of CO into H₂ by WGS reaction can be found in a similar way using forward reaction rate, $k_{CO_WGS}(T_{fin_FSM})$, and equilibrium constant, $K_{P_WGS}(T_{fin_FSM})$;

$$\dot{n}_{CO}|_{WGS} = k_{CO_WGS}(T_{fin_FSM}) \left(Q_{CO} Q_{H_2O} - \frac{Q_{H_2} Q_{CO_2}}{K_{P_WGS}(T_{fin_FSM})} \right) \quad (4.15)$$

Once the reforming and shifting rates have been determined, the consumption rate of steam and the generation rate of CO₂ follow the molar stoichiometric ratio described in Eqs. (4.12) and (4.13).

The reaction rates are usually expressed in the unit of moles per second. The Arrhenius Equation relates the activation energy, absolute temperature, and the specific rate constant for a reaction [60], which is given by

$$k_{reaction} = A_{reaction} \exp \left(\frac{-E_{a_reaction}}{RT_{fin_FSM}} \right); \text{ reaction} = CH_4_SR/CO_WGS \quad (4.16)$$

The numerical values of pre-exponential factors used in this simulation are $A_{CH_4_SR} = 4.225 \times 10^{15} \text{ mol} \cdot \text{s}^{-1}$ for the SR reaction and $A_{CO_WGS} = 1.955 \times 10^6 \text{ mol} \cdot \text{s}^{-1}$ for the WGS reaction [61]. The activation energies are $E_{a_CH_4_SR} = 240,100 \text{ J} \cdot \text{mol}^{-1}$ for the SR reaction, and $E_{a_CO_WGS} = 67,130 \text{ J} \cdot \text{mol}^{-1}$ for the WGS reaction [61]. R is the universal gas constant in the unit of $\text{J} \cdot \text{mol}^{-1} \cdot \text{K}^{-1}$. The equilibrium constants are given by

$$K_{p_SR} = \exp\left(\frac{-\Delta G_{f_SR}}{RT_{fin_FSM}}\right) \quad (4.17)$$

$$K_{p_WGS} = \exp\left(\frac{-\Delta G_{f_WGS}}{RT_{fin_FSM}}\right) \quad (4.18)$$

, where ΔG_f is the change in Gibbs free energy of formation over the given reaction.

Applying the dynamic mass balance to each molar species inside the FSM channels, a set of non-linear dynamic equations for molar concentration of each species at $(i, j)^{th}$ control volume (index are omitted for brevity in the following equations) in the FSM channels can be found. For example, for hydrogen and water;

$$\frac{\partial n_{H_2}}{\partial t} = \dot{n}_{H_2_in} + 3\dot{n}_{CH_4}|_{SR} + \dot{n}_{CO}|_{WGS} - \dot{n}_{H_2_out} \quad (4.19)$$

$$\frac{\partial n_{H_2O}}{\partial t} = \dot{n}_{H_2O_in} - \dot{n}_{CH_4}|_{SR} - \dot{n}_{CO}|_{WGS} - \dot{n}_{H_2O_out} \quad (4.20)$$

Dynamic equations for other species can be found in a similar way. In the above equations, \dot{n}_{X_in} and \dot{n}_{X_out} (X =species) correspond to into- and out of the $(i, j)^{th}$ control volume, respectively.

The thermal dynamics of gas channels considers convective thermal enthalpy exchange between the reactants and products associated with SR and WGS reactions, convection with the plates, and thermal enthalpy flux along the flow direction;

$$n_{FSM}\hat{c}_{v_FSM}\frac{\partial T_{ch_FSM}^j}{\partial t} = \left(\sum_X \dot{n}_{X_in}\hat{c}_{p,X}\right)T_{ch_FSM}^{j-1} - \left(\sum_X \dot{n}_{X_out}\hat{c}_{p,X}\right)T_{ch_FSM}^j + \dot{q}_{MI} + \dot{q}_{plate_FSM}^{conv} + \dot{q}_{fin_FSM}^{conv} \quad (4.21)$$

, where superscript j describes the control volume location along the flow direction (superscript i denoting the in-plane direction was omitted for brevity), \dot{q}_{conv_plate} is a convection with plate, and

\dot{q}_{MI} is a net thermal enthalpy exchange between the reactants and products due to SR and WGS reactions;

$$\begin{aligned} \dot{q}_{MI} = & -T_{ch_FSM} \left\{ \left(\dot{n}_{CH_4} \big|_{SR} \hat{c}_{p,CH_4} \right) + \left(\dot{n}_{H_2O} \big|_{SR} \hat{c}_{p,H_2O} \right) + \left(\dot{n}_{CO} \big|_{WGS} \hat{c}_{p,CO} \right) \right\} \\ & + T_{fin_FSM} \left\{ \left(\dot{n}_{H_2O} \big|_{WGS} \hat{c}_{p,H_2O} \right) \right. \\ & \left. + \left(\dot{n}_{CO} \big|_{SR} \hat{c}_{p,CO} \right) + 3 \left(\dot{n}_{H_2} \big|_{SR} \hat{c}_{p,H_2} \right) + \left(\dot{n}_{CO_2} \big|_{WGS} \hat{c}_{p,CO_2} \right) \right\} \end{aligned} \quad (4.22)$$

In the above equation, T_{fin_FSM} is a catalyst-coated fin temperature that is governed by the following energy equation;

$$\begin{aligned} \rho_{fin} c_{v_fin} \frac{\partial T_{fin_FSM}}{\partial t} = & k_{fin} \left(\frac{\partial^2 T_{fin_FSM}}{\partial y^2} \right) - \dot{q}_{MI} + \Delta h_{f_SR} \dot{n}_{CH_4} \big|_{SR} \\ & + \Delta h_{f_WGS} \dot{n}_{CO} \big|_{WGS} + \dot{q}_{FSM_fin}^{conv} + \dot{q}_{plate_fin}^{cond} \end{aligned} \quad (4.23)$$

, where $\Delta h_{f_SR/WGS}$ are reaction enthalpies. The flux terms in (4.19)~(4.21) are calculated from the total molar flux \dot{n}_{total} given by

$$\dot{n}_{total} = \frac{\dot{m}_{ch_FSM}}{\sum_i y_i M_i} \quad (4.24)$$

, where y_i is the mole fraction of species i . Even if local pressure would vary due to reactions, the total mass flow, \dot{m}_{ch_FSM} (along the channel) should be conserved, and it is found in a similar way to Eq.(4.25), i.e.,

$$\dot{m}_{ch_FSM} = \frac{\rho_{avg_FSM} D_h^2 A_{ch_FSM}}{32 \mu_{FSM}} \frac{\Delta p_{ch_FSM}}{L_y} \quad (4.25)$$

The average FSM viscosity (for $f_{L_ch_FSM}$) and gas constant (ρ_{FSM}) were evaluated from the Chapman-Enskog theory of ideal gas mixture [62] at the center of each reformer channel. Then, molar flux of each species i , is written as

$$\dot{n}_i = y_i \dot{n}_{total} = y_i \frac{\dot{m}_{ch_FSM}}{\sum_i y_i M_i} \quad (4.26)$$

5.6 Results

5.6.1 Simulation

As indicated in the scope of this research, the focus of simulation is the transient characteristics of CHER during the initial phase of Stage 2 described in Figure 2-1(b), when the stack and CHER have been already heated up to the specified design temperature, and FSM is ready to be fed into the CHER. In addition, the FSM should be at certain elevated temperature before it enters the CHER to initiate reforming reaction from the entrance of the CHER.

SCR is evaluated at the inlet of FSM channels as

$$SCR = \frac{\dot{n}_{H_2O}}{\dot{n}_{CH_4}} \quad (4.27)$$

, where molar fluxes of fuel and steam are evaluated by the following equations;

$$\begin{aligned} \dot{n}_{CH_4}|_{Inlet} &= \frac{M_{CH_4}}{(y_{CH_4} M_{CH_4} + y_{H_2O} M_{H_2O})^2} y_{CH_4} \dot{m}_{FSM} \\ \dot{n}_{H_2O}|_{Inlet} &= \frac{M_{H_2O}}{(y_{CH_4} M_{CH_4} + y_{H_2O} M_{H_2O})^2} y_{H_2O} \dot{m}_{FSM} \end{aligned} \quad (4.28)$$

For example, $y_{CH_4} = 0.359$, $y_{H_2O} = 0.641$ at the inlet result in SCR of 2, while $y_{CH_4} = 0.31$,

$y_{H_2O} = 0.69$ result in SCR of 2.5.

The total number of the control volumes along the flow direction is 30 ($=N_y$) for air channels, FSM channels, fins, and plate. In addition, there are a total of 10 channels along the

x-direction. The simulation conditions are as follows. Due to the series connection of the main HEX and CHER in Figure 2-1, it is assumed that the initial temperature of the CHER is at 500°C. It is also assumed that the hot air temperature is increased to 600°C when FSM at 500°C is fed into the CHER. The initial SCR is set to 2.5 to avoid carbon coking inside the FSM channels [63]. The total pressure drop from the plenum to discharge side is assumed 1,000Pa for both air and FSM, and channel length, $L=762\text{mm}$.

Temperature distributions of both gases and plate are presented in Figure 5-8 after 90 seconds of simulation.

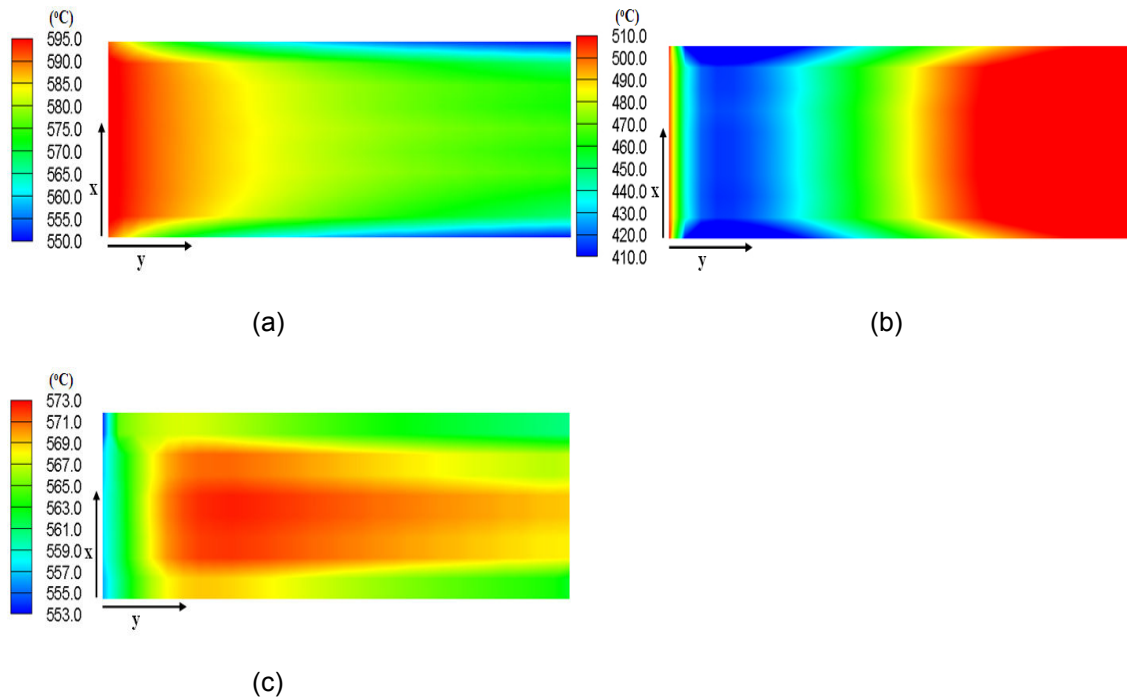


Figure 5-8 Temperature distributions in each channel and plate (90 sec.) $T_{\text{air}}=600^{\circ}\text{C}$, $T_{\text{FSM}}=500^{\circ}\text{C}$, $T_{\text{initial}}=500^{\circ}\text{C}$, $\text{SCR}=2.5$, $\Delta P=1,000\text{Pa}$, $L=762\text{mm}$; (a) Air channel, (b) FSM channel, and (c) Plate

The maximum temperature of air is shifted toward the central channel due to the heat loss to outer walls on both sides, which exchanges heat with surrounding (natural convection). As soon

as FSM enters the channels, both SR and WGS reactions occur inside the channels. Because the combined effect of both SR and WGS reactions is endothermic, the FSM temperature decreases abruptly at the entrance and recovers due to the heat transfer from the air side.

The effect of a different operating temperature was investigated by changing the air temperature, FSM temperature, and initial CHER temperature by the same amount with keeping $SCR = 2.5$, $\Delta P = 1,000 \text{ Pa}$, and $L = 762 \text{ mm}$. For example, (c)

Figure 5-9 presents the temperature distributions of each channel and plate when all the initial temperatures are increased by 100°C , i.e., air at 700°C , FSM at 600°C , and initial CHER temperature at 600°C . The general trend of temperature distribution is similar to that in Figure 5-8.

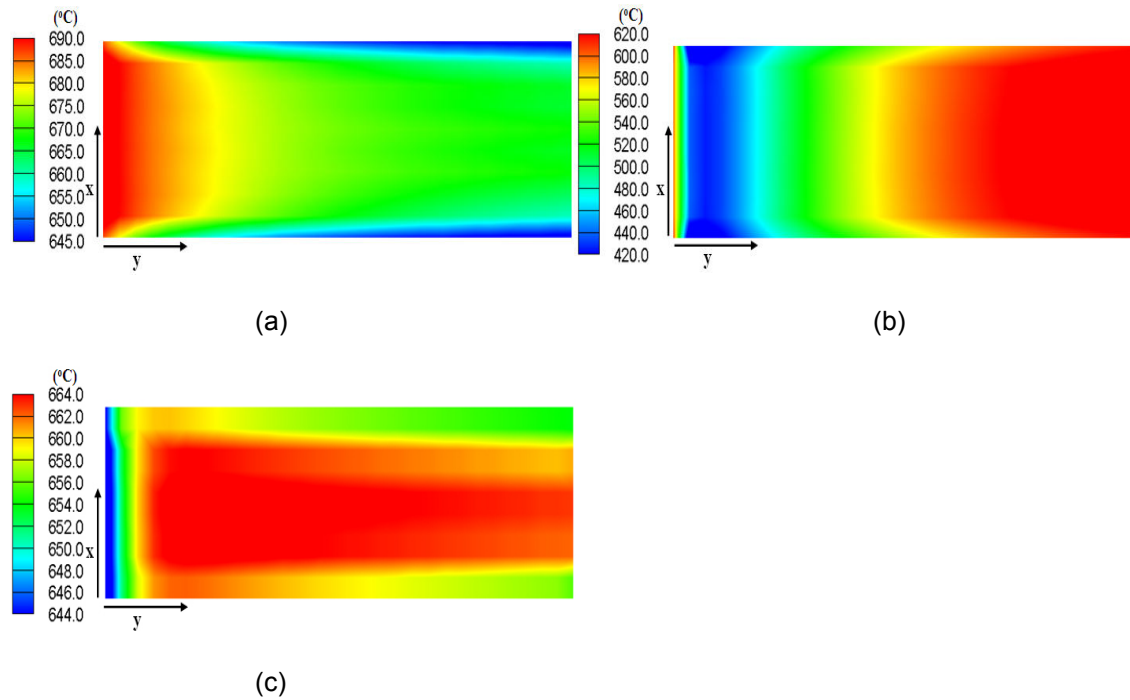
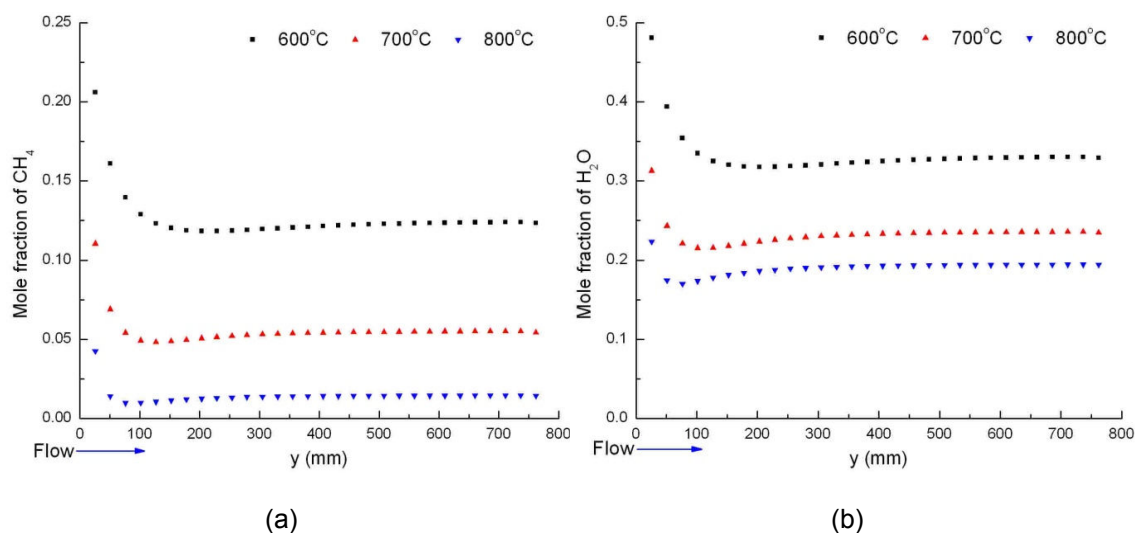


Figure 5-9 Temperature distributions in each channel and plate (90 sec.) $T_{\text{air}} = 700^\circ\text{C}$, $T_{\text{FSM}} = 600^\circ\text{C}$, $T_{\text{initial}} = 600^\circ\text{C}$, $SCR = 2.5$, $\Delta P = 1,000 \text{ Pa}$, $L = 762 \text{ mm}$; ; (a) Air channel, (b) FSM channel, and (c) Plate

Figure 5-10 shows the molar fraction of each species in the central FSM channel. The temperature legend in the graph is for the inlet air temperature. When the temperatures were increased from $T_{\text{air}}=600^{\circ}\text{C}$ ($T_{\text{FSM}}=500^{\circ}\text{C}$ and $T_{\text{initial}}=500^{\circ}\text{C}$) to $T_{\text{air}}=800^{\circ}\text{C}$ ($T_{\text{FSM}}=700^{\circ}\text{C}$, $T_{\text{initial}}=700^{\circ}\text{C}$), higher mole fraction of H_2 and CO are observed at the exit while mole fractions of CH_4 , H_2O and CO_2 are reduced. However, the actual mass flow rate of FSM in the central channel at steady state (after 90 sec) decreases with temperature as presented in Figure 5-11(a) due to increased flow resistance (i.e., viscosity) with temperature. The higher mole fraction of H_2 and CO combined with reduced total FSM mass flow rate results in no significant difference in the mass flow rate of H_2 at the exit within the range of temperature variations in this paper as shown in Figure 5-11(b). In addition, it takes more time to reach the steady state at lower temperature due to smaller flow residence time (due to lower flow resistance).



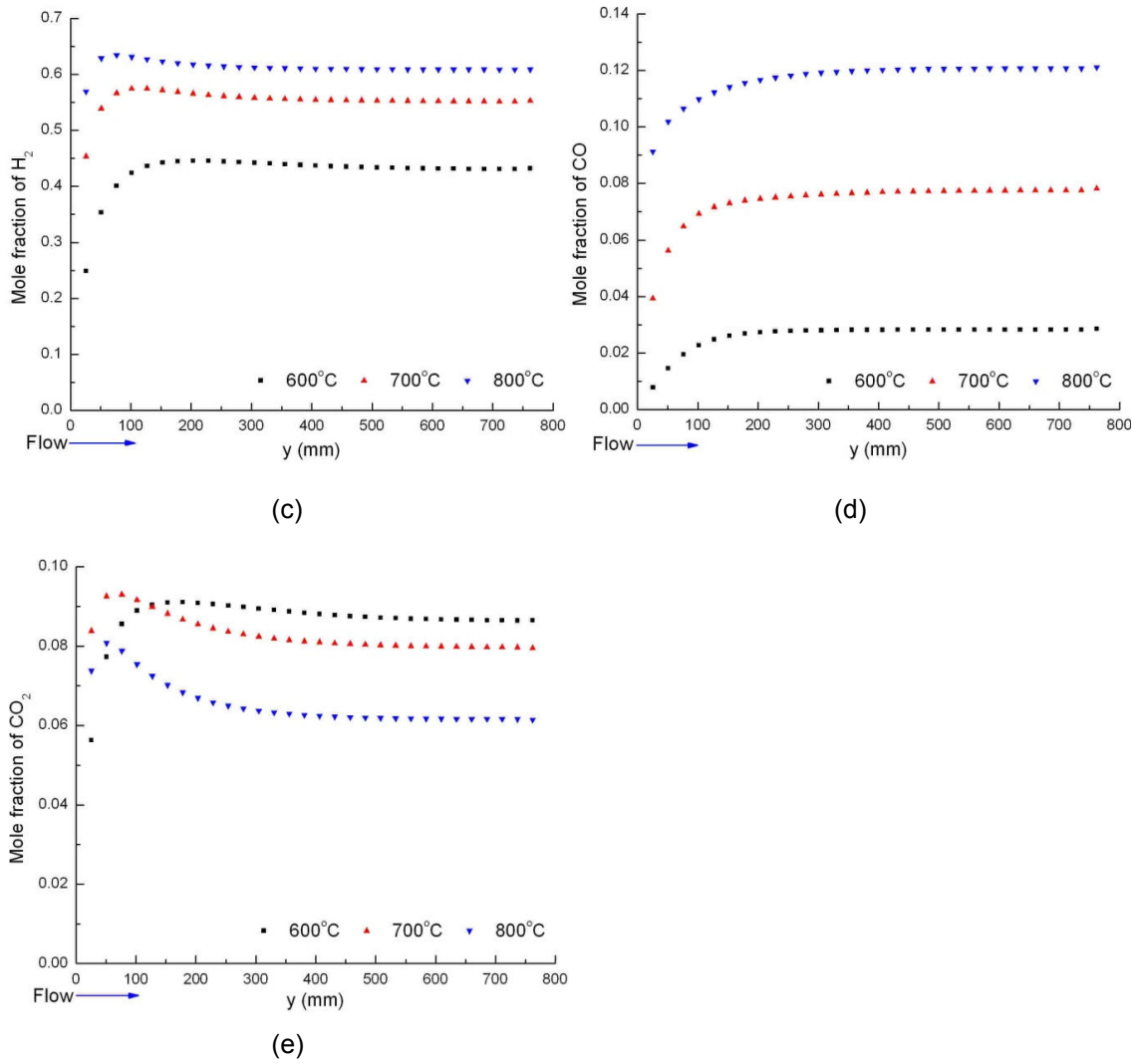


Figure 5-10 Molar fractions of each species with different temperature sets at steady state in the central channel, $SCR=2.5$, $\Delta P=1,000$ Pa, $L=762$ mm; (a) CH_4 , (b) H_2O , (c) H_2 , (d) CO , and (e) CO_2

The effects of various SCR s (2.0, 2.5, and 3.0) are presented in Figure 5-12~(e)

Figure 5-16 with $T_{air}=700^\circ C$, $T_{FSM}=600^\circ C$, $T_{initial}=600^\circ C$, $\Delta P=1,000$ Pa, and $L=762$ mm. The temperature of FSM channels is slightly increased with SCR as shown in Figure 5-12 due to increased amount of thermal energy carried by the steam.

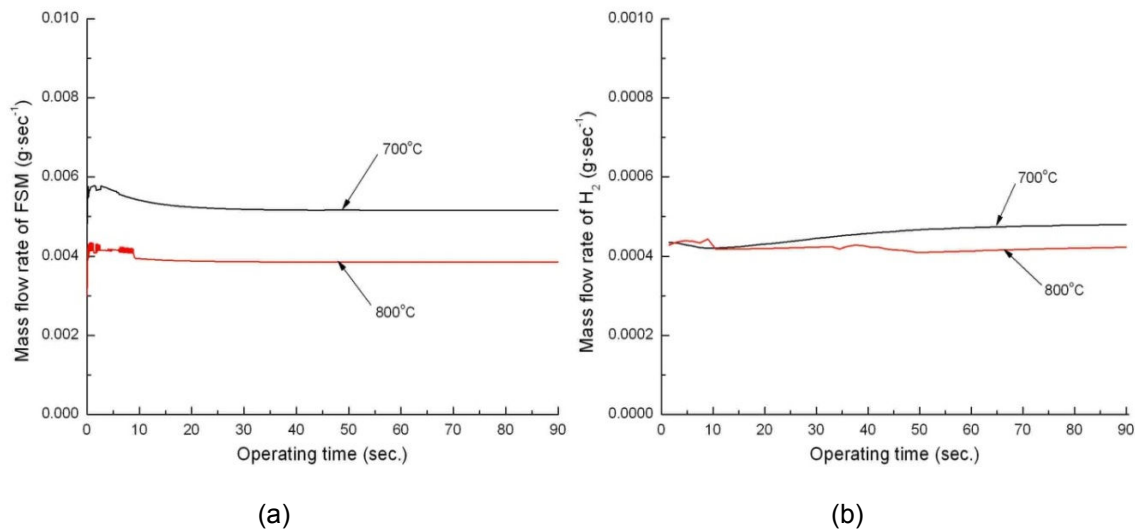


Figure 5-11 Mass flow rate of FSM and H₂ in central channel at different temperature; (a) FSM and (b) H₂

The molar fractions of each species in the FSM channels are shown in (e)

Figure 5-13~ (e)

Figure 5-15 for different SCRs. For example in Figure 5-14, the mole fractions are: 5.44% of CH₄, 23.50% of H₂O, 55.28% of H₂, 7.82% of CO, and 7.96% of CO₂ at the exit of center channel. Results are summarized in (e)

Figure 5-16, where lower SCR shows slightly better performance in terms of the molar fraction of H₂.

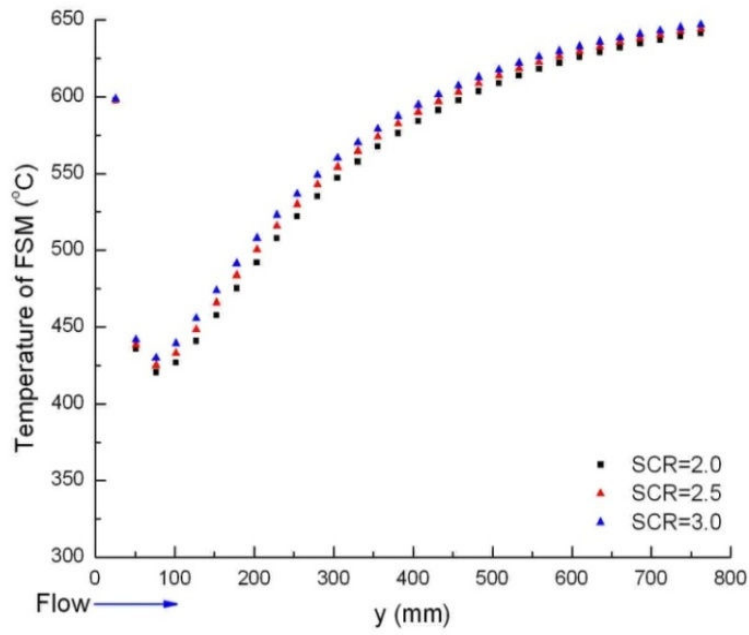
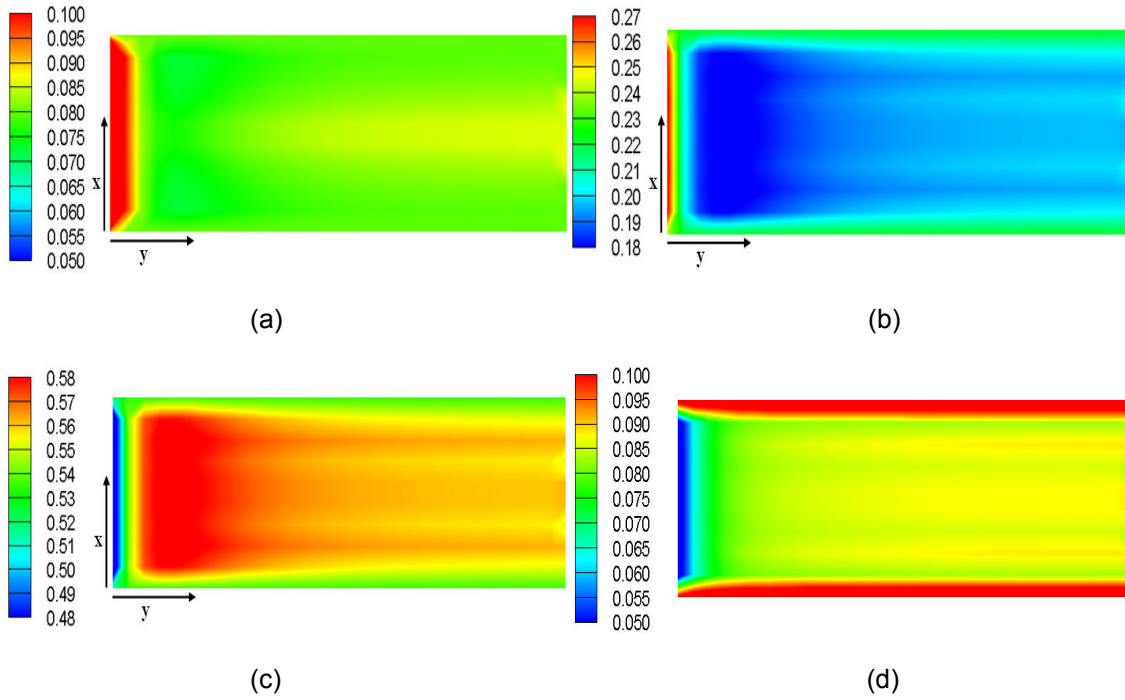
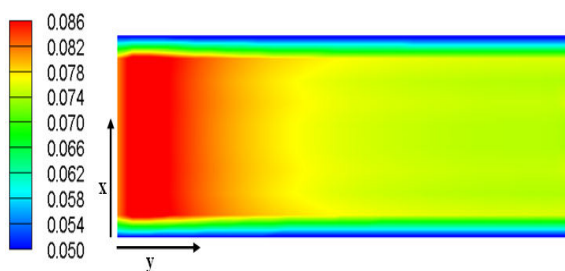


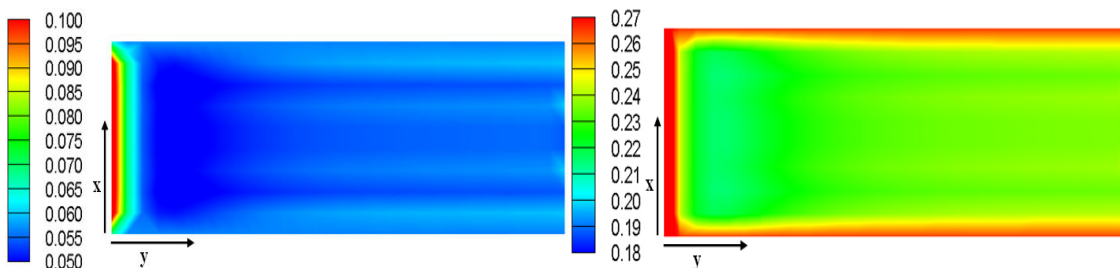
Figure 5-12 Temperature of FSM at various SCRs in the central channel





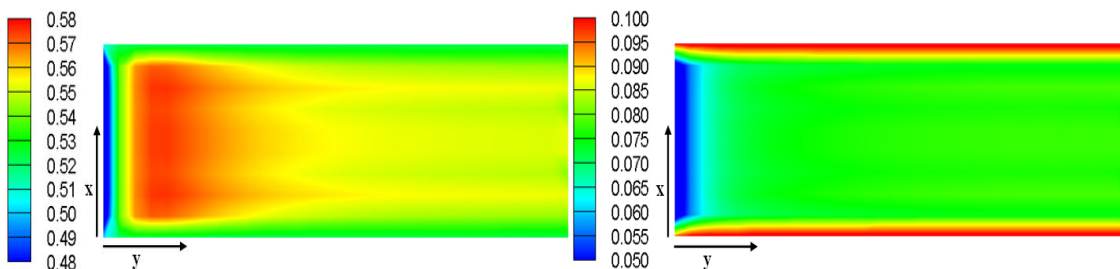
(e)

Figure 5-13 Molar fraction of each species inside FSM channel (SCR: 2.0, 90 sec.); (a) CH₄, (b) H₂O, (c) H₂, (d) CO, and (e) CO₂



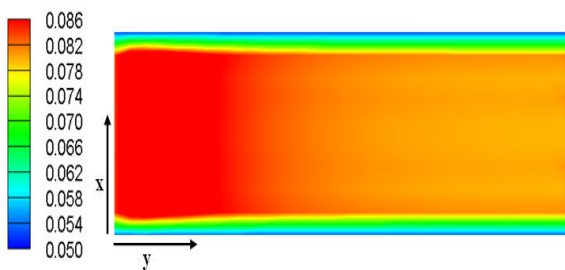
(a)

(b)



(c)

(d)



(e)

Figure 5-14 Molar fraction of each species inside FSM channel (SCR: 2.5, 90 sec.); (a) CH₄, (b) H₂O, (c) H₂, (d) CO, and (e) CO₂

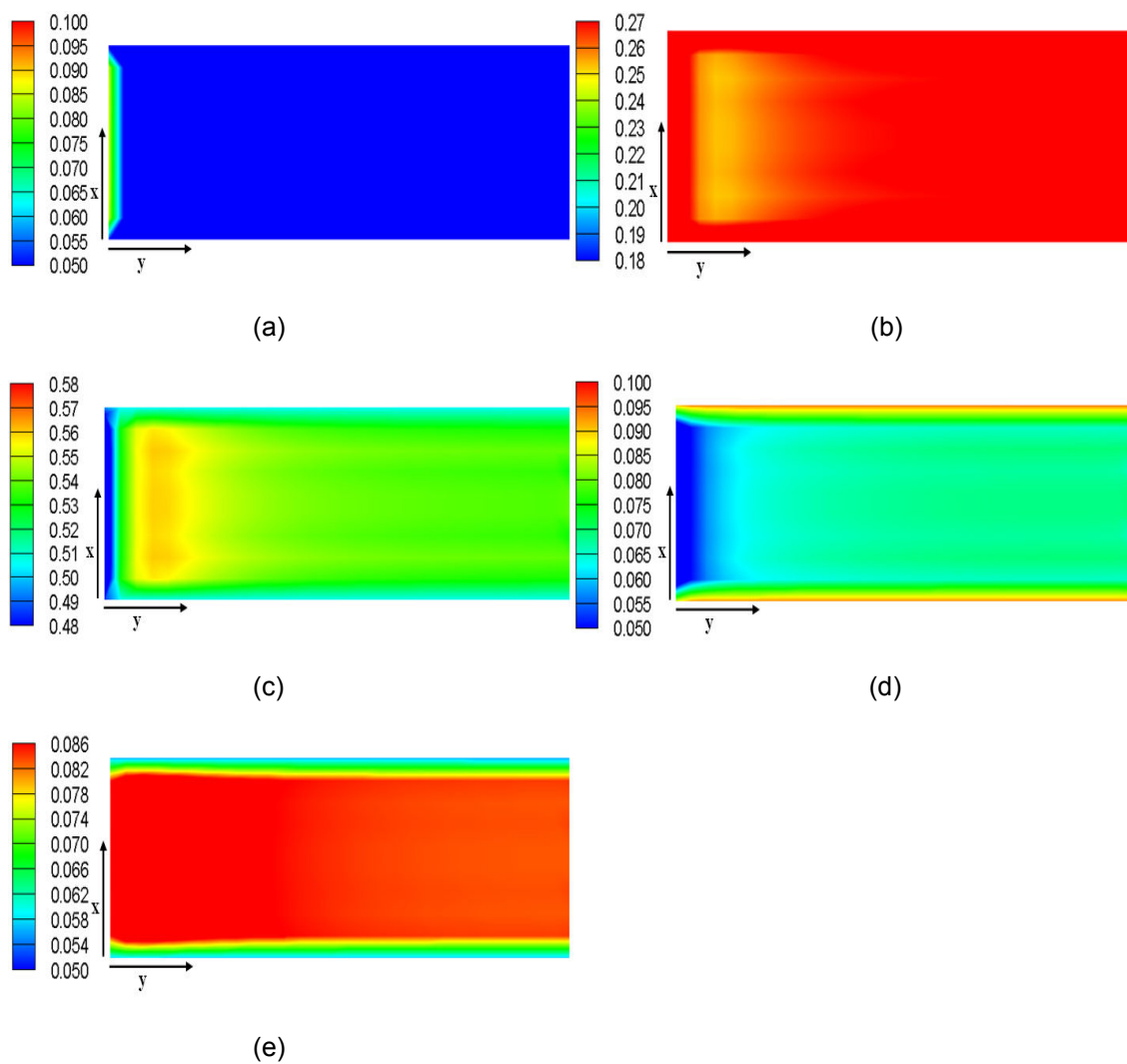
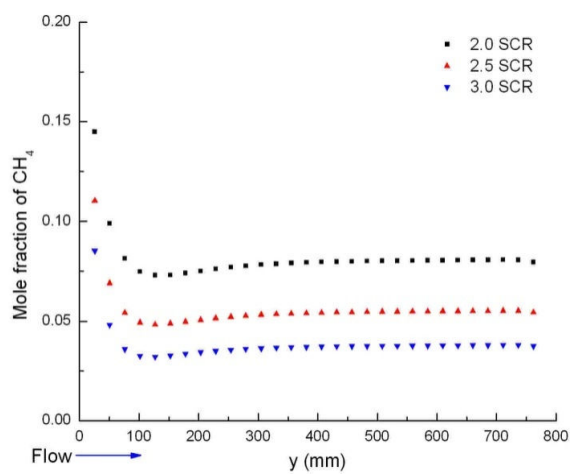
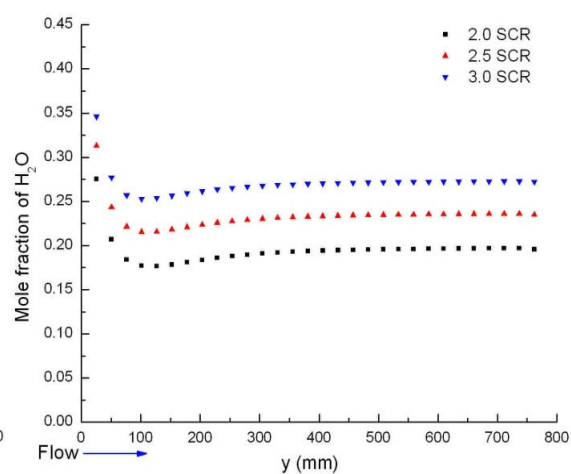


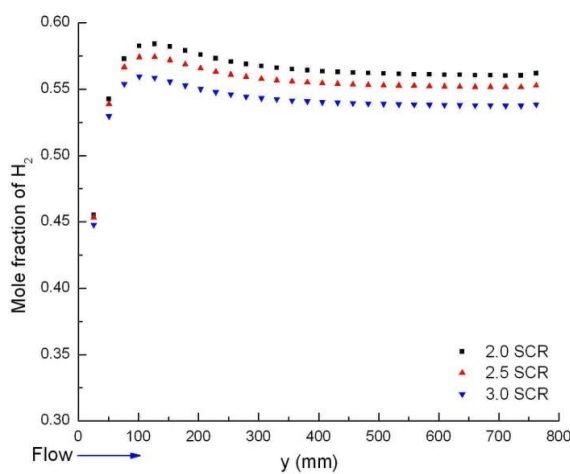
Figure 5-15 Molar fraction of each species inside FSM channel (SCR: 3.0, 90 sec.); (a) CH_4 , (b) H_2O , (c) H_2 , (d) CO , and (e) CO_2



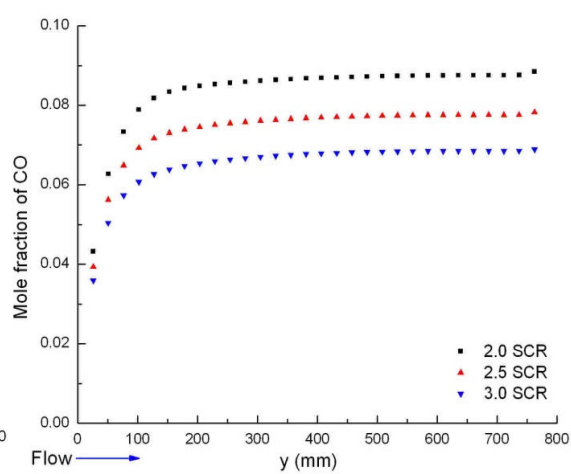
(a)



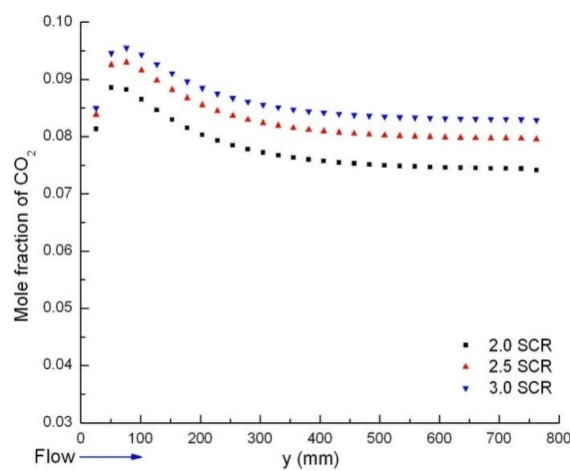
(b)



(c)



(d)

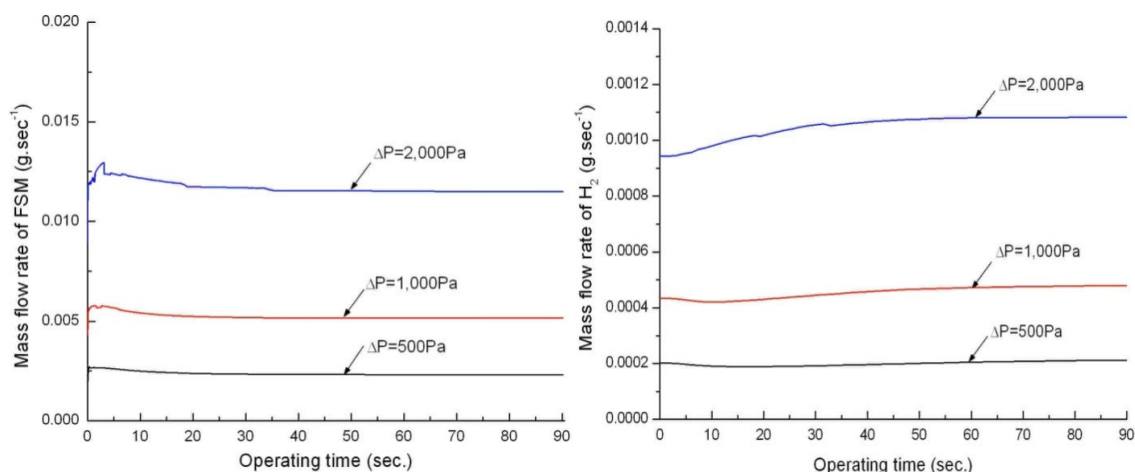


(e)

Figure 5-16 Molar fractions of each species at various SCRs in the central channel; (a) CH₄, (b) H₂O, (c) H₂, (d) CO, and (e) CO₂

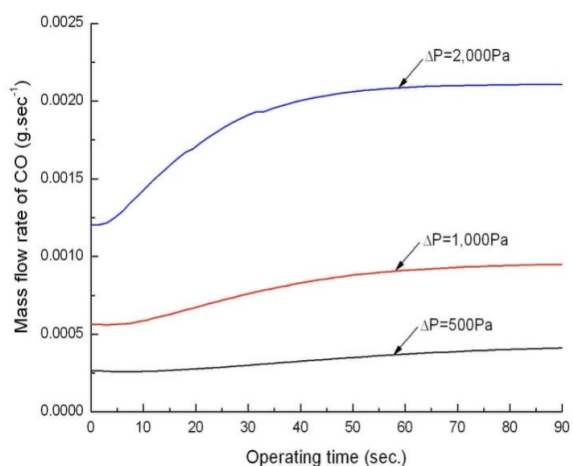
Simulations were performed with different pressures at both air and FSM sides at SCR=2.5, T_{air}=700°C, T_{FSM}=600°C, T_{initial}=600°C, and L=762mm. (c)

Figure 5-17 shows the mass flow rate of FSM, H₂ and, CO at the center channel. As the pressure was increased from 500Pa to 2,000Pa, the mass flow rate of FSM was increased from 2.32 mg · s⁻¹ to 11.50 mg · s⁻¹.



(a)

(b)



(c)

Figure 5-17 Mass flow rate of FSM, H₂ and CO in central channel with different ΔP ; (a) FSM, (b) H₂, and (c) CO

(a)

(b)

Figure 5-18 presents the temperature distributions of the air channels and FSM channels. While the air channel temperatures increase with pressure due to more mass flow (and thermal energy carried by the air mass flow), FSM channel temperatures decrease with pressure due to more active endothermic reactions.

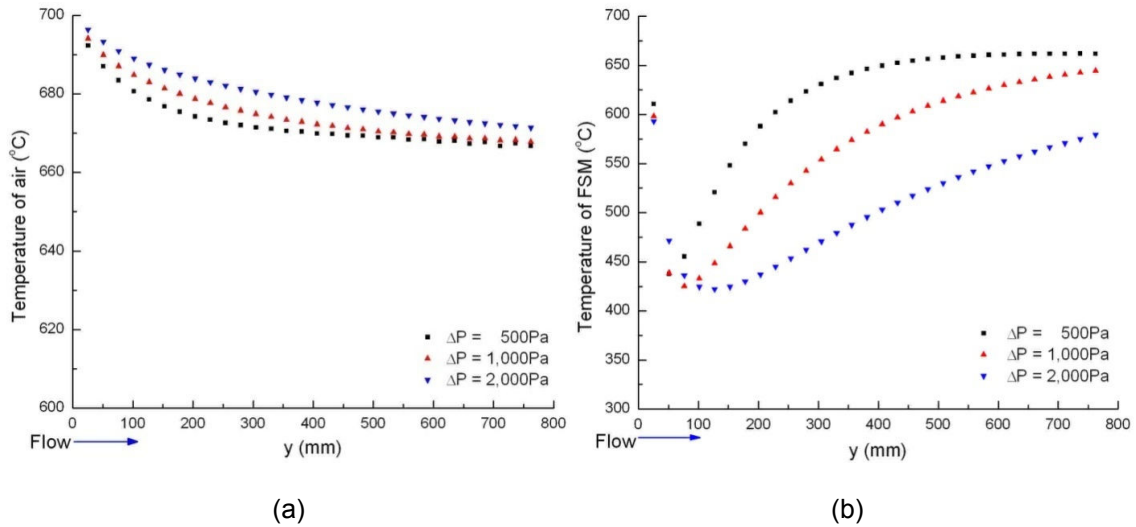


Figure 5-18 Temperature distributions in the central channel at different ΔP ; (a) Air and (b) FSM

Figure 5-19 presents the mass flow rate of H₂ in the central channel and temperatures of FSM and catalyst-coated fins at the outlet for different CHER channel lengths at SCR=2.5, $T_{\text{air}}=700^\circ\text{C}$, $T_{\text{FSM}}=600^\circ\text{C}$, $T_{\text{initial}}=600^\circ\text{C}$, and $\Delta P=1,000\text{Pa}$. Longer CHER length results in smaller air mass flow rate and also smaller FSM flow rate. The smaller air flow rate means reduced thermal energy supply rate to the FSM channels, which in turn slows down the endothermic reforming reaction.

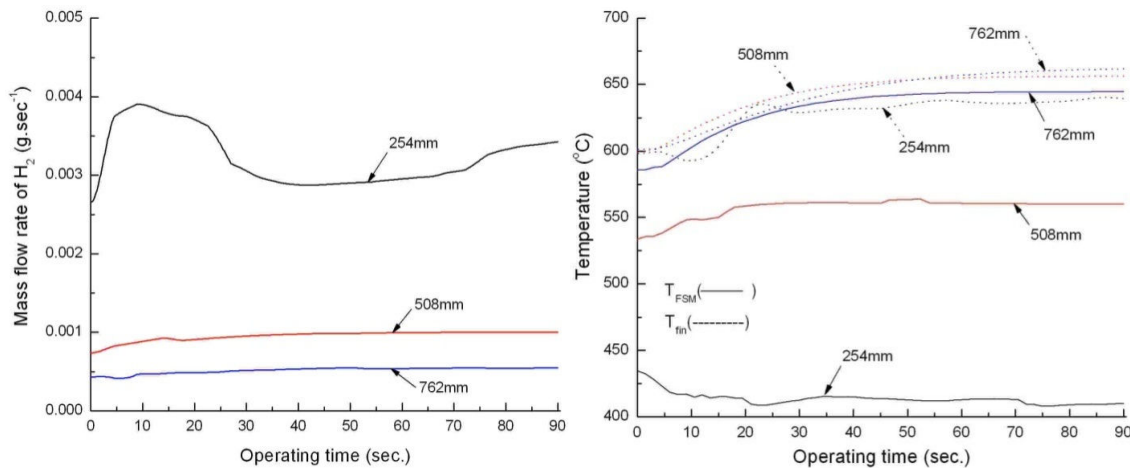


Figure 5-19 Mass flow rate of H_2 in central channel & temperatures of FSM and catalytic fin at outlet with different channel lengths

Figure 5-19(a) shows the reduced H_2 flow rate at a longer channel length. Total reforming reaction decreases and mass flow rate of H_2 decreases with increasing length. There is a correlation between the reduced heat input from air side to FSM side and reduced reforming rate (less heat supply from FSM to catalytic fins). The net combined effect of the reduced heat input and reduced reforming rate (less endothermic) results in the increased FSM temperature with increasing length. In other words, the heat exchange rate due to reforming reaction between FSM and fins is significantly dominant compared to the heat transfer from the air side to FSM side. As shown in Figure 5-19(b), there is no distinct difference about the temperature of fins with various CHER lengths.

CHER was also characterized with different flow directions. All the previous simulations were performed with co-flow configuration.

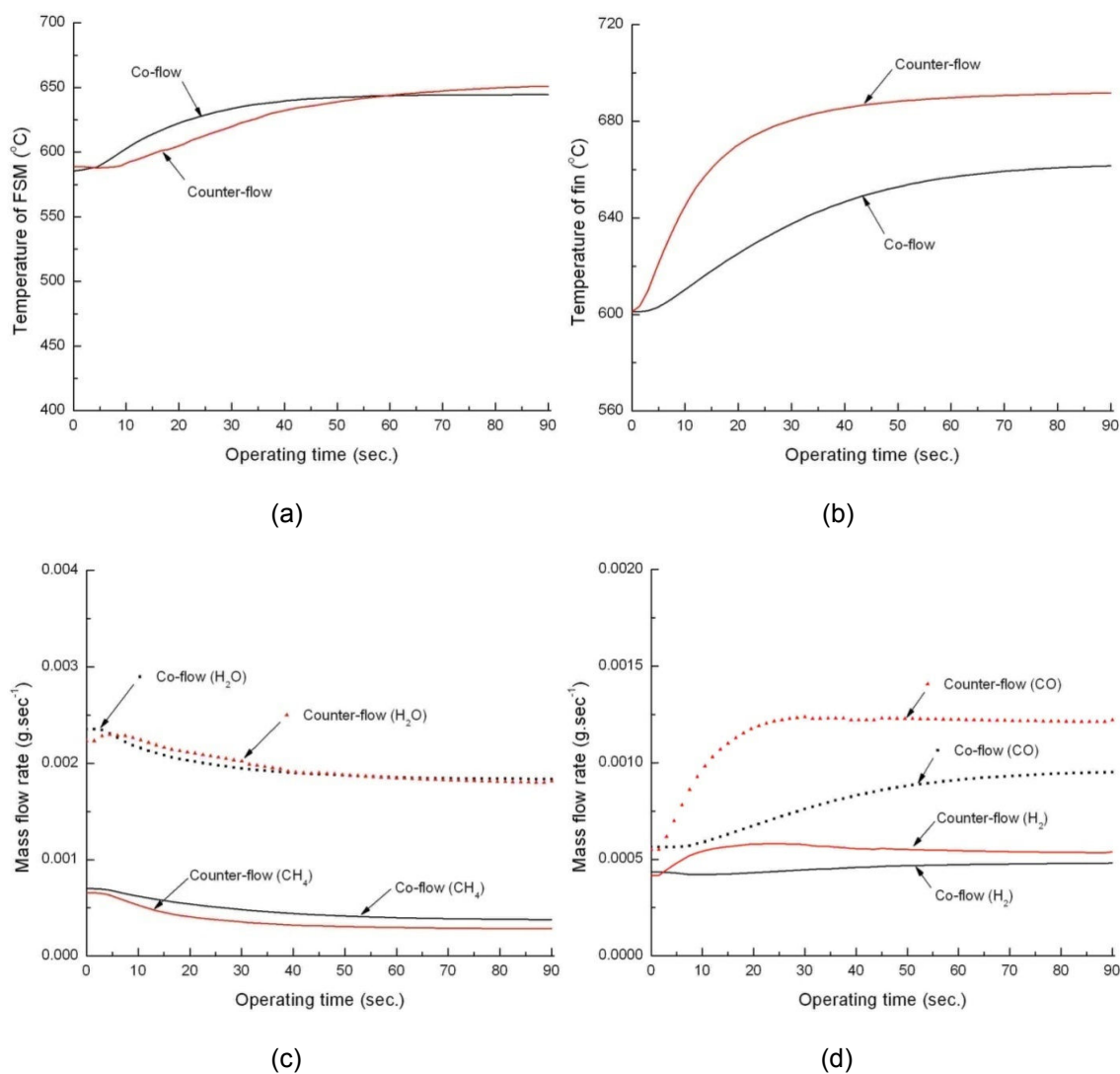


Figure 5-20 Temperatures and chemical compositions with different flow directions; (a) FSM, (b) Fin, (c) CH₄ & H₂O, and (d) H₂ & CO

Figure 5-20 compares the simulation results at the outlet of the center channel for the co- and counter-flow configurations at $SCR = 2.5$, $T_{air}=700^{\circ}C$, $T_{FSM}=600^{\circ}C$, $T_{initial}=600^{\circ}C$, $\Delta P=1,000Pa$, and $L=762mm$. Molar fractions of H₂ and CO (not shown) and FSM channel temperatures (

Figure 5-20a) were almost non-distinguishable between the co-flow and counter-flow configurations. However, counter-flow configuration allows the fin temperature slightly higher

((c) (d)

Figure 5-20b), and H₂ and CO yields are also higher with the counter-flow configuration

((c) (d)

Figure 5-20d).

5.6.2 Equilibrium calculation of the molar fraction of each species due to the SR and WGS reactions

As mentioned in section 5.5, the chemical reactions such as the SR and WGS reactions are simultaneously considered in the CHER. The reference [64] presents a theoretical explanation of the processes about the chemical equilibrium calculation for both reactions. When two independent reactions such as the SR and WGS reactions proceed at the same time, a separate reaction coordinate applies to each reaction. Table 5-2 shows the stoichiometric coefficients of each species due to the SR and WGS reactions.

Table 5-2 Stoichiometric coefficients of each species due to the SR and WGS reactions

i=	CH ₄	H ₂ O	CO	CO ₂	H ₂	
j						v _j
1	-1	-1	1	0	3	2
2	0	-1	-1	1	1	0

For example, if there are present initially 1 mole CH₄ and 2 moles H₂O, the expressions for the molar fraction of each species can be determined by the following equations;

$$\begin{aligned}
 y_{CH_4} &= \frac{1 - \varepsilon_1}{(1 + 2) + 2\varepsilon_1}, y_{H_2O} = \frac{2 - \varepsilon_1 - \varepsilon_2}{(1 + 2) + 2\varepsilon_1}, y_{H_2} = \frac{3\varepsilon_1 + \varepsilon_2}{(1 + 2) + 2\varepsilon_1} \\
 y_{CO} &= \frac{\varepsilon_1 - \varepsilon_2}{(1 + 2) + 2\varepsilon_1}, y_{CO_2} = \frac{\varepsilon_2}{(1 + 2) + 2\varepsilon_1}
 \end{aligned} \tag{4.29}$$

Here, y is the molar fraction and ε is the reaction coordinate. To find the reaction coordinate for each reaction, the equilibrium constant, K can be calculated by both the standard Gibbs energy and the ratio of molar fraction between reactants and products as shown in Eq.(4.30);

$$K = \exp\left(\frac{-\Delta G}{RT}\right) = \prod_i (y_i)^{\nu_i} \quad (4.30)$$

, where ΔG is the change of Gibbs energy between the reactants and products and ν_i is the stoichiometric coefficient of species i .

The equilibrium constants for each reaction become Eq.(4.31) and (4.32).

$$\frac{\left(\frac{\varepsilon_1 - \varepsilon_2}{3 + 2\varepsilon_1}\right) \left(\frac{3\varepsilon_1 + \varepsilon_2}{3 + 2\varepsilon_1}\right)^3}{\left(\frac{1 - \varepsilon_1}{3 + 2\varepsilon_1}\right) \left(\frac{2 - \varepsilon_1 - \varepsilon_2}{3 + 2\varepsilon_1}\right)} = K_{SR} \quad (4.31)$$

$$\frac{\left(\frac{\varepsilon_2}{3 + 2\varepsilon_1}\right) \left(\frac{3\varepsilon_1 + \varepsilon_2}{3 + 2\varepsilon_1}\right)}{\left(\frac{\varepsilon_1 - \varepsilon_2}{3 + 2\varepsilon_1}\right) \left(\frac{2 - \varepsilon_1 - \varepsilon_2}{3 + 2\varepsilon_1}\right)} = K_{WGS} \quad (4.32)$$

One simultaneous equation that includes two unknown reaction coordinates for each reaction can be generated by the Eq.(4.30). Generated Eqs.(4.31) and (4.32) can be solved by the Newton-Raphson method [55]. (a)

(b)

Figure 5-21 shows the molar fraction of each species varying with temperature from both the SR and WGS reactions.

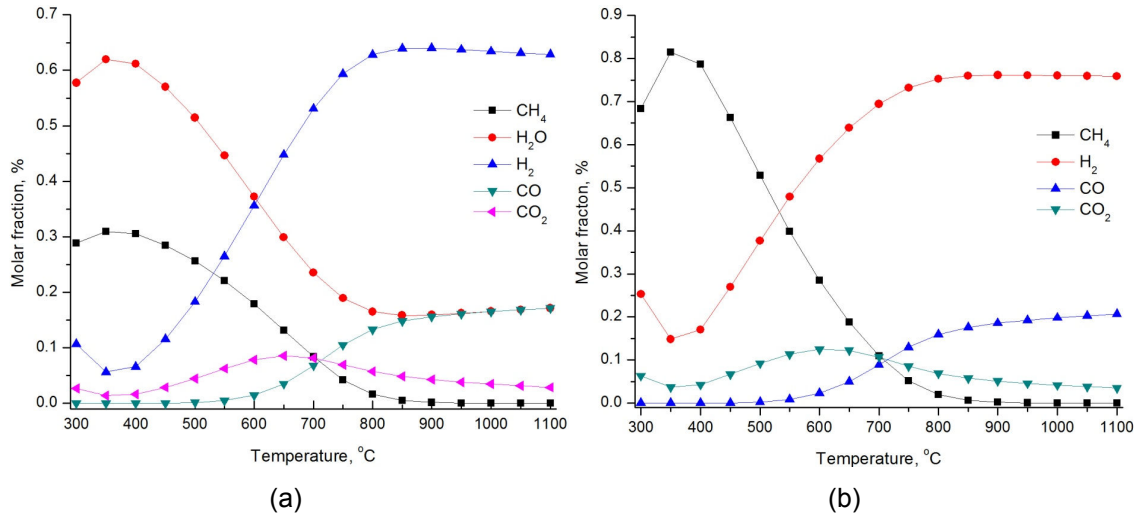


Figure 5-21 Theoretic molar fraction of each species from the SR and WGS reaction; (a) with steam and (b) without steam

5.6.3 Experiment

In the experiment, the measurement of mass flow rates of methane was performed by a digital MFC and the mass flow rate of steam is controlled by a metering pump for water. And the set SCR is directly calculated by the following equation;

$$SCR_{set} = \frac{\dot{m}_{H_2O}}{M_{H_2O}} \cdot \frac{M_{CH_4}}{\dot{m}_{CH_4}} \quad (4.33)$$

5.6.3.1 Temperature effect for the molar fraction of each species

The initial temperature of the CHER is set to the room temperature of laboratory, 20°C and the initial SCR is set to 2.5 to avoid carbon coking inside the FSM channels. Based on the modeling methods as mentioned earlier, several simulations were conducted at three air inlet temperatures (550°C, 600°C, and 650°C) and three SCRs (1.5, 2.0, and 2.5). In total six cases were experimented with the CHER in the developed test rig under the same simulational operating conditions. The air inlet temperature was varied from 550°C to 650°C by 50°C over the SCR range of 1.5~2.5 to determine the optimal inlet air temperature and SCR and to be compared with the simulational results. The experimental results about the effect of the air inlet

temperature come with the fixed other conditions such as the constant FSM inlet temperature (200°C), SCR (2.0), and mass flow rates for both sides.

Figure 5-22 shows a comparative result of the molar fraction of each species among three cases such as the equilibrium calculations in (a)
(b)

Figure 5-21(b), the simulational results based on the aforementioned modeling method, and the experimental results at various operating temperatures. The molar fractions of each species for each case were closely analogous to one another. This indicates that a sufficient heat energy from the hot air supplies to the CHER to promote the SR reactions actively in the experiment.

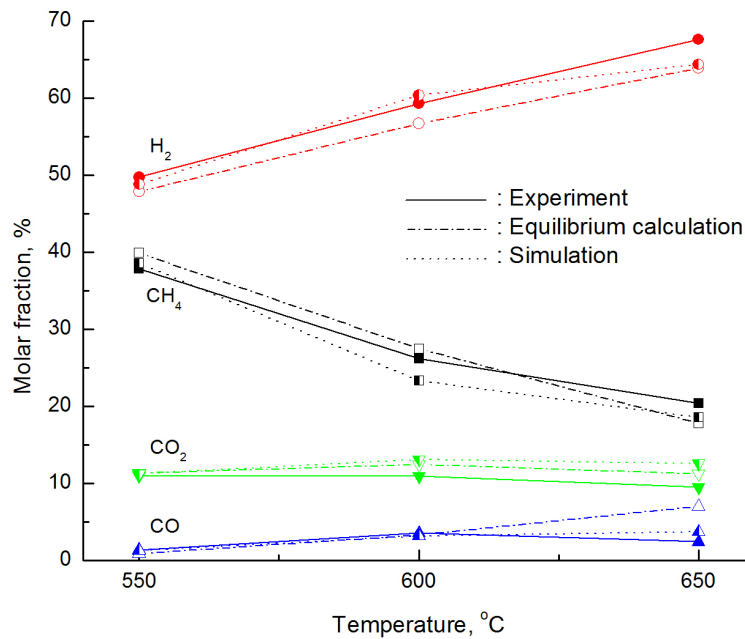


Figure 5-22 Comparison of molar fraction for each species among the experiment, equilibrium calculation, and simulation with the temperature variation

The developed simulational model for this type of CHER in the previous research [65] was well validated by the experiment. In addition, the equilibrium calculation with the reaction coordinates also validates the properness of both the developed model and experiment. With increasing the

CHER air inlet temperature, the molar fraction of H_2 increased from 49.76% to 67.66%. As shown in Figure 5-22, the molar fraction of the steam was not considered from the analysis with the GC because the GC in the laboratory does not have a function to detect the amount of the steam. This result was predictable to some extent because the SR reaction is the endothermic reaction such that the hotter inlet air conveys more thermal energy into the CHER for more active SR reaction. However, the WGS reaction rate has a certain limit with increasing the operating temperature as shown in Figure 5-23. Based on this experimental observation, the CHER inlet temperature of 650°C was chosen to perform the CHER test with various SCRs.

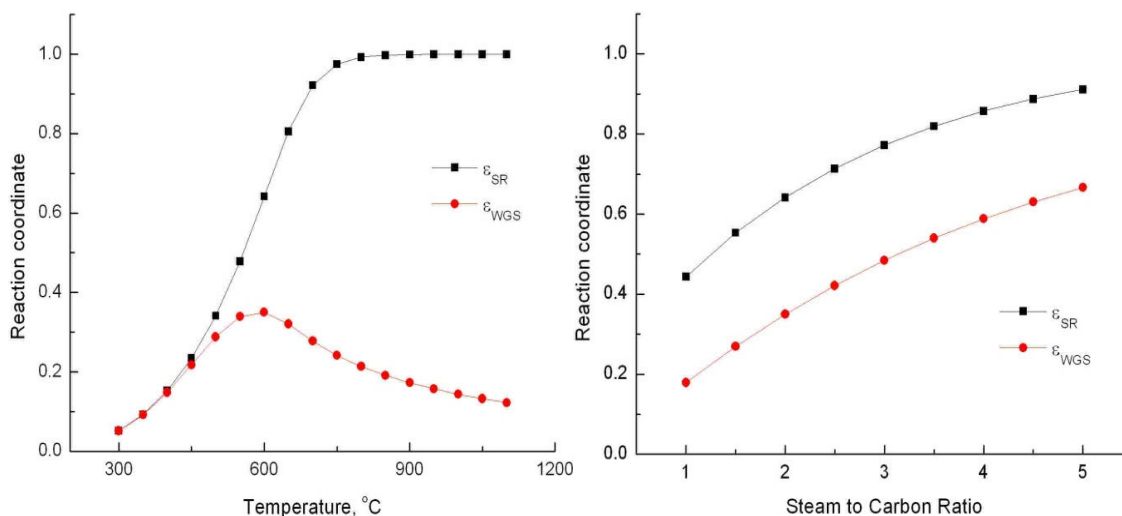


Figure 5-23 Reaction coordinates for the SR and WGS reaction with various temperatures and SCRs

5.6.3.2 SCR effect for the molar fraction of each species

Carbon formation on the catalyst surface is a major problem in the methane SR process. Due to the carbon formation, side reactions such as methane cracking may occur at the catalyst surface leading to carbon deposition in different forms. The formed carbon can encapsulate the catalyst surface or diffuse inside the catalyst pellet and causes the reduction of catalyst activity. In order to decrease the risk of carbon formation, industrial steam reformers are fed with gas

streams with a SCR over about 3.0 because a large excess of steam is favorable for both low methane and low carbon monoxide. But, important economical benefits would be obtained if a lower SCR, typically below 2.5, can be used because low SCRs in hydrogen plants can reduce the mass flow rate through the plant and the reduced size of equipment can therefore save the production cost for the plants. Building the hydrogen plant with the low SCRs is generally applied for the SR facilities. In this context, the SCR less than equal to 2.5 was chosen to experiment and simulate the CHER with various the SCRs.

Five experiments for each specific SCR were performed to increase the accuracy of an experiment. As mentioned earlier, the CHER inlet temperature, 650°C was chosen to perform the CHER test with various SCRs. Table 5-3 presents all numerical values and average values of the molar fraction of each species for each SCR.

Table 5-3 Experimental results with various SCRs

	Test 1			Test 2			Test 3		
	SCR			SCR			SCR		
	1.5	2.0	2.5	1.5	2.0	2.5	1.5	2.0	2.5
CH ₄	0.2650	0.2250	0.1936	0.2575	0.2408	0.2081	0.3074	0.2181	0.2008
H ₂	0.6068	0.6443	0.6486	0.6254	0.6402	0.6917	0.5717	0.6582	0.6881
CO	0.0358	0.0388	0.0367	0.0368	0.0218	0.0199	0.0334	0.0317	0.0246
CO ₂	0.0924	0.0918	0.1211	0.0803	0.0971	0.0803	0.0875	0.0920	0.0864
	Test 4			Test 5					
	SCR			SCR					
	1.5	2.0	2.5	1.5	2.0	2.5			
CH ₄	0.3095	0.2059	0.2084	0.2942	0.2155	0.2101			
H ₂	0.5637	0.6737	0.6798	0.5867	0.6630	0.6747			
CO	0.0357	0.0332	0.0199	0.0302	0.0360	0.0201			
CO ₂	0.0911	0.0871	0.0920	0.0889	0.0855	0.0951			

Average data

	1.5	2.0	2.5
--	-----	-----	-----

CH ₄	0.286708	0.221070	0.204188
H ₂	0.590868	0.655898	0.676574
CO	0.034384	0.032312	0.024244
CO ₂	0.088036	0.090722	0.094996

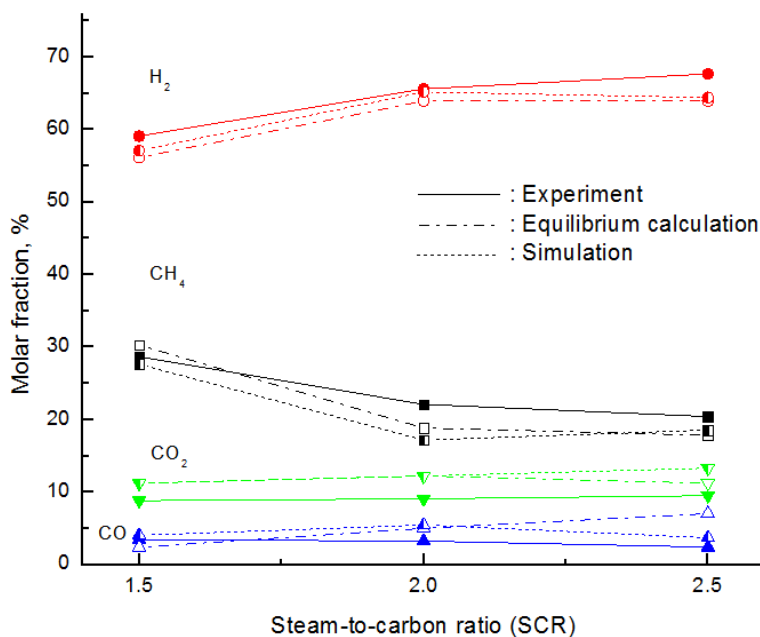


Figure 5-24 Comparison of molar fraction for each species among the experiment, case study, and simulation with the SCR variation

Figure 5-24 shows the comparative results with changing the SCR on the inlet gas composition of the CHER from the experiment, equilibrium calculation, and developed simulation model. Figure 5-24 demonstrates the acceptable agreement between the developed simulation model and experimental results: the developed module for the commercial CHER is individually validated against experimental data and chemical equilibrium calculations. At high SCRs, the CHER produced more H₂ for all cases due to more SR reaction with CH₄ and WGS reaction as shown in Figure 5-23, while the molar fraction of CO₂ has no distinct difference (~3%) from each case. In other words, the H₂ production rate is not quite dependent on the WGS reaction because the WGS reaction is not most favorable at the temperature, 650°C.

5.6.3.3 Verification of thermal dynamics of the CHER

To validate the thermal dynamics of the simulation of the CHER with the experiment for the heat exchanging process inside the CHER, several temperatures were measured at four different locations such as both the inlets and outlets of the air and FSM. All operating conditions such as the SCR, temperatures, mass flow rates, and CHER length were maintained at a constant level between the experiment and simulation.

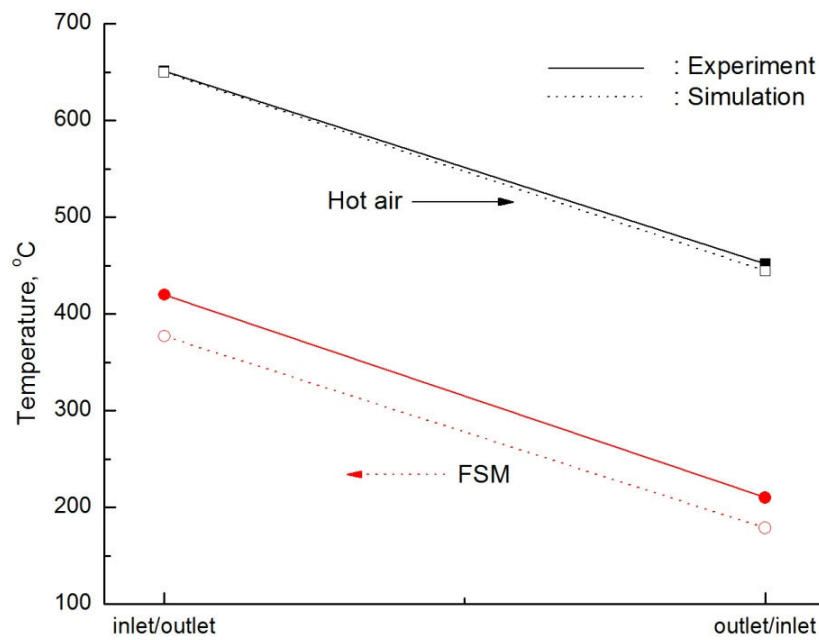


Figure 5-25 Comparison of measured temperature with the simulation, where arrows show the flow direction of both the hot air and FSM

Figure 5-25 presents the comparative results between the measured temperature and simulated temperature at both the inlet and outlet of the air and FSM. When the hot air at 650°C flows through the channels, both temperatures of the air at the outlet were 451.685°C from the measurement and 444.754 °C from the simulation. In the experiment, the FSM at 210.01°C travels through the channels, the outlet temperature of the FSM was 419.722°C. In the

simulation, the temperature of the FSM at inlet was 178.742°C and that of the FSM at outlet was 377.025°C.

The thermal dynamics of the hot air side matched each other very well such that there was only about 7°C difference at the outlet between the experiment and simulation. For the FSM side, there exists relatively large temperature differences (30~40°C) on both sides between the measurement and simulation. The presumable reason for this phenomenon is that the inlet temperature of the FSM instantaneously decreases due to the immediate endothermic SR reaction in spite of fixing the initial boundary condition for the FSM inlet to 200°C in the simulation. However, controlling the FSM inlet temperature over 200°C in the experiment was possible by using the PID controller installed in the electric cabinet. Consequently, the outlet temperature of the FSM of the simulation was also smaller than that of the experiment while the same amount of thermal energy was transferred to the reforming channel from the hot air side.

Chapter 6

SOFC Electric Power Generation Mode

6.1 Modeling

Except an electric circuit modeling, the method for all theoretic equations and discretization are the same with the SOFC start-up process and CHER reforming process. For the reference of modeling method, read the contents as described in section 2.3 of Chapter 2 and section 4.4 of Chapter 4.

6.1.1 Resistivity

An electric resistivity (ρ), which is a reciprocal quantity of an electric conductivity (σ), is a measure of how strongly a material opposes the flow of electric current. The unit of resistivity is normally $\Omega \cdot m$ in SI unit. Conductivity is generally a temperature dependent property. In this module, conductivities of each component are as functions of temperature, and can be evaluated by the following equations;

$$\sigma_{s.s.} = 7.962 e^{\frac{4690}{T}} \quad (5.1)$$

$$\sigma_{anode} = 3.35 \times 10^4 e^{\frac{1392}{T}} \quad (5.2)$$

$$\sigma_{cathode} = 1.23 \times 10^4 e^{\frac{500}{T}} \quad (5.3)$$

$$\sigma_{electrolyte} = 1 / \left(3.685 \times 10^{-3} + 2.838 \times 10^{-5} e^{\frac{10300}{T}} \right) \quad (5.4)$$

, where σ is electric conductivity and s.s. stands for stainless steel for interconnector.

6.1.2 Contact and Ionic Resistances

Contact resistances, R'' between self supporting ceramic elements cannot be avoided and losses due to contact resistance between the cells and interconnectors have been reported [66]. The contact resistance can be divided into two main contributions. The small area of

contact between ceramic components results in a resistance due to the current constriction. Resistive phases or potential barriers at the interface result in an interface contribution to the contact resistance, which may be smaller or larger than the constriction resistance. The contact resistance of the investigated materials was dominated by current constriction at high temperatures [67]. The numerical values of contact resistances of each component are listed in Table 6-1.

Table 6-1 Contact Resistances of each component in SOFC

Components	Unit ($\Omega \cdot \text{cm}^2$)
Interconnector–GDL _a	0.14
Interconnector–GDL _c	0.14
GDL _a –anode	0.5
GDL _c –cathode	0.5
Anode-electrolyte	0.25
Cathode-electrolyte	0.25

The physical mechanism of ionic conductivity (σ_{ionic}), which is reciprocal with ionic resistivity, is a diffusivity of hopping ions. Diffusivity is defined as

$$D = D_0 e^{-\Delta G_a / RT} [m^2 / s] \quad (5.5)$$

where ΔG_a is the activation barrier (50~120 kJ/mol) for hopping process. And, for instance, D_0 is $1e-11 \text{ m}^2/\text{s}$ for ceramic electrolyte (700~1000°C). Ionic resistance R_{ionic} for MEA can be represented by the following equation;

$$\begin{aligned}
 R_{\text{ionic,MEA}} [\Omega] &= R_{\text{anode,ionic}} + R_{\text{electrolyte,ionic}} + R_{\text{cathode,ionic}} + \frac{R''_{\text{contact}}}{A_{\text{contact}}} \\
 &= \frac{t_{\text{anode}} \mathcal{E}_{\text{electrolyte}}^t}{\sigma_{\text{anode,ionic}} A} + \frac{t_{\text{electrolyte}}}{\sigma_{\text{electrolyte,ionic}} A} + \frac{t_{\text{cathode}} \mathcal{E}_{\text{electrolyte}}^t}{\sigma_{\text{cathode,ionic}} A} + \frac{R''_{\text{contact}}}{A_{\text{contact}}}
 \end{aligned} \quad (5.6)$$

, where t_X is thickness of each component (X=anode, electrolyte, and cathode), ε^t is the partial thickness where the effective reaction plane is defined and it is typically assumed 0.5. In addition, A is the overall active area, and A_{contact} is the contact area. Land ratio $\varepsilon_{\text{land}}$ is defined as equation(5.7);

$$\varepsilon_{\text{land}} = \frac{A_{\text{contact}}}{A_{\text{contact}} + A_{\text{channel}}} = \frac{A_{\text{contact}}}{A} \quad (5.7)$$

6.1.3 Reversible voltage

The following equation shows a general chemical reaction, where A, B are reactants, M, N are products, and a, b, m, n are mole numbers of each chemical component.



From this equation, Gibbs' free energy change can be represented such as equation(5.9);

$$\Delta G = \Delta G^0 + RT \ln \frac{a_M^m a_N^n}{a_A^a a_B^b} \quad (5.9)$$

Equation (5.9) is Van't Hoff isotherm equation, which is a function of activities of reactants and products. And, there is a correlation between Gibbs' free energy and reversible cell voltage like equation(5.10).

$$\Delta G = -nFE \quad (5.10)$$

By combining (5.9) and(5.10), reversible voltage can be represented as a function of activities of chemicals;

$$E = E^0 - \frac{RT}{nF} \ln \frac{a_M^m a_N^n}{a_A^a a_B^b} \quad (5.11)$$

This important equation (5.11) is called the Nernst equation that considers reversible electrochemical voltage change as a function of concentration, partial pressure, etc.

6.1.4 Activation loss and Ohmic loss

When current is drawn, the Fermi level inside the cathode is increased pumping electron out of the electrode, resulting in net reduction reaction. While, Fermi level inside the anode is decreased drawing electrons from electrolyte, resulting in net oxidation reaction. As anode potential increases (Fermi level decreases) and cathode potential decreases (Fermi level increases), resultant cell voltage (=cathode potential-anode potential) is decreased. The amount of “cell voltage drop” is regarded as voltage loss compared to OCV (Nernst reversible potential). This voltage loss is called activation loss, η_{act} .

Many fuel cell books explain the activation loss in detail. In this simulation, the Butler-Volmer (B-V) equation [33] and Tafel's electrochemical kinetics [68] relating the rate of an electrochemical reaction to the overpotential were applied for the calculation of activation loss. Firstly, if oxidation reaction (at anode) is given as forward reference reaction, the corresponding B-V equation is given by

$$i = i_0 \left[\exp\left(\frac{n\alpha F \eta_{act}}{R_u T}\right) - \exp\left(-\frac{n(1-\alpha)F \eta_{act}}{R_u T}\right) \right] \quad \text{with } \eta_{act} > 0 \quad (5.12)$$

, where i_0 is exchange current density, and α is transfer coefficient. In most cases, a more important engineering factor that determines fuel cell performance is the exchange current density i_0 rather than α . Usually $\alpha=0.5$ is accepted in most cases. Secondly, if η_{act} is greater than 0.05V at near room temperature, the second terms can be neglected in the B-V equation. Therefore, at anode;

$$i_a = i_{0,a} \exp\left(\frac{n_a \alpha_a F \eta_{a,a}}{R_u T}\right) \quad \text{or} \quad \eta_{a,a} = \frac{R_u T}{n_a \alpha_a F} \ln \frac{i}{i_{0,a}} \quad (5.13)$$

at cathode;

$$i_c = i_{0,c} \exp\left(-\frac{n_c \alpha_c F \eta_{a,c}}{R_u T}\right) \quad \text{or} \quad \eta_{a,c} = -\frac{R_u T}{n_c \alpha_c F} \ln \frac{i}{i_{0,c}} \quad (5.14)$$

These equations are called Tafel's equation. By combining both activation losses;

$$\eta_{act} = \eta_a - \eta_c = \frac{R_u T}{n_a \alpha_a F} \ln \frac{i}{i_{0,a}} + \frac{R_u T}{n_c \alpha_c F} \ln \frac{i}{i_{0,c}} \quad (5.15)$$

Experimentally measured exchange current densities at both electrodes using concentration of species participating in the reactions can be found as [18];

$$i_{0,a} = \gamma_{anode} \frac{P_{H_2}}{P_{ref}} \left(\frac{P_{H_2O}}{P_{ref}} \right)^{-0.5} \exp \left(-\frac{E_{a0,a}}{R_u T} \right), \text{ where } \gamma_{anode} = 5.7e6 \text{ A/cm}^2, E_{a0,a} = 140,000 \text{ kJ/kmol}$$

$$i_{0,c} = \gamma_{cathode} \left(\frac{P_{O_2}}{P_{ref}} \right)^{0.25} \exp \left(-\frac{E_{a0,c}}{RT} \right), \text{ where } \gamma_{cathode} = 7e5 \text{ A/cm}^2, E_{a0,c} = 160,000 \text{ kJ/kmol}$$

The loss due to the transfer of charge is the friction loss. Because the medium which charge transfers has an intrinsic resistivity, the voltage loss always exists during the transfer process. This voltage loss follows the Ohmic law; it is called ohmic loss (η_{ohmic}).

$$\eta_{ohmic} = i \cdot R_{ohmic} \quad (5.16)$$

In this simulation, the ohmic contact resistance, R_{ohmic} is being updated corresponding to the calculation at each time step. And, the electric circuit model in the next section contains all resistance and resistivity in all the equations for the calculation of ohmic loss.

6.2 Electric circuit modeling

When the total stack current is specified, actual current density distribution across the stack depends on local hydrogen and oxygen concentrations (through activation loss, etc.) and the electric resistance network inside the ribs and MEAs that in turn depends on their local temperatures.

Figure 6-1 shows the schematic of single planar SOFC stack, the names of each component, and locations for nodal voltage calculation. Although Figure 6-1 represents single stack, repetitive structure can be achieved by stacking with bipolar plate or interconnector as shown in Figure 3-1.

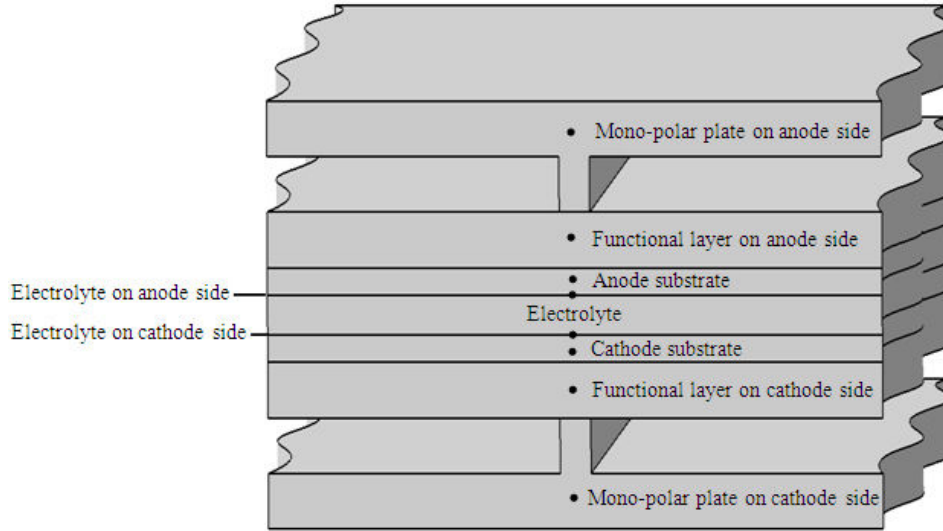


Figure 6-1 The names of each component and the nodal point in a planar SOFC stack

Figure 6-2 shows the electric circuit network with nodal voltages located in every bipolar plates, ribs, and MEAs. $\widehat{V}_{i,j}^X$ ($X= A, C, k, \text{Rib}_A, \text{MEA}_A, \text{Rib}_C, \text{MEA}_C, \text{FL}_A, \text{ and } \text{FL}_C$) represents voltages in each nodal point. For example, $V_{i,j}^k$ is the voltage of bipolar plate (k is index for stack layer, $k=1\sim N_{FC}-1$). If we assume each stack layer has the same characteristics, $\widehat{V}_{i,j}^X$ are all the same along the vertical directions.

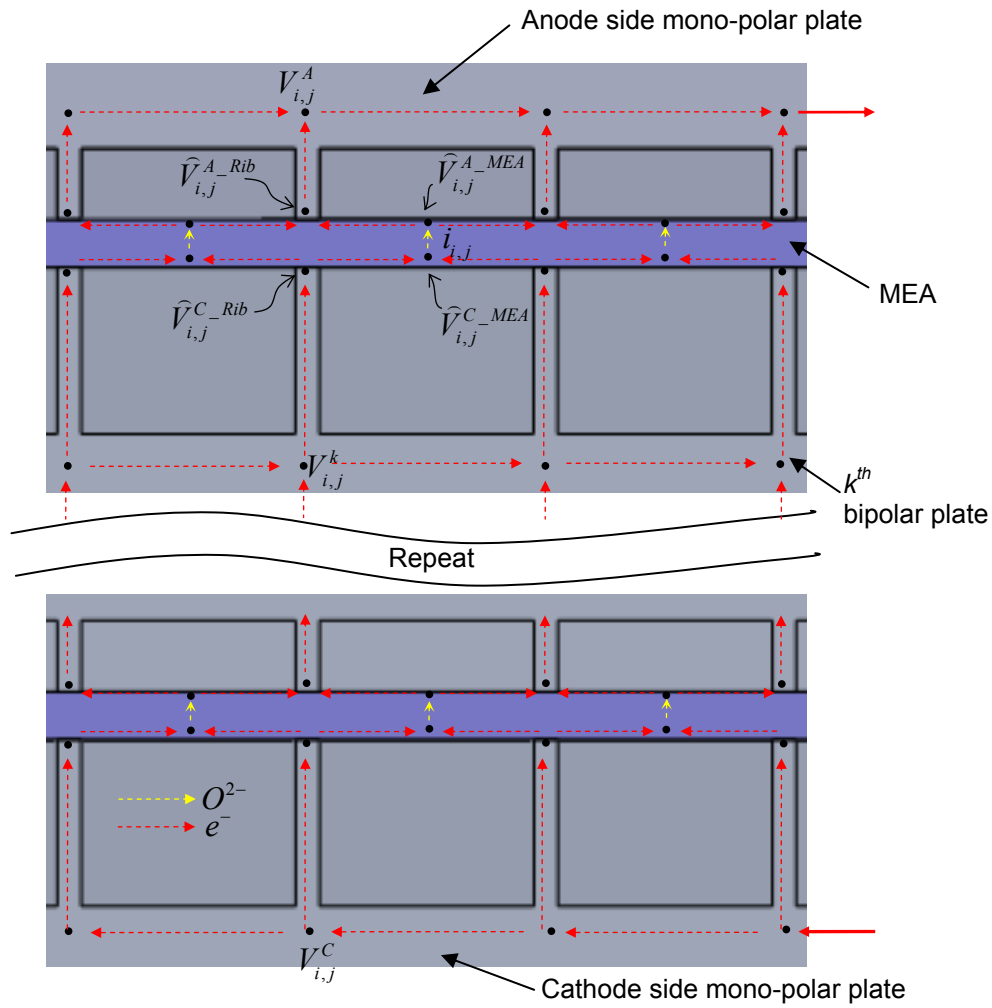


Figure 6-2 Cross section view of equivalent electrical circuit; i is flow direction, j is in-plane direction, and $k=1 \sim N_{FC}-1$

Kirchhoff's current law (KCL) can be applied to each nodal point and they are summarized in Table 6-2 with $k=N_{FC}-1$.

Table 6-2 KCL Equations for nodal points

Nodal point	KCL equation
$V_{i,j}^A$	$\frac{\Delta y(V_{i,j+1}^A - V_{i,j}^A)}{R_{i,j}^A} + \frac{\widehat{V}_{i,j}^{A_rib} - V_{i,j}^A}{RC_{i,j}^{A_rib}} + \frac{\Delta x(V_{i-1,j}^A - V_{i,j}^A)}{R_{i,j}^A}$ $= \frac{\Delta y(V_{i,j}^A - V_{i,j-1}^A)}{R_{i,j}^A} + \frac{\Delta x(V_{i,j}^A - V_{i+1,j}^A)}{R_{i,j}^A} \quad (5.17)$
$V_{i,j}^C$	$\frac{\Delta y(V_{i,j+1}^C - V_{i,j}^C)}{R_{i,j}^C} + \frac{\widehat{V}_{i,j}^{C_rib} - V_{i,j}^C}{RC_{i,j}^{C_rib}} + \frac{\Delta x(V_{i-1,j}^C - V_{i,j}^C)}{R_{i,j}^C}$ $= \frac{\Delta y(V_{i,j}^C - V_{i,j-1}^C)}{R_{i,j}^C} + \frac{\Delta x(V_{i,j}^C - V_{i+1,j}^C)}{R_{i,j}^C} \quad (5.18)$
$V_{i,j}^{An}$	$\frac{V_{i,j}^{elec_A} - V_{i,j}^{An}}{RC_{i,j}^{An_elec}} + \frac{\Delta x(V_{i+1,j}^{An} - 2V_{i,j}^{An} + V_{i-1,j}^{An})}{R_{i,j}^{An}} +$ $\frac{\Delta y(V_{i,j+1}^{An} - 2V_{i,j}^{An} + V_{i,j-1}^{An})}{R_{i,j}^{An}} + \frac{V_{i,j}^{A_rib} - V_{i,j}^{An}}{RC_{i,j}^{GDL_An}} = 0 \quad (5.19)$
$V_{i,j}^{Cat}$	$\frac{V_{i,j}^{elec_C} - V_{i,j}^{Cat}}{RC_{i,j}^{Cat_elec}} + \frac{\Delta x(V_{i+1,j}^{Cat} - 2V_{i,j}^{Cat} + V_{i-1,j}^{Cat})}{R_{i,j}^{Cat}}$ $+ \frac{\Delta y(V_{i,j+1}^{Cat} - 2V_{i,j}^{Cat} + V_{i,j-1}^{Cat})}{R_{i,j}^{Cat}} + \frac{V_{i,j}^{C_rib} - V_{i,j}^{Cat}}{RC_{i,j}^{GDL_Cat}} = 0 \quad (5.20)$
$V_{i,j}^k$	$\frac{\Delta y(V_{i,j+1}^k - V_{i,j}^k)}{R_{i,j}^k} + \frac{\widehat{V}_{i,j}^{A_rib} - V_{i,j}^k}{RC_{i,j}^{A_rib}} + \frac{\Delta x(V_{i-1,j}^k - V_{i,j}^k)}{R_{i,j}^k}$ $= \frac{\Delta y(V_{i,j}^k - V_{i,j-1}^k)}{R_{i,j}^k} + \frac{\Delta x(V_{i,j}^k - V_{i+1,j}^k)}{R_{i,j}^k} + \frac{V_{i,j}^k - \widehat{V}_{i,j}^{C_rib}}{RC_{i,j}^{C_rib}} \quad (5.21)$
$\widehat{V}_{i,j}^{A_rib}$	$\frac{V_{i,j}^{An} - V_{i,j}^{A_rib}}{RC_{i,j}^{An_A_rib}} + \frac{\Delta y(\widehat{V}_{i,j+1}^{A_rib} - 2V_{i,j}^{A_rib} + V_{i,j-1}^{A_rib})}{R_{i,j}^{A_rib}}$ $+ \frac{\Delta x(V_{i+1,j}^{A_rib} - 2V_{i,j}^{A_rib} + V_{i-1,j}^{A_rib})}{R_{i,j}^{A_rib}} + \frac{V_{i,j}^k - V_{i,j}^{A_rib}}{RC_{i,j}^{k_A_rib}} = 0 \quad (5.22)$

$\widehat{V}_{i,j}^{C_rib}$	$\frac{V_{i,j}^{Cat} - V_{i,j}^{C_rib}}{RC_{i,j}^{Cat_C_rib}} + \frac{\Delta y (\widehat{V}_{i,j+1}^{C_rib} - 2V_{i,j}^{C_rib} + V_{i,j-1}^{C_rib})}{R_{i,j}^{C_rib}} + \frac{\Delta x (V_{i+1,j}^{C_rib} - 2V_{i,j}^{C_rib} + V_{i-1,j}^{C_rib})}{R_{i,j}^{C_rib}} + \frac{V_{i,j}^k - V_{i,j}^{C_rib}}{RC_{i,j}^{k_C_rib}} = 0 \quad (5.23)$
$\widehat{V}_{i,j}^{C_MEA}$	$\frac{V_{i,j}^{Cat} - V_{i,j}^{C_elec}}{RC_{i,j}^{Cat_C_elec}} + \frac{\Delta y (\widehat{V}_{i,j+1}^{C_elec} - 2V_{i,j}^{C_elec} + V_{i,j-1}^{C_elec})}{R_{i,j}^{C_elec}} + \frac{\Delta x (V_{i+1,j}^{C_elec} - 2V_{i,j}^{C_elec} + V_{i-1,j}^{C_elec})}{R_{i,j}^{C_elec}} + \frac{V_{i,j}^{A_elec} - V_{i,j}^{C_elec}}{R_{i,j}^{ionic}} = 0 \quad (5.24)$
$\widehat{V}_{i,j}^{A_MEA}$	$\frac{V_{i,j}^{An} - V_{i,j}^{A_elec}}{RC_{i,j}^{An_A_elec}} + \frac{\Delta y (\widehat{V}_{i,j+1}^{A_elec} - 2V_{i,j}^{A_elec} + V_{i,j-1}^{A_elec})}{R_{i,j}^{A_elec}} + \frac{\Delta x (V_{i+1,j}^{A_elec} - 2V_{i,j}^{A_elec} + V_{i-1,j}^{A_elec})}{R_{i,j}^{A_elec}} + \frac{V_{i,j}^{C_elec} - V_{i,j}^{A_elec}}{R_{i,j}^{ionic}} = 0 \quad (5.25)$

All boundary nodes should be slightly modified to accommodate non-existent nodes. Solutions for all unknowns' nodal voltages and local current densities can be found by solving all of these equations using the Gauss-Seidal iteration method, which is a well-known standard numerical method to solve highly non-linear multiple algebraic equations. Electronic resistances for bipolar plates ($R_{i,j}^{A/C}$) and ribs ($R_{i,j}^{A/C_Rib}$) will be evaluated at a local temperature of these elements. $R_{i,j}^{ionic}$ in (5.24)~(5.25) corresponds to summation of reciprocal of ionic conductance of YSZ and equivalent resistance from activation loss at both the anode and cathode surface. $R_{i,j}^{C/A_MEA}$ corresponds to the electronic resistance of the catalyst layer. Once all the nodal voltages are found, local current density can be found as $i_{i,j} = (\widehat{V}_{i,j}^{C_MEA} - \widehat{V}_{i,j}^{A_MEA}) / R_{i,j}^{ionic}$.

6.3 Thermal Dynamics of SOFC

Thermal dynamics of stacks follows a similar approach to compact heat exchanger reformer (CHER) except the heat of SR/WGS reaction, the heat of electrochemical oxidation of

hydrogen, and electrical power are included in the energy equation for membrane electrode assembly (MEA). The heat of SR/WGS reactions in the $(i, j)^{th}$ MEA element is;

$$\begin{aligned} \dot{q}_{i,j_SR+WGS} = & \dot{n}_{CH_4-i,j}^A \Big|_{SR} \left(\bar{h}_{f_CH_4}(T_{i,j}^{MEA}) + \bar{h}_{f_H_2O}(T_{i,j}^{MEA}) - \bar{h}_{f_CO}(T_{i,j}^{MEA}) - 3\bar{h}_{f_H_2O}(T_{i,j}^{MEA}) \right) / V_{i,j}^{MEA} \\ & + \dot{n}_{CO-i,j}^A \Big|_{WGS} \left(\bar{h}_{f_CO}(T_{i,j}^{MEA}) + \bar{h}_{f_H_2O}(T_{i,j}^{MEA}) - \bar{h}_{f_CO_2}(T_{i,j}^{MEA}) - \bar{h}_{f_H_2}(T_{i,j}^{MEA}) \right) / V_{i,j}^{MEA} \end{aligned} \quad (5.26)$$

The heat of electrochemical oxidation of hydrogen in the $(i, j)^{th}$ MEA element and local electric work determined from Nernst open circuit potential minus activation and Ohmic losses is;

$$\begin{aligned} \dot{q}_{i,j_ELC} = & \frac{1}{V_{i,j}^{MEA}} \left(\bar{h}_{f_H_2}(T_{i,j}^A) \frac{i_{i,j}}{2F} + \bar{h}_{f_O_2}(T_{i,j}^C) \frac{i_{i,j}}{4F} - \bar{h}_{f_H_2O}(T_{i,j}^{MEA}) \frac{i_{i,j}}{2F} \right); \\ \dot{w}_{i,j_FC} = & \frac{\dot{W}_{i,j_FC}}{V_{i,j}^{MEA}} \end{aligned} \quad (5.27)$$

Molecular interaction (MI) between MEA and anode channels due to the thermal enthalpy exchange of reacting gases can be interpreted as heat exchange mechanism similar to convection. There is hydrogen and water exchange due to the oxidation of hydrogen;

$$\begin{aligned} \dot{q}_{i,j_MI_A} = & \left(\bar{c}_{p_H_2O} T_{i,j}^{MEA} - \bar{c}_{p_H_2} T_{i,j}^A \right) \frac{i_{i,j}}{2F} \frac{1}{V_{i,j}^A} \\ & + \dot{n}_{CH_4-i,j}^A \Big|_{SR} \left(\bar{c}_{p_CO} T_{i,j}^{MEA} + 3\bar{c}_{p_H_2} T_{i,j}^{MEA} - \bar{c}_{p_CH_4} T_{i,j}^A - \bar{c}_{p_H_2O} T_{i,j}^A \right) / V_{i,j}^A \\ & + \dot{n}_{CO-i,j}^A \Big|_{WGS} \left(\bar{c}_{p_CO_2} T_{i,j}^{MEA} + \bar{c}_{p_H_2} T_{i,j}^{MEA} - \bar{c}_{p_CO} T_{i,j}^A - \bar{c}_{p_H_2O} T_{i,j}^A \right) / V_{i,j}^A \end{aligned} \quad (5.28)$$

Molecular interaction between MEA and cathode channels is a pure loss of thermal enthalpy of oxygen from the cathode channels, and it is given by

$$\dot{q}_{i,j_MI_C} = -\bar{c}_{p_O_2} T_{i,j}^C \frac{i_{i,j}}{4F} \frac{1}{V_{i,j}^C} \quad (5.29)$$

It is noteworthy that (5.28) and (5.29) are heat transfer terms replacing convection between MEA and anode/cathode channels while (5.27) is the heat of reactions involved with electrochemical oxidation of hydrogen at MEA.

The conductive heat transfer schematic between the rib and connecting plate is as shown in Figure 6-3.

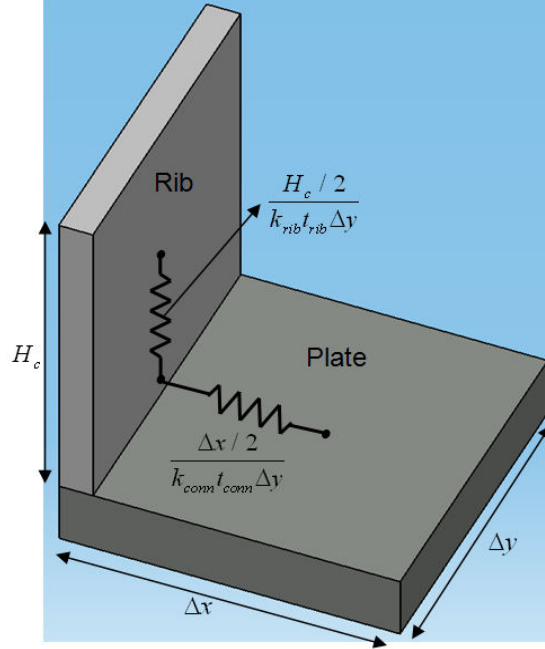


Figure 6-3 Conductive heat transfer schematic between the rib and plate

The conductive heat flux between the rib and plate is given by

$$\dot{q}_{cond} = \frac{\Delta T}{\frac{H_c / 2}{k_{rib} t_{rib} \Delta y} + \frac{\Delta x / 2}{k_{conn} t_{conn} \Delta y}} \quad (5.30)$$

, where \dot{q}_{cond} is the conductive heat transfer rate between two nodal points of the rib and plate respectively, ΔT is the temperature difference between two nodal points, H_c is the height of cathode channel, and k and t are the thermal conductivity and thickness of each component. In addition, these two assumptions are performed by equation (5.31)

$$\frac{\Delta H_h}{2} + \frac{t_{conn}}{2} \approx \frac{\Delta H_h}{2}, \quad \frac{\Delta x}{2} + \frac{t_{fin}}{2} \approx \frac{\Delta x}{2} \quad (5.31)$$

The thermal dynamics equations for stacks consider convection between bipolar plate/ribs and anode/cathode channels, molecular interactions between MEA and anode/cathode channels (i.e., convections), heat conduction within solid structures, and local electric works, and they are summarized in Table 6-3.

Table 6-3 Equations for thermal dynamics of stack

$\left(\sum_X n_{X_i,j}^A \bar{c}_{v_X} \right) \frac{\partial T_{i,j}^A}{\partial t} = \dot{q}_{i,j_MI_A} + \dot{q}_{i,j_MEA_A} + \dot{q}_{i,j_Plate_A} + \dot{q}_{i,j_RibA_A} + \left(\sum_X \dot{n}_{X_in_i,j}^A \bar{c}_{p_X} \right) T_{i-1,j}^A - \left(\sum_X \dot{n}_{X_out_i,j}^A \bar{c}_{p_X} \right) T_{i,j}^A \quad (5.32)$
$\left(\sum_X n_{X_i,j}^C \bar{c}_{v_X} \right) \frac{\partial T_{i,j}^C}{\partial t} = \dot{q}_{i,j_MI_C} + \dot{q}_{i,j_MEA_C} + \dot{q}_{i,j_Plate_C} + \dot{q}_{i,j_RibC_C} + \left(\sum_X \dot{n}_{X_in_i,j}^C \bar{c}_{p_X} \right) T_{i-1,j}^C - \left(\sum_X \dot{n}_{X_out_i,j}^C \bar{c}_{p_X} \right) T_{i,j}^C \quad (5.33)$
$\rho_{MEA} C_{v_MEA} \frac{\partial T_{i,j_MEA}}{\partial t} = \dot{q}_{i,j_SR+WGS} + \dot{q}_{i,j_ELC} - \dot{q}_{i,j_MEA_A} - \dot{q}_{i,j_MEA_C} - \dot{w}_{i,j_FC} + k_{MEA} \left(\frac{d^2 T_{i,j_MEA}}{d\tilde{x}^2} + \frac{d^2 T_{i,j_MEA}}{d\tilde{y}^2} \right) - \dot{q}_{i,j_MI_A} - \dot{q}_{i,j_MI_C} \quad (5.34)$
$\rho_{Plate} C_{v_Plate} \frac{\partial T_{i,j_Plate}}{\partial t} = -\dot{q}_{i,j_Plate_A} - \dot{q}_{i,j_Plate_C} + \dot{q}_{i,j_RibA_Plate} + \dot{q}_{i,j_RibC_Plate} + k_{Plate} \left(\frac{d^2 T_{i,j_Plate}}{d\tilde{x}^2} + \frac{d^2 T_{i,j_Plate}}{d\tilde{y}^2} \right) \quad (5.35)$
$\rho_{Rib} C_{v_Rib} \frac{\partial T_{i,j_RibA}}{\partial t} = -\dot{q}_{i,j_RibA_A} - \dot{q}_{i,j_RibA_Plate} + k_{Rib} \frac{d^2 T_{i,j_RibA}}{d\tilde{x}^2}$ $\rho_{Rib} C_{v_Rib} \frac{\partial T_{i,j_RibC}}{\partial t} = -\dot{q}_{i,j_RibC_C} - \dot{q}_{i,j_RibC_Plate} + k_{Rib} \frac{d^2 T_{i,j_RibC}}{d\tilde{x}^2} \quad (5.36)$

6.4 Case studies

A case study is performed to explore the researches about the planar type of SOFC and compare those results with my simulational result. Li et al. [69] provide a simulational tool for researchers to conduct parametric studies of the SOFC. The three types of over-potentials

caused by different polarizations in a planar type solid oxide fuel cell was identified and compared. Aguiar et al. [70] present a mathematical modeling method that is an efficient analyzing tool for the design of the SOFC. From both researches, the electrochemical performances of the SOFC are analyzed at several temperatures by means of the voltage versus relatively high current density curves. In other words, the steady-state performance of the SOFC with various operating conditions such as air and fuel utilization factors, temperatures, and flow configurations are studied. Jung et al. [71] develop the SOFC with various materials for electrodes, and tested the SOFC assembly to investigate for the most desirable material for low polarization losses of the unit-cell performance. The most important part for the performance was reducing the Ohmic and polarization resistance of the cathode. The cell voltages as a function of the current density at 1073K are as shown in Figure 6-4.

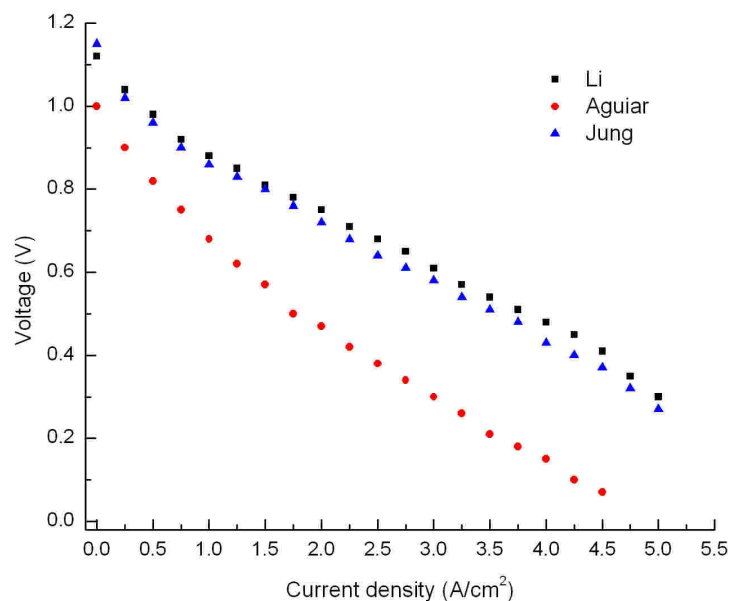


Figure 6-4 Cell voltage as a function of current density at 1073K

6.5 Results

In this research, the performances of SOFC stack were investigated with varying current densities. 20 cm by 20 cm cells were designed for 1kW power output and each cell was

connected by using stainless steels as interconnectors at certain operating temperature (800°C). As seen in Figure 6-5, I-V characteristic curve (current density vs. voltage) of the SOFC stacks was investigated by the aforementioned modeling methods in previous sections and using reformat gases from the CHER as fuels.

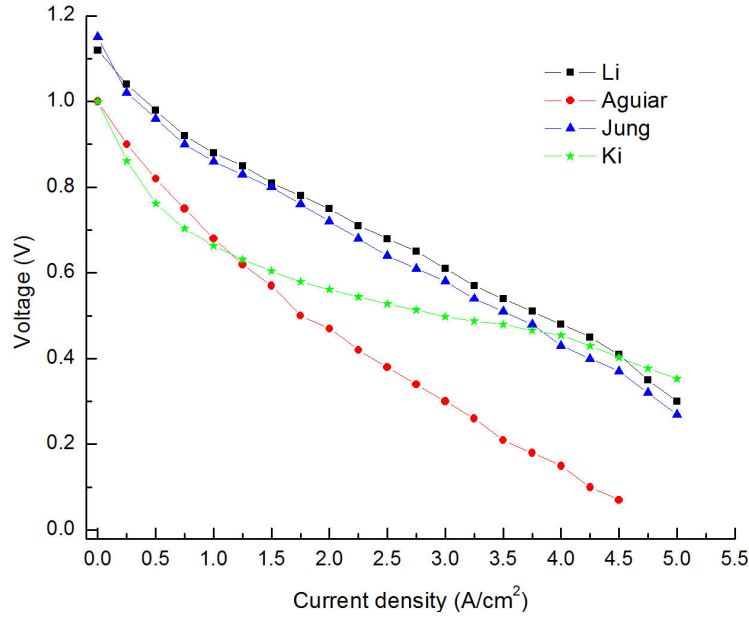


Figure 6-5 I-V characteristic curves comparison

During the electrochemical process, a layer is formed near the surface of the electrolyte, whereby the solution immediately adjacent to the electrolyte surface becomes depleted in the permeating solute on the feed side of the electrolyte, and its concentration is lower than that in the bulk fluid. On the other hand, the concentration of the non-permeating component increases at the electrolyte surface. A concentration gradient is formed in the fluid adjacent to the electrolyte surface. This phenomenon is known as concentration polarization and it serves to reduce the permeating component's concentration difference across the electrolyte, thereby lowering its flux. In the developed SOFC power generation module, the concentration loss/polarization is not considered. Normally, the cell is unstable because a cell showed a large

concentration polarization at a high applied current density. In that context, the voltages at the high current density in this research shows a relatively higher voltage compared to other researches. Although the concentration polarization is not considered in this analysis for the simplicity, the effects may be neglected without causing any substantial errors. Therefore, it can be concluded that the developed power generation module is applicable for the integrated SOFC system.

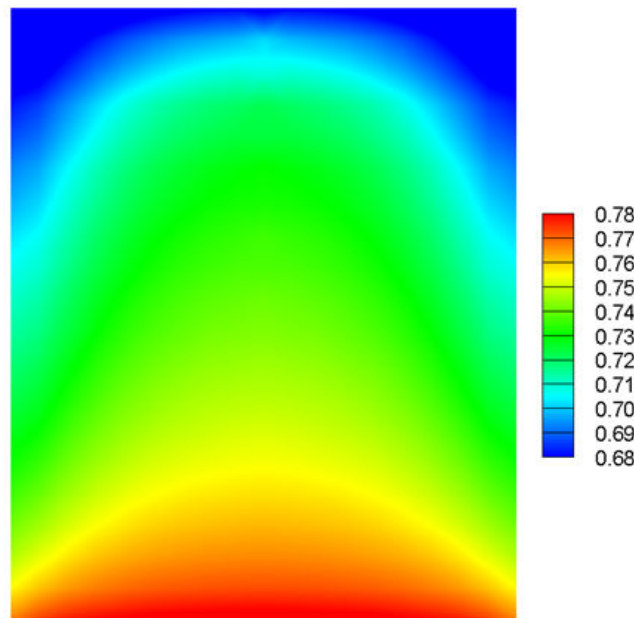
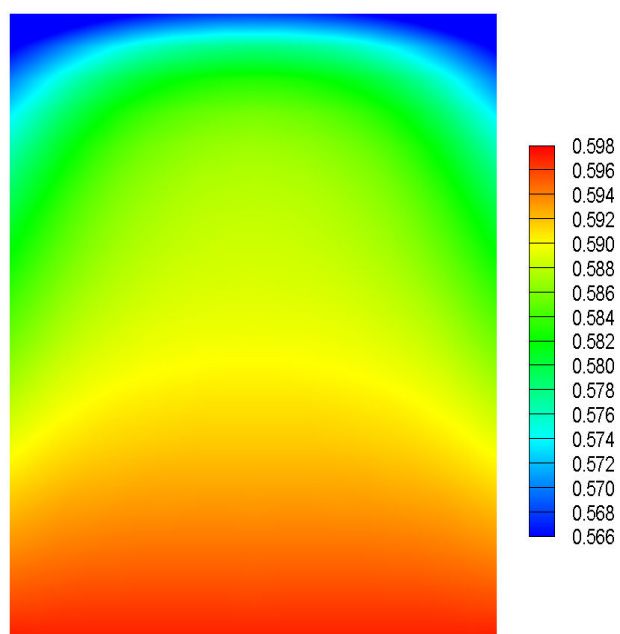
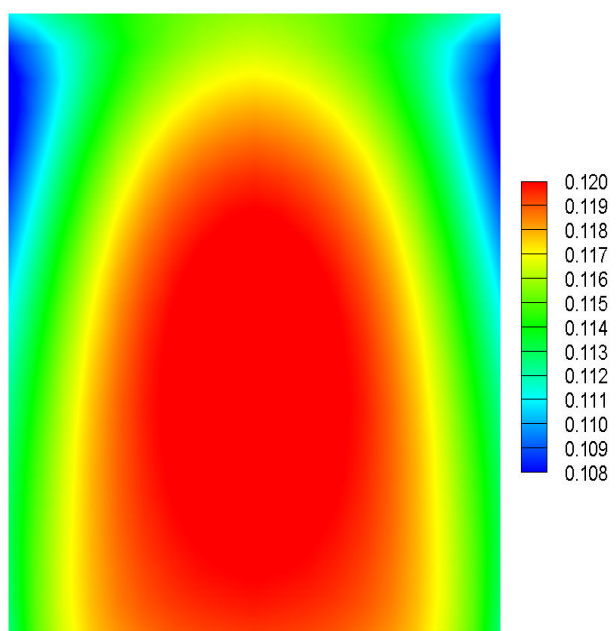


Figure 6-6 Cell voltage distribution in a planar SOFC at 0.5A/cm²

The electrical potential distribution in the designed planar SOFC at a specific current density is depicted in Figure 6-6. Any result can be obtained for other physical characteristics in the model such as temperature, current density distribution, molar concentration distribution, etc.



(a)



(b)

Figure 6-7 Molar fraction in the channels of H_2 and CO; (a) Molar fraction of H_2 and (b) Molar fraction of CO

As shown in Figure 6-7, the cell voltage distribution is related to the molar fraction of both H_2 and CO in the channels. In particular, the electrical potential in unit cell is normally tailored for the compositions of chemical species.

Chapter 7

Integration of each sub-module

A system is a group of interacting components that collaborate to achieve certain common purpose. Any type of energy system requires an efficient, reliable, and safe function. The design of a fuel cell system involves many trade-off options to optimize the fuel cell section with regard to an efficiency or economics or environment. It also considers minimizing the cost of producing electricity within the limitations of the desired application. For most applications, the proper arrangements among each component should be integrated into an efficient system with a low cost and a high efficiency. Often, these purposes are controversial; therefore, the system needs a precise design process and an appropriate design decision must be made. In addition, system performances should be met with each sub-component such as the SOFC stack, reformer (for an efficient fuel processing), HEX and afterburner (for the exhaust heat process to increase the system efficiency).

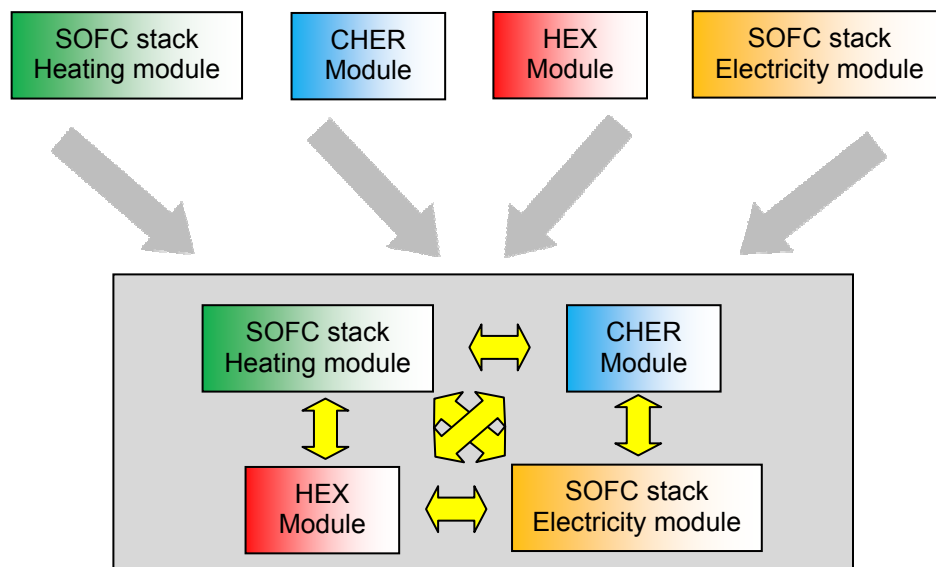


Figure 7-1 Schematic of the integrated SOFC system module

Figure 7-1 shows the schematic of the integrated SOFC system module. After completing developments of each sub, they were integrated into one module. The modeling method that comprises the integrated SOFC system is explained. The performance and endurance of the integrated SOFC system can be improved by operating at the most efficient operating range.

The objectives of this research are to develop a computational model of the SOFC system described in Figure 2-1 and to provide useful fundamental design guideline of HEX, reformer, compressor, etc. This model is on the basis of the satisfaction of conservation laws mass, energy and concentration of chemical species with specific source terms through the whole system. In other words, all boundary conditions for temperature, pressure, etc. should be satisfied with all conservation laws. For example, the cathode air inlet condition of the SOFC is directly affected by operating conditions of cold air from the outlet of HEX (located in front of SOFC) as shown in Figure 2-1 at the same time.

Significant fuel cell parameters that can be varied are the pressure, temperature, and fuel/oxidant composition and utilization. In order to manipulate design parameters of the SOFC system with various design practices of each component, a wide range of operating design parameters are examined. In addition, the integrated SOFC system model is designed not only to simulate each of the operating conditions, but also to simulate different configurations, etc.

However, pressurizing small systems is often not useful because the cost of the associated equipment outweighs the performance benefits. Changing the pressure from one to ten atmospheres would change the cell voltage by ~60mV for the SOFC. Therefore, in this research, a pressure parameter is not deeply considered. As explained earlier, the performance at operating conditions increases with increasing temperature due to reduced mass transport polarizations ohmic losses. The temperature increase is limited by material constraints. Again, the temperature difference in the cell is an important design parameter that affects not only SOFC stack performance but also mechanical integrity of the MEA.

As explained in previous chapters, each component module such as the SOFC stack start-up, HEX, reformer, and SOFC power generation module was successfully developed to be ready for building up the dynamic integrated SOFC system. And, all simulational results were found in agreements with experimental results.

7.1 Introduction

Figure 2-1 shows a possible configuration of the SOFC systems (other configurations may exist) composed of the fuel supply system (including reformer and HEX), SOFC stack, air HEX, combustor, and anode recirculation system. At stage 1, fuel is supplied to combustor and air is supplied to the HEX through the air line (HEX → SOFC stack → combustor → HEX/CHER). In other words, the exhaust gas from the combustor supplies thermal energies to the HEX and CHER using 3-way valve until the SOFC stack and CHER reaches desired temperatures without providing FSM to the CHER. At stage 2, once the SOFC and CHER reaches the prescribed temperatures, CH₄/steam mixture is supplied to the mixing chamber which is located in front of CHER. Steam is supplied through an external steam generator (evaporator). The FSM enters the CHER, which provides hydrogen-rich reformat gas to the stack through the AI. The non-reacted residual FSM is completely burned inside the combustor to increase fuel efficiency. At stage 3, once the stack begins to generate an electric power, a blower begins to recirculate the anode exhaust to M/C. At this stage, steam-neutral normal operation begins. Like mentioned earlier, the continuous operation of the combustor is essential to burn non-reacted residual fuel (20~30% of total supplied fuel). Additional fuel supply to the combustor would be optional depending on the required operating conditions of downstream components such as the inlet temperature of hot air for the HEX, etc.

Summarizing each stage, the efficient heat transfer from the hot air to the cold air occurs through the HEX. And, the fuel for SOFC stack is provided through anode channels by reformat gas from the CHER. To increase the temperature of the CHER, the hot air from the combustor is bypassed to the inlet of the CHER. At the CHER, the SR and WGS reactions are

assumed to occur. The amount of the steam supplied to the CHER is decided by STCR. Both H_2 and CO generated by the CHER participate in the electrochemical reaction in the SOFC stack. And, non-reacted residual reformat from the CHER is being internally reformed inside anode chambers. The cell voltage is a major parameter that determines the cell performance and depends on the various operating conditions and also depends on the cell material and structural geometry. Since this study does not focus on a specific fuel cell design, a simplified SOFC model is used.

7.2 Design process

Flows through the SOFC stack, HEX, and CHER depend on pressure and thermal boundary conditions at their respective inlets and outlets, which change continuously but are truly unknown. Cut timing of the bypassed air supply and external steam to the M/C relies on several thermodynamic conditions at the stack and CHER, which are very difficult to measure in-situ. The electric load control from the stack is followed by very slow dynamics of the stack itself, HEX, and CHER due to their long flow passages and large thermal mass. System level integration of the whole system relies mostly on the picking up of the off-the shelf HEX, blower, etc., which makes the optimization of each subsystem very difficult in terms of size and capacity. The air compressor and blower should be in optimal condition and should not reach “surge” in any operating condition of entire system. The surge is a well-known flow instability typically observed in the centrifugal compressor or blower. When the surge happens in the compressor, the total flow resistance downstream of the impeller becomes too high. Concerning the surge of the air compressor, total air flow resistance of the system relies on viscosity (increases with temperature) and flow geometry of the stack and HEXs, and it is very difficult to estimate in the design stage. Total system activation energy is much higher than typical internal combustion engines due to the long start-up time.

Pressures at both inlets and outlets of each sub-system should be considered to satisfy the mass conservation in entire system. It is noteworthy that the pressures at the inlets of the sub-system are unknown and those should be found through a mass conservation equation.

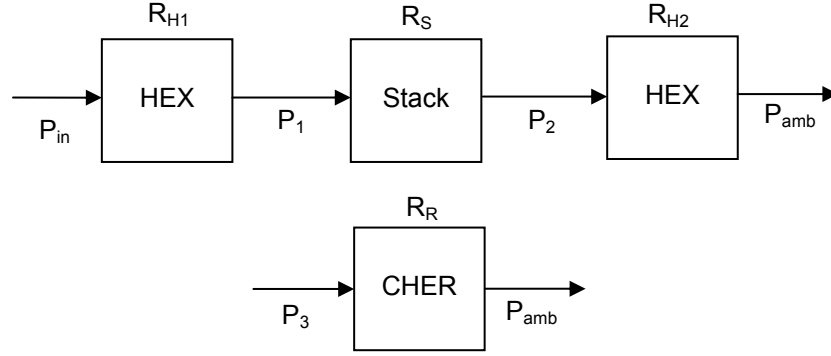


Figure 7-2 Schematic of pressures and flow resistances at stage 1

Figure 7-2 shows pressures and flow resistances at each location. Here, P means pressure and R is flow resistance. Mass flow rate is set to a constant. With increasing flow resistances, pressures should be increased by increasing the speed of the blower to maintain the mass flow rate. Considering the mass conservation between two sub-systems;

$$\begin{aligned} \frac{P_{in} - P_1}{R_{H1}} &= \frac{P_1 - P_2}{R_S} = \frac{1}{(1-\beta)} \frac{P_2 - P_{amb}}{R_{H2}} \\ \frac{1}{(1-\beta)} \frac{P_2 - P_{amb}}{R_{H2}} &= \frac{1}{\beta} \frac{P_3 - P_{amb}}{R_R} \end{aligned} \quad (6.1)$$

where β is a bypass ratio, defined as the rate between the amount of air flowing from the stack and the amount of air passing through the CHER.

Equation (6.1) builds a set of simultaneous equation as follows.

$$\frac{P_{in}}{R_{H1}} - P_1 \left(\frac{1}{R_S} + \frac{1}{R_{H1}} \right) + \frac{P_2}{R_S} = 0 \quad (6.2)$$

$$\frac{P_1}{R_S} - P_2 \left(\frac{1}{R_S} + \frac{1}{1-\beta} \frac{1}{R_{H2}} \right) + \frac{1}{1-\beta} \frac{P_{amb}}{R_{H2}} = 0 \quad (6.3)$$

$$\frac{1}{1-\beta} \frac{P_2}{R_{H2}} - P_3 \frac{1}{\beta} \frac{1}{R_R} - P_{amb} \left(\frac{1}{1-\beta} \frac{1}{R_{H2}} - \frac{1}{\beta} \frac{1}{R_R} \right) = 0 \quad (6.4)$$

These equations (6.2)~(6.4) can be changed into one matrix form such as equation (6.5).

$$\begin{bmatrix} -\left(\frac{1}{R_S} + \frac{1}{R_{H1}}\right) & \frac{1}{R_S} & 0 \\ \frac{1}{R_S} & -\left(\frac{1}{R_S} + \frac{1}{1-\beta} \frac{1}{R_{H2}}\right) & 0 \\ 0 & \frac{1}{1-\beta} \frac{1}{R_{H2}} & -\frac{1}{\beta} \frac{1}{R_R} \end{bmatrix} \begin{bmatrix} P_1 \\ P_2 \\ P_3 \end{bmatrix} = \begin{bmatrix} -\frac{P_{in}}{R_{H1}} \\ -\frac{1}{1-\beta} \frac{P_{amb}}{R_{H2}} \\ P_{amb} \left(\frac{1}{1-\beta} \frac{1}{R_{H2}} - \frac{1}{\beta} \frac{1}{R_R} \right) \end{bmatrix} \quad (6.5)$$

Therefore, inlet/exit pressures of each sub-system can be calculated in equation(6.5) during the transient operation (Stage 1) at the constant mass flow rate.

On the other hand, the inlet/exit pressures of the CHER and stack can be calculated with the same method as previously mentioned during the transient operation (Stage 2) at the constant mass flow rate.

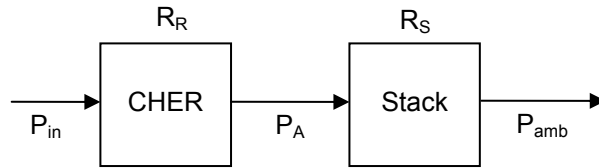


Figure 7-3 Schematic of pressures and flow resistances at stage 2

Figure 7-3 shows pressures and flow resistances at each location. With increasing flow resistances, pressures should be increased by increasing the speed of the blower to maintain the mass flow rate. Considering the mass conservation between two sub-systems;

$$\frac{P_{in} - P_A}{R_R} = \frac{P_A - P_{amb}}{R_S} \quad (6.6)$$

Therefore, inlet pressures of the SOFC stack can be calculated in equation(6.6) during the transient operation (stage 2) at the constant mass flow rate.

$$P_A = \frac{\frac{P_{in}}{R_R} + \frac{P_{amb}}{R_S}}{\frac{1}{R_R} + \frac{1}{R_S}} \quad (6.7)$$

7.3 Results

As mentioned earlier, the SOFC system requires the integration of many sub-components including the SOFC stack itself. In this context, various sub-system components such as the HEX, CHER, blower/compressor, and combustor are appropriately incorporated into an integrated SOFC system to achieve a desired performance and increase the efficiency. Numerous phenomena within the integrated SOFC system can be described with partial differential equations with unknown parameters such as the temperature, partial pressure, concentration of chemical species, while some phenomena would be described as global mass and energy balance equations.

Figure 7-4 shows the total mass flow rates of air flowing through 1) the cold channels in the HEX, 2) the cathode channels in the SOFC stack, and 3) the air channels in the CHER. In every case, the mass flow rate of air become steady state within very short time in the system.

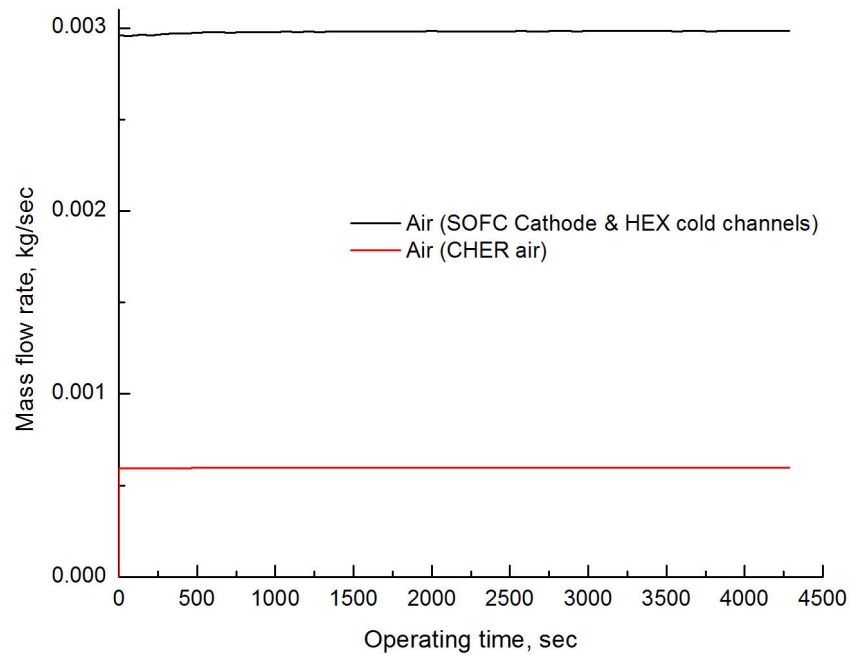


Figure 7-4 Mass flow rates of air flowing through the HEX and cathode channels

Figure 7-5 plots transient temperature curves at various locations in the SOFC stack at Stage 1. The temperatures of solid structures such as the interconnector, MEA, and fins increased with the cathode air at Stage 1. Temperatures of solid structures are the average temperatures of entire control volumes.

Figure 7-6 shows the temperature distribution of the MEA in the SOFC stack at the steady state. Although any temperature profile at any interested location can be obtained by the simulational results, all temperature distributions were not presented in the paper.

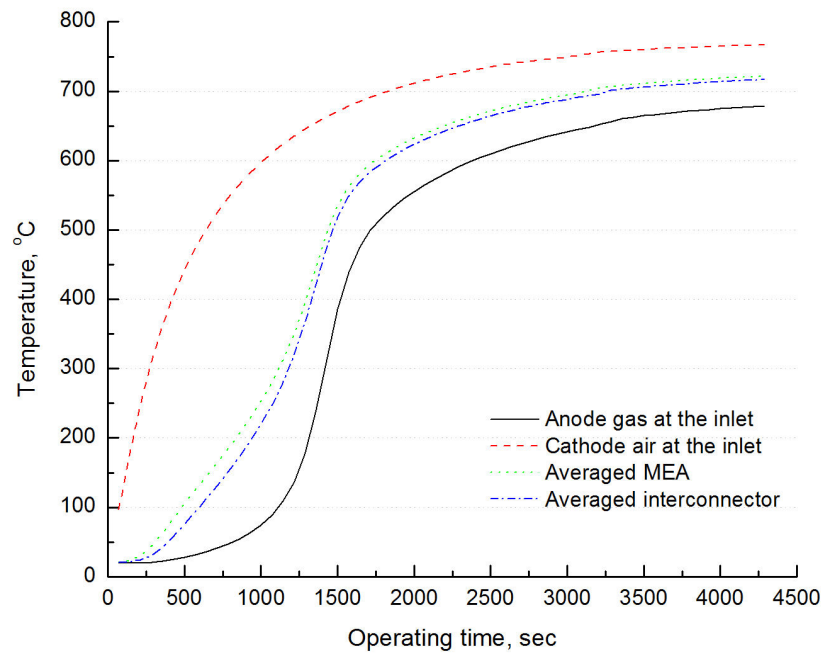


Figure 7-5 Temperature profile of SOFC stack in the integrated system

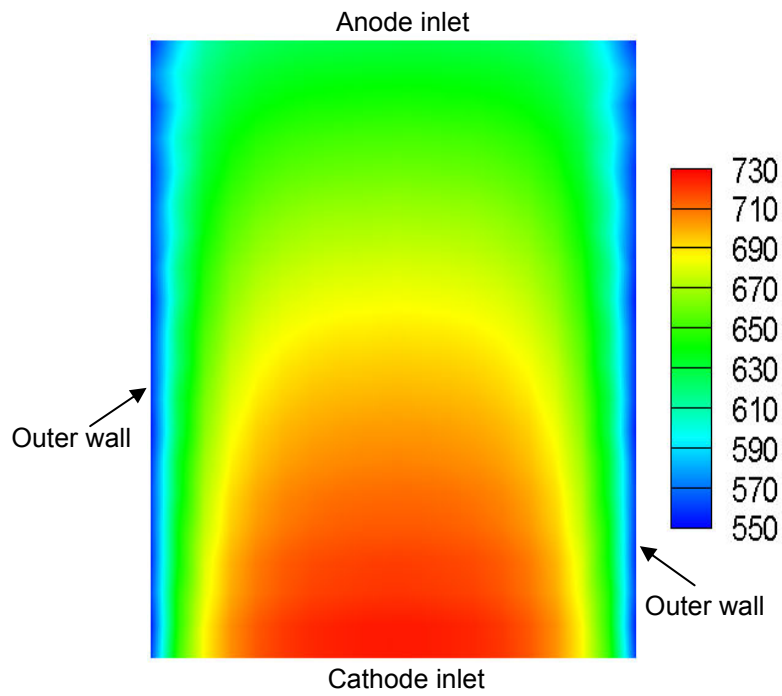
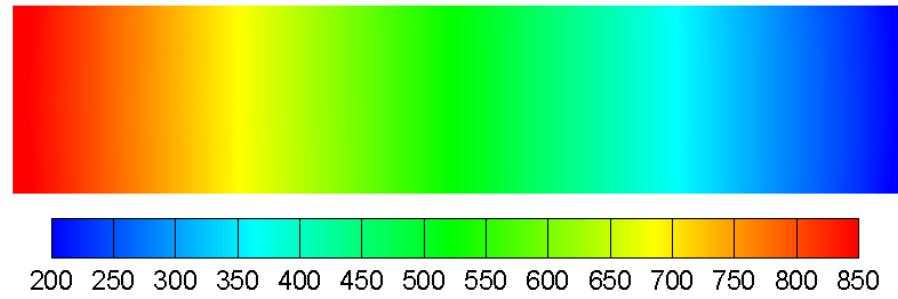
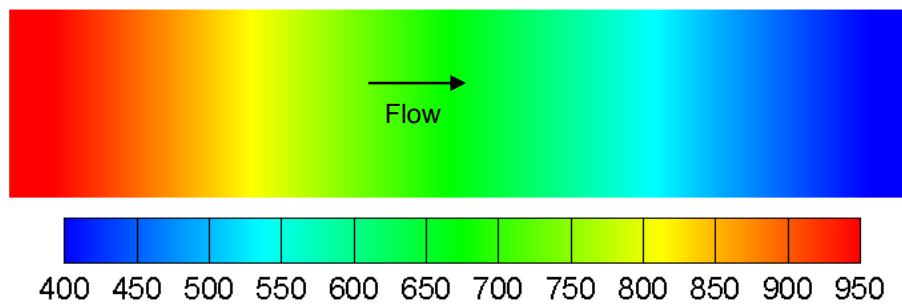


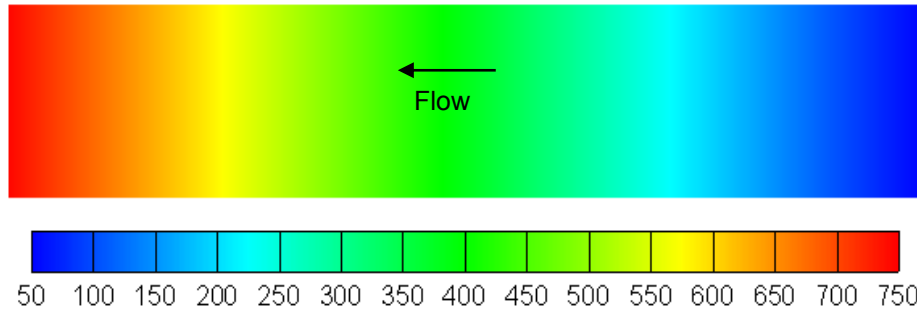
Figure 7-6 Temperature profile of MEA in the SOFC stack



(a)



(b)



(c)

Figure 7-7 Temperature profiles of hot air, cold air, and plate in the HEX; (a) Interconnector, (b) Hot air, and (c) Cold air

Figure 7-7 presents the temperature profiles of both the cold air and hot air inside the HEX and the plate inserted in the HEX at the steady state. These simulational results provide a guideline for evaluating the performances of the developed integrated SOFC system.

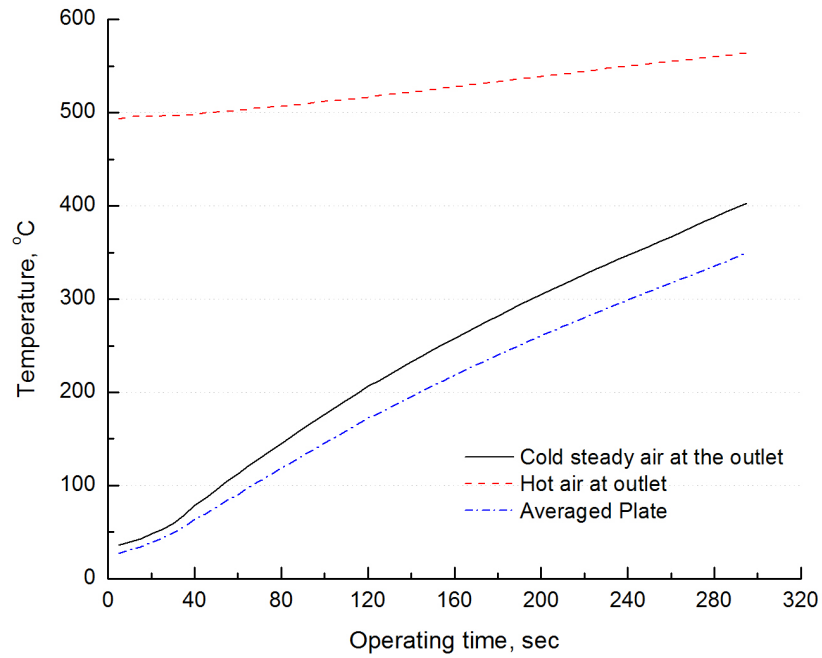


Figure 7-8 Temperature profile of the CHER at the Stage 1

Figure 7-8 presents the temperature profiles of both the cold steady air at the outlet and hot air at outlet, and the plate inserted in the CHER during the Stage 1. These simulational results provide a guideline for evaluating the performances of the developed integrated SOFC system.

Figure 7-9 shows the temperature profiles of both the reformate gases and air inside channels at Stage 2. As the CHER reaches a certain desired temperature toward the reforming reaction, the FSM is supplied to the inlet of the CHER while the air continuously flows through the channels at the opposite direction. Due to the endothermic SR reaction, the temperature of the FSM immediately decreases at the inlet as shown in Figure 7-9. And the heat energy from the hot air transfers to the channels that take place the SR and WGS reactions.

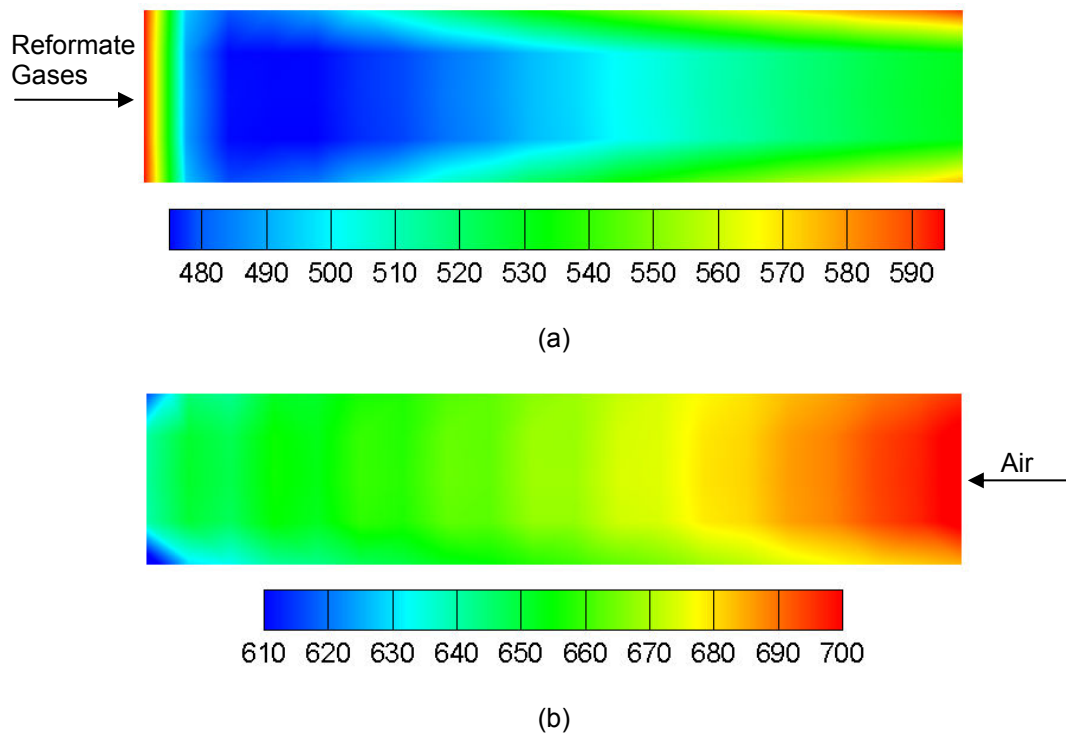


Figure 7-9 Temperature profiles of reformat gases and air in the CHER; (a) Reformat gases and (b) Air

Figure 7-10 shows the averaged molar fraction of each species at the outlet of the CHER. It is observed from the figure that the reforming reaction instantaneously becomes steady state within one minute.

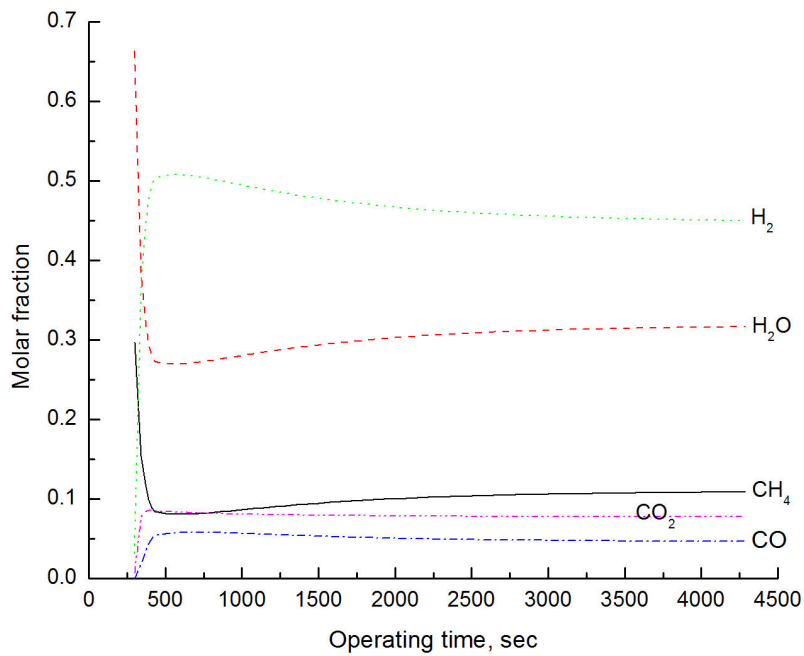
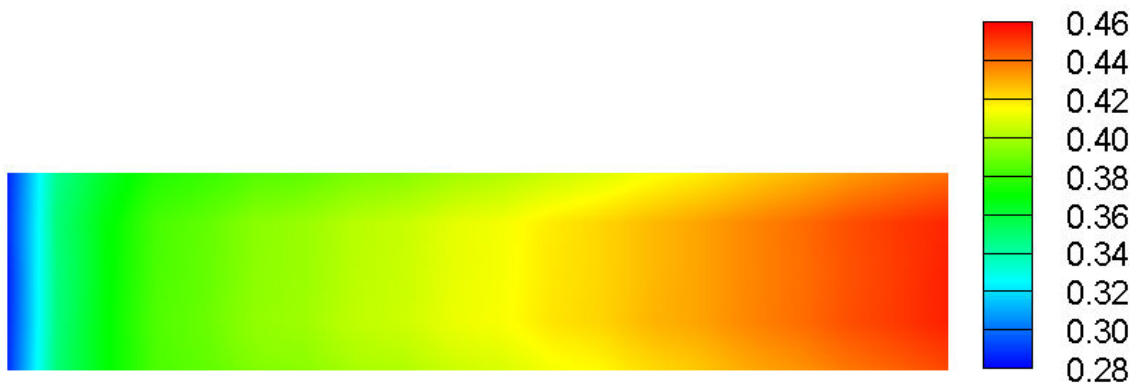
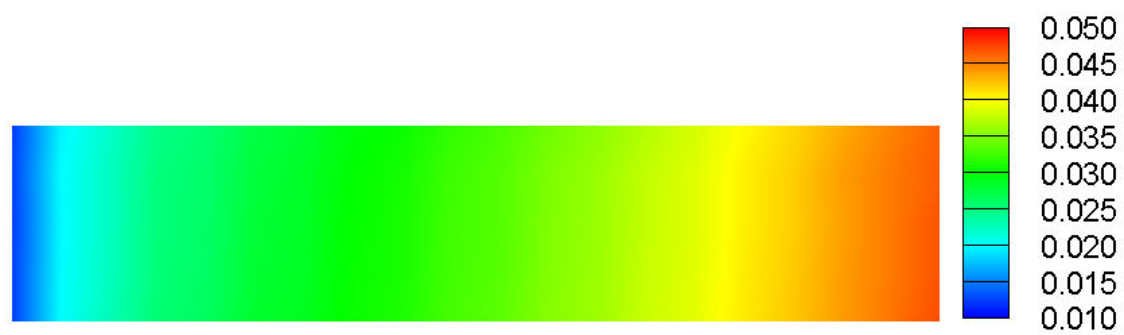


Figure 7-10 Molar fraction of each species at reformer exit since fuel supply begins

The species molar fractions in the FSM channels are shown in Figure 7-11. It may be observed that the WGS reaction takes place through entire channels by looking at the CO_2 molar fraction while the SR reaction is dominant in the region close to the outlet by looking at the CO molar fraction. This is due to the different preference of the SR and WGS reactions with respect to various operating temperatures as shown in Figure 5-23.



(a)



(b)



(c)

Figure 7-11 Molar fraction of each species inside the FSM channels of the CHER; (a) H_2 , (b) CO , and (c) CO_2

Chapter 8

Summary

8.1 SOFC start-up process

A computational model was developed to find temperature distributions of solid structures and gas channels in a SOFC stack during the start up process using both cathode hot air and electrical furnace heating. Using the developed model, temperature distribution of solid structures and gas channels can be found at any specific time step. The computational model is a very effective tool to understand the thermal transient response of stack during start-up heating.

The model was applied to 1 kW planar SOFC stack to investigate transient behavior of the stack during both hot cathode air heating and electrical heating inside the furnace. In the case of using hot cathode air with a constant mass flow rate, the inlet pressure required to maintain the constant mass flow rate increases significantly over time as the flow resistance inside the stack increases with temperature. The selection of an air blower and its required performance map should be tuned to meet the pressure requirement for proper air delivery.

Electrical heating requires controlled heating to avoid rapid temperature rise of the stack surface. Depending on the thickness of MEA and interconnectors, thermal conduction through these thin structures varies and the heating rate should be controlled accordingly to avoid large thermal gradient during heating.

Both heating methods require similar net heating energy to achieve a uniform stack temperature within prescribed limit. However, air heating with constant mass flow rate results in a waste of a large amount of heat energy through exiting air with high enthalpy. Operating the blower at a constant speed mode allows the gradual decrease of air mass flow rate when the stack is heated and may result in higher heating efficiency. However, for either constant mass flow rate or constant speed case, the thermal energy of the exiting air should be recovered

through heat exchangers for the reformer or steam generator which are integral parts of most SOFC systems.

8.2 Both Simulation and Experiment of HEX

In this research of HEX, the concept of computational model was implemented to a commercial HEX, and its dynamic model was developed.

Simulation results show the temperature distributions of solid structures and both air channels in HEX during the heat exchanging process. Using the developed model, temperature distribution of solid structures and both air channels can be found at any specific time step. The computational model is a very effective tool to understand thermal transient response of HEX during heat exchanging process. This research also shows the test rig setup for the experiment and verifies the results against simulation.

The developed simulation model has been validated against the experimental measurements, showing acceptable accuracy for a HEX of SOFC system.

8.3 Simulation of CHER

The developed computational model is based on the thermal-fluid transport theories of plate-fin gas heat exchangers combined with dynamic molar balance equations, transient energy equations to the fuel-steam mixture and air, and currently available reforming reaction kinetics in the open literature. Several parametric simulations were performed to evaluate the performance of CHER.

A higher operating temperature results in a smaller total FSM mass flow rate due to the increased flow resistance (i.e., viscosity) while mole fractions of H_2 and CO at the exit increase with temperature. The combined effect of the reduced total FSM mass flow rate and the increased mole fraction of H_2 results in a similar mass flow rate of H_2 at the reformer exit within the range of simulation. Pressure affects the performance of CHER significantly. While the air channel temperatures increase with pressure due to more mass flow and thermal energy carried by the air mass flow, the FSM channel temperatures decrease with pressure due to

more active endothermic reforming reactions. Longer CHER length under the same pressure results in smaller mass flow rates on both the air and FSM sides. Due to the reduced air flow rate, total heat supply rate to the FSM channels also decreases, which slows down the reforming rate. Even if molar fractions of H_2 and CO do not show a noticeable difference between the two flow configurations, actual H_2 and CO yields are higher with the counter-flow configuration.

The computational model can be easily extended to other types of fuels and different reaction kinetics. Also transient responses such as load-following characteristics or transient thermal response to sudden change of inlet temperature of the air side can be easily simulated.

The current model simulations were based on the specific SR and WGS reaction rates (pre-exponential factors and activation energies) available in the literature. However, the reaction kinetics depends not only on the environmental conditions (species activity, temperature, etc) but also on the catalyst type and surface morphology of the catalyst. This catalyst-specific information is not generally well-documented in the open literature, and more systematic parameterization of reaction kinetics should be done as a function of not only the catalyst material and loading method but also the surface morphology and total active reaction surface area.

Lastly, the simulated temperature range of the air side is based on the assumption of the in-series arrangement of the main HEX and CHER as shown in Figure 2-1. The parallel distribution of combustion gas (modeled as air in the paper) to the main HEX and CHER would allow a much higher inlet temperature of the air side in the CHER.

8.4 Experiment of CHER

In previous research, a theoretical thermal dynamic and thermal chemical simulation model has been developed to investigate the transient characteristics of the CHER based on the thermal-fluid transport theories of plate-fin gas HEXs combined with dynamic molar balance equations, transient energy equations to the air and FSM. In the research, the developed

computational model was validated by the experimental results with various operating conditions such as an air inlet temperature and a steam to carbon ratio (SCR) during the initial phase of start-up procedure of the typical small SOFC systems.

Under given conditions, the results indicated that there exist the optimal air inlet temperature and SCR for both the air and FSM to reach equilibrium for the reforming reaction. The previously developed transient thermal chemical model was well validated with the experimental results by comparing the molar fraction of each species with varying the air inlet temperatures and SCRs. Thermal dynamics for the heat exchanging process was also validated by measuring temperatures of the air and FSM at both the inlet and outlet.

The developed simulation model was based on the specific SR and WGS reaction rates such as the specific pre-exponential factors and activation energies that were available in the open literature. In this research, the chosen reaction parameters were acceptable by the comparison with the experimental results. However, the found reaction kinetics may not be relevant to any reformer type because the reaction kinetics depend on the coated catalyst type on the inserted corrugated fin surface and surface morphology of the catalyst. In addition, the catalyst-specific information is not generally well documented in the open literature. The purpose of this research was not to investigate the used catalyst information such as the material, loading method, surface morphology and total active reaction surface area. But, the chosen reaction variables were steadily applicable for the developed simulation model.

8.5 SOFC Electric Power Generation Mode

This research focuses on the development of a detailed numerical model of the SOFC power generation mode. The complete modeling methods for resistivity, contact and ionic resistances, reversible voltage calculation, and activation and ohmic polarizations are presented. And, the electric circuit modeling method for each element of the SOFC is built on the basis of the conservation law (KCL). In addition, the thermodynamic model is developed to calculate the transient temperature of each component of the SOFC. The thermodynamic model for SOFC

stacks consider convection between bipolar plate/ribs and anode/cathode channels, molecular interactions between MEA and anode/cathode channels (i.e., convections), heat conduction within solid structures, and local electric works.

A case study for the performance of SOFC stack is conducted in order to validate the developed SOFC power generation module. The results from the models previously developed by the authors or found in the literature survey are presented. I-V characteristic curve of the SOFC was investigated by the aforementioned modeling methods in previous sections. The cell performance at the high current density shows a relatively higher voltage level compared to other research methods since the concentration polarization is not considered in the analysis. The purposes of the development of the SOFC stack power generation module are not the complete development of the power generation module but the pilot research preliminary to a full-scale study for the integrated SOFC system. However, the simulation results confirm that the developed SOFC power generation model can be useful to comprehend the dynamics of the SOFC in a system and can be integrated for control and operability studies of the integrated system.

8.6 Integrated SOFC system

Design characteristics and performance of the integrated SOFC system are analyzed in this research. The simulation model for each sub-component such as the SOFC stack heating and power generation module and auxiliary parts (HEX and CHER) are developed and the simulation models for the HEX and CHER were validated with experiments. And, the validated sub-modules are appropriately incorporated into an integrated SOFC system to achieve a desired performance.

The integrated SOFC system module is designed not only to simulate each of the operating conditions but also to test the performances of each component including the SOFC stack. In every case, the module produces a time-dependent profile of temperatures, molar fractions of each species, electrical potentials, and thermal gradients for the entire system. The

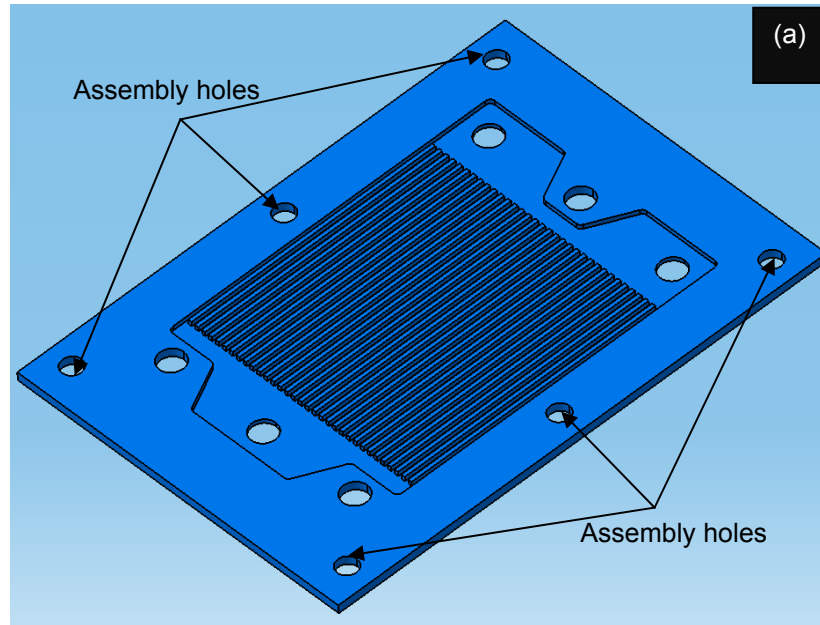
obtained results confirm that the developed model can be used to simulate the integrated SOFC system. For instance, the essential time to reach the steady-state temperature distribution for the SOFC stack in the integrated SOFC system can be estimated by the developed module.

Appendix A

A manual for 1-kW SOFC stack design

This manual outlines the design procedures and instructions for designing a 1-kW SOFC stack. The active area per cell was defined for the desired power generation. Depending on the chosen active area, proper geometric dimensions were selected through the literature reviewed. Table 3-1 and Table 3-2 show the designed parameters and geometric dimensions of 1kW SOFC stack. The thickness of MEA is not specified in detail in Table 3-2. The numerical dimensions for thickness of each component among MEA are $36\mu\text{m}$ for anode, $64\mu\text{m}$ for cathode, and $180\mu\text{m}$ for electrolyte.

For the SOFC start-up process, widths of both the anode and cathode channel were selected by choosing the discretized number of control volume along x-direction and the thickness of ribs. For this simulation, the channel width was designed as 8mm which is a relatively large dimension compared to a commercial SOFC. This was for the reduction of simulation time.



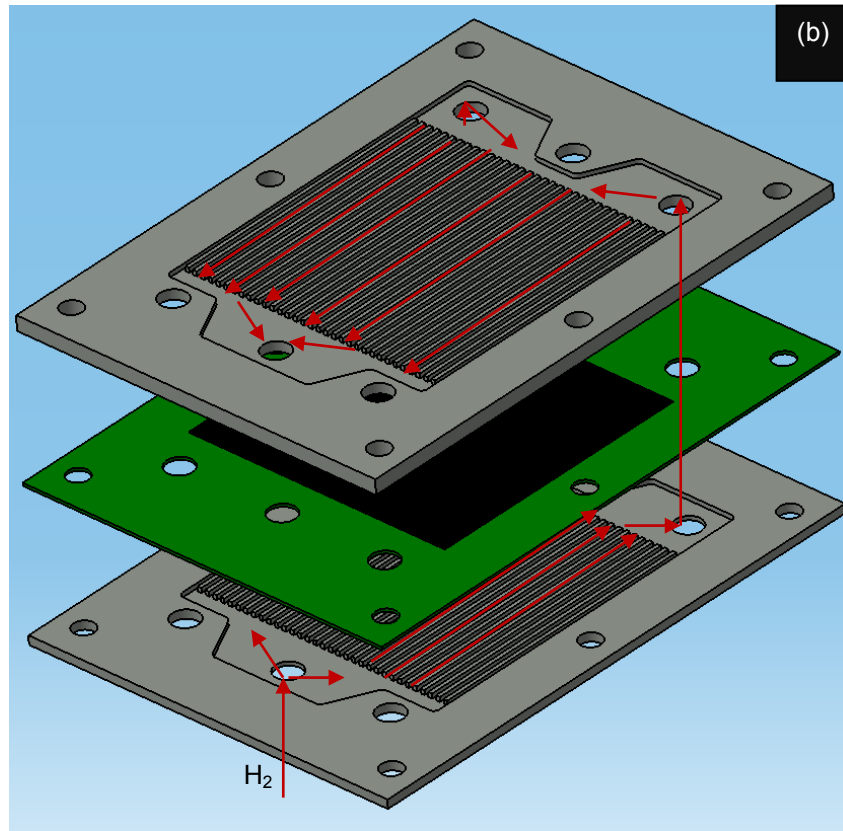


Figure A. 1 Designed SOFC (a) Anode channel, (b) Anode channel, MEA, and Bipolar plate to show the flow direction of H_2

As shown in Figure A. 1(a), 6 holes in outer region of the mono-polar plate are assembly holes to make the stack. Figure A. 1 (b) shows the flow direction of hydrogen inside the SOFC stack. Likewise, the flow direction of air can be understood in a similar way to the flow of hydrogen. With this kind of design, the mixing of fuel and air never occurs inside the stack, but sealing between the plate and inactive MEA becomes critical around the holes. Many researchers are trying to develop better sealing technologies for SOFC stack assembly.

Appendix B

ANSYS Fluent SOFC module manual [72]

Introduction

The SOFC with Unresolved Electrolyte Model is provided as an add-on module with the standard ANSYS FLUENT licensed software.

The ANSYS FLUENT SOFC with Unresolved Electrolyte Model provides the following features:

- Local electrochemical reactions coupling the electric field and the mass, species, and energy transport.
- Electric field solution in all porous and solid cell components, including ohmic heating in the bulk material.
- The ability to handle H₂ and combined CO/H₂ electrochemistry.
- The inclusion of tortuosity for porous regions
- The treatment of an arbitrary number of electrochemical cells arranged as a stack.
- Significant geometric flexibility for treating planar, tubular, and other nonstandard SOFC configuration.
- The use of non-conformal interface meshing (as long as these interfaces are not the electrolyte interfaces).
- The ability to model high-temperature electrolysis.

Modeling

All aspects of fluid flow, heat transfer, mass transfer in the flow channels and porous electrodes, current transport and potential field are handled by ANSYS FLUENT. All theoretical backgrounds of modeling are explained in this manual in detail.

Using the SOFC with Unresolved Electrolyte Model

The SOFC with Unresolved Electrolyte Model is loaded into ANSYS FLUENT through the text user interface (TUI). Remember that the module can only be loaded after a valid ANSYS FLUENT mesh or case file has been set or read. The text command to load the addon module is define → models → addon-module

After typing `/define/models> addon-module`, ANSYS FLUENT will display sentences below.

FLUENT Addon Modules:

- 0. None
- 1. MHD Model
- 2. Fiber Model
- 3. Fuel Cell and Electrolysis Model
- 4. SOFC Model with Unresolved Electrolyte
- 5. Population Balance Model

Enter Module Number: [0] 4

Select the SOFC with Unresolved Electrolyte Model by entering the module number 4. Once, the module has been loaded, to open the SOFC model dialog, select Models under Problem Setup in the navigation pane to display the Models task page. In the Models task page, select the SOFC Model (Unresolved Electrolyte) option in the Models list and click the Edit... button. When the SOFC Model dialog appears, select the Enable SOFC Model option as shown in Figure B. 1.

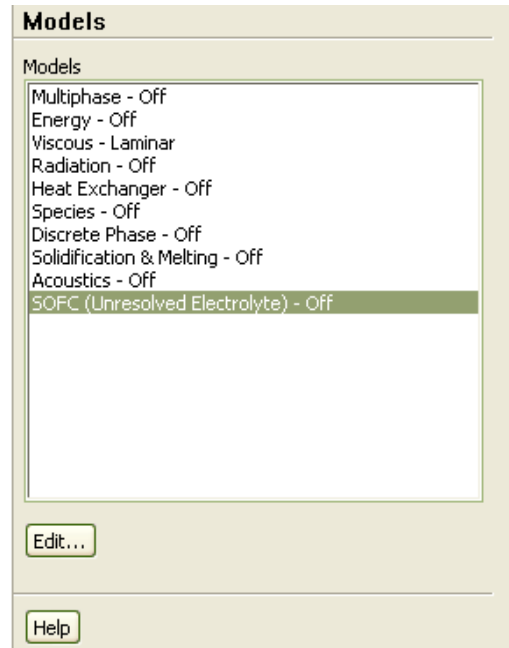


Figure B. 1 Opening the SOFC Model Dialog in the Models Task Page

For the next procedures required in order to use the SOFC Model in ANSYS FLUENT, following the manual instructions step by step is sufficient for using this software.

However, there are important features in ANSYS FLUENT that need more explanation for various parameters such as Model, Electrochemistry, Electrode-Electrolyte Interfaces, Electric Field Model parameters.

For Model Parameters, the Enable Electrolyte Conductivity Submodel option allows the ionic conductivity (or resistivity) of the electrolyte to change as a function of temperature. At the moment, there is one correlation that provides ionic conductivity of the electrolyte as the function of temperature as shown in the next equation.

$$resistivity = \frac{0.3685 + 0.002838e^{\frac{10300}{T}}}{100}$$

Note that this is valid only for temperature ranging from 1073 to 1373K. By turning off the Enable Electrolyte Conductivity Submodel option, ANSYS FLUENT excludes the heat addition

due to electrochemistry and all the reversible processes. This option should be turned on at all time. The Enable Volumetric Energy Source option includes the ohmic heating throughout the electrically conducting zones. This option needs to be turned off to avoid slowing the convergence rates until a certain rate of convergence for the potential field has been achieved, at which point, the option should be turned on manually. Note that this option is important so that the solution can account for the effects of the internal Ohmic heating.

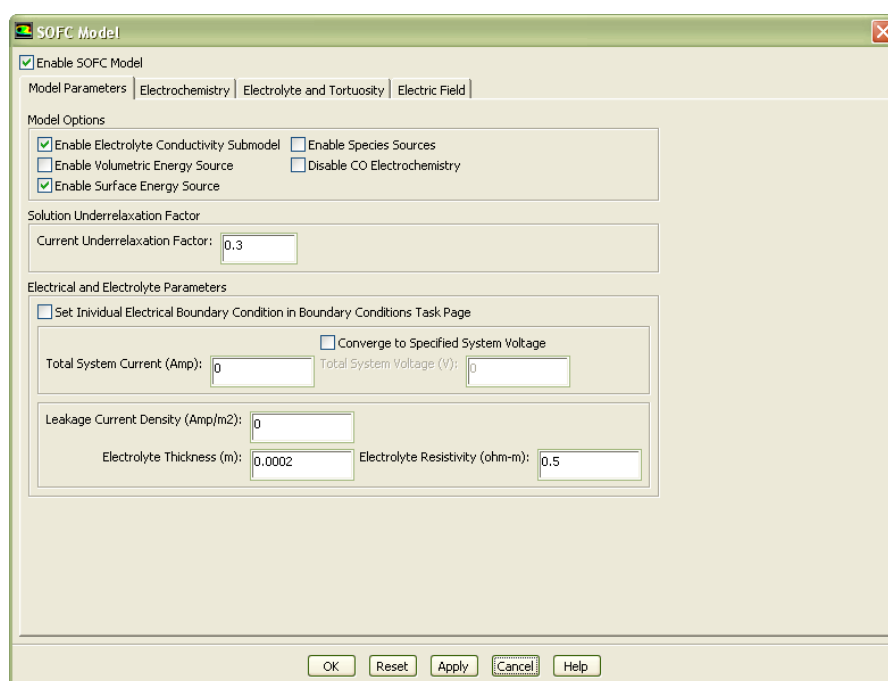


Figure B. 2 The Model Parameters Tab in the SOFC Model Dialog

In the Electrochemistry Parameters, we can set the anode and cathode exchange current density, the anode and cathode mole fraction reference values, the concentration exponents, the Butler-Volmer coefficient, and the temperature-dependent exchange current density as shown in Figure B. 3 .

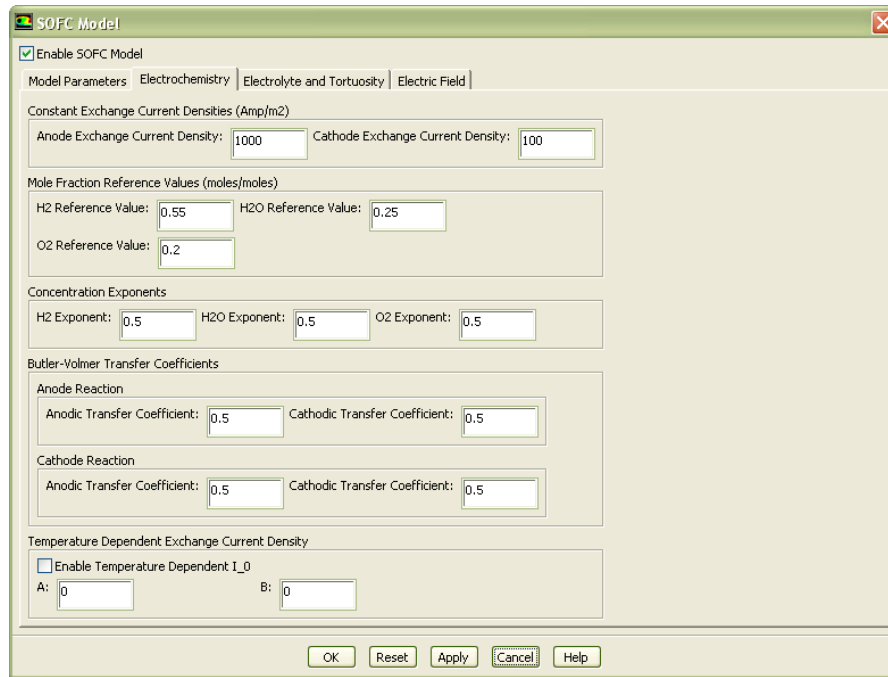


Figure B. 3 The Electrochemistry Tab in the SOFC Model Dialog

The Enable Temperature Dependent I_0 option allows the exchange current density to change as a function of temperature in an exponential fashion

$$i_0 = Ae^{-\frac{1}{BT}}$$

where the constants A and B values can be provided.

For both anode and cathode interfaces as well as set tortuosity parameters, setting up the Electrolyte and Tortuosity tab in the SOFC Model Dialog properly is required. For example, in the fuel cell modeling, tortuosity is thought of as an effective diffusive path length factor. We can specify tortuosity settings for the SOFC Model by enabling the Enable Tortuosity option in the Electrolyte and Tortuosity tab in the SOFC Model dialog as shown in Figure B. 4.

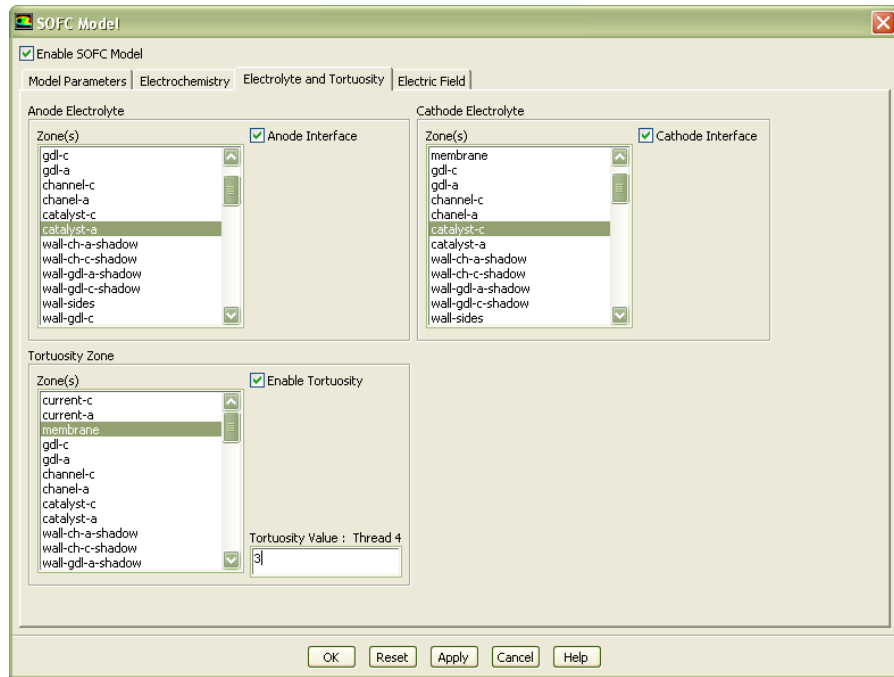


Figure B. 4 The Electrolyte and Tortuosity Tab in the SOFC Model Dialog

After enabling the Enable Tortuosity option, select an appropriate zone from the corresponding Zone(s) list and click Apply. In a porous zone, the mass diffusion coefficient is reduced as follows due to the porosity effect;

$$D_{eff} = \frac{porosity}{tortuosity} D$$

There typically are no standard means of measuring tortuosity as it either needs to be measured experimentally or tuned to match other experimental data. Tortuosity value may typically be in the range of 2 to 4, although it can be used for much higher values.

Appendix C

Classification of all variables in each module

1) SOFC stack heating module

a) Global variables

Parameter	Definition	Value	Unit
a1~a3	Regression constants for air viscosity		
alpha_conn	Thermal diffusivity of interconnector		m ² /s
alpha_MEA	Thermal diffusivity of MEA		m ² /s
Area_a	Channel area of anode		m ²
Area_a_w	Virtual channel area of anode exit region		m ²
Area_c	Channel area of cathode		m ²
Area_c_w	Virtual channel area of cathode inlet region		m ²
C_conn	Specific heat of interconnector	460	J/kg/K
C_MEA	Specific heat of MEA	606	J/kg/K
Cell_voltage	Single cell voltage	0.7	V
cp1~ cp6	Regression constants for specific heat for constant pressure		
Current_density	Current density of a single stack	0.51	A/cm ²
cv1~ cv6	Regression constants for specific heat for constant volume		
Cv_a	Specific heat for constant volume of anode gas		J/kg/K
Cv_a_ex	Specific heat for constant volume of anode gas in anode exit region		J/kg/K
Cv_a_in	Specific heat for constant volume of anode gas in anode inlet region		J/kg/K
Cv_c	Specific heat for constant volume of cathode air		J/kg/K
Cv_c_ex	Specific heat for constant volume of cathode air in cathode exit region		J/kg/K
Cv_c_in	Specific heat for constant volume of cathode air in cathode inlet region		J/kg/K
del_k	Horizontal length of a control volume for outer solid structure		m
Del_K	Nondimensional del_k		
del_m	Vertical length of a control volume for outer solid structure on cathode inlet side		m

Del_M	Nondimensional del_m		
del_r	Vertical length of a control volume for cathode exit region		m
Del_R	Nondimensional del_r		
del_w	Vertical length of a control volume for cathode inlet region		m
Del_W	Nondimensional del_w		
del_x	Horizontal length of a control volume for active region		m
Del_X	Nondimensional del_x		
del_y	Vertical length of a control volume for active region		m
Del_Y	Nondimensional del_y		
del_z	Vertical length of a control volume for outer solid structure on cathode exit side		m
Del_Z	Nondimensional del_z		
delp_a	Pressure drop through anode channel	0	Pa
delp_a1	Temporary parameter of pressure calculation for anode channel on active region		Pa
delp_a3	Temporary parameter of pressure calculation for anode channel on cathode inlet region		Pa
delp_a7	Temporary parameter of pressure calculation for anode channel on cathode exit region		Pa
delp_c	Pressure drop through cathode channel	30	Pa
delp_c1	Temporary parameter of pressure calculation for cathode channel on active region		Pa
delp_c3	Temporary parameter of pressure calculation for cathode channel on cathode inlet region		Pa
delp_c7	Temporary parameter of pressure calculation for cathode channel on cathode exit region		Pa
density0	Density of air at standard state	1.2	kg/m ³
density_a	Density of anode gas		kg/m ³
density_a_ex	Density of anode gas in anode exit region		kg/m ³
density_a_in	Density of anode gas in anode inlet region		kg/m ³

density_avg_a	Average density of anode gas		kg/m ³
density_avg_c	Average density of cathode air		kg/m ³
density_c	Density of cathode air		kg/m ³
density_c_ex	Density of cathode air in cathode exit region		kg/m ³
density_c_in	Density of cathode air in cathode inlet region		kg/m ³
density_conn	Density of interconnector	7640	kg/m ³
density_MEA	Density of MEA	6100	kg/m ³
Dh_a	Hydraulic diameter of anode channel		m
Dh_a_w	Hydraulic diameter of virtual channel in anode exit region		m
Dh_c	Hydraulic diameter of cathode channel		m
Dh_c_w	Hydraulic diameter of virtual channel in cathode inlet region		m
dt	Delta time		s
f1_ma~f4_ma	Parameters for Runge-Kutta (RK) calculation for mass flow rate of anode gas		
f1_mc~f4_mc	Parameters for RK calculation for mass flow rate of cathode air		
f1_TX~f4_TX	Parameters for RK calculation for temperature of each region, where X is each region		
f_La	Summation of friction coefficients of anode gas		
f_La_ex	Summation of friction coefficients of anode gas on anode exit region		
f_La_in	Summation of friction coefficients of anode gas on anode inlet region		
f_Lc	Summation of friction coefficients of cathode gas		
f_Lc_ex	Summation of friction coefficients of cathode gas on cathode exit region		
f_Lc_in	Summation of friction coefficients of cathode gas on cathode inlet region		
fa	Friction coefficient of anode gas		
fa_ex	Friction coefficient of anode gas on anode exit region		
fa_in	Friction coefficient of anode gas on anode inlet		

	region		
fc	Friction coefficients of cathode gas		
fc_ex	Friction coefficient of cathode gas on cathode exit region		
fc_in	Friction coefficient of cathode gas on cathode inlet region		
h_a	Convective heat coefficient of anode gas		W/m ² /K
h_a_ex	Convective heat coefficient of anode gas on anode exit region		W/m ² /K
h_a_in	Convective heat coefficient of anode gas on anode inlet region		W/m ² /K
h_c	Convective heat coefficient of cathode gas		W/m ² /K
h_c_ex	Convective heat coefficient of cathode gas on cathode exit region		W/m ² /K
h_c_in	Convective heat coefficient of cathode gas on cathode inlet region		W/m ² /K
Height_a	Height of anode channel	0.001	m
Height_c	Height of cathode channel	0.002	m
i_flow_control	Parameter for blower operating mode control	1	
i_max_flow	Parameter for blower operating mode control		
i_speed_control	Parameter for blower operating mode control	0	
iStep	Number of step		
k_conn	Thermal conductivity of interconnector	21.4	W/m/K
k_MEA	Thermal conductivity of MEA	2.6	W/m/K
ka1~ka3	Regression constants for air		
L_m	Vertical length for outer solid structure on cathode inlet side	0.0666	m
L_r	Vertical length for cathode exit side	0.0286	m
L_w	Vertical length for cathode inlet side	0.0286	m
L_x	Horizontal length for reaction region	0.1	m
L_y	Vertical length for reaction region	0.2	m
L_z	Vertical length for outer solid structure on cathode exit side	0.0666	m
m1_a	Parameters for Runge-Kutta (RK) calculation for		

	mass flow rate of anode gas		
m1_c	Parameters for RK calculation for mass flow rate of cathode air		
ma	Mass flow rate of anode gas		
ma_dot	ma/dt		
matotal	Total mass flow rate of anode gas		
mc	Mass flow rate of cathode air		
mc_dot	mc/dt		
mctotal	Total mass flow rate of cathode air		
mctotal_set	Setting mass flow rate of cathode air	0.003	kg/s
mdot_avg	Average of mass flow rate		
N_k	Number of control volume along k-coordinate	4	
N_m	Number of control volume along m-coordinate	6	
N_r	Number of control volume along r-coordinate	4	
N_stack_cell	Number of stacks for designed power output		
N_w	Number of control volume along w-coordinate	4	
N_x	Number of control volume along x-coordinate	10	
N_y	Number of control volume along y-coordinate	20	
N_z	Number of control volume along z-coordinate	6	
Ncycle	Parameter for deciding operating time		
Ncycle_write	Number of time frame shot of monitor output		
No_frame_shot	Number of frame shot for monitor output		10
No_out	Number of RK calculation		500
No_print	Number of data saving		500
No_step	Parameter for defining dt		400
omega_t	1/ts		1/s
p1~p6	Regression constants for air Prandtl number		
P_avg_a	Average pressure of anode gas		Pa
P_avg_c	Average pressure of cathode air		Pa
P_exit_a	Exit pressure of anode gas		Pa
P_exit_c	Exit pressure of cathode air		Pa
P_inlet_a	Inlet pressure of anode gas		Pa
P_inlet_c	Inlet pressure of cathode air		Pa

Pa	Pressure of anode gas		
Pa_ex	Pressure of anode gas on anode exit region		
Pa_in	Pressure of anode gas on anode inlet region		
Pc	Pressure of cathode air		
Pc_ex	Pressure of cathode air on cathode exit region		
Pc_in	Pressure of cathode air on cathode inlet region		
Perimeter_a	Perimeter of anode channel		m
Perimeter_a_w	Perimeter of virtual anode channel on anode exit region		m
Perimeter_c	Perimeter of cathode channel		m
Perimeter_c_w	Perimeter of virtual cathode channel on cathode inlet region		m
Power	Output of designed SOFC	1000	W
Q_anode_riba	Convective heat transfer between anode gas and rib on anode side		W
Q_cathode_conn	Convective heat transfer between cathode air and interconnector		W
Q_cathode_MEA	Convective heat transfer between cathode air and MEA		W
Q_cathode_ribc	Convective heat transfer between cathode air and rib on cathode side		W
Q_conn_anode	Convective heat transfer between interconnector and anode gas		W
Q_MEA_anode	Convective heat transfer between MEA and anode gas		W
Rgas_a	Gas constant of anode gas		J/kg/K
Rgas_c	Gas constant of cathode air		J/kg/K
T1_X	Parameters for Runge-Kutta (RK) calculation for each region, where X is each region		
t_actual	Actual physical operating time		s
TX	Nondimensional temperature for each region, where X is each region		
TX_dot	Nondimensional temperature gradient for each region, where X is each region		

tend	Total simulational time		s
thickness_conn	Thickness of interconnector	0.001	m
thickness_MEA	Thickness of MEA	0.00028	m
thickness_rib	Thickness of rib	0.002	m
thickness_s	Thickness of outer solid structure	0.00428	m
Tmax_SS	Maximum temperature of outer solid structure		K
Tmin_anode	Minimum temperature of anode gas		K
Tmin_SS	Minimum temperature of outer solid structure		K
ts	Residence time		
vis0	Dynamic viscosity of air		Pa.s
vis_a	Dynamic viscosity of anode gas		Pa.s
vis_a_ex	Dynamic viscosity of anode gas on anode exit region		Pa.s
vis_a_in	Dynamic viscosity of anode gas on anode inlet region		Pa.s
vis_c	Dynamic viscosity of cathode air		Pa.s
vis_c_ex	Dynamic viscosity of cathode air on cathode exit region		Pa.s
vis_c_in	Dynamic viscosity of cathode air on cathode inlet region		Pa.s
Volume_conn	Volume of a control volume of interconnector		m ³
Volume_conn_w	Volume of a control volume of interconnector on cathode air inlet region		m ³
Volume_MEA	Volume of a control volume of MEA		m ³
Volume_MEA_w	Volume of a control volume of MEA on cathode air inlet region		m ³
Volume_rib_a	Volume of a control volume of anode rib		m ³
Volume_rib_c	Volume of a control volume of cathode rib		m ³
Volume_s	Volume of a control volume of outer solid structure		m ³
Volume_s_m	Volume of a control volume of outer solid structure on cathode inlet region		m ³
Volume_s_w	Volume of a control volume of outer solid structure on cathode inlet region		m ³

W_FCS	Short length of solid structure	0.04	m
Width	Width of channel		m

b) All sub-routines

Sub-routines	Definitions
evaluate_channel_properties	To evaluate properties such as convective heat coefficient, specific heat, etc. for both anode and cathode channel
evaluate_entrance_properties	To evaluate properties for entrance of cathode air
evaluate_exit_properties	To evaluate properties for exit of cathode air
function()	1) Calculation of pressure and temperature 2) Calculation of all heat transfers 3) Definition of Partial Differential Equations (PDEs) such as energy equation and momentum equation by combining with continuity equation
get_max_temp	To find the maximal temperature of all solid structure
get_min_temp	To find the minimal temperature of all solid structure and anode inlet gas
main()	1) Definition of non-global variables 2) Reading input files 3) Initialization of global variables 4) Production of output file as results of running program 5) Monitor output to check a running status of program 6) 4 th order RK method for solving PDE by using while loop 7) Extra calculations such as heating energy, area, etc.

2) HEX module

a) Global variables

The common (shared) global variables with a different sub-module were skipped in the following table. The most different thing of this sub-module with SOFC stacking heating module is the subscript c and h, where c stands for cold air and h means hot air. While a stands for anode gas and c stands for cathode air in stack heating module.

Parameter	Definition	Value	Unit
alpha_fin	Thermal diffusivity of corrugated fin		m ² /s
alpha_mid	Thermal diffusivity of middle plate		m ² /s
Area_c	Channel area of cold air side		m ²
Area_h	Channel area of hot air side		m ²
C_fin	Specific heat of fin	460	J/kg/K
C_mid	Specific heat of mid	444	J/kg/K
del_h	Half of hypotenuse of each channel		m
Del_H	Nondimensional del_h		
delp_c	Pressure drop through cold air channel		Pa
delp_h	Pressure drop through hot air channel		Pa
density_fin	Density of fin	7169.094	kg/m ³
density_mid	Density of middle plate	8470	kg/m ³
h_n	Natural convection coefficient	4.0	W/m ² /K
Height_c	Height of cold air channel	0.0018	m
Height_h	Height of hot air channel	0.0018	m
Hypo_c	Length of hypotenuse of cold air channel		m
Hypo_h	Length of hypotenuse of hot air channel		m
k_fin	Thermal conductivity of fin	16.0	W/m/K
k_mid	Thermal conductivity of middle plate	26.1	W/m/K
L_k	Thickness of outer solid structure	0.0004	m
L_r	Length of entrance region of cold air	0.0189	m
L_w	Length of entrance region of hot air	0.0189	m
L_x	Horizontal length of HEX	0.0381	m
L_y	Vertical length of HEX	0.225	m
m1_c	Parameters for Runge-Kutta (RK) calculation for mass flow rate of cold air in upper channel		
m1_cd	Parameters for Runge-Kutta (RK) calculation for mass flow rate of cold air in lower channel		
m1_h	Parameters for Runge-Kutta (RK) calculation for mass flow rate of hot air in lower channel		
m1_hu	Parameters for Runge-Kutta (RK) calculation for mass flow rate of hot air in upper channel		
N_f	Number of inclined fins		

pc1~pc5	Regression constants for inlet pressure of cold air from experimental result		
Pc_old	Old value for pressure of cold air		
ph1~ph5	Regression constants for inlet pressure of hot air from experimental result		
Ph_old	Old value for pressure of hot air		
pr1~pr6	Regression constants for Prandtl number		
Q_con_cold	Convective heat transfer between interconnector and cold air		W
Q_hot_con	Convective heat transfer between hot air and interconnector		W
Q_hot_mid	Convective heat transfer between hot air and middle plate		W
Q_mid_cold	Convective heat transfer between middle plate and cold air		W
Q_wall_cold	Convective heat transfer between wall and cold air		W
Q_wall_hot	Convective heat transfer between wall and hot air		W
Rate_c	Correction ratio for heating input from cold air	0.7	
Rate_h	Correction ratio for heating input from hot air	1.3	
ratio_c	Area correction factor for cold air channel	0.98	
ratio_h	Area correction factor for hot air channel	1.02	
Res_duct	Flow resistance through channel		
T_initial	Initial temperature of HEX	25	°C
T_initial_non	Nondimensional initial temperature of HEX		
tc1~tc5	Regression constants for inlet temperature of cold air from experimental result		
Tc_inlet	Inlet temperature of cold air		°C
Tc_inlet_K	Inlet temperature of cold air with unit of Kelvin		K
Tc_inlet_non	Nondimensional inlet temperature of cold air		
th1~th7	Regression constants for inlet temperature of hot air from experimental result		
Th_inlet	Inlet temperature of hot air		°C

Th_inlet_K	Inlet temperature of hot air with unit of Kelvin		K
Th_inlet_non	Nondimensional inlet temperature of hot air		
thickness_fin	Thickness of fin	0.000102	m
thickness_mid	Thickness of middle plate	0.001905	m
thickness_wall	Thickness of wall	0.005505	m

b) All sub-routines

Sub-routines	Definitions
evaluate_channel_properties	To evaluate properties of both hot and cold air such as convective heat coefficient, specific heat, etc. as a function of temperature
function()	1) Calculation of all heat transfers 2) Calculation of pressure and temperature 3) Definition of Partial Differential Equations (PDEs) such as energy equation and momentum equation by combining with continuity equation
Gauss_Seidal_method	Finding pressure of cold air inside channels with respect to flow resistance of channel
Gauss_Seidal_method_air()	Finding pressure of hot air inside channels with respect to flow resistance of channel
main()	1) Definition of non-global variables 2) Reading input files 3) Reading experimental data at inlet for both temperature and pressure 4) Initialization of global variables 5) Production of output file as results of running program 6) Monitor output to check a running status of program 7) 4 th order RK method for solving PDE by using while loop 8) Extra calculations such as heating energy, area, etc.

3) CHER module

a) Global variables

The common (shared) global variables with a different sub-module were also skipped in the following table. The distinctive feature of this sub-module is the subscript c and h, where c stands for relatively cold reformat and h means hot air. While c stands for cold air and h stands for hot air in HEX module.

Parameter	Definition	Value	Unit
Act_energy_SR	Activation energy for SR reaction	-240100	J/mol
Act_energy_WGS	Activation energy for WGS reaction	-67130.0	J/mol
activity	Activity of reformat in upper channel		
activity_d	Activity of reformat in lower channel		
CE1	Molar flux coefficients going in		
CE2	Molar flux coefficients going out		
CE3	Stoichiometric coefficients of SR reaction		
CE4	Stoichiometric coefficients of WGS reaction		
Cp_gas_mix	Specific heat for constant pressure of gas mixture in upper channel		J/mol/K
Cp_gas_mix_inlet	Specific heat for constant pressure of gas mixture at inlet		J/mol/K
Cp_gas_mixed	Specific heat for constant pressure of gas mixture in lower channel		J/mol/K
Cp_gas_part	Specific heat for constant pressure of each gas in upper channel		J/mol/K
Cp_gas_part_inlet	Specific heat for constant pressure of each gas at inlet with considering mole fraction		J/mol/K
Cp_gas_partd	Specific heat for constant pressure of each gas in lower channel in lower channel		J/mol/K
Cp_inlet	Specific heat for constant pressure of each gas at inlet		J/mol/K
D_tube	Diameter of connecting tube between plenum & inlet	0.0127	m
enthalpy_rxn_SR	Reaction enthalpy of SR reaction		J/mol
enthalpy_rxn_WGS	Reaction enthalpy of WGS reaction		J/mol
entropy_rxn_SR	Reaction entropy of SR reaction		J/mol/K
entropy_rxn_WGS	Reaction entropy of WGS reaction		J/mol/K

fh	Friction coefficients of hot air in lower channel		
fhu	Friction coefficients of hot air in upper channel		
Gibbs_energy_SR	Gibbs energy for SR reaction		J/mol
Gibbs_energy_WGS	Gibbs energy for WS reaction		J/mol
Hf0	Enthalpy of formation of each component at standard state		J/mol
inlet_mass_fraction	Mass fraction at inlet		
k_reforming	Reaction rate of SR reaction in upper channel		mol/s
k_reforming_d	Reaction rate of SR reaction in lower channel		mol/s
k_shifting	Reaction rate of WGS in upper channel		mol/s
k_shifting_d	Reaction rate of WGS in lower channel		mol/s
Kp_reforming	Equilibrium constants of SR in upper channel		
Kp_reformingd	Equilibrium constants of SR in lower channel		
Kp_shifting	Equilibrium constants of WGS in upper channel		
Kp_shiftingd	Equilibrium constants of WGS in lower channel		
L_ct	Length of connecting tube	0.1	m
M	Molecular weight of each component		g/mol
M_air	Molecular weight of air	28.97	g/mol
mdot_CH4_inlet	Mass flow rate of CH ₄ at inlet		kg/s
mdot_H2O_inlet	Mass flow rate of H ₂ O at inlet		kg/s
Mgas_mix_inlet	Molecular weight of gas mixture at inlet		g/mol
molarity	Molarity		mol/L
molarity_flux_total_in	Total molarity flux going inward in upper channel		mol/L/s
molarity_flux_total_out	Total molarity flux going outward in upper channel		mol/L/s
molarity_flux_total_in	Total molarity flux going inward in lower channel		mol/L/s
molarity_flux_total_out	Total molarity flux going outward in lower channel		mol/L/s
molarity_total	Total molarity in upper channel		mol/L
molarity_total_inlet	Total molarity at inlet in upper channel		mol/L
molarity_totald	Total molarity in lower channel		mol/L
molarity_totald_inlet	Total molarity at inlet in lower channel		mol/L

molecular_interaction	Molecular interaction in upper channel		J/s
molecular_interaction_d	Molecular interaction in lower channel		J/s
mu	Viscosity of each gas in upper channel		g/cm/s
mud	Viscosity of each gas in lower channel		g/cm/s
mu_inlet	Viscosity of each gas at inlet		g/cm/s
mumix	Viscosity of each gas with molar fraction in upper channel		g/cm/s
ndot_CH4_inlet	Mole flow rate of CH ₄ at inlet		mol/s
ndot_H2O_inlet	Mole flow rate of H ₂ O at inlet		mol/s
omega	Intermittent variable to find the viscosity of each gas in upper channel		g/cm/s
omega_inlet	Intermittent variable to find the viscosity of each gas at inlet		g/cm/s
omegad	Intermittent variable to find the viscosity of each gas in lower channel		g/cm/s
P_plenum_c	Pressure of plenum on reformat side	1000	Pa
P_plenum_c_non	Nondimensional plenum pressure of reformat		
P_plenum_h	Pressure of plenum on hot air side	1000	Pa
P_plenum_h_non	Nondimensional plenum pressure of hot air		
P_cr	Critical pressure of each species		Pa
phiab	Intermittent variable to find the viscosity of gas mixture in upper channel		
power_SR	Power index for pre-exponential factor of SR	15	
power_WGS	Power index for pre-exponential factor of WGS	6	
pre_exp_factor_SR	Coefficient of pre-exponential factor of SR	4.225	mol/s
pre_exp_factor_WGS	Coefficient of pre-exponential factor of WGS	1.955	mol/s
product	Intermittent variable to find the viscosity of gas mixture in upper channel		
product_inlet	Intermittent variable to find the viscosity of gas mixture at inlet		
productd	Intermittent variable to find the viscosity of gas mixture in lower channel		

productym	Summation of molar fraction of each gas times molecular weight of each gas in upper channel		g/mol
Productym_inlet	Summation of molar fraction of each gas times molecular weight of each gas at inlet		g/mol
productymd	Summation of molar fraction of each gas times molecular weight of each gas in lower channel		g/mol
R_univ	Universal gas constant	8.314	J/mol/K
Reforming_rate	Reforming rate of SR reaction in upper channel		mol/s
Reforming_rated	Reforming rate of SR reaction in lower channel		mol/s
Res_duct	Resistance of channel		
Res_tube_h	Flow resistance of tube for hot air		
Res_tube_c	Flow resistance of tube for reformat gas		
Rgas	Gas constant of each gas		J/kg/K
Rgas_inlet	Gas constant of each gas at inlet		J/kg/K
Rgas_mix	Gas constant of gas mixture in upper channel		J/kg/K
Rgas_mixd	Gas constant of gas mixture in lower channel		J/kg/K
Rgas_mix_part	Gas constant of gas mixture in upper channel times molar fraction		J/kg/K
Rgas_mix_partd	Gas constant of gas mixture in lower channel times molar fraction		J/kg/K
Sf0	Entropy of formation of each component at standard state		J/mol/K
Shifting_rate	Shifting rate of WGS reaction in upper channel		mol/s
Shifting_rated	Shifting rate of WGS reaction in lower channel		mol/s
sigma_1	Intermittent variable to find the viscosity of gas mixture in upper channel		
sigma_1d	Intermittent variable to find the viscosity of gas mixture in lower channel		
STCR	Steam to Carbon Ratio		
sum	Summation of product		
sumd	Summation of productd		
T_cr	Critical temperature of each species		K
T_star	Intermittent temperature to calculate viscosity		
Volume_liters	Volume of a control volume in liter unit		

y	Molar fractions in upper channel of CHER		
y_CH4	Initial molar fraction of CH ₄ at inlet		
y_H2O	Initial molar fraction of H ₂ O at inlet		
y_inlet	Mole fraction at inlet		
y_d	Molar fractions in lower channel of CHER		

b) All sub-routines

Sub-routines	Definitions
evaluate_properties()	Evaluation of properties of hot air such as convective heat coefficient, specific heat, etc. as a function of temperature
find_activities()	Finding of activities of each gas species for both upper and lower channel of reformat
find_convection()	To find molecular interaction (convective heat transfer) between fin and reformat gas
find_flux_terms()	To find productym and the total molar flux going in and out of control volume
find_gas_properties()	To find the specific heat for constant volume and pressure of each gas component and gas mixture
find_inlet_properties()	To find properties such as viscosity and specific heat for constant volume and pressure of each gas component and gas mixture at inlet
find_reaction_parameters()	To find reaction rate and equilibrium constant of both SR and WGS reaction
find_reforming_shifting_reaction_rates()	To find reforming rate and shifting rate of both SR and WGS reaction
find_viscosity()	To find viscosity of reformat inside both upper and lower channel
function()	1) Calculation of all heat transfers 2) Calculation of enthalpy in and out 3) Definition of Partial Differential Equations (PDEs) such as molarity equation and energy equation
Gauss_Seidal_method()	Finding pressure of gas mixture inside channels with respect to flow resistance of channel

Gauss_Seidal_method_air()	Finding pressure of hot air inside channels with respect to flow resistance of channel
Gibbs_energy_calculation()	Gibbs energy calculation for both SR and WGS reaction
main()	1) Definition of non-global variables 2) Reading input files 3) Initialization of global variables 4) Production of output file as results of running program 5) Molar fraction calculation from molarity and total molarity 6) Monitor output to check a running status of program 7) 4 th order RK method for solving PDE by using while loop 8) Extra calculations such as mass flow rate, heating energy, area, etc.

4) SOFC electric power generation mode

a) Global variables

The common (shared) global variables with a different sub-module were also skipped in the following table. The distinctive feature of this sub-module is electric power generation. Many new variables related to power generation were added in this sub-module.

Parameter	Definition	Value	Unit
CE5	Stoichiometric coefficients of H ₂ and H ₂ O for electricity generation reaction		
CE6	Stoichiometric coefficients of O ₂ for electricity generation reaction		
Con_an	Conductivity of anode		S/cm
Con_an_elec	Conductivity of electrolyte on anode side		S/cm
Con_an_rib	Conductivity of GDL on anode side		S/cm
Con_ca	Conductivity of cathode		S/cm
Con_ca_elec	Conductivity of electrolyte on cathode side		S/cm
Con_ca_rib	Conductivity of GDL on cathode side		S/cm
Con_elec	Conductivity of electrolyte		S/cm
Con_k	Conductivity of repetitive bipolar plate		S/cm
Con_mono_an	Conductivity of mono-polar plate on anode side		S/cm

Con_mono_ca	Conductivity of mono-polar plate on cathode side		S/cm
Cp_a_ex_kg	Specific heat for constant pressure of anode gas (kg unit) which is going out of channel		J/kg/K
Cp_a_ex_mol	Specific heat for constant pressure of anode gas (mol unit) which is going out of channel		J/mol/K
Cp_a_in_kg	Specific heat for constant pressure of anode gas (kg unit) which is going into channel		J/kg/K
Cp_a_in_mol	Specific heat for constant pressure of anode gas (mol unit) which is going into channel		J/mol/K
Cp_a_kg	Specific heat for constant pressure of anode gas (kg unit)		J/kg/K
Cp_a_mol	Specific heat for constant pressure of anode gas (mol unit)		J/mol/K
Cp_ex_kg	Specific heat for constant pressure of each gas (kg unit) which is going out of channel		J/kg/K
Cp_ex_mol	Specific heat for constant pressure of each gas (mol unit) which is going out of channel		J/mol/K
Cp_gas_part	Specific heat for constant pressure of each gas (mol unit) after multiplying mole fraction		J/mol/K
Cp_gas_part_ex	Specific heat for constant pressure of each gas (mol unit) after multiplying mole fraction at exit		J/mol/K
Cp_gas_part_ex_kg	Specific heat for constant pressure of each gas (kg unit) after multiplying mole fraction at exit		J/kg/K
Cp_gas_part_in	Specific heat for constant pressure of each gas (mol unit) after multiplying mole fraction at inlet		J/mol/K
Cp_gas_part_in_kg	Specific heat for constant pressure of each gas (kg unit) after multiplying mole fraction at inlet		J/kg/K
Cp_gas_part_kg	Specific heat for constant pressure of each gas (kg unit) after multiplying mole fraction		J/kg/K
Cp_H2_amb	Specific heat of H ₂ at ambient temperature		kJ/kg/K
Cp_H2O_amb	Specific heat of H ₂ O at ambient temperature		kJ/kg/K
Cp_O2_amb	Specific heat of O ₂ at ambient temperature		kJ/kg/K
Cp_in_kg	Specific heat for constant pressure of each gas		J/kg/K

	(kg unit) which is going into channel		
Cp_in_mol	Specific heat for constant pressure of each gas (mol unit) which is going into channel		J/mol/K
Cp_kg	Specific heat for constant pressure of each gas (kg unit) in channel		J/kg/K
Cp_mol	Specific heat for constant pressure of each gas (mol unit) in channel		J/mol/K
Cv_a_ex_mol	Specific heat for constant volume of anode gas (mol unit) which is going out of channel		J/mol/K
Cv_a_in_mol	Specific heat for constant volume of anode gas (mol unit) which is going into channel		J/mol/K
Cv_a_mol	Specific heat for constant volume of anode gas (mol unit)		J/mol/K
Cv_ex_mol	Specific heat for constant volume of each gas (mol unit) which is going out of channel		J/mol/K
Cv_gas_part	Specific heat for constant volume of each gas (mol unit) after multiplying mole fraction		J/mol/K
Cv_gas_part_ex	Specific heat for constant volume of each gas (mol unit) after multiplying mole fraction at exit		J/mol/K
Cv_gas_part_ex_kg	Specific heat for constant volume of each gas (kg unit) after multiplying mole fraction at exit		J/kg/K
Cv_gas_part_in	Specific heat for constant volume of each gas (mol unit) after multiplying mole fraction at inlet		J/mol/K
Cv_gas_part_in_kg	Specific heat for constant volume of each gas (kg unit) after multiplying mole fraction at inlet		J/kg/K
Cv_mol	Specific heat for constant volume of each gas (mol unit) in channel		J/mol/K
del_x_cm	Horizontal length of a control volume for active region in cm unit		cm
del_y_cm	Vertical length of a control volume for active region in cm unit		cm
F	Faraday constant	96485	C/mol
G_rxn	Gibbs energy of formation		J/mol
h_rxn	Reaction enthalpy		J/mol

hf0_H2	Enthalpy of formation of H ₂ at the standard state	0.0	J/mol
hf0_H2O	Enthalpy of formation of H ₂ O at the standard state	-241814	J/mol
Hf0_O2	Enthalpy of formation of O ₂ at the standard state	0.0	J/mol
hf_H2	Enthalpy of formation of H ₂ at a given state		J/mol
hf_H2O	Enthalpy of formation of H ₂ O at a given state		J/mol
hf_O2	Enthalpy of formation of O ₂ at a given state		J/mol
hs_H2	Sensible enthalpy of H ₂ at a given state		J/mol
hs_H2O	Sensible enthalpy of H ₂ O at a given state		J/mol
hs_O2	Sensible enthalpy of O ₂ at a given state		J/mol
i_elec	Current that flows through cell		A
inlet_mass_fraction	Mass fraction of each gas at inlet		
Mgas_mix_inlet	Molecular weight of mixed gas at inlet		g/mol
molarity_flux_total_inlet_in	Total molarity flux going inward at inlet		mol/L/s
molarity_flux_total_inlet_out	Total molarity flux going outward at inlet		mol/L/s
molarity_flux_total_outlet_in	Total molarity flux going inward at outlet		mol/L/s
molarity_flux_total_outlet_out	Total molarity flux going outward at outlet		mol/L/s
mu_ex	Viscosity of each gas at exit region		g/cm/s
mu_in	Viscosity of each gas at inlet region		g/cm/s
mumix_ex	Viscosity of each gas with molar fraction at exit region		g/cm/s
mumix_in	Viscosity of each gas with molar fraction at inlet region		g/cm/s
Ohm_act_a	Activation resistance on anode side		$\Omega \cdot \text{cm}^2$
Ohm_act_c	Activation resistance on cathode side		$\Omega \cdot \text{cm}^2$
omega_ex	Intermittent variable to find the viscosity of each gas at exit region		g/cm/s
omega_in	Intermittent variable to find the viscosity of		g/cm/s

	each gas at inlet region		
phiab_ex	Intermittent variable to find the viscosity of gas mixture at exit region		
phiab_in	Intermittent variable to find the viscosity of gas mixture at inlet region		
R_an	Resistivity of anode		
R_an_elec	Resistivity of electrolyte on anode side		$\Omega \cdot \text{cm}$
R_an_rib	Resistivity of GDL on anode side		$\Omega \cdot \text{cm}$
R_ca	Resistivity of cathode		$\Omega \cdot \text{cm}$
R_ca_elec	Resistivity of electrolyte on cathode side		$\Omega \cdot \text{cm}$
R_ca_rib	Resistivity of GDL on cathode side		$\Omega \cdot \text{cm}$
R_elec	Resistivity of electrolyte		$\Omega \cdot \text{cm}$
R_k	Resistivity of repetitive bipolar plate		$\Omega \cdot \text{cm}$
R_mono_an	Resistivity of mono-polar plate on anode side		$\Omega \cdot \text{cm}$
R_mono_ca	Resistivity of mono-polar plate on cathode side		$\Omega \cdot \text{cm}$
RC_an_elec	Contact Resistance between anode and electrolyte		$\Omega \cdot \text{cm}^2$
RC_ca_elec	Contact Resistance between cathode and electrolyte		$\Omega \cdot \text{cm}^2$
RC_GDL_an	Contact Resistance between GDL and anode		$\Omega \cdot \text{cm}^2$
RC_GDL_ca	Contact Resistance between GDL and cathode		$\Omega \cdot \text{cm}^2$
RC_ma_GDL	Contact Resistance between plate on anode side and GDL		$\Omega \cdot \text{cm}^2$
RC_mc_GDL	Contact Resistance between plate on cathode side and GDL		$\Omega \cdot \text{cm}^2$
Rgas_mix_ex	Gas constant of gas mixture at exit		J/kg/K
Rgas_mix_in	Gas constant of gas mixture at inlet		J/kg/K
Rgas_mix_part_ex	Gas constant of gas mixture at exit times molar fraction		J/kg/K
Rgas_mix_part_in	Gas constant of gas mixture at inlet times molar fraction		J/kg/K
s0_H2	Entropy of H ₂ at the standard state	130.7	J/mol/K
s0_H2O	Entropy of H ₂ O at the standard state	188.8	J/mol/K
s0_O2	Entropy of O ₂ at the standard state	205.1	J/mol/K

s_H2	Entropy of H ₂ at a given state		J/mol/K
s_H2O	Entropy of H ₂ O at a given state		J/mol/K
s_O2	Entropy of O ₂ at a given state		J/mol/K
s_rxn	Reaction entropy		J/mol/K
sigma_1_ex	Intermittent variable to find the viscosity of gas mixture at exit		
sigma_1_in	Intermittent variable to find the viscosity of gas mixture at inlet		
sum_ex	Summation of product at exit		
sum_in	Summation of product at inlet		
T_star_ex	Intermittent temperature to calculate viscosity at exit		
T_star_in	Intermittent temperature to calculate viscosity at inlet		
V_act	Activation loss of cell		V
V_act_a	Activation loss on anode side		V
V_act_c	Activation loss on cathode side		V
V_an	Voltage of anode		V
V_X_old	Voltage of X at the previous time step		V
V_an_elec	Voltage of electrolyte on anode side		V
V_an_rib	Voltage of anode rib (GDL)		V
V_ca	Voltage of cathode		V
V_ca_elec	Voltage of electrolyte on cathode side		V
V_ca_rib	Voltage of cathode rib (GDL)		V
V_g	Reversible voltage		V
V_k	Voltage of repetitive bipolar plate		V
V_mono_an	Voltage of mono-polar plate on anode side		V
V_mono_ca	Voltage of mono-polar plate on anode side		V
V_rev_cell	Reversible cell voltage		V
y_ex	Molar fractions at exit region		
y_in	Molar fractions at inlet region		

b) All sub-routines

Sub-routines	Definitions
activation_loss()	Evaluation of activation loss of cell
contact_resistance()	Calculation of contact and ionic resistances
current_calculation()	Calculation of current density of cell
evaluate_channel_properties()	Evaluation of properties of hot air such as convective heat coefficient, specific heat, etc. as a function of temperature
find_flux_terms_inlet()	To find productym and the total molar flux going at inlet
find_flux_terms_outlet()	To find productym and the total molar flux going at outlet
find_reformate_entrance_specific_heat()	To find the specific heat of gas mixture (reformate) at inlet
find_reformate_entrance_viscosity()	To find viscosity of reformate at inlet
find_reformate_exit_specific_heat()	To find the specific heat of gas mixture (reformate) at outlet
find_reformate_exit_viscosity()	To find viscosity of reformate at outlet
function_e()	This function is the similar with function(), but this function is for electricity production mode 1) Calculation of all heat transfers 2) Calculation of enthalpy in and out 3) Definition of Partial Differential Equations (PDEs) such as molarity equation and energy equation
get_voltage()	With Gauss-Seidal method, calculation of all voltage distributions
monitor_output()	For monitor output of electricity production module
reformate_entrance_properties()	To find the convective heat transfer coefficient of gas mixture (reformate) at inlet
reformate_exit_properties()	To find the convective heat transfer coefficient of gas mixture (reformate) at outlet
resistivity()	Calculation of each resistivity with conductivity
reversible_voltage()	Calculation of reversible cell voltage
save_data_file()	For saving output data of voltage, current, etc.
update_resistance()	Update of contact resistance including ohmic losses

Appendix D

The HEX Experimental Set-up

This appendix summarizes experimental setup procedures and instructions for the operation of the HEX test rig. Procedures for the hardware wire connection and alignment, and instrumentation specifications were introduced.

Air Preheater

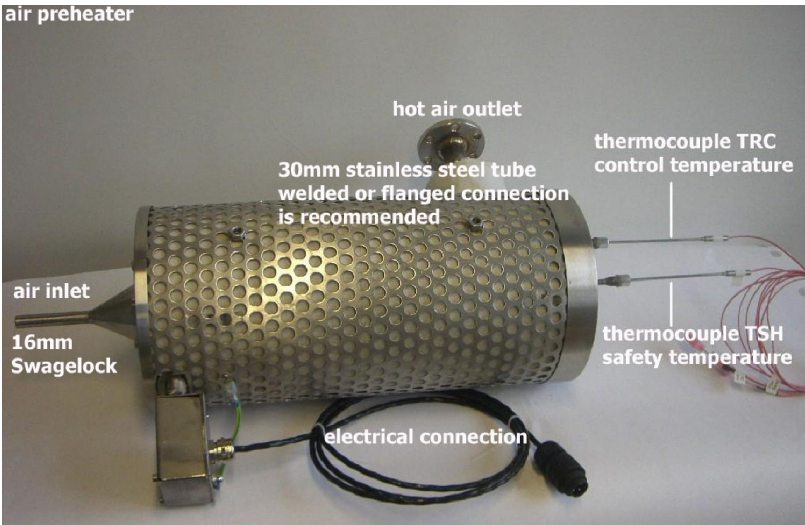


Figure D. 1 Electrical Air Preheater with indication of air inlet, air outlet, electrical connections as well as thermocouples for control and safety

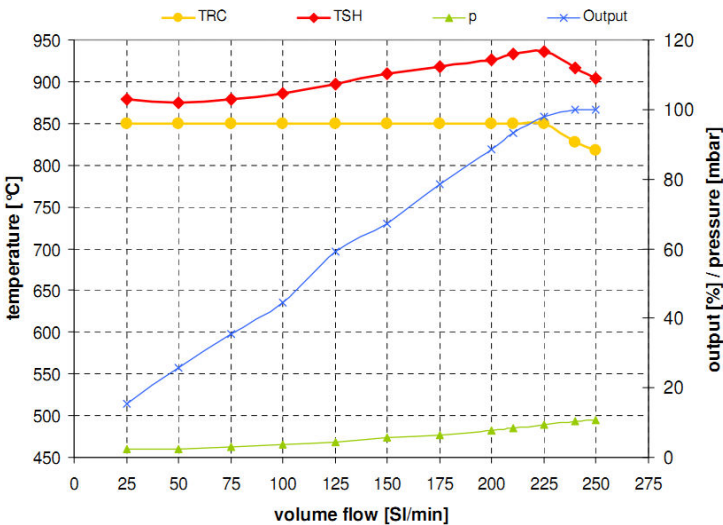


Figure D. 2 Characteristic curve of air preheater

Figure D. 1 shows the electrical air preheater with an indication of the air inlet, air outlet, electrical connections as well as thermocouples for temperature control and safety. Mass flow rate range of the air is between 25~250 SLPM. With respect to various mass/volume flow rates, the temperature of TRC, TSH, output temperature, percentage output, and pressure were shown in Figure D. 2. The air preheater has been installed as close as possible to the inlet of the HEX, since heat loss at small flow rates drastically decreases the fluid temperature. Precise wiring procedures will be explained in the electrical cabinet section. The operation limits and gradients that are given in Table D. 1 must not be exceeded.

Table D. 1 Maximal allowed gradients and operation limits

Parameter change	Operation limit	Remark
Flow rate	20 SLPM	Prevents temperature over shooting
Heat up temperature rate	20 K/min < 700°C	
	10 K/min > 700°C	
Max. heater temperature	965 °C	Temperature safeguard (TSH)
Max. gas temperature	850 °C	Control temperature (TRC)

Electric cabinet

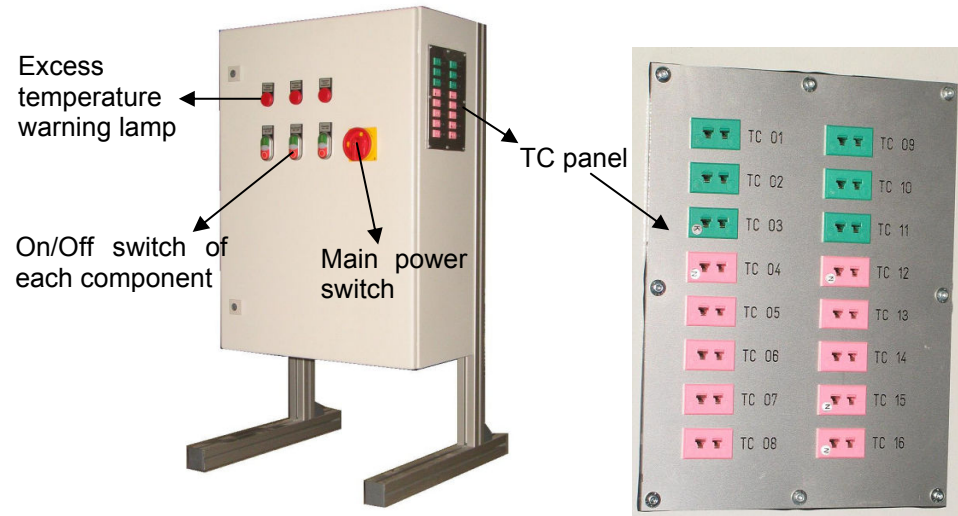


Figure D. 3 Electric cabinet and an enlarged view of TC panel

The test rig is equipped with thermocouples for the control and safety management system as well as for measuring tasks. All thermocouples are connected to the measurement system via a connecting Thermocouple (TC) panel inside the test rig. Access to the TC panel is possible on the right side of the cabinet as shown in Figure D. 3.

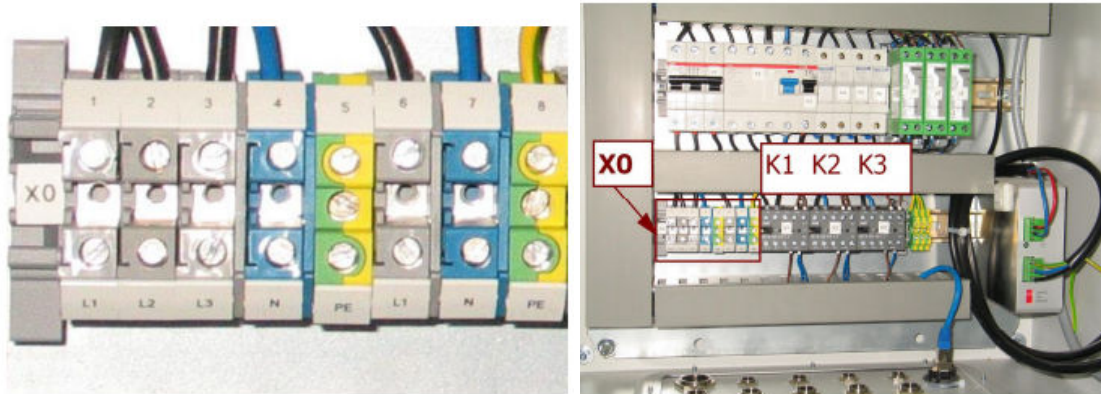


Figure D. 4 Terminals on X0 (Left) and Position of X0, K1, K2, and K3 (Right)

Table D. 2 Overview of cabling

Device 1	To Device 2	Details
Power supply components	Grid	277V/480V, 3 × 16A
Power supply cabinet	Grid	120V, 1 × 16A
Contactors K1:2 and K1:4 terminal + PE (protective earth)	Air preheater	480V (L1 and L2), 6.1kW
Contactors K2:3 and K2:4 terminal + PE (protective earth)	Gas preheater	277V (L3 and N), 1.9kW
Contactors K3:3 and K3:4 terminal + PE (protective earth)	Evaporator	277V (L3 and N), 0.75kW

Each component such as the air preheater, gas preheater and evaporator needs electric power, which is provided by the proper cabling with the electric cabinet. Figure D. 4 and Table D. 2 show names, positions of each contactor terminal, and an overview of the cabling. For more details of the electric wiring of the cabinet, have a look to the schematic in Figure D. 5.

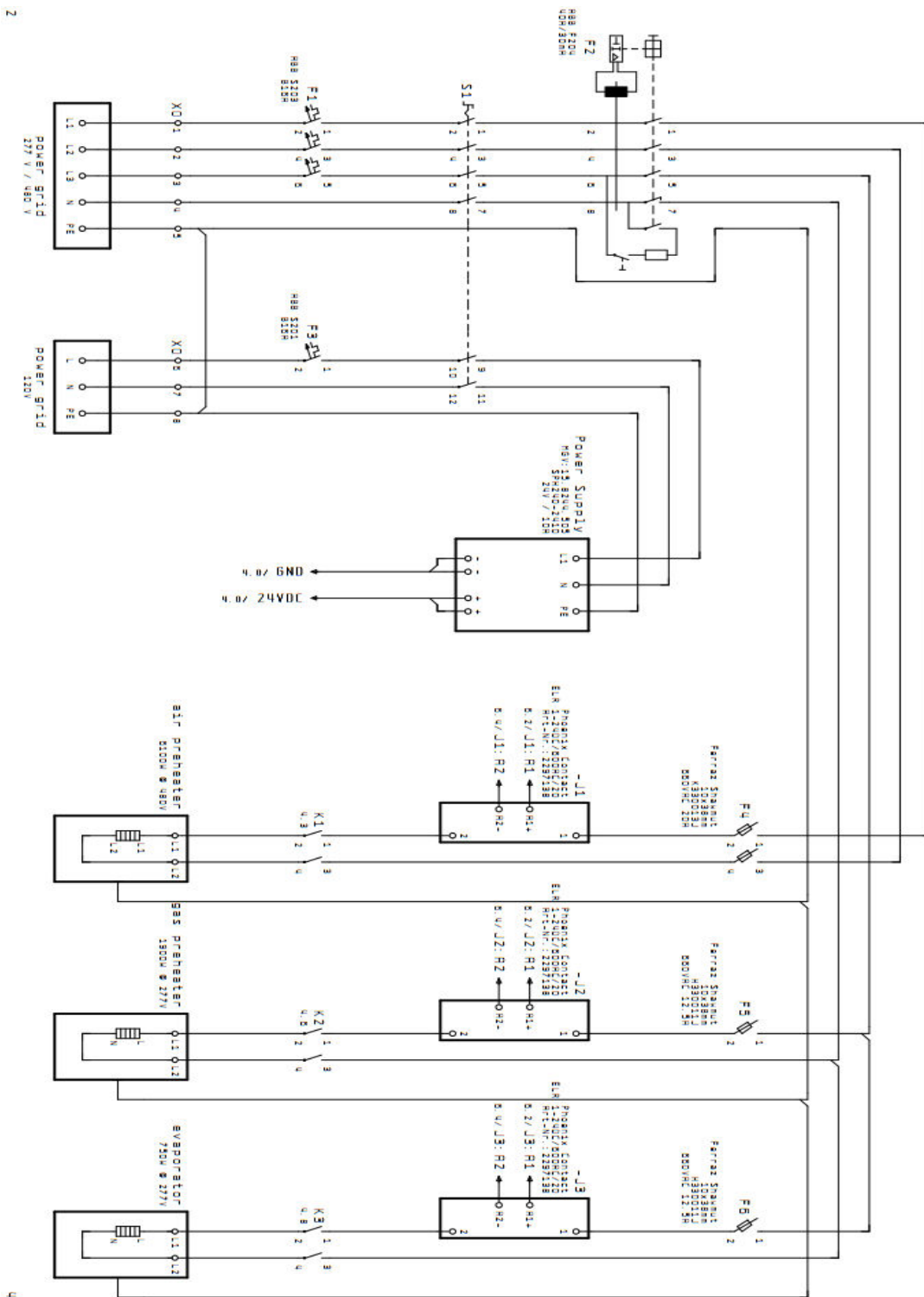


Figure D. 5 120V and 277/480V networks

Table D. 3 shows the overview of temperature measurement using the electric cabinet. Except listed slots in Table D. 3, remaining slots are free to be used by other TCs.

Table D. 3 Overview of temperature measurement

Location	PID name	TC Type	TC Type
Control temperature evaporator	TRC evaporator	K	TC 01
Steam temperature evaporator outlet	TR steam	K	TC 02
Control temperature air preheater	TRC air preheater	N	TC 04
Control temperature gas preheater	TRC gas preheater	N	TC 05
Evaporator safety temperature	Safety TC evaporator	K	TC 09
Air preheater safety temperature	Safety TC air preheater	N	TC 12
Gas preheater safety temperature	Safety TC gas preheater	N	TC 13

Appendix E

The CHER Experimental Set-up

This appendix summarizes the experimental setup procedures and instructions for the operation of the CHER test rig. The procedures for the hardware wire connection and alignment, and instrumentation specifications were introduced.

Gas preheater

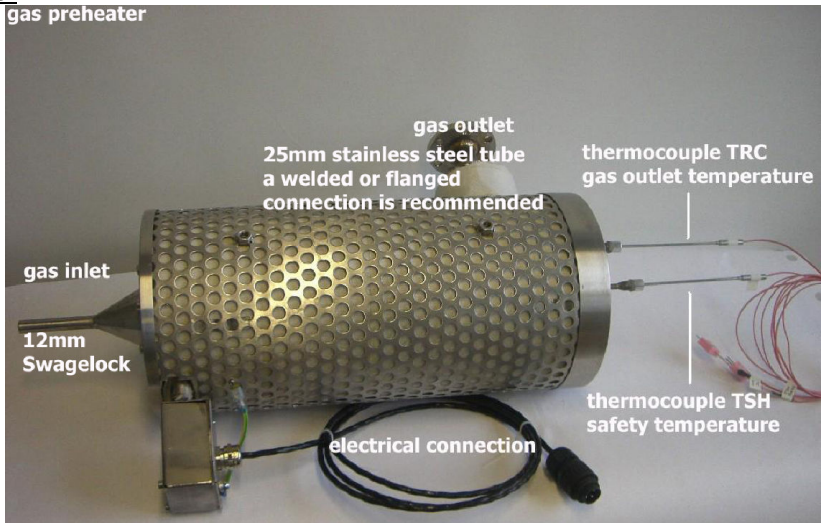


Figure E. 1 Electrical Gas Preheater with indication of gas inlet, gas outlet, electrical connections as well as thermocouples for control and safety

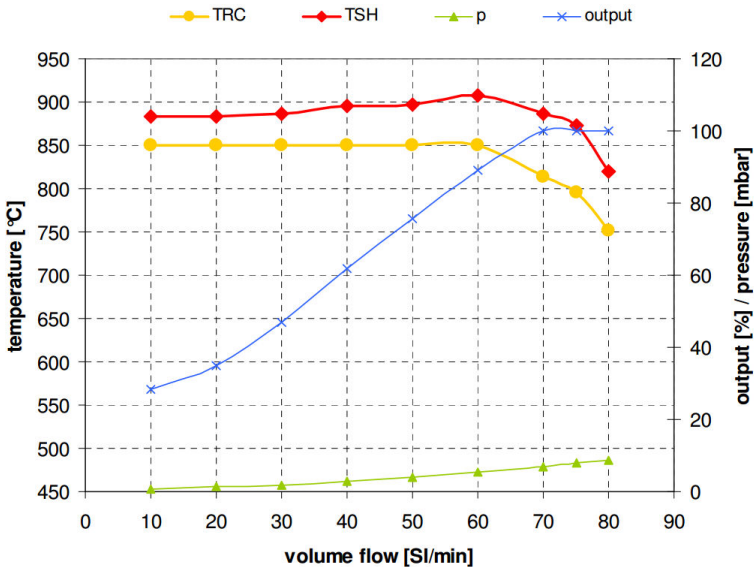


Figure E. 2 Characteristic curve of air preheater

Figure E. 1 shows the electrical gas preheater with indication of gas inlet, gas outlet, electrical connections as well as thermocouples for control and safety. The volume flow rate range for the device is between 10~80 SLPM. With respect to various mass/volume flow rates, the temperature of TRC, TSH, output temperature, and controller output were shown in Figure E. 2. The gas preheater has been installed as close as possible to the air inlet of the CHER, since heat loss at small flow rates drastically decreases the fluid temperature. Precise wiring procedures were explained in the electrical cabinet section in Appendix D.

Water metering pump

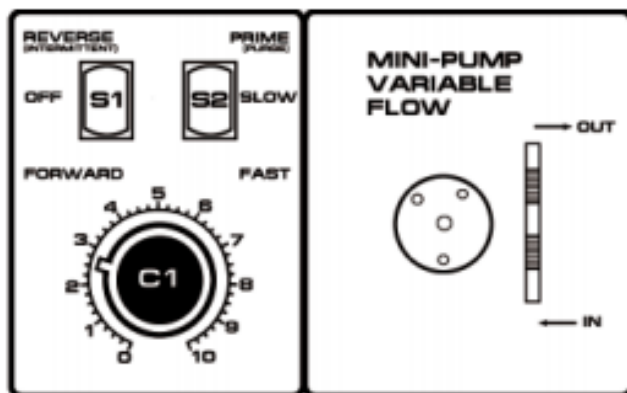


Figure E. 3 Control Panel of Variable-Speed Peristaltic Tubing Pump (S1: Power/Direction switch; S2: Pump speed switch; C1: Variable flow control)

Figure E. 3 shows compact, variable-flow, bi-directional, self-priming, peristaltic tubing pump that offers precise flow deliveries. Using a power/direction switch, three functions (selecting forward, reverse, and power off) are possible. It provides outstanding flow control and flexibility for transferring and dosing liquids. Fluid contacts only the tubing for contamination-free pumping. Temperature range of fluids is from -80 to -500°F (-62 to 260°C). The 120-VAC CSA-approved wall power supply ensures that a safe 12 volts drive the pump motor. Flow rates are from 0.005 milliliters per minute to 600 milliliters per minute. Variable-speed flow control and six different tubing sizes provide fine resolution with a wide flow range. The revolution of one roller delivers a precise measured volume specific to the tubing size and motor speed. It may be used

with up to 120 feet of tubing for remote sampling. Table E. 1 shows approximate flow rates for different ID and length of tubing.

For the application of an evaporator, a 1/4" tubing ID was selected because around 0.1g/sec (6 ml/min) mass flow rate, according to the capacity of evaporator was chosen to supply the steam for the evaporator inlet.

Table E. 1 Tubing dimensions for various mass flow rates

Tubing ID	Approximate Tubing length	Approximate Flow Rate
1/50", 0.5mm	3.25", 83mm	0.03~0.06 ml/min
1/32", 0.8mm	3.5", 89mm	0.04~0.14 ml/min
1/16", 1.6mm	4.25", 108mm	0.25~0.8 ml/min
3/32", 2.4mm	4.5", 114mm	0.4~1.7 ml/min
3/16", 4.8mm	5.0", 127mm	1.7~4.6 ml/min
1/4", 6.4mm	4.375", 111mm	1.8~8.2 ml/min

As shown in Figure E. 3, variable flow control is possible to vary the mass flow rate with this type of pump. However, a precise mass flow is not available although changing the mass flow rate is achievable. Therefore, a straightforward experiment was performed to find out the exact mass flow rate for each flow speed number on the control panel. For this experiment, a precise digital scale and a stopwatch were used to measure mass flow rate of distilled water for one minute at each flow speed from 0 to 10. Table E. 2 shows the exact mass flow rate for each flow speed of C1 knob with the fast mode of S2 switch in Figure E. 3. As a result, the specific speed rates (0 ~ 3) are available for the evaporator (30~350 g/hr).

Table E. 2 Digital mass flow rate for each flow speed of C1 knob

Speed	gram/minute	gram/second
0	4.956	0.0826
1	5.483	0.0914
2	5.809	0.0968
3	5.959	0.0993
4	6.459	0.1077
5	7.240	0.1207
6	7.584	0.1264
7	7.861	0.1310
8	8.210	0.1368
9	8.691	0.1449
10	9.106	0.1518

Evaporator

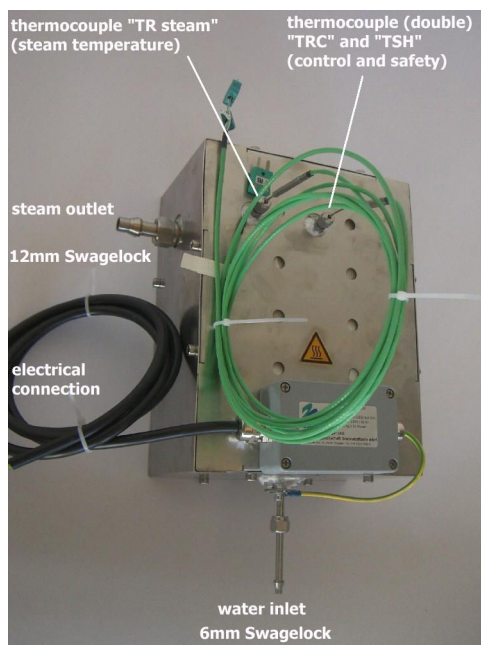


Figure E. 4 Evaporator with indication of water inlet, steam outlet, electrical connections as well as thermocouples for control and safety

Figure E. 4 shows the evaporator with indication of water inlet, steam outlet, electrical connections as well as thermocouples for control and safety. The evaporator has to be operated in a vertical position with the cold inlet at the bottom. The operation limits and gradients in Table E. 3 must not be exceeded.

Table E. 3 Maximal allowed gradients and operation limits

Parameter change	Operation limit	Remark
Gradient flow rate	10 (g/h)/min	For > 50g/hour
Flow rate	30 g/hour	Minimal flow rate
Flow rate	350 g/hour	Maximal flow rate
Heat up temperature	15K/min	
Max. heater temperature	500 °C	Temperature safeguard

If the steam supply has to be changed, it is recommend performing small steps with some hold times in order to always guarantee a correct steam-to-carbon ratio in the reforming process. In order to keep the functioning of the heating elements, it is recommended not to pass 300°C heater temperature if the evaporator is operated without flow supply.

Mass flow rate calculation of each species

As mentioned before, the maximum flow rate for the evaporator is 350 g/hour=0.09722 g/second. To maintain the STCR over 2.0 for the SR process, the following relationship

$$\left(\frac{\dot{m}_{H_2O}}{\dot{m}_{CH_4}} > 2.0 \right) \text{ should be met between the mass flow rate of } H_2O \text{ and } CH_4. \text{ Due to the limited}$$

capacity of the evaporator, the lowest mass flow rate (0.0826 g/sec) was chosen for the flow rate of the water metering pump.

Appendix F

Etc.

Future work

The effective functional range can be found by connecting a digital controlling apparatus of BOP to the developed SOFC power generating system. Building a proper digital control unit is a future goal of the research. In other words, future projects are the design and implementation of the fuel cell control system and a design of power control scheme for the fuel cell power generation system.

The BOP system should be made to ensure the application of the SOFC. The object of this research is to establish the system technology for SOFC Power Generation System (Plant). The main goal is to come up with a compact power plant system and components. The SOFC power plant BOP system consists of several components such as reformer, after burner, HEX, etc.

In my future research, I will develop dynamic integrated modules that can be communicated with any auxiliary devices of an entire system. I will also collaborate with colleagues in the area of control to improve the developed technology up to a suitable level that has a control function to choose proper sub-devices such as the blower/compressor and GT. Through the research, I will develop several in-house computer programs. With my future project sponsors, I will consider licensing one of the computer software programs developed in my lab. I am very enthusiastic about pursuing these goals in an academic setting where opportunities for collaborations across diverse fields are abundant and where revolutionary thinking is encouraged.

As reported in the DOE BESAC report "Directing Matter and Energy: five Challenges in Science and Imagination", understanding the physical behavior of complicated energy systems with multi-physical domains operating beyond equilibrium conditions poses significant scientific and engineering challenges. The SOFC system has multiple physical domains interacting with each other through different physical phenomena in a different time scale. Due to the complicated flows characterized by a large thermal mass, mass storage effect within ducts and

channels, flow inertia, and electrochemical reactions, the system is operating at far beyond a thermodynamic steady state during many operating conditions.

The evolving integrated computational model can be used as a valuable tool for the system-level optimization of individual sub systems and the balance of plants. The individual optimization of each subsystem is very difficult in current practices due to so many unknown thermal/electrochemical boundary conditions once they are placed within the flow passages of complete SOFC systems. The developed computational model combines all the subsystems using transient mass (or molar) continuity and energy equations allowing one to predict all the thermodynamic and chemical properties over the flow passages once only the global boundary conditions at system-level inlets and outlets are specified. Once the developing research is successfully finished, the computational model will provide the most innovative engineering design tool of SOFC systems to academia and industry.

The developing research will have a significant impact on the academic and industry professionals working on SOFC system development. For economic consideration, the research enables the US to remain a leader in the fuel cell industry in both commercial and military applications. The knowledge and understanding of the thermal dynamics of the SOFC system obtained through the research will provide the most efficient engineering solution reducing the lead-time for the development of the SOFC systems. The research outcomes will be disseminated through industrial seminars, local ASME meetings, presentations at international conferences, journal publications, and the graduate-level course curriculum.

References

- [1] Larminie, J., 2003, *Fuel Cell Systems Explained (2nd edition)*, John Wiley & Sons, Inc, London, England.
- [2] Lu, Y., Schaefer, L., and Li, P., 2005, "Numerical Study of a Flat-Tube High Power Density Solid Oxide Fuel Cell Part I. Heat/mass Transfer and Fluid Flow," *Journal of Power Sources*, 140, pp. 331-339.
- [3] "Development of a Low Cost 3-10kW Tubular SOFC Power System" available at http://www.hydrogen.energy.gov/pdfs/review10/fc032_bessette_2010_o_web.pdf.
- [4] Mench, M.M., 2008, *Fuel Cell Engines*, JOHN WILEY & SONS, INC., Hoboken, NJ, pp. 438-441.
- [5] Singhal, S. C., 2000, "Advances in Solid Oxide Fuel Cell Technology," *Solid State Ionics*, 135(1-4), pp. 305-313.
- [6] Singhal, S. C., 2002, "Solid Oxide Fuel Cells for Stationary, Mobile, and Military Applications," *Solid State Ionics*, 152/153, pp. 405-410.
- [7] Pramuanjaroenkij, A., Kakaç, S., and Zhou, X. Y., 2008, "Mathematical Analysis of Planar Solid Oxide Fuel Cells," *International Journal of Hydrogen Energy*, 33, pp. 2547-2565.
- [8] Bae, J., Lim, S., and Jee, H., 2007, "Small Stack Performance of Intermediate Temperature-Operating Solid Oxide Fuel Cells using Stainless Steel Interconnects and Anode-Supported Single Cell," *Journal of Power Sources*, 172, pp. 100-107.
- [9] "DOE SECA Program" available at <http://www.netl.doe.gov/technologies/coalpower/fuelcells/seca/>.
- [10] "SOFC Developer: Acumentrics Corporation" available at <http://www.acumentrics.com/products-power-generators.htm>.
- [11] "SOFC Developer: Cummins Power Generation" available at <http://www.cumminspower.com/na/about/environmental/fuelcells/>.
- [12] "SOFC Developer: Delphi Automotive Systems LLC" available at <http://delphi.com/manufacturers/auto/fuelcells/seca/>.
- [13] "SOFC Developer: Fuel Cell Energy, Inc." available at [http://www.fuelcellenergy.com/files/SOFC%20Thrust%20Area.pdf#search="SECA"](http://www.fuelcellenergy.com/files/SOFC%20Thrust%20Area.pdf#search=).
- [14] "SOFC Developer: Siemens Power Generation" available at <http://www.powergeneration.siemens.de/products-solutions-services/products-packages/fuel-cells/seca-program-schedule/>.

- [15] "Developer of SOFC-MGT Hybrid: Siemens Westinghouse" available at <http://www.powergeneration.siemens.com/products-solutions-services/products-packages/fuel-cells/sofc-gt-hybrid/SOFC-GT-hybrid.htm>.
- [16] Traverso, A., Massardo, A. F., and Scarpellini, R., 2006, "Externally Fired Micro-Gas Turbine: Modelling and Experimental Performance," *Applied Thermal Engineering*, 26(16), pp. 1935-1941.
- [17] Achenbach, E., 1994, "Three-Dimensional and Time-Dependent Simulation of a Planar Solid Oxide Fuel Cell Stack," *Journal of Power Sources*, 49, pp. 333-348.
- [18] Costamagna, P., and Honegger, K., 1998, "Modeling of Solid Oxide Heat Exchanger Integrated Stacks and Simulation at High Fuel Utilization," *Journal of Electrochemical Society*, 145(11), pp. 3995-4007.
- [19] Li, J., Cao, G. Y., Zhu, X. J., and Tu, H. Y., 2007, "Two-Dimensional Dynamic Simulation of a Direct Internal Reforming Solid Oxide Fuel Cell," *Journal of Power Sources*, 171, pp. 585-600.
- [20] Yi, Y., Rao, A. D., Brouwer, J., and Samuelson, G. S., 2004, "Analysis and Optimization of a Solid Oxide Fuel Cell and Intercooled Gas Turbine (SOFC-ICGT) Hybrid Cycle," *Journal of Power Sources*, 132, pp. 77-85.
- [21] Tucker, D., Lawson, R., VanOsdol, J., Kislear, J., and Akinbobuyi, A., 2006, "Examination of Ambient Pressure Effects on Hybrid Solid Oxide Fuel Cell Turbine System Operation using Hardware Simulation," *Turbo Expo 2006*, Barcelona, Spain, May 8–11, 2006, ASME Paper GT2006-91291.
- [22] Robert, R. A., Brouwer, J., and Samuelson, G. S., 2006, "Fuel cell/gas Turbine Hybrid System Control for Daily Load Profile and Ambient Condition Variation," *Turbo Expo 2006*, ASME Paper GT2006-90741.
- [23] Costamagna, P., Magistri, L., and Massardo, A. F., 2001, "Design and Part-Load Performance of a Hybrid System Based on a Solid Oxide Fuel Cell Reactor and a Micro Gas Turbine," *Journal of Power Sources*, 96(2), pp. 352-368.
- [24] Shelton, M., Celik, I., Liese, E., Tucker, D., and Lawson, L., 2005, "A Transient Model of A Hybrid Fuel Cell/Gas Turbine Test Facility using Simulink," *Proceedings of Turbo Expo 2005*, Power for Land, Sea and Air, Reno-Tahoe, Nevada, USA, June 6-9, ASME Paper No GT2005-68467.
- [25] Mueller, F., Gaynor, R., Auld, A. E., Brouwer, J., Jabbari, F., and Samuelson, G. S., 2008, "Synergistic Integration of a Gas Turbine and Solid Oxide Fuel Cell for Improved Transient Capability," *Journal of Power Sources*, 176(1), pp. 229-239.
- [26] A. J. Slippey, 2009, *Dynamic Modeling and Analysis of Multiple SOFC System Configurations*, M.S. thesis, Rochester Institute of Technology.

- [27] Apfel, H., Rzepka, M., Tua, H., and Stimming, U., 2006, "Thermal Start-Up Behaviour and Thermal Management of SOFC's," *Journal of Power Sources*, 154, pp. 370-378.
- [28] Rancruel, D., and Spakovsky, M., 2005, "Investigation of the Start-Up Strategy for a Solid Oxide Fuel Cell Based Auxiliary Power Unit Under Transient Conditions," *Int. J. of Thermodynamics*, 8, pp. 103-113.
- [29] Ferrari, M., Traverso, A., Pascenti, M., and Massardo, A., 2007, "Early Start-Up of Solid Oxide Fuel Cell Hybrid Systems with Ejector Cathodic Recirculation: Experimental Results and Model Verification," *J. Power and Energy*, 221, pp. 627-635.
- [30] Barzi, Y., Ghassemi, M., and Hamed, M., 2009, "Numerical Analysis of Start-Up Operation of a Tubular Solid Oxide Fuel Cell," *International Journal of Hydrogen Energy*, 34, pp. 2015-2025.
- [31] Kakaç, S., Pramuanjaroenkij, A., and Liu, H., 2002, *Heat Exchangers: Selection, Rating, and Thermal Design (2nd Edition)*, CRC Press, Boca Raton, FL.
- [32] "Heat exchanger - Wikipedia" available at http://en.wikipedia.org/wiki/Heat_exchanger#cite_note-0.
- [33] O'Hayre, R.P., Cha, S., Colella, W., 2006, *FUEL CELL FUNDAMENTALS*, JOHN WILEY & SONS, INC., pp. 282-304.
- [34] Willamas, M. C., and George, T. J., 1992, "Research Issues in Molten Carbonate Fuel Cells: Pressurization," *IECEC*, 3, pp. 263-267.
- [35] Buchanan, T., Hirschenhofer, J., Stauffer, D., September, 1994, "Carbon Dioxide Capture in Fuel Cell Power Systems," *G/C*, 2981, .
- [36] Ahn, S., Krumpelt, M., Kumar, R., Lee, S., Carter, J., Wilkenhoener, R., and Marshall, C., "CATALYTIC PARTIAL OXIDATION REFORMING OF HYDROCARBON FUELS," , Palm Springs, CA, November 16-19, 1998.
- [37] Pukrushpan, J., Stefanopoulou, A., Varigonda, S., Pedersen, L., Ghosh, S., and Peng, H., "Control of Natural Gas Catalytic Partial Oxidation for Hydrogen Generation in Fuel Cell Applications," *American Control Conference*, Denver, Colorado, June 4-6, 2003.
- [38] Chaniotis, A., and Poulidakos, D., 2005, "Modeling and Optimization of Catalytic Partial Oxidation Methane Reforming for Fuel Cells," *Journal of Power Sources*, 142, pp. 184-193.
- [39] Achenbach, E., and Riensche, E., 1994, "Methane/steam Reforming Kinetics for Solid Oxide Fuel Cells," *Journal of Power Sources*, 52, pp. 283-288.
- [40] Peters, R., Dahl, R., Kluttgen, U., Palm, C., and Stolten, D., 2002, "Internal Reforming of Methane in Solid Oxide Fuel Cell Systems," *Journal of Power Sources*, 106, pp. 238-244.
- [41] Agnew, G. D., Bernardi, D., Collins, R. D., and Cunningham, R. H., 2006, "An Internal Reformer for a Pressurised SOFC System," *Journal of Power Sources*, 157, pp. 832-836.

- [42] Nikooyeh, K., Ayodeji, A., Jeje, A., and Hill, J. M., 2007, "3D Modeling of Anode-Supported Planar SOFC with Internal Reforming of Methane," *Journal of Power Sources*, 171, pp. 601-609.
- [43] Janardhanan, V. M., Heuveline, V., and Deutschmann, O., 2007, "Performance Analysis of a SOFC Under Direct Internal Reforming Conditions," *Journal of Power Sources*, 172, pp. 296-307.
- [44] Patel, K. S., and Sunol, A. K., 2006, "Dynamic Behavior of Methane Heat Exchange Reformer for Residential Fuel Cell Power Generation System," *Journal of Power Sources*, 161, pp. 503-512.
- [45] Klein, J., Bultel, Y., Georges, S., and Pons, M., 2007, "Modeling of a SOFC Fuelled by Methane: From Direct Internal Reforming to Gradual Internal Reforming," *Chemical Engineering Science*, 62, pp. 1636-1649.
- [46] Aguiar, P., Chadwick, D., and Kershenbaum, D., 2002, "Modelling of an Indirect Internal Reforming Solid Oxide Fuel Cell," *Chemical Engineering Science*, 57, pp. 1665-1677.
- [47] Dicks, A. L., 1998, "Advances in Catalysts for Internal Reforming in High Temperature Fuel Cells," *Journal of Power Sources*, 71, pp. 111-122.
- [48] Anxionnaz, Z., Cabassud, M., Gourdon, C., and Tochon, P., 2008, "Heat exchanger/reactors (HEX Reactors): Concepts, Technologies: State-of-the-Art," *Chemical Engineering and Processing*, 47(12), pp. 2029-2050.
- [49] Pan, L., and Wang, S., 2005, "Modeling of a Compact Plate-Fin Reformer for Methanol Steam Reforming in Fuel Cell Systems," *Chemical Engineering Journal*, 108, pp. 51-58.
- [50] Stefanidis, G., and Vlachos, D., 2008, "Millisecond Methane Steam Reforming Via Process and Catalyst Intensification," *Chemical Engineering and Technology*, 31(8), pp. 1201-1209.
- [51] Zhang, H., Wang, L., Weng, S., and Su, M., 2008, "Performance Research on the Compact Heat Exchange Reformer used for High Temperature Fuel Cell Systems," *Journal of Power Sources*, 183, pp. 282-294.
- [52] Lee, A. L., Zabransky, R. F., and Huber, W. J., 1990, "Internal Reforming Development for Solid Oxide Fuel Cells," *Industrial & Engineering Chemistry Research*, 29, pp. 766-773.
- [53] Fox, R.W., and McDonald, A.T., 1999, *INTRODUCTION TO FLUID MECHANICS*, John Wiley & Sons, Inc., pp. 359-361.
- [54] Incropera, F.P., and Dewitt, D.P., 2002, *Introduction to Heat Transfer (4th Edition)*, John Wiley & Sons, Inc., New York, pp. 453-468.
- [55] Chapra, S.C., 2008, *Applied Numerical Methods with MATLAB (2nd)*, McGraw Hill, pp. 460.

- [56] Ahmed, S., McPheeters, C., and Kumar, R., 1991, "Thermal-Hydraulic Model of a Monolithic Solid Oxide Fuel Cell," *Journal of the Electrochemical Society*, 138(9), pp. 2712-2718.
- [57] Petruzzi, L., Cocchi, S., and Fineschi, F., 2003, "A Global Thermo-Electrochemical Model for SOFC Systems Design and Engineering," *Journal of Power Sources*, 118(1-2), pp. 96-107.
- [58] Iwata, M., Hikosaka, T., Morita, M., Iwanari, T., Ito, K., Onda, K., Esaki, Y., Sakaki, Y., and Nagata, S., 2000, "Performance Analysis of Planar-Type Unit SOFC Considering Current and Temperature Distributions," *Solid State Ionics*, 132(3-4), pp. 297-308.
- [59] Ferguson, J. R., Fiard, J. M., and Herbin, R., 1996, "Three-Dimensional Numerical Simulation for various Geometries of Solid Oxide Fuel Cells," *Journal of Power Sources*, 58(2), pp. 109-122.
- [60] Whitten, K.W., Davis, R.E., and Peck, M.L., 2004, *General Chemistry*, Brooks/Cole.
- [61] Xu, J., and Froment, G., 1989, "Methane Steam Reforming, Methanation and Water-Gas Shift: 1. Intrinsic Kinetics," *AIChE. Journal*, 35(1), pp. 88-96.
- [62] Bird, R.B., Stewart, W.E., and Lightfoot, E.N., 2001, *Transport Phenomena*, John Wiley & Sons, Inc., pp. 27.
- [63] Mueller, F., and Jabbari, F., 2007, "Novel Solid Oxide Fuel Cell System Controller for Rapid Load Following," *Journal of Power Sources*, 172, pp. 308-323.
- [64] Smith, J.M., Van Ness, H.C., and Abbott, M.M., *Introduction to Chemical Engineering Thermodynamics*, 7th edition, McGraw-Hills.
- [65] Ki, J., Kim, D., and Honavara-Prasad, S., 2012, "Dynamic Modeling of a Compact Heat Exchange Reformer for High Temperature Fuel Cell Systems," *Journal of Fuel Cell Science and Technology*, 9, pp. 011013-01-16.
- [66] Minh, N. Q., 1993, "Ceramic Fuel Cells," *Journal of the American Ceramic Society*, 76(3), pp. 563-588.
- [67] Soren Koch, 2002, *Contact Resistance of Ceramic Interfaces Between Materials Used for Solid Oxide Fuel Cell Applications*, Ph.D. thesis, The Technical University of Denmark at the Department of Chemistry.
- [68] Bard, A.J., and Faulkner, L.R., 2001, *Electrochemical Methods. Fundamentals and Applications (2nd Edition)*, Wiley, New York.
- [69] Li, P., and Kotwal, A., 2009, "An Easy-to-Approach and Comprehensive Model for Planar Type SOFCs," *International Journal of Hydrogen Energy*, 34, pp. 6393-6406.
- [70] Aguiar, P., Adjiman, C., and Brandon, N., 2004, "Anode-Supported Intermediate Temperature Direct Internal Reforming Solid Oxide Fuel Cell. I: Model-Based Steady-State Performance," *Journal of Power Sources*, 138, pp. 120-136.

[71] Jung, H., Kim, W., and Choi, S., 2006, "Effect of Cathode Current-Collecting Layer on Unit-Cell Performance of Anode-Supported Solid Oxide Fuel Cells," *Journal of Power Sources*, 155, pp. 145-151.

[72] ANSYS FLUENT, "Fuel Cells Module Manual," .

Biographical Information

I was born in Daegu, South Korea. I was especially interested in mechanical engineering and energy system. Luckily, my parents encouraged those interests. I earned B.S. degree in mechanical engineering at Hongik University and M.S. degree in mechanical engineering at University of Arizona, Ph.D. degree at University of Texas at Arlington.

My research interests are Thermal/Fluid sciences in renewable energy systems such as alternative fuel reforming process and integration, multiphase flow, heat and mass transfer in thermo-fluids, modeling and system dynamics of solid oxide fuel cell (SOFC) and gas turbine hybrid systems, turbo machinery aerodynamics, and micro turbomachinery.